# HIE-ISOLDE

Technical Design Report for the Energy Upgrade

Editors: Y. Kadi
M. A. Fraser
A. Papageorgiou-Koufidou

This volume is indexed in: CERN Document Server (CDS), INSPIRE.
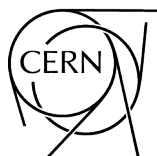
This volume should be cited as:

HIE-ISOLDE: Technical Design Report for the Energy Upgrade, edited by Y. Kadi, M. A. Fraser and A.
Papageorgiou-Koufidou, CERN Yellow Reports: Monographs, Vol. 1/2018, CERN-2018-002-M
(CERN, Geneva, 2018). https//doi.org/10.23731/CYRM-2018-001

# Abstract

The Isotope mass Separator On-Line facility (ISOLDE) at CERN occupies a leading position in the field of radioactive ion beams research, as it can produce the largest range of isotopes worldwide —over 1000 isotopes of more than 70 elements. HIE-ISOLDE (High Energy and Intensity – ISOLDE) is an upgrade that aims to increase the facility's energy and intensity reach, opening the way to new opportunities in multiple fields of physics: nuclear and atomic physics, astrophysics and fundamental interactions. This technical design report presents the HIE-ISOLDE energy upgrade as built. The report is divided in six parts. The first details the motivation behind the project, as well as previous experiences with post-accelerated beams at the facility. The second part presents the design of the new linear accelerator and its components, including cryomodules, superconducting cavities and solenoids, while the third focuses on beam dynamics. General services and systems are presented in the fourth part, while the fifth and sixth concern safety procedures and commissioning respectively.

# Contributors

J. Bauche[1], A-P. Bernardes[1], C. Bertone[1], E. Bravin[1],  E. D. Cantero[2], N. Delruelle[1], M. A. Fraser[1],
M. J. G. Borge[1], J-C. Gayde[1], B. Goddard[1], Y. Kadi[1], G. Kautzmann[1], F. Klumb[1], F. Locci[1],
Y. Leclercq[1], M. Martino[1], R. Mompo[1], R. Necca[1], V. Parma[1], P. Pepinster[1], E. Siesling[1],
J. A. Rodriguez[1], S. Russenschuk[1], J. Somoza[1], D. Smekens[1], D. Valuch[1], W. Venturini Delsolaro[1],
L. Williams[1], F. Wenander[1]

[1]CERN - 1211 Geneva 23 - Switzerland

[2]Consejo Nacional de Investigaciones Científicas y Técnicas (CONICET) and Comisión Nacional de Energía Atómica (CNEA), Centro Atómico Bariloche, Argentina

# Contents

CHAPTER 16—Beam instrumentation

CHAPTER 17—Normal conducting magnets

CHAPTER 18—Survey for assembly, installation and alignment

CHAPTER 19—Controls and interlocks

CHAPTER 20—Civil engineering and infrastructure

CHAPTER 21—Cranes and handling tools

# VI Commissioning 227

# Tables

# Figures

xvii

# Acronyms and abbreviations

ADC         Analogue–Digital Converter
ASTM        American Society for Testing and Materials
BINP        Budker Institute of Nuclear Physics, Russia
BNL         Brookhaven National Laboratory, USA
BPM         Beam Position Monitor
CCDTL       Cell-Coupled Drift Tube Linac
CEA         Commissariat pour l'Energie Atomique, France
CEBAF       Continuous Electron Beam Accelerator Facility, USA
CNRS-IPN    Centre National de la Recherche Scientifique–Institut de Physique Nucléaire d'Orsay
CP          Chemical Polishing
CST         Computer Simulation Technology AG, Germany
CW          Continuous Wave (operation)
DAC         Digital–Analogue Converter
DC          Direct Current
DESY        Deutsches Elektronen SYnchrotron, Germany
DSP         Digital Signal Processor
DTL         Drift Tube Linac
DWT         double-walled tube
EB          Electron-Beam (welding)
ECL         Emitter-Coupled Logic
EMQ         Electromagnetic Quadrupole
EP          Electropolishing
ESS         European Spallation Source
EURISOL     EURopean Isotope Separation On-Line (study)
EUROnu      European Commission FP7 Design Study, 'A High Intensity Neutrino Oscillation
            Facility in Europe'
FLUKA       FLUktuierende KAskade, Monte Carlo simulation package
FNAL        Fermi National Accelerator Laboratory, USA
FP7         European Framework Programme 7
FPGA        Field-Programmable Gate Array
GSI         GSI Helmholtzzentrum für Schwerionenforschung GmbH
HFSS        High Frequency Structural Simulator, Ansys Inc., USA
HOM         Higher-Order Mode
HP-SPL      High-Power SPL
HPR         High-Pressure Water Rinsing
HV          High Voltage; Vickers pyramid number
IF          Intermediate Frequency
INFN        Istituto Nazionale di Fisica Nucleare, Italy
IOT         Inductive Output Tube
ISIS        ISIS Pulsed Neutron Source, UK
ISO         International Organization for Standardization
ISOLDE      Isotope Separator On Line DEvice, experiment at CERN
ISR         Intersecting Storage Rings
ISTC        International Science and Technology Center, Russia
JLAB        Jefferson Laboratory, USA

| | |
|---|---|
| LANL | Los Alamos National Laboratory, USA |
| LEBT | Low-Energy Beam Transport |
| LEP | Large Electron–Positron Collider at CERN |
| LHC | Large Hadron Collider at CERN |
| Linac | Linear Accelerator |
| Linac4 | 160 MeV proton linac at CERN |
| LLRF | Low-Level RF |
| LO | Local Oscillator |
| LP-SPL | Low-Power SPL |
| MEBT | Medium-Energy Beam Transport |
| MLI | Multilayer Insulation |
| MOSFET | Metal–Oxide–Semiconductor Field Effect Transistor |
| MTBM | Mean Time Between Maintenance |
| NC | Normal-Conducting |
| NCBJ | National Centre for Nuclear Physics, Poland |
| nTOF | Neutron Time-Of-Flight Experiment at CERN |
| OFE | Oxygen-Free Electronic (copper) |
| OST | Oscillating Superleak Transducer |
| PIMS | PI-Mode Structure |
| PMQ | Permanent Magnetic Quadrupole |
| ppp | protons per pulse |
| PS | Proton Synchrotron at CERN |
| PS2 | Proton Synchrotron 2 at CERN (study) |
| PSB | PS Booster at CERN |
| RCS | Rapid Cycling Synchrotron |
| RF | Radio Frequency |
| RFQ | Radio Frequency Quadrupole |
| r.m.s. | root mean square |
| RRR | Residual Resistivity Ratio (resistivity at 300 K/residual resistivity at operating temperature) |
| SC | Superconducting |
| SCL | Side-Coupled Linac |
| sLHCpp | super Large Hadron Collider preparatory phase |
| SMD | Simulation of Higher-Order Mode Dynamics |
| SNS | Spallation Neutron Source, USA |
| SPC | Scientific Policy Committee, CERN |
| SPL | Superconducting Proton Linac at CERN (study) |
| SPS | Super Proton Synchrotron at CERN |
| TEM | Transverse Electric Magnetic |
| TESLA | TeV Energy Superconducting Linear Accelerator project. Lead laboratory, DESY, Germany (study) |
| UHV | Ultrahigh Vacuum |
| VME | Versa Module Europa (bus standard) |
| VNA | Vector Network Analyser |
| VNIITF | All-Russian Scientific Research Institute of Technical Physics, Russia |
| XFEL | X-ray Free Electron Laser, Europe |

# Part I

# Introduction

# Chapter 1

# Physics motivation and beam requirements

M.J.G. BORGE

## 1.1 Physics opportunities

The HIE-ISOLDE project is part of a world-wide effort to improve upon radioactive beams, a branch of nuclear structure physics that during the past years has moved from a speciality subject to the mainstream. This dramatic move has been triggered by the observation of significant changes in nuclear structure [1], as one moves away from the stable nuclei towards the neutron (and proton) drip lines. In addition, it has been boosted by substantial technical progress that has provided the experiments with higher quality and intensity radioactive beams.

One of the challenges, and charms, of nuclear physics is that nuclei exhibit many different degrees of freedom. The most important distinction, and unique to nuclear matter, is between single particle and collective degrees of freedom. The fact that nuclei are composed of two different types of fermions—protons (Z) and neutrons (N)—adds considerably to the richness of the phenomena observed. It is the task of nuclear structure physics to unravel the myriad of quantum structure effects and to find the ordering principles. Presently, the field of nuclear structure is seeing a boost due to the ability to do detailed experiments with short-lived nuclei, often called exotic.

The study of radioactive ion beams (RIB) from close to stability to the far limit of production allows us to follow the evolution of nuclear structure over an extensive region of the nuclear chart. Studies of the structural evolution are a source of fundamental information on the nuclear many-body system, for example the modification and possible breakdown of the concept of shell structure at the drip lines and the investigation of new collective modes of exotic nuclei with extreme neutron-to-proton ratios. Exotic nuclei with extreme differences in the number of protons and neutrons (large isospin values) will provide stringent constraints on the microscopic description of nuclear structure as well as nuclear dynamics. Many new phenomena have been observed by the exploration of a series of isotopes (elements with equal Z numbers) and isotones (elements with equal N numbers) moving away from stability, for instance halo nuclei, new shapes, intruder states, phase and shape coexistence, proton-neutron pairing and isospin mixing. Learning about the evolution of nuclear structure when moving away from stability will give access to a deeper understanding of nuclear interactions.

Nuclear astrophysics is a key interdisciplinary field concerned with the mechanism of energy production in stars and creation of elements in the universe. The synthesis of elements up to iron in normal stellar environments is well understood. However, the origin of the heaviest elements is still subject to debate. Nuclear properties are crucial for understanding the processes leading to the isotopic abundances in the universe. Stellar explosions such as novae, supernovae, X-ray bursts, neutron mergers and cataclysmic events release energy rapidly at great rates and release chemical elements into stellar space. The sequence of reactions that involve short-lived isotopes depends upon the balance between capture/fusion reaction rates and $\beta$ decay or the photo-disintegration process. Thus, the properties of these exotic nuclei are crucial and our understanding of them is presently incomplete.

The production of radioactive beams, therefore, is a high priority in the present planning of nuclear physics facilities on all continents, as it opens unprecedented possibilities in nuclear structure and nuclear astrophysics research, as discussed above. The main difficulty is that the two major ways of producing radioactive beams, in-flight and ISOL (Isotope Separation On Line), both rapidly decrease in intensity as we approach the exotic nuclei due to decreasing cross sections. In the in-flight method, beam fragments

continuing out of the target are employed so the target thickness is limited and with it the production of exotic nuclei, see article 014023 of [1]. In the ISOL method, slowed down (target) fragments are extracted, which introduces an extra delay. The two methods lead respectively either to high energies of hundreds of MeV/$u$ or to low energies ($30 - 60$ keV) of the radioactive beam. Although many beam manipulation procedures have been developed to cover as large an energy range as possible, the region from a few MeV/$u$ up to a few tens of MeV/$u$ has been the last energy region to be properly covered.

ISOLDE, in its 50 years of existence, has gone through many phases and upgrades to assure a physics programme at the forefront of nuclear physics research. This ISOL facility has improved its capabilities dramatically over the years, growing from an experiment into a facility fully integrated in the CERN infrastructure [2]. A key ingredient of its long lifetime is the wide range of purified beams of individual nuclei that can be produced using CERN's high-energy beams and the accumulated experience in the construction of target-ion source units. ISOLDE's success lies in the uniqueness of the methods developed there.

In the 1990s, the ISOLDE community developed new ways to accelerate singly-charged radioactive ion beams to several MeV/$u$ in a universal, fast, efficient and cost-effective way. The proposal for REX-ISOLDE (Radioactive beam EXperiment at ISOLDE) was put forward in 1994 [3] and was approved as experiment IS347. A conceptual novelty of the REX-ISOLDE acceleration scheme, in operation since 2001, was the decoupling of the production of radioactive ions from the ionisation to highly-charged ions, the latter needed for efficient acceleration. The two steps can thereby be optimised independently, and one can in particular benefit from the availability of many low-energy radioactive beams from ISOLDE.

The original aim of the REX-ISOLDE project [4] was to post-accelerate the beam to energies up to 2 MeV/$u$ and masses below $A = 50$. However the concept proved to be very successful and soon upgraded in energy. Thus, beams with $A/q$ ratio $< 4.5$ and with masses up to 224 were accelerated up to 3 MeV/$u$ (total energy 672 MeV), with efficiencies reaching 10%. To learn more about REX-ISOLDE, the experimental devices used and the scientific achievements see [5].

In order to broaden the scientific opportunities at ISOLDE beyond the reach of the existing facility, the HIE-ISOLDE upgrade (HIE stands for High Intensity and Energy) intends to improve the experimental capabilities at ISOLDE over a wide front [6]. The main aims are boosting the energy of the post-accelerated beams and increasing roughly sixfold the production of radioactive beams due to an increase in intensity and energy of the proton injector. The new physics domains that will open with the energy upgrade will be outlined here. However, experimentalists have more requirements for a beam than its intensity and energy. The purity of the beam (the level of contaminants) is often a crucial factor. For some experiments, the beam optical properties, its time structure, its energy definition or the flexibility of changing the energy could also be important. The HIE-ISOLDE initiative therefore also includes intensity upgrades as well as improvements of the beam quality. The increase of the final energy of the post-accelerated beams to 10 MeV/$u$ for elements throughout the periodic table will enable new nuclear physics domains to be studied at ISOLDE.

A facility upgrade of the magnitude of the HIE-ISOLDE project is justified based on the opportunities of the physics programme. The main attraction of the increase of beam energy at HIE-ISOLDE is that the reaction mechanisms evolve significantly from 3 MeV/$u$ to 10 MeV/$u$ with an strong enhancement of the inelastic reactions versus the elastic channel. One has to keep in mind that different types of reactions can address different nuclear degrees of freedom.

The new energy regime enables users to address most aspects of modern nuclear structure. The different facets of the programme will be briefly illustrated below using examples from the physics cases already approved.

When approaching the limits of existence, the decreasing binding energies and the proton-neutron asymmetry lead to a loosely bound quantum system with properties different to those of stable nuclei.

Many aspects of nuclear interaction are enhanced far away from stability. Halo nuclei occur when the last nucleons have low energy and momentum, so they appear in cases where the last nucleons occupy mainly s or p states. Close to the drip lines even low-lying excited states will be situated in the continuum, and Coulomb excitation will then instead lead to the break-up of the nucleus. Coulomb induced break-up has been employed at relativistic beam energy during the last few decades as a tool to study the most exotic nuclei, in particular the electric dipole response, but the potential for such reactions at a few MeV/$u$ has only been probed sporadically. Elastic scattering reactions also provide interesting information on exotic nuclei [7], in particular halo nuclei can give a response to elastic scattering different from the standard one. Due to the coupling to continuum states, the low-energy elastic scattering is strongly affected, see e.g. [8]. In order to study this effect, the reaction of the 1p-halo $^8$B will be studied. Proceeding further to unbound states, one elegant way of probing them is elastic resonance scattering. One of the approved experiments aims to employ this technique to study the proton-unbound nucleus $^{21}$Al using of the active target MAYA [9]. The objective is to test the conservation of symmetry between unbound and bound mirror nuclei, i.e. those isobars where the number of neutrons in one is equal to the number of protons in the other.

The structural evolution in atomic nuclei as a function of the neutron number N and the proton number Z can be largely understood as a result of the neutron–proton interaction. With the availability of a long series of isotopes at HIE-ISOLDE, this evolution can be probed. The neutron–proton interaction also plays an important role in the development of collectivity, configuration mixing and ellipsoidal shapes, single particle energies and magic numbers. Coulomb excitation studies give interesting physics with reduced beam intensities around $10^4$ ions/s, or even lower. When the analysis is performed at "safe" energies below the Coulomb barrier, known as Coulex, one can extract not only excitation energies and suggested spin-assignments from the observed gamma rays, but also information on the matrix elements for transitions among the observed states.

The higher beam energies at HIE-ISOLDE will significantly improve conditions for Coulomb excitation. One-step excitation can proceed to higher excitation energies; multi-step processes become more important and expand the number of transition matrix elements that can be extracted. Collective degrees of freedom, in particular deformation, are therefore clearly identified. Moreover, the evolution, e.g. along an isotopic chain, can give very direct information on the underlying shell structure. Quite a few of the approved experiments will exploit this property. Coulomb excitation studies are planned in the region of the so-called magic numbers N and $Z = 50$, N and $Z = 82$ and $N = 126$. For instance, the doubly magic nucleus $^{132}$Sn with its significantly higher $2^+$ state would be studied. This will allow for the possibility of having $2^+$ states based on both protons and neutrons and the exact configurations—full symmetry, mixed symmetry, proton or neutron dominance of the lowest two $2^+$ state—will be determined for first time. An important addition to the experimental capabilities is the installation of a plunger, which would allow the measurement of lifetimes of excited nuclear states in the picosecond range.

It is surprising that for a certain number of N and Z, a subtle rearrangement of a few nucleons among the orbital at the Fermi surface can result in a dramatic change of the nuclear shape. The phenomenon of nuclear coexistence is due to the fact that the potentials corresponding to different deformation have similar energies. Although much has been learnt about shape coexistence, several key questions remain, such as the degree of mixing between configurations. In order to address the question related to shape coexistence, Coulex is an attractive technique: (i) it preferentially excite states strongly coupled to the ground state, (ii) the sign of the diagonal quadrupole matrix element can be deduced so that prolate and oblate deformation can be distinguished, (iii) the degree of collectivity in the rotational band (deformation parameter) and mixing between the different structures can be obtained. The shape coexistence effect is expected in N=Z= 34 or 36 and in the neutron mid-shell nuclei, for instance near $Z = 82$ proton shell closure. In the same way, the interplay between quadrupole and octupole collectivities can be identified. The octupole structure is the consequence of the proximity of single-particle orbitals close to the Fermi surface and differing in three units in angular momentum. The best region to

explore this very exotic shape is around A = 225, where Coulex was used for inferring the state octupole collectivity in $^{224}$Ra and at the level of excited states in the n-rich Ba isotopes.

It has been described how to study the collective behaviour of nuclei, including how to identify shape coexistence, the single-particle degrees of freedom of nuclei are revealed in transitions populated by one-nucleon transfer reactions. In particular, single neutron or proton transfer mediated by (d,p), (p,d) and ($^{3}$He,d) reactions populate very selectively states in the recoiling nucleus and are very useful for unravelling the evolution of shell structure. The energy balance of the reaction gives information about the excitation energy of the states, the angular distribution is related with the spin and parity of the states. The total cross section provides information about the overlap of the structure of the original and recoiling nucleus (spectroscopic factor). The restriction of the energy range at REX-ISOLDE to at most 3.1 MeV/$u$ has so far confined transfer experiments to the lighter nuclei A $<$ 30. The optimum energy for nucleon transfer is closer to 10 MeV/$u$, where the angular distributions are more easily interpreted. The single-particle strength near N= 40, N= 50 and beyond will be explored by the study of $^{68}$Ni(d,p) and $^{70}$Ni(d,p) and $^{80}$Zn(d,p) reactions. In a separate line of investigation, the (d,p) reaction will be used to induce fission in heavy radioactive beams and thereby determine the fission barrier height, using in this case the active target ACTAR. The most efficient way to study (d,p) transitions will be the ISOLDE Solenoidal Spectrometer (ISS).

The highest energy at HIE-ISOLDE is enough to allow for two-nucleon transfer reactions, such as (t,p). Taking advantage of the increase in beam energy and employing the same tritium target technique, two HIE-ISOLDE experiments plan to use $^{9}$Li and $^{11}$Be beams to investigate unbound states at the neutron-drip line, namely excited states just above the two-neutron threshold in $^{11}$Li and the levels in the unbound nucleus $^{13}$Be. Continuing to even heavier targets, multi-nucleon transfer becomes important and allows access to other phenomena. When using a mid-mass nucleus on a $^{7}$Li target, one populates levels at high excitation energy such that several neutrons can be emitted. This mechanism will be used with a $^{132}$Sn beam to populate states in $^{133}$Sb that are so far unobserved. According to calculations, transfer from a heavy neutron-rich projectile could be used to populate nuclei such as $^{210}$Hg, where the current experimental data present puzzles for shell-model calculations.

Two neutron transfer (p,t) and ($^{10}$Be,$^{8}$Be) can be employed to get information on the pairing properties or resonant elastic scattering being the dominant process for resonances with a pronounced single-particle or cluster structure. In general, these techniques require beams over a wide energy range to match the conditions for optimal transfer and resonant scattering, such as the ones expected at HIE-ISOLDE.

The number of reaction studies motivated by nuclear astrophysics has increased at HIE-ISOLDE. The $^{7}$Li abundance anomaly in cosmology, where better knowledge on the $^{7}$Be reaction rates is needed is addressed using the $^{7}$Be(d,p) reaction. The $^{17}$N(d,p) reaction will be used to deduce the $^{17}$N(n,$\gamma$) rate that could be relevant for the r-process in neutrino-driven winds. In addition, the $^{59}$Cu(p,$\alpha$) reaction will be studied. This reaction plays a key role in the $\nu$p-process in core collapse supernovae and its rate is crucial in determining whether the process may produce sufficient amounts of the lighter p-nuclei, such as $^{92,94}$Mo whose abundance remains a problem. This is furthermore one of the few cases where the reaction rate is needed at high temperatures for the astrophysical scenario so that a direct measurement is possible at the energies of interest.

To summarise, there are plenty of challenging physics to be studied with the higher energy of the post-accelerated beams at ISOLDE. The variety and characteristics of beams available at HIE-ISOLDE will allow for the application of different methods to obtain the interesting information. In this introduction, we have addressed physics already approved for experiments. A wider view of the physics cases is reflected in the overview of HIE-ISOLDE scientific opportunities [6]. The experiments approved will mainly be realised in the beam time period until the CERN Long Shutdown 2, which starts in 2019. Figure 1.1 shows the chart of the nuclides; the nuclei of interest for the physics cases already approved for HIE-ISOLDE are indicated with red dots. The proposed studies will be realised with the existing

workhorses: the Miniball [10] $\gamma$ array for Coulex and T-REX [11] for transfer reaction studies. New instrumentation for transfer reaction studies is planned to be installed, such as the active targets MAYA [9] and the future ACTAR, a new general purpose scattering chamber, the two arms CORSET setup from GSI, etc. The ISS for high efficiency (d,p) reaction studies was also added. The Miniball array [10] is complemented with a plunger of lifetime measurements and with an electron spectrometer, SPEDE, to realise Coulomb excitation studies of odd-mass heavy nuclei. The addition of a Test Storage Ring is explored as an option, as it would allow for the realisation of experiments with stored secondary beams, a capability currently unique in the world. The proposed physics programme spans from investigations of nuclear ground state properties and reaction studies of astrophysical relevance to research with highly-charged ions and pure isomeric beams, for more details see [12].

The initial phase of HIE-ISOLDE started physics with its first radioactive beam on 22 October 2015. The very first experiment explored the evolution of nuclear structure near $^{78}$Ni by performing multi-step Coulomb excitation in n-rich Zn isotopes.
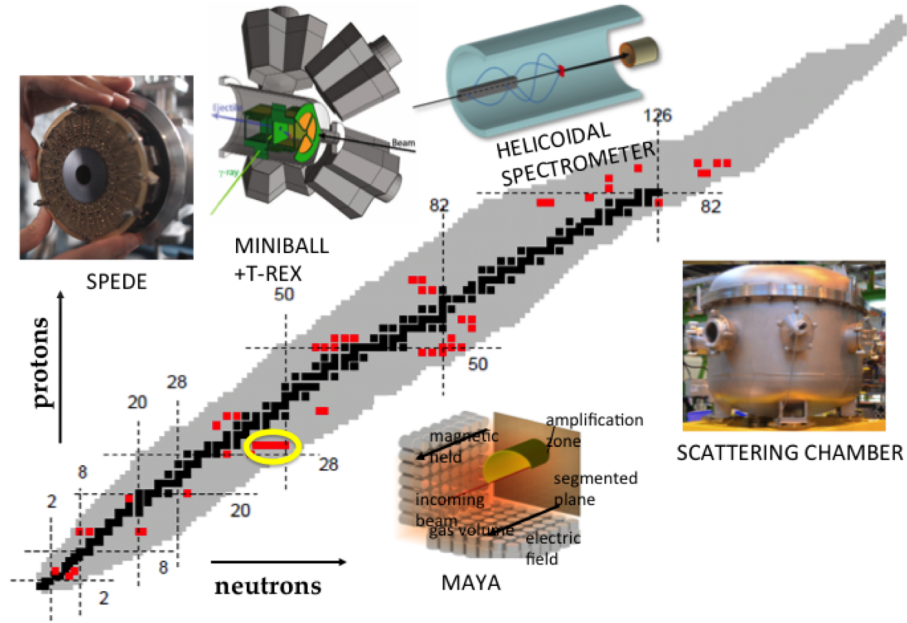


**Fig. 1.1:** The nuclear chart shows in red the cases approved in 2015 for nuclear studies at HIE-ISOLDE. The first physics cases studied in 2015, the n-rich Zn isotopes studied with Miniball, are indicated with a circle.

## 1.2 Beam design parameters

The wide-range of experimental techniques and instrumentation proposed in the accepted Letters of Intent submitted for research at HIE-ISOLDE have resulted in a large variety of beam specifications. Although the priority of each request is still to be finalised, the specification of the beam parameters is broadly summarised in Table 1.1.

Apart from the specification of increased energy with variability, the user community would like to see a reduction in beam halo and spot size at the experimental secondary targets. A beam diameter of approximately 6 mm ($\sim$ 3 mm FWHM) is currently achievable at the target position in Miniball at an energy of 3 MeV/$u$ [5]. The beam diameter will reduce on installation of the new superconducting HIE-linac, because of the adiabatic damping associated with the increasing beam energy, however the ultimate beam size will be limited by the transverse emittance of the ion source and the emittance growth in the REX front end. The time structure of the beam is also limited by the REX front end and any modifications made to achieve longer beam pulse lengths, quasi-continuous cw beams or even beams with an increased

**Table 1.1:** Requested beam characteristics at HIE-ISOLDE.

| Beam parameter | Description or value |
|---|---|
| Energy | continuous from $< 0.7$ to at least 10 MeV/$u$ |
| Beam spot diameter | $< 1 - 3$ mm FWHM |
| Beam divergence | $< 1 - 3$ mrad FWHM |
| Micro-bunch structure[a] | no requirement of micro-bunching to bunch at $< 1$ ns FWHM with $\sim 100$ ns bunch spacing |
| Macro-bunch structure[a] | longer pulse lengths or cw operation |
| Energy spread | $< 0.1\%$ |
| Absolute energy resolution[b] | no specific details given |

[a] The time structure of the beam is determined by the charge breeder and the REX front end, see Figure 2.4.

[b] No system currently exists to measure the absolute beam energy; time-of-flight systems are being discussed.

bunch spacing will require significant upgrades of the charge breeder or the installation of additional RF cavities, namely a multi-harmonic buncher upstream of the RFQ and a chopper downstream.

# References

[1] C. Fahlander and B. Jonson, editors, *Nobel Symposium 152: Physics with Radioactive Beams*, Göteborg, 2013.

[2] R Catherall et al., *J. Phys. G: Nucl. Part. Phys.* **44** (2017) 094002.

[3] D. Habs et al., Radioactive beam experiments at ISOLDE: Coulomb excitation and neutron transfer reactions of exotic nuclei, ISC-94-25. ISC-P-68 (CERN, 1994).

[4] F. Ames, J. Cederkäll, T. Sieber and F. Wenander, *The REX-ISOLDE Facility: Design and Commissioning Report* (CERN, Geneva, 2005).

[5] P. Van Duppen and K. Riisager, *J. Phys. G: Nucl. Part. Phys.* **38** (2011) 024005.

[6] M. J. G. Borge and K. Riisager, *Eur. Phys. J. A* **52** (2016) 334.

[7] N. Keeley, N. Alamanos, K. W. Kemper and K. Rusek, *Prog. Part. Nucl. Phys.* **63** (2009) 396.

[8] A. Diaz-Torres and A. M. Moro, *Phys. Lett. B* **733** (2014) 89.

[9] C. E. Demonchy et al., *Nucl. Instrum. Methods Phys. Res. A* **573** (2007) 145.

[10] J. Eberth et al., *Prog. Part. Nucl. Phys.* **46** (2001) 389.

[11] V. Bildstein et al., *Eur. Phys. J. A* **48** (2012) 1.

[12] M. Grieser et al., *Eur. Phys. J. ST* **207** (2012) 1.

# Chapter 2

# REX linac as injector

M.A. FRASER

The Radioactive ion beam EXperiment (REX) [1] was constructed at ISOLDE to test a unique charge breeding concept, coupling a Penning trap and an Electron Beam Ion Source (REXEBIS) to boost the charge state of radioactive ions before acceleration in a compact normal conducting linac. As its name suggests, REX was integrated at CERN as an experiment, which was designed and built by a range of collaborators under the auspices of the REX-ISOLDE Collaboration [1]. The linac was installed and commissioned at ISOLDE by the collaboration before being handed over to CERN later. The present status and latest developments at REX-ISOLDE can be found in [2]. A three-dimensional realisation of the REX post-accelerator is shown in Figure 2.1, with pictures of the charge breeder and the open accelerating cavities with their drift tubes exposed. An in-depth overview of the design and commissioning of the REX-ISOLDE facility can be found in [3] and a very brief technical introduction follows here.
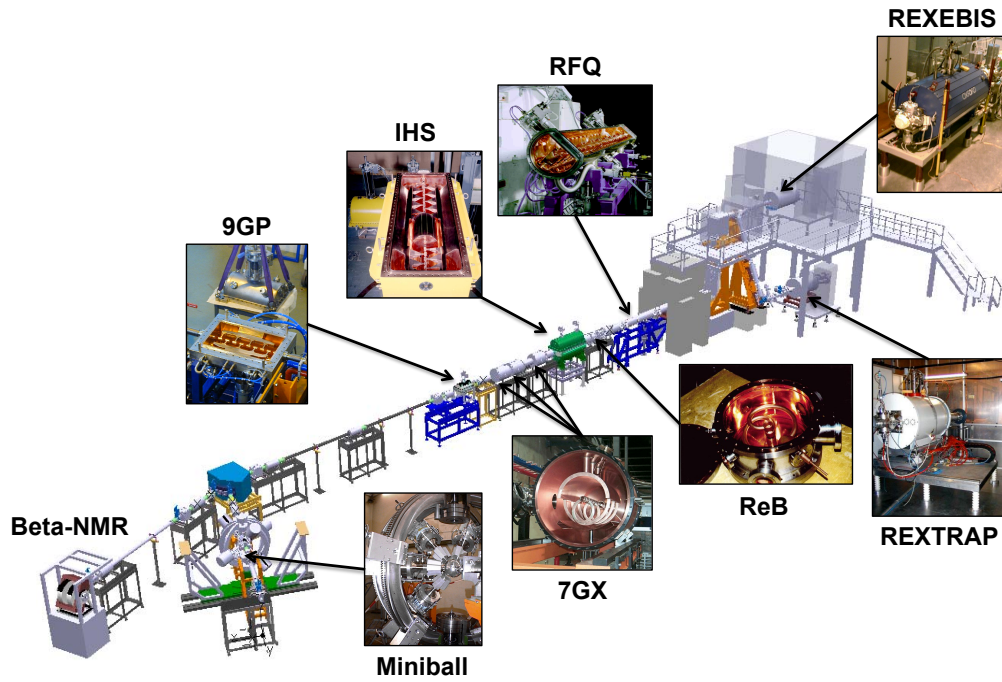


**Fig. 2.1:** The REX post-accelerator, delivering beams up to 3 MeV/$u$.

## 2.1 ISOLDE

The ISOLDE facility is shown schematically in Figure 2.2. Following the completion of the Proton Synchrotron Booster (PSB) ISOLDE upgrade in 1992, radioactive beams are produced by impinging

high intensity bunches of protons accelerated in the PSB up to between 1 - 1.4 GeV onto thick, heated ISOL targets located at either of two target stations: the General Purpose Separator (GPS) or High Resolution Separator (HRS) targets. The facility has a long history of target and ion source development, which can be found reviewed in [4]. ISOLDE is the heaviest user of the PSB and is able to take beam from the CERN accelerator complex in a parasitic mode whilst the Proton Synchrotron (PS) is ramping up and accelerating beams destined for the numerous other experimental areas.
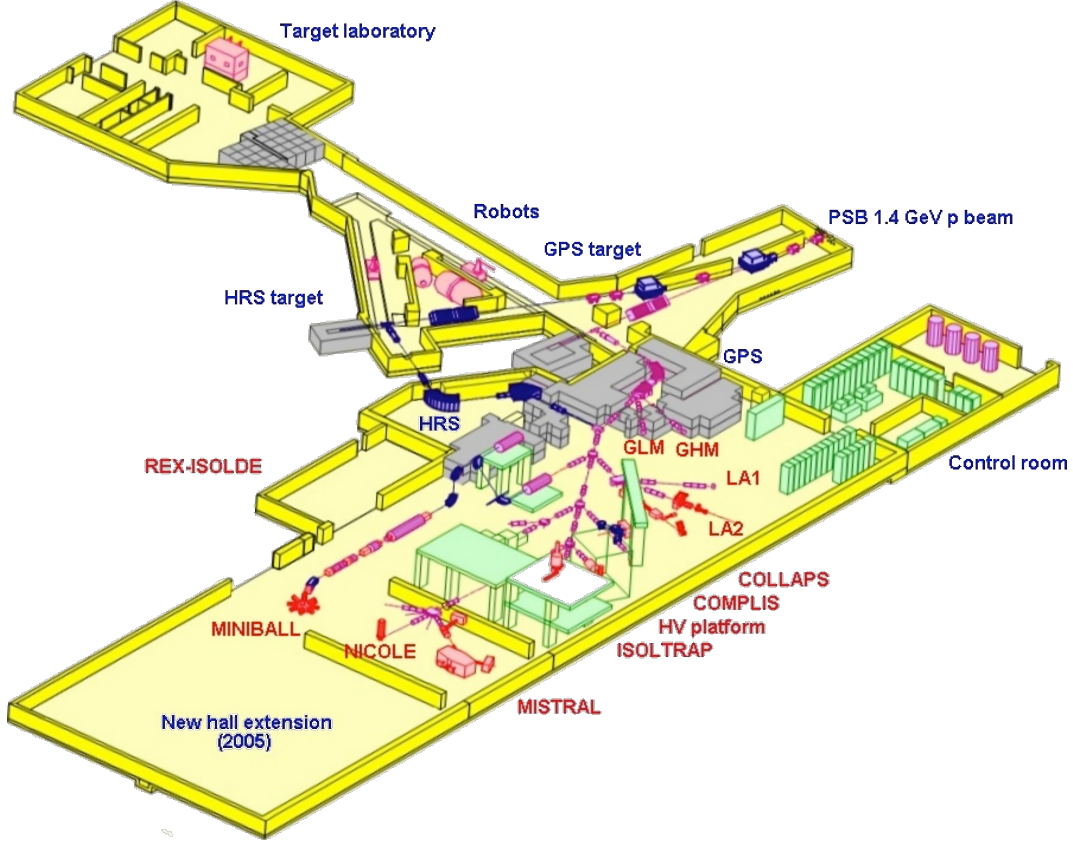


**Fig. 2.2:** Layout of the ISOLDE facility, including the extension to the experimental hall for the HIE-ISOLDE project.

Nominally, ISOLDE takes about half of all PSB batches in any given supercycle,[1] which consists of about a dozen or so PSB cycles and lasts about 15 s. The PSB repetition period is 1.2 s, providing an average proton current of 1.92 µA and an average beam power of a little under 3 kW at the ISOLDE target stations. After diffusion and effusion out of the target, the mixture of radionuclides is ionised to form singly-charged ions, which are accelerated through an electrostatic potential of either 30 or 60 kV and separated by the GPS ($\Delta M/M = 1/2400$) or HRS ($\Delta M/M = 1/11000$) magnetic mass spectrometers. The development of a laser ion source has been very successful at ISOLDE, which is reflected in its use for about half of the available beam time. The Resonance Ionisation Laser Ion Source (RILIS) [5] can selectively ionise isotopes of radioactive elements efficiently and quickly, even allowing isomeric beams to be isolated. The selected ions are then transported to experiments at either low energy, where they can be trapped at energies as low as $10^{-6}$ eV, or transported to REX where they can be accelerated up to 3 MeV/$u$. The facility has helped to make important contributions to the fields of nuclear structure and

---

[1]CERN's heart beats with the PSB every 1.2 s. A periodic sequence of PSB cycles taking protons to each experimental area is termed a supercycle and can last tens of seconds, e.g. protons could be sent to the PS and then the SPS for delivery to the North Area for the Fixed Target experimental physics programme, sent directly to ISOLDE, accelerated in the PS and sent for antiproton production and storage in the AD or sent up the complex to the LHC.

astrophysics, as well as atomic physics, solid-state physics, the life sciences and fundamental physics. An overview of the modern experimental programme can be found in the laboratory portrait [6].

## 2.2   Charge breeding: REXTRAP and REXEBIS

The tandem Penning trap and REXEBIS charge breeding system is shown schematically in Figure 2.3. The Penning trap cools the emittance of the quasi-continuous singly-charged ISOLDE beam from emittances typically greater than $30\,\pi$ mm mrad to below $10\,\pi$ mm mrad at 30 kV, so that it can be efficiently trapped and ionised in the narrow acceptance of the electron beam of REXEBIS. A mass separator [7] based on the Nier spectrometer [8] ($\Delta(A/q)/(A/q) = 1/150$) separates the beam extracted from REXEBIS, removing ionised residual gas impurities and selecting the mass-to charge state of the radioactive beam to be accelerated.
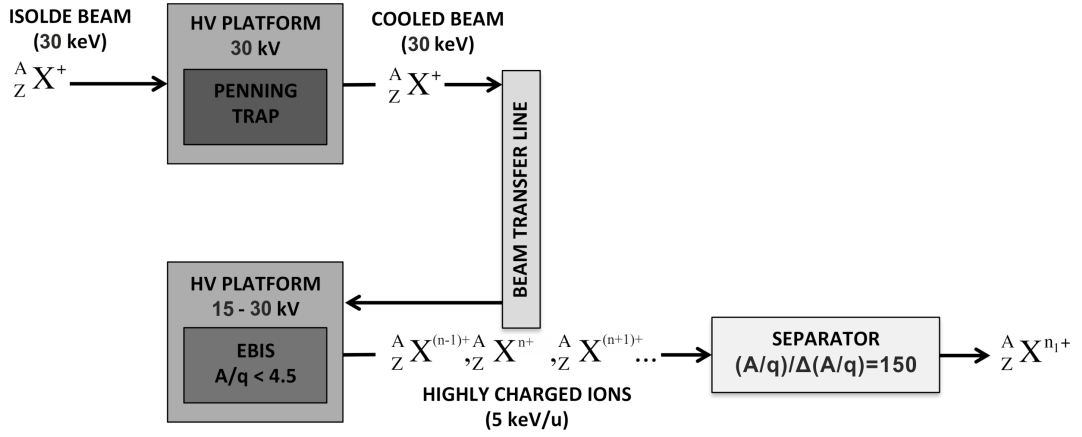


**Fig. 2.3:** Schematic layout of the charge breeding components at REX.

REXTRAP [9, 10] accumulates, bunches and cools the beam by having it interact with an inert buffer gas of neon or argon whilst it is trapped longitudinally in an electrostatic field applied on drift-tubes and transversely by a magnetic field produced by a 3 T superconducting solenoid. In addition, transverse electric RF fields are applied to damp the magnetron motion that becomes radially unstable under buffer gas collisions inside the trap, leading to cooling times of $\lesssim 20$ ms. Two differential pumping stages [11] provide good vacuum in the beam lines that lead in and out of REXTRAP.

REXEBIS [12, 13] uses a strongly focused electron beam compressed in the magnetic field of a superconducting solenoid to successively ionise trapped radioactive nuclides to the desired charge-state. The singly-charged radioactive ions are injected and trapped in the electron beam using a longitudinal electrostatic potential created by drift-tubes and transversely by the negative space-charge of the electron beam itself. Once the desired charge-state has been reached, the electrostatic trap is opened and the ions are extracted. The potential of the EBIS at extraction is scaled with the $A/q$ to match the velocity acceptance of the RFQ. The normalised transverse beam emittance is typically less than $0.3\,\pi$ mm mrad. The system was designed with light ions of $A < 50$ in mind and is capable of charge-boosting all singly-chargedc ions in this mass range up to $A/q < 4.5$ within 20 ms, which corresponds to the mass-to-charge state acceptance of the linac. The system has been used as a test bench for different methods of beam purification and breeding schemes. Space-charge effects in the Penning trap limit the ion throughput of the system to a few $10^8$ ions per pulse at 50 Hz. Although REXEBIS can in principle deliver over 1 particle-nA of radioactive beam, the intensities from ISOLDE are typically much lower. In addition, space-charge effects in the Penning trap limit the ion throughput of the system to a few $1 \cdot 10^8$ ions per pulse at 50 Hz. The efficiency for the combined Penning trap and charge breeder system is normally between $4\%$ and $15\%$, and the breeding time ranges from 5 ms for the lightest elements (Li and Be) up

to as long as $300 - 400$ ms for $A > 200$. The time structure of the charge-breeder and REX-linac can be summarised as follows in reference to Figure 2.4:

- A: Proton bunches strike the ISOLDE target at a rate dependent on the supercycle.
- B: Release of radionuclides from the target is heavily modulated by the PSB cycle.
- C: REXTRAP accumulates, bunches and cools the quasi-continuous beam.
- D: REXEBIS breeds synchronously with REXTRAP at e.g. 10 Hz.
- E: Linac is synchronised to the timing of REXEBIS with a duty cycle permitting an RF pulse of up to 1000 $\mu$s at 100 Hz.
- F: Extracted beam from REXEBIS:
    - Self-extraction: the pulse length is typically 50 $\mu$s, decaying exponentially.
    - Slow extraction: the pulse length is typically as long as 1 ms.
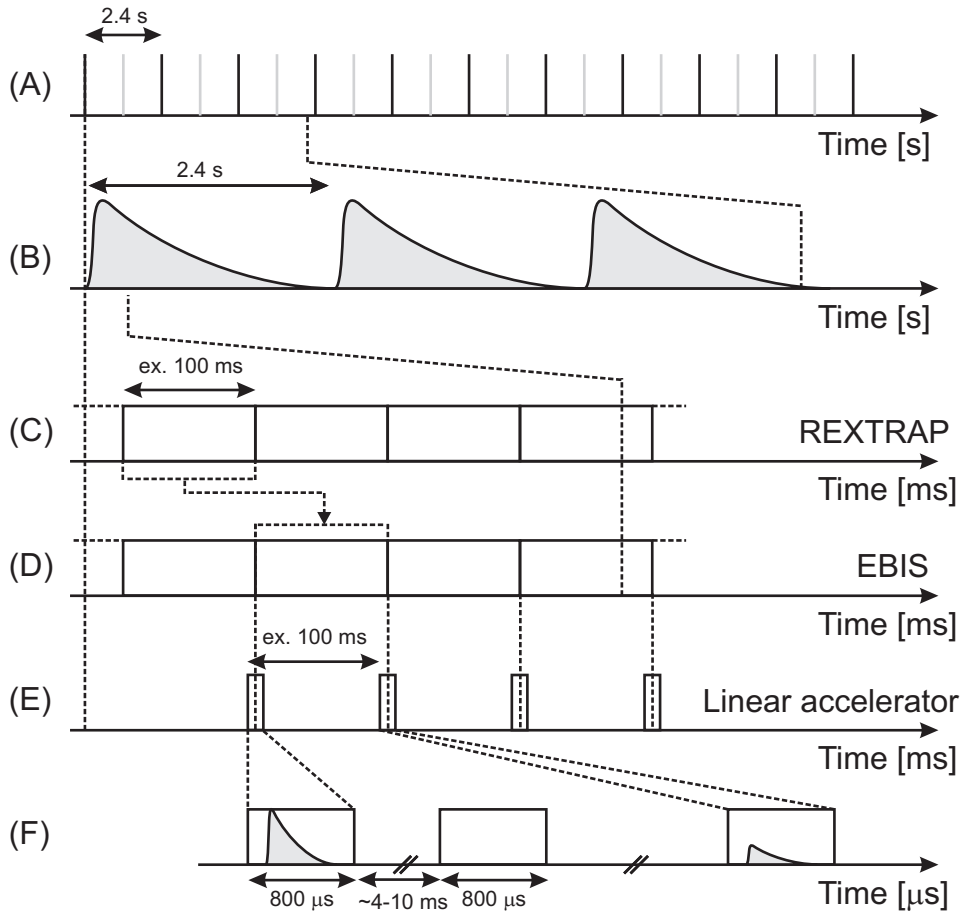


**Fig. 2.4:** REX beam time structure. Figure courtesy of J. van de Walle.

## 2.3 REX linac

After the HIE-ISOLDE upgrade is complete, a substantial part of REX will remain to boost the beam up to 1.2 MeV/$u$. The linac was originally built to accelerate beams with $A/q < 4.5$ up to 2.2 MeV/$u$, allowing the Coulomb barrier to be reached for isotopes with $A < 50$. The addition of a 9-gap IH cavity in 2004 pushed the energy range up to 3 MeV/$u$ for $A/q < 3.5$ and extended the reach of the Coulomb barrier to $A < 85$ [14]. Today, the REX linac consists of the following normal conducting RF structures operating at 101.28 or 202.56 MHz:

- **Radiofrequency Quadrupole (RFQ)** [15]: a four-rod-$\lambda/2$ design [16], similar to those installed at the GSI HLI [17] and the MPIK HCI [18], optimised for $A/q < 4.5$ and used to efficiently bunch and accelerate beams from the ion source energy of 5 keV/$u$ to 300 keV/$u$.
- **Rebuncher (ReB)** [19]: a three-gap split-ring cavity used to longitudinally match the beam from the RFQ into the succeeding IH structure.
- **20-gap IH Structure (IHS)** [20, 21]: a compact and highly efficient $TE_{11(0)}$-type[2] [22] structure employing Combined Zero-Degree Structure (KONUS) [23, 24] beam dynamics that boosts the beam up to 1.2 MeV/$u$; the two KONUS drift-tube sections with 8 and 9 gaps are separated by a grounded quadrupole triplet magnet and a 3-gap rebunching section housed inside the structure.
- **7-gap Split-ring Resonators (7GX: 7G1, 7G2 and 7G3)** [25]: three split-ring cavities, based on the design of cavities made for the HCI at MPIK [26], with constant geometric velocities of 5.4, 6.0 and 6.6 % are used to provide variable beam energy up to 2.2 MeV/$u$.
- **9-gap IH Structure (9GP)** [27]: a 7-gap IH structure designed for the MAFF project [28] was converted to a 9-gap structure with a modified drift-tube structure.

The main parameters of the RF structures are summarised in Table 2.1 and defined later in Section III.

**Table 2.1:** Parameters of the REX linac structures.

| Parameter | RFQ | ReB | IHS | 7GX | 9GP |
|---|---|---|---|---|---|
| $f$ [MHz] | 101.28 | 101.28 | 101.28 | 101.28 | 202.56 |
| No. of gaps/cells | 232 | 3 | 20 | 7 | 9 |
| $\beta_{in} \rightarrow \beta_{out}$ [%] | 0.3 $\rightarrow$ 2.5 | 2.5 $\rightarrow$ 2.5 | 2.5 $\rightarrow$ 5.1 | 5.1 $\rightarrow$ 6.9[a] | 6.9 $\rightarrow$ 7.8[a] |
| $W_{in} \rightarrow W_{out}$ [MeV/$u$] | 0.005 $\rightarrow$ 0.3 | 0.3 $\rightarrow$ 0.3 | 0.3 $\rightarrow$ 1.2 | 1.2 $\rightarrow$ 2.2[a] | 2.2 $\rightarrow$ 2.8[a] |
| $E_{acc}$ [MV/m] | 0.44 | 0.36 | 2.7 | $\sim$ 2.5 | 5.2 |
| $L_a$ [m] | 3 | 0.2 | 1.5 | $\sim$ 0.60 | 0.52 |
| $Z_{eff} = Z_0 T^2$ [M$\Omega$/m][b] | - | 20 | 225 | $\sim$ 55 | 165 |
| $R'_p$ [k$\Omega$m][b] | 146 | - | - | - | - |
| $Q$ (unloaded) | 4050 | 3700 | 13000 | $\sim$ 5250 | 10100 |
| $P$ [kW][b] | 36.3 | 1.6 | 50 | $\sim$ 75 | 90 |
| $A/q$ limits | $\lesssim$ 5.5 | $\gtrsim$ 2.5 | $\lesssim$ 4.5 | $\gtrsim$ 2.5 | $\gtrsim$ 2.5 |

[a] Intermediate energies at entry to 7G2 and 7G3 are 1.55 and 1.88 MeV/$u$, respectively.
[b] $A/q = 4.5$.

The difficulty in maintaining the RF stability at low fields restricts the $A/q$ acceptance of the linac to $\gtrsim 2$ and the internal quadrupole triplet of the IHS limits the upper end of the acceptance to $\lesssim 4.5$. The duty cycle of the linac is variable up to 10% and was designed to match the time structure of the ion source operating with nuclides in the mass range $A < 50$, corresponding to RF pulses no longer than 2 ms at a maximum repetition rate of 50 Hz.

REX proved to be a success, thanks to its versatility: it can accelerate a wide variety of ions from light elements, such as $^6$He and $^8$Li, to heavy mass nuclei such as $^{224}$Ra [29], and other isotopes across the periodic table. Isotopes with lifetimes as short as 20 ms ($^{12}$Be) have successfully been delivered for experiments. Furthermore, the delivered beam is in most cases very clean from contamination thanks to the excellent vacuum inside REXEBIS. REX is ideal for a large range of experiments, especially those that focus on Coulomb excitation, as well as those that investigate transfer reactions and elastic and inelastic scattering in the light mass region.

---

[2]The brackets on the third index imply that the variation of the longitudinal field distribution of the actual $TE_{111}$ mode has been significantly flattened to resemble an $TE_{110}$-like mode.

## References

[1] D. Habs et al., *Nucl. Instrum. Methods Phys. Res. B* **139** (1998) 128.

[2] D. Voulot et al., *Nucl. Instrum. Methods Phys. Res. B* **266** (2008) 4103, Proceedings of the XVth International Conference on Electromagnetic Isotope Separators and Techniques Related to their Applications.

[3] F. Ames, J. Cederkäll, T. Sieber and F. Wenander, *The REX-ISOLDE Facility: Design and Commissioning Report* (CERN, Geneva, 2005).

[4] R. Kirchner, *Nucl. Instrum. Methods Phys. Res., Sect. B* **204** (2003) 179.

[5] V. I. Mishin et al., *Nucl. Instrum. Methods Phys. Res., Sect. B* **73** (1993) 550.

[6] D. Forkel-Wirth and B. Bollen, *Hyperfine Interact.* **129** (2000) .

[7] R. Rao et al., *Nucl. Instrum. Methods Phys. Res. A* **427** (1999) 170.

[8] H. Wollnik, *Optics of charged particles* (Academic Press, Orlando, FL, 1987).

[9] P. Schmidt et al., *AIP Conf. Proceedings* **606** (2000) 609.

[10] F. Ames et al., *Nucl. Instrum. Methods Phys. Res. A* **538** (2005) 17.

[11] P. Schmidt et al., *Nucl. Phys. A* **701** (2002) 550.

[12] F. Wenander, B. Jonson, L. Liljeby and G. H. Nyman, REXEBIS the Electron Beam Ion Source for the REX-ISOLDE project, CERN-OPEN-2000-320 (CERN, Geneva, Dec 1998).

[13] F. Wenander, *JINST* **5** (Oct 2010) C10004. 33 p.

[14] T. Sieber, D. Habs and O. Kester, Test and first experiments with the new REX-ISOLDE 200 MHz IH structure, Proceedings of LINAC'04, Lubeck, 2004, pp 318–320.

[15] T. Sieber, PhD thesis, Ludwig-Maximilians University Munich, 2001.

[16] A. Schempp et al., *Nucl. Instrum. Methods Phys. Res. B* **10** (1985) 831.

[17] J. Friedrich et al., Properties of the GSI HLI-RFQ structure, Proceedings of PAC'91, San Francisco, 1991, pp 3044–3046.

[18] C. M. Kleffner et al., The RFQ-accelerator for the high current injector of the TSR, Proceedings of EPAC'92, Berlin, 1992, pp 1340–1342.

[19] K. U. Kühnel, Master's thesis, Institute for Applied Physics, Goethe University Frankfurt, 1999.

[20] S. Emhofer, Master's thesis, Ludwig-Maximilians University Munich, 1999.

[21] S. Emhofer, PhD thesis, Ludwig-Maximilians University Munich, 2004, Unpublished.

[22] U. Ratzinger, H-type linac structures, Proceedings of CAS: RF Engineering, Seeheim, 2000, pp 374–375.

[23] U. Ratzinger, The IH structure and its capability to accelerate high current beams, Proceedings of PAC'91, San Francisco, 1991, pp 567–571.

[24] R. Tiede et al., KONUS beam dynamics designs using H-mode cavities, Proceedings of HB'08, Nashville, 2008, pp 223–230.

[25] T. Sieber, Master's thesis, Heidelberg University, 1999.

[26] R. von Hahn et al., *Nucl. Instrum. Methods Phys. Res. A* **328** (1993) 270.

[27] H. Bongers, Master's thesis, Ludwig-Maximilians University Munich, 2003.

[28] D. Habs et al., *Nucl. Instrum. Methods Phys. Res. B* **204** (2003) 739.

[29] P. Van Duppen and K. Riisager, *J. Phys. G: Nucl. Part. Phys.* **38** (2011) 024005.

# Chapter 3

# HIE-ISOLDE project and energy upgrade

M.A. FRASER

The HIE-ISOLDE project [1] represents a major upgrade of the ISOLDE facility with a mandate to significantly improve the quality and increase the intensity and energy of radioactive nuclear beams. The project will expand the nuclear physics programme at ISOLDE and was approved as an official project by CERN in the autumn of 2009. Thirty-four HIE-ISOLDE Letters of Intent were submitted by 284 researchers from 76 laboratories in 22 countries and accepted. Of these, $88\%$ propose to make use of the increase in energy and intensity, whereas only $12\%$ propose to exclusively use the increase in intensity [2]; this places the upgrade of the post-accelerator at the forefront of the project. The scientific opportunities offered by the HIE upgrade are outlined at length in [3] and the technological options for the upgrade can be found outlined in [4]. The linac upgrade, which is discussed at length in this report, will replace most of the existing REX post-accelerator and is based on a compact superconducting linac made up of quarter-wave resonators and solenoids, housed in six cryomodules, as shown schematically in Figure 3.1.
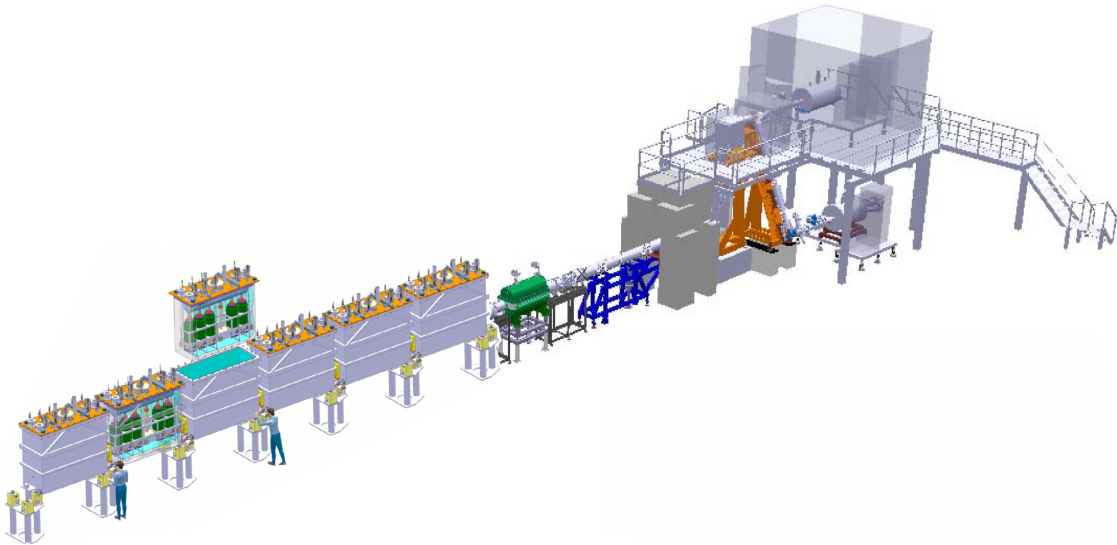


**Fig. 3.1:** The HIE-linac. The installation of six cryomodules will provide almost 40 MV of accelerating potential after the IHS, delivering beams of over 10 MeV/$u$. The top-loading cryomodule is shown and the superconducting quarter-wave resonators and solenoids are exposed.

## 3.1 Intensity

Aside from longer term plans to upgrade the Proton Synchrotron Booster (PSB) [5], the beam intensity of the CERN accelerator complex is to be increased in accordance with the LHC luminosity upgrade and the replacement of Linac 2 with Linac 4 [6]. The upgrade will increase the injection energy of the PSB from 50 MeV to 160 MeV and reduce the space-charge bottleneck in the PSB so that the beam intensity can be increased by a factor of 2.

Along with $H^-$ charge-exchange injection and an increased cycling rate of the PSB, a factor of

between 2 and 3 increase in the average driver beam power can be realistically expected at the ISOLDE target stations. Radiation protection studies have been launched to understand the effects of the increase in proton intensity at the target stations. The radioactive beam intensities will benefit from the increase in the driver beam intensity and developments in target technology are being pursued. Various upgrades to the charge breeder are being investigated including the test of a new ECR ion source [7] and an RFQ cooler named ISCOOL [8, 9] is already on the HRS beam line and capable of injecting cooled beams directly into REXEBIS, overcoming the present space-charge bottleneck in the Penning trap.

## 3.2 Quality

The HRS will be significantly upgraded and with ISCOOL its mass resolution will be much improved. Other methods of beam purification are being investigated for the low-energy section of REX [7] and research and development activities with the Resonance Ionization Laser Ion Source (RILIS) are ongoing.

## 3.3 Superconducting linac

The energy upgrade comes in the form of a new superconducting linear post-accelerator with 40 MV of accelerating potential. The installation of the upgrade is divided in three phases, presented in Figure 3.2.
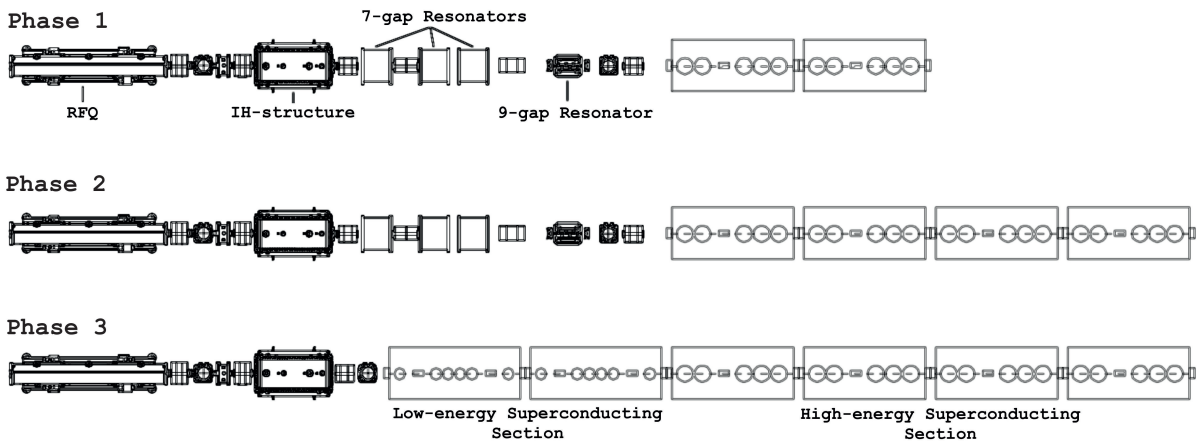


**Fig. 3.2:** Installation phases of the superconducting linac.

In the first phase, two cryomodules were added to the existing REX machine to provide energies of up to at least 5.5 MeV/$u$ to allow Coulomb excitation studies to be carried out across the entire range of radionuclides available at ISOLDE. The second phase of the upgrade continues in this manner until all four high-$\beta$ cryomodules have been added to provide energies of up to at least 10 MeV/$u$, which will make available a wider range of reactions aside from Coulomb excitation. In the final phase, all the existing REX accelerating structures after the IHS will be replaced with two low-$\beta$ cryomodules to improve beam quality and ensure that the energy is continuously variable between 0.45 and 10 MeV/$u$.

A review of the superconducting and normal conducting upgrade options was undertaken by an International Advisory Board (IAB) following preliminary studies at CERN, with the board unanimously supporting the pursuit of the superconducting option. The main trade-offs between the application of the two technologies highlighted by the IAB are summarised in [10]. The increased cost and demand on resources of the superconducting option was weighed against the superior beam quality it could provide, its ability to tailor the beam energy precisely to the experiment and its future viability with ion source and injector upgrades in terms of potential CW operation. The space available in the experimental hall is also critical and it was concluded that even with further optimisation of the normal conducting designs

the superconducting option would be shorter. In addition, the choice to pursue niobium sputter-coated copper cavities was viewed positively in light of the experience at CERN of sputtering accelerating cavities, albeit in a different velocity regime and geometry.

Standard design procedures were employed to ensure a cost-effective but high-performance superconducting accelerator design, see e.g. [11]. The low intensity of the beams at ISOLDE permits the use of long focusing periods with a densely packed lattice of superconducting cavities operating at high gradient, which helps to minimise the length and cost of the accelerator. The design objectives of the linac upgrade can be summarised as follows:

- Accelerate all nuclei up to at least 10 MeV/$u$.
- Provide full flexibility in the beam energy.
- Preserve beam quality.
- Maintain high transmission for all beams.

The flexibility that is demanded by the users' wish to post-accelerate the entire range of radionuclides available at ISOLDE up to and beyond the Coulomb barrier is reflected in the choice of a superconducting linac. The upgrade, based on short and independently tunable accelerating cavities, is capable of providing continuous flexibility in energy whilst maintaining high beam quality and transmission. The specifications of the basic design parameters for the upgrade are outlined in Table 3.1. The limited space available in the ISOLDE experimental hall presents a real-estate gradient target of 2 MV/m, which would be challenging for a normal conducting machine providing both continuous energy variability and good beam quality.

The lattice was designed to be as compact as possible to maximise the acceptance of the linac and optimise the beam quality, but also to allow adequate space in the experimental hall for physics instrumentation. The linac was divided by grouping the two cavity families together in different cryomodules. The low-energy section contains two cryomodules, each housing six low-$\beta$ cavities and two solenoids, and the high-energy section contains four cryomodules, each housing five high-$\beta$ cavities and one solenoid. For reasons of economy, the designs of the cryomodules were standardised and the sizes of the low- and high-energy cryomodules were kept similar. The lattice is shown schematically in Figure 3.3 and the important properties and dimensions of the lattice are summarised in Table 3.2.

**Table 3.1:** Basic design parameters for the HIE-linac.

| Linac design parameter | Description or value |
|---|---|
| Particle type | radionuclides with $A \lesssim 250$ |
| Mass-to-charge acceptance ($A/q$) | $2.5 \lesssim A/q \lesssim 4.5$ |
| Fundamental beam frequency[a] ($f$) | 101.28 MHz |
| Output beam kinetic energy ($W$) | variable up to at least 10 MeV/$u$ |
| Effective accelerating voltage ($V_{\text{eff}}$) | 39.6 MV |
| Length available for linac | $\sim 20$ m |
| Real-estate gradient | $\sim 2$ MV/m |
| RF duty cycle | at least 10 % |
| Transmission | $> 95$ % |

[a] A multi-harmonic buncher and beam chopper are being considered for HIE-ISOLDE to reduce the beam frequency by a factor of 10.

The lattice of the low-energy section is somewhat irregular to facilitate the longitudinal matching of the beam after the IHS by separating the first cavity from the others and using it as a rebuncher with the succeeding drift region containing a solenoid. This removes the need for a dedicated rebuncher
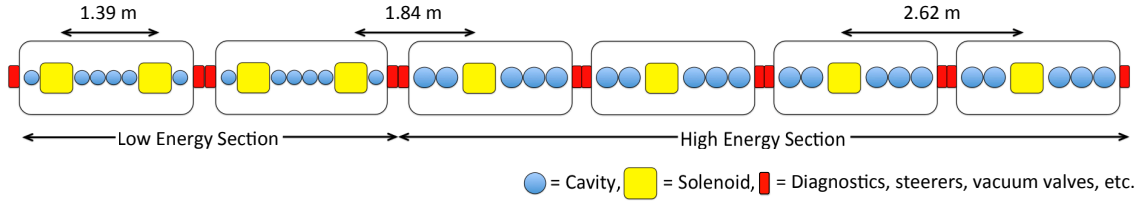
**Fig. 3.3:** Schematic of the lattice of the HIE-linac.

outside the cryomodule and as a consequence reduces the length of the machine. A synchronous phase of just $-40°$ in the first cavity is adequate to capture the beam after the IHS, by minimising the bunch length in the second cavity. The last cavity in the low energy cryomodule is also separated by a solenoid, making itself and the fifth cavity useful for completing the longitudinal phase space gymnastics early in the acceleration.

The cavities are placed asymmetrically about the solenoid in the high-energy section with two cavities before and three after the solenoid. The 'missing' first cavity is replaced by the drift-space between the cryomodules, compensating for the inter-cryomodule distance and permitting smooth and period beam envelopes to be matched. The 'missing' cavity reduces the beam divergence across the transition region between the low and high-energy section and allows the beam to be matched into the high-energy section without a dedicated matching section. The transverse phase advance is lowered in the second low-energy cryomodule to facilitate a match into a focusing channel with a transverse phase advance of $90°$ per period in the high-energy section [12]. The length of the focusing period changes across the transition region between the two sections of the linac, from $1.39$ m in the low-energy section to $2.62$ m in the high-energy section, with an intermediate transition period length of $1.84$ m. No adjustment of the synchronous phases is needed to match the beam longitudinally into the high-energy section once the upgrade is complete and the low-energy section is in place.

**Table 3.2:** HIE-linac lattice parameters.

| Design parameter | Low energy section | High energy section |
|---|---|---|
| No. of cryomodules | 2 | 4 |
| No. of cavities | 12 | 20 |
| Cavity geometric velocity ($\beta_g$) [%] | 6.3 | 10.3 |
| No. of solenoids | 4 | 4 |
| No. of focusing periods | 4 | 4 |
| Length of focusing period [m] | 1.39 | 2.62 |
| Transverse phase advance per period ($\mu_T$) [deg] | $60-90$ | 90 |
| Solenoid strength $\left(\int B_z^2 \mathrm{d}z\right)\left[\mathrm{T^2 m}\right]$ | $\leq 8.8$ | $\leq 15.0$ |
| Long phase advance per period ($\mu_L$) [deg] | $\sim 100$ | $\sim 100$ |
| Inter-cryomodule distance[a] [m] | 0.50 | 0.50 |
| Inter-cavity distance [m] | 0.02 | 0.02 |
| Inter-cavity distance with solenoid [m] | 0.46 | 0.46 |
| Length of cryomodule [m] | 2.77 | 2.62 |
| Total length [m] | 5.54 | 10.48 |
| Packing factor ($F$) [%] | 47 | 61 |

[a] Distance between the closest cavities in adjacent cryomodules.

## 3.4 High energy beam transfer lines

The High Energy Beam Transfer (HEBT) lines were designed to transport the post-accelerated beams from the HIE-linac to the experimental stations. They consist of three similar beam lines (XT01, XT02, XT03), shown in Figure 3.4, that can transfer beams with various energies (from $0.3$ MeV/$u$ to $10$ MeV/$u$) and mass-to-charge states [12]. A modular design was chosen for all three lines to ease assembly and operation. The HEBT was built over two years and the first two beam lines were operational in early 2015. Installation works for the third one started in 2017. It is possible to extend the third beam line in the future to bring the beam to either a storage ring or a larger experimental station at the back of the ISOLDE hall.
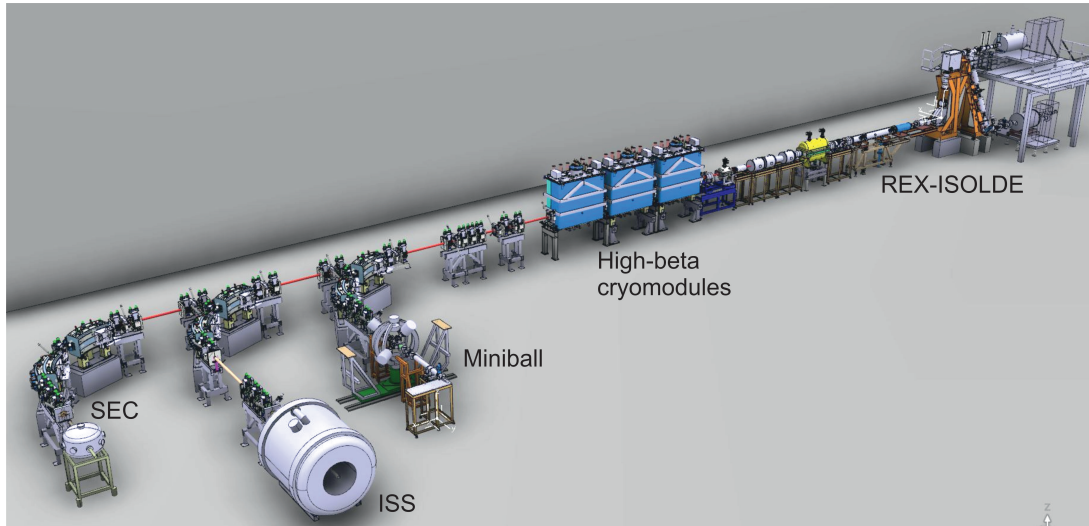


**Fig. 3.4:** A 3D visual of the HIE-ISOLDE linac, composed of three cryomodules and the three experimental stations in the HEBT, as presently installed.

The HEBT consists of doublet cells, achromatic 90-degree bends and focusing triplets positioned before the experimental stations. The doublet units shown in Figure 3.5 are composed of quadrupoles, dual-plane trajectory corrector magnets (dipoles) and beam instrumentation devices. As upgradability was a key consideration, the length of a doublet cell was designed to be the same as the length of a cryomodule. As a result, it is relatively easy to replace a doublet cell with a cryomodule to increase the energy reach of the linac in a staged manner.
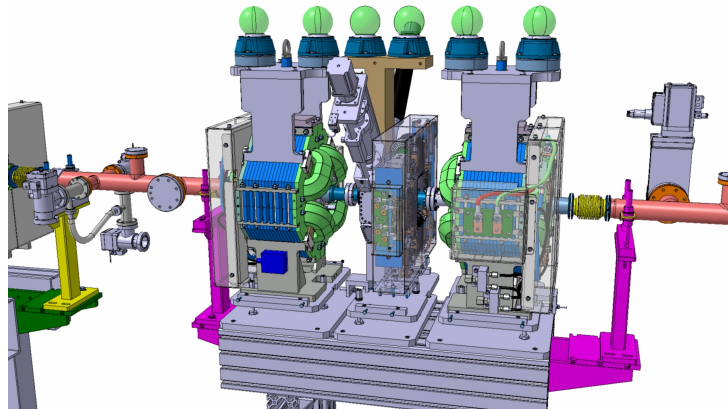


**Fig. 3.5:** A doublet unit composed of a beam diagnostics box and trajectory steerer magnet (horizontal and vertical) sandwiched between two quadrupoles.

Experimental instrumentation at HIE-ISOLDE includes a variety of set-ups. The first beam line hosts the high-resolution germanium detector array Miniball [13], which is used for Coulomb excitation and transfer reactions. It has been in operation at ISOLDE for more than ten years. Three complementary set-ups are often employed alongside Miniball: T-REX [14], a set of double sided silicon strip detectors, the CD-type Double sided Silicon Detector and SPEDE (Spectrometer for Electron Detection) [15], which performs electron conversion studies. In the second beam line, a general purpose scattering chamber was installed at first. In 2017, it was replaced by the ISOLDE Solenoidal Spectrometer (ISS), intended for transfer reaction studies. ISS will be available for physics exploitation after CERN's second long shutdown (LS2). The active target SpecMAT will be used in separate experiments inside the ISS magnet. The third beam line is reserved for smaller, movable set-ups, e.g. the scattering chamber, with different charged particle detector arrays such as CORSET (CORrelation SETup) for quasi-fission measurements. The scattering chamber will have to be removed eventually, when ACTAR (Active Target Detector) [16] or the optical time projection chamber are installed in its place.

Over thirty experiments have already been approved; two of them finished data-taking in autumn 2016 and 13 are scheduled for the 2017 physics run. Experiments at HIE-ISOLDE cover a wide range of topics, such as isospin symmetry, collectivity vs. single particle structure, magic numbers far from stability, shape coexistence, as well as quadrupole and octupole degrees of freedom.

## 3.5 Design study for 10 MHz beams: increased bunch spacing

An increased bunch spacing of approximately 100 ns has been requested by several research groups targeting experimental physics at HIE-ISOLDE [17]. A proposal has been made to install a multi-harmonic buncher (MHB) initiating the formation of the longitudinal emittance outside and upstream the RFQ at a sub-harmonic frequency 10 times lower than its 101.28 MHz resonant frequency. This will extend the bunch spacing to 98.7 ns permitting time-of-flight particle identification and background suppression techniques to be used by the experiments, as well as increasing the $A/q$-resolution of the facility. In order to meet the specification requested by the experiments, a chopper structure will be needed after the RFQ to remove the satellite bunches that are populated due to the non-ideal bunching efficiency of the MHB. The bunching and chopping systems could be installed during the final stage of the HIE-ISOLDE linac upgrade, when the linac can be extended by 2.62 m, i.e. the length of one high-$\beta$ cryomodule, as shown below in Figures 3.6 and 3.7.
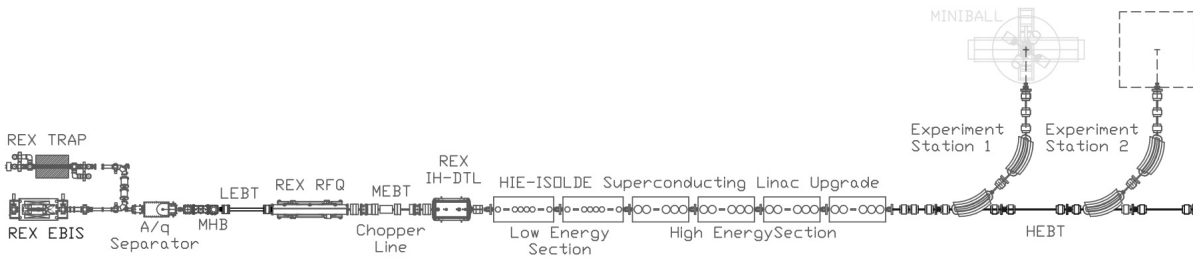


**Fig. 3.6:** Schematic layout of the HIE-ISOLDE linac installation: MHB, chopper line and six superconducting cryomodules.

For low-current applications where space-charge forces are not important, e.g. in radioactive heavy-ion post-accelerators, a discrete buncher located either internally or externally to an RFQ accelerator can be used to reduce both the length of the RFQ and the longitudinal emittance. Several nuclear physics accelerator laboratories have employed this design approach including TRIUMF with the ISAC RFQ [18], LNL with the PIAVE heavy ion injector RFQ [19], ANL with the ATLAS upgrade RFQ [20] and NSCL with the ReA3 RFQ [21]. In most cases the RFQ was designed without adiabatic bunching sections and an external MHB was placed upstream of the RFQ; the length of the RFQ was reduced, its shunt
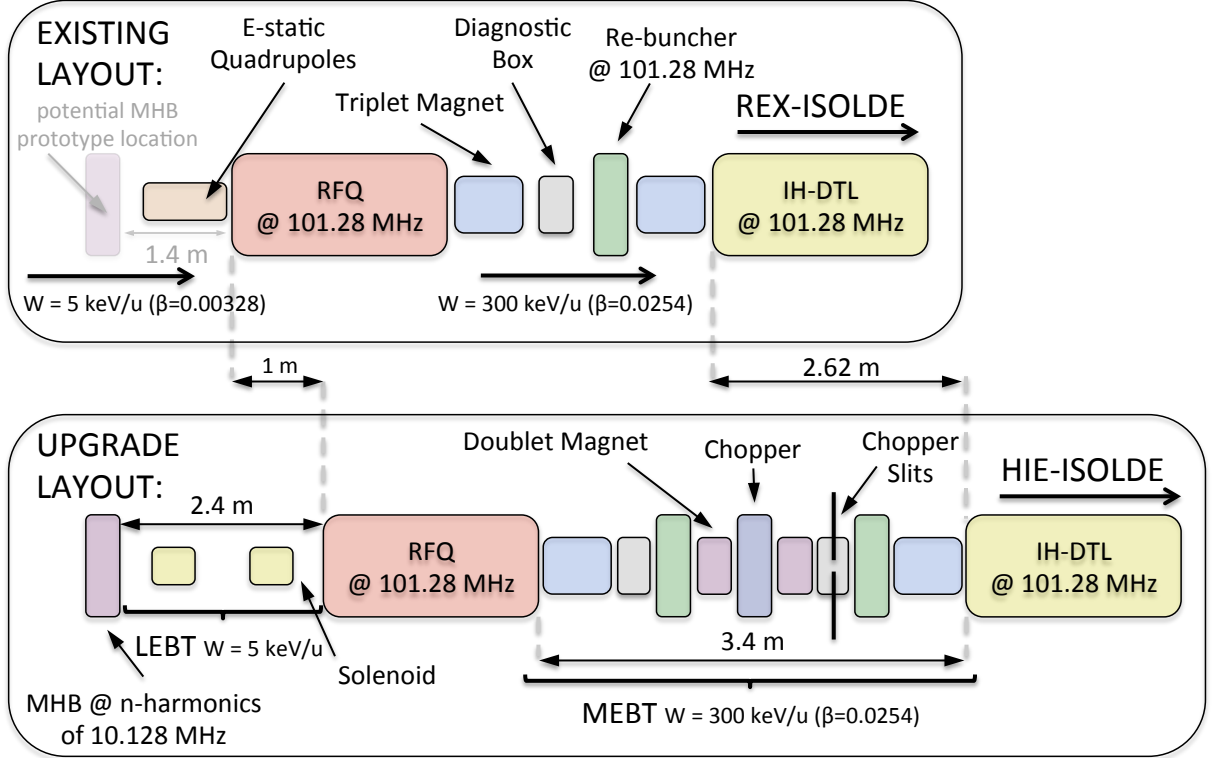
**Fig. 3.7:** Schematic of the existing (top) and upgrade layout (bottom) with 10 MHz bunching system.

impedance increased and the beam emittance improved. In the HIE-ISOLDE case, it is proposed to retrofit the existing REX-ISOLDE RFQ [22], which has an adiabatic bunching section, with an external MHB in order to change the beam frequency. The 101.28 MHz fundamental frequency is similar to the frequencies of both the ANL and TRIUMF MHB systems, however, the ratio between the RFQ resonant frequency and the fundamental MHB frequency (beam frequency) is much larger ($h = 10$). Some key parameters of the systems are summarised in Table 3.3 and compared with the proposed HIE-ISOLDE system. There were plans to retrofit an RFQ similar to the REX-ISOLDE RFQ, also possessing an adiabatic bunching section, with an MHB for the MAFF project in Munich [23]. Although the project was never realised, design studies were carried out to prove the feasibility of such a system.

The principle of sub-harmonic pre-bunching is illustrated in Figure 3.8 where the longitudinal acceptance on the beam axis of the REX-ISOLDE RFQ is shown over half a 10.128 MHz period; five 101.28 MHz buckets are clearly identifiable with the target bucket shaded and centred. The red points in phase-space lie outside of the acceptance and are not captured by the RF system. The energy acceptance of the RFQ is large ($\pm 5\%$), which has recently been verified experimentally [24]. Superimposed are ideal 'pencil' beams matched using an MHB mixing the first four harmonics of 10.128 MHz in different scenarios: located at $L = 1.4$ and $2.4$ m upstream of the RFQ, with effective voltages[1] $V_0 = 840$ and $520$ V, respectively. The intersection of the beam tails with the acceptance of the other buckets illustrates how the satellite bunches are populated. In the latter scenario, the $A/q$-resolution is demonstrated as $\frac{\Delta(A/q)}{A/q} \sim \frac{1}{150}$; this beam contaminant would be accelerated by the RFQ in the adjacent satellite bunch and removed by the chopper.

The feasibility of such a bunching system at HIE-ISOLDE has been validated [22] and followed

---

[1] $V_0$ is the effective amplitude of the fundamental harmonic frequency, including transit time factor; the amplitudes of the other harmonics are scaled accordingly to give a least-squares fit to a linear 'saw-tooth' energy modulation within a phase range of $\pm 150°$ at $\frac{\omega_0}{2\pi} = 10.128$ MHz: $V_{\text{eff}} = V_0 \left( \sin \omega_0 t - 0.43 \sin 2\omega_0 t + 0.21 \sin 3\omega_0 t - 0.10 \sin 4\omega_0 t \right)$.

up with comprehensive beam dynamics design studies evaluating the performance reach of potential installation scenarios [25]. The study is detailed further in Chapter 14.

**Table 3.3:** Comparison of the key parameters of a selection of relevant worldwide MHB-RFQ systems.

| Facility | ATLAS (ANL) | ISAC (TRIUMF) | PIAVE (LNL) | ISOLDE (CERN) |
|---|---|---|---|---|
| RFQ frequency [MHz] | 60.625 | 35.4 | 80 | 101.28 |
| MHB fundamental (beam) frequency [MHz] ($h = \frac{f_{\mathrm{RFQ}}}{f_{\mathrm{MHB}}}$) | 12.125 ($h = 5$) | 11.8 ($h = 3$) | 40 ($h = 2$) | 10.128 ($h = 10$) |
| No. of MHB harmonics | 4 | 3 | 3 | $\geq 3$ |
| RFQ structure type | multisegment split-coaxial | 4-rod split-ring | superconducting | 4-rod ($\lambda/2$) |
| MHB RF structure type | lumped circuit (resonant) | transmission line (non-resonant) | QWR (resonant) | to be defined |
| MHB drift-tube type | single-gap | single-gap | 2· double-gap | single-gap |
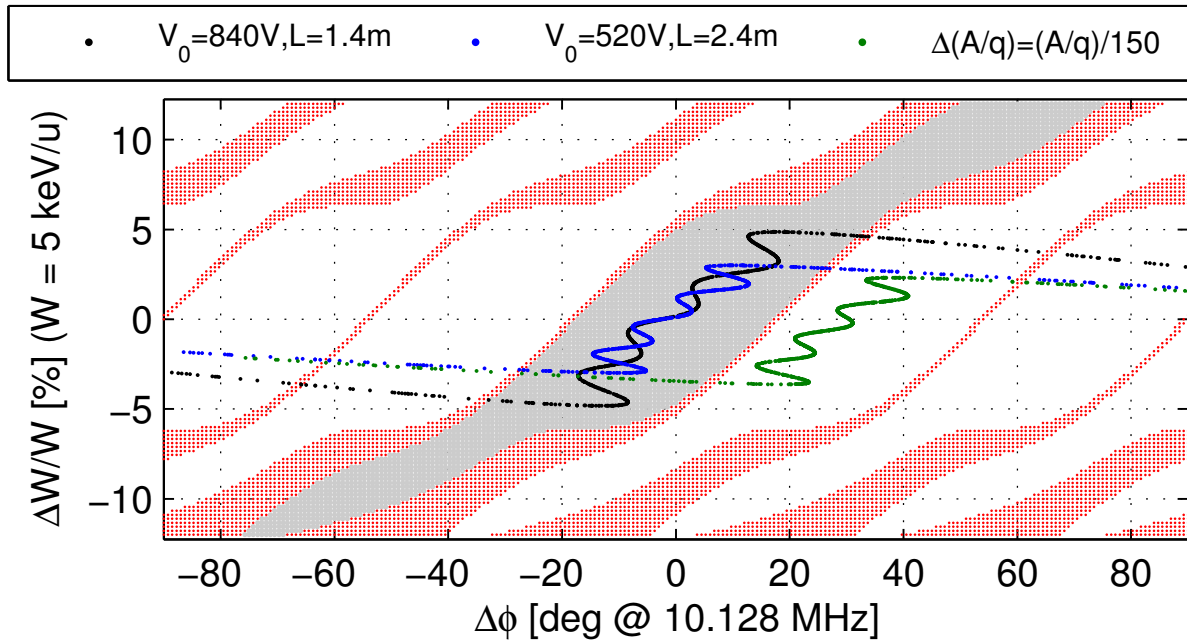


**Fig. 3.8:** Longitudinal acceptance of the REX-ISOLDE RFQ.

## References

[1] M. Lindroos, P. Butler, M. Huyse and K. Riisager, *Nucl. Instrum. Methods Phys. Res. B* **266** (2008) 4687.

[2] Y. Blumenfeld (chair), Minutes of the 1st HIE-ISOLDE Physics Steering Committee: Investigating how HIE-ISOLDE technical developments meet the physics requirements, 2010.

[3] K. Riisager, P. Butler, M. Huyse and R. Krücken, *HIE-ISOLDE: the scientific opportunities* (CERN, Geneva, 2007).

[4] M. Lindroos and T. Nilsson, *HIE-ISOLDE: the technical options* (CERN, Geneva, 2006).

[5] K. Hanke et al., Study of an energy upgrade of the CERN PS Booster, Proceedings of IPAC'11, St Sebastian, 2011, pp 2526–2528.

[6] M. Vretenar et al., The Linac4 project at CERN, Proceedings of IPAC'11, St Sebastian, 2011, pp 900–902.

[7] F. Wenander, T. Lamy and A. C. Müller, Report on beam purification at REX-ISOLDE and ISOLDE PHOENIX charge breeder, T-J03-5 (EURONS, CERN-ISOLDE, 2008).

[8] H. Frånberg et al., *Nucl. Instrum. Methods Phys. Res. B* **266** (2008) 4502.

[9] I. P. Aliseda et al., *Nucl. Phys. A* **746** (2004) 647.

[10] A. Müller, R. Laxdal and O. Kester, International Advisory Board for the REX-ISOLDE linac energy upgrade, 2006.

[11] P. N. Ostroumov, *New J. Phys.* **8** (2006) 281.

[12] M. A. Fraser, R. M. Jones and M. Pasini, *Phys. Rev. ST Accel. Beams* **14** (2011) 020102.

[13] N. Warr et al., *Eur. Phys. J. A* **49** (2013) 40.

[14] V. Bildstein et al., *Eur. Phys. J. A* **48** (2012) 1.

[15] P. Papadakis et al., The SPEDE spectrometer: combined in-beam $\gamma$-ray and conversion electron spectroscopy with radioactive ion beams, Proceedings of ARIS2014, 2015, p 030023.

[16] R. Raabe and others, ACTAR: the New Generation of Active Targets, AIP Conference Proceedings Volume 1165, 2009, pp 339–342.

[17] S. J. Freeman et al., Letter of Intent to the ISOLDE and Neutron Time-of-Flight Experiments Committee for experiments with HIE-ISOLDE: A HELIcal Orbit Spectrometer (HELIOS) for HIE-ISOLDE, CERN-INTC-2010-031. INTC-I-099 (CERN, Geneva, May 2010).

[18] S. R. Koscielniak, Beam Dynamics Design of the TRIUMF ISAC RFQ, Proceedings LINAC'96, Geneva, 1996, pp 402–404.

[19] A. Pisent, G. Bisoffi, M. Cavenago et al., *Proceedings Linac'06* (2006) 227.

[20] P. N. Ostroumov et al., *Physical Review Special Topics - Accelerators and Beams* **15** (2012) 1.

[21] O. Kester et al., *Proceedings of the SRF2009, Berlin, Germany* (2009) 57.

[22] T. Sieber, PhD thesis, Ludwig-Maximilians University Munich, 2001.

[23] D. Habs et al., *Nucl. Instrum. Methods Phys. Res. B* **204** (2003) 739.

[24] M. A. Fraser and F. Wenander, Study of Effect of Ion Source Energy Spread on RFQ Beam Dynamics at REX-ISOLDE, HIE-ISOLDE-PROJECT-Note-0018 (CERN, 2013).

[25] M. A. Fraser, CERN-HIE-ISOLDE-PROJECT-Note-0035 (CERN), to be published.

# Part II

# Linac Design Overview

# Chapter 4

# Accelerating structures: SC cavities

W. Venturini Delsolaro, A.R.M. Sublet

Superconducting quarter-wave resonators were identified early on in the design process as a reliable and robust structure, able to provide the stable high gradients and the velocity acceptance demanded by the beam specification at HIE-ISOLDE. Superconducting quarter-wave cavities are used in many facilities around the world for applications in heavy ion beam acceleration, e.g. ANL, LNL-INFN and TRIUMF [1].



(a) Side-view        (b) Perspective
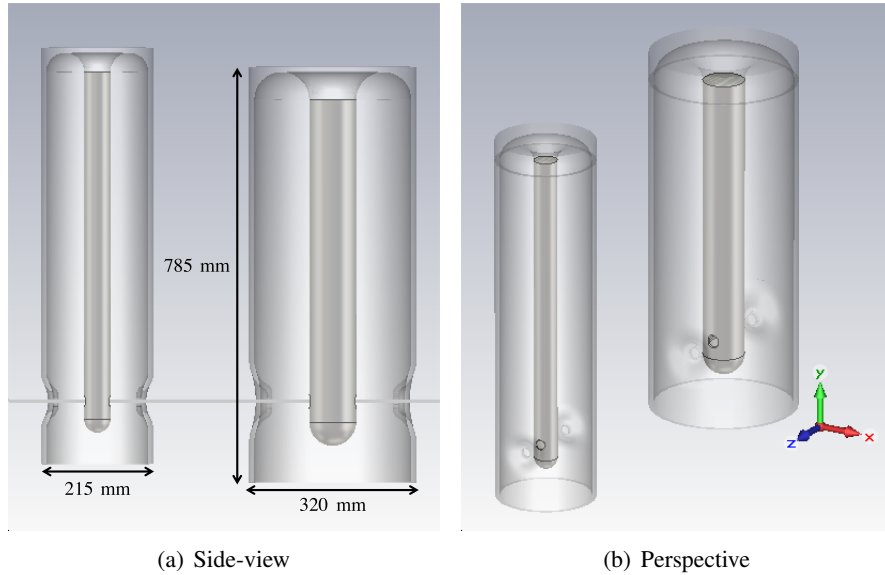
**Fig. 4.1:** The low and high-$\beta$ quarter-wave cavity geometries, realised in `CST-MWS` [2].

In the initial proposal, the design energy reach (10 MeV/u for $A/q = 4.5$) was achieved by the use of 32 cavities, which were optimised for two normalised velocities of $(\beta_g)$ of 6.3 and 10.3%. There were 12 low beta and 20 high beta cavities. The low beta section would replace some of the normal conducting structures of the REX injector. In this scenario, the total accelerating voltage of 39.6 MV is to be reached, assuming an average gradient per cavity of 6 MV/m with average synchronous phase of $-20°$. The two optimum velocities are chosen to minimise the total number of cavities and to provide a quick transition to the high beta section, where the energy gains per cavity are higher [3]. The output energy can be varied by modulating the voltage partition between cavities, thanks to an independent phasing. Figure 4.2 shows the energy profiles along the linac for different $A/q$ and choices of the synchronous phase. At the low end of the $A/q$ acceptance band, particles can be accelerated up to 17 MeV/u. For $A/q = 4.5$, the transit time factor is kept higher than $0.8$ in all but the first cavities of each section. The low beta section offers the possibility to decelerate beams down to $0.45$ MeV/u. The main cavity parameters for the high and low beta resonators are shown in Table 4.1, limited by the degradation to the beam quality on decelerating through the zero of the first-order transit-time factor.

(a) Energy profile

(b) Transit-time factor
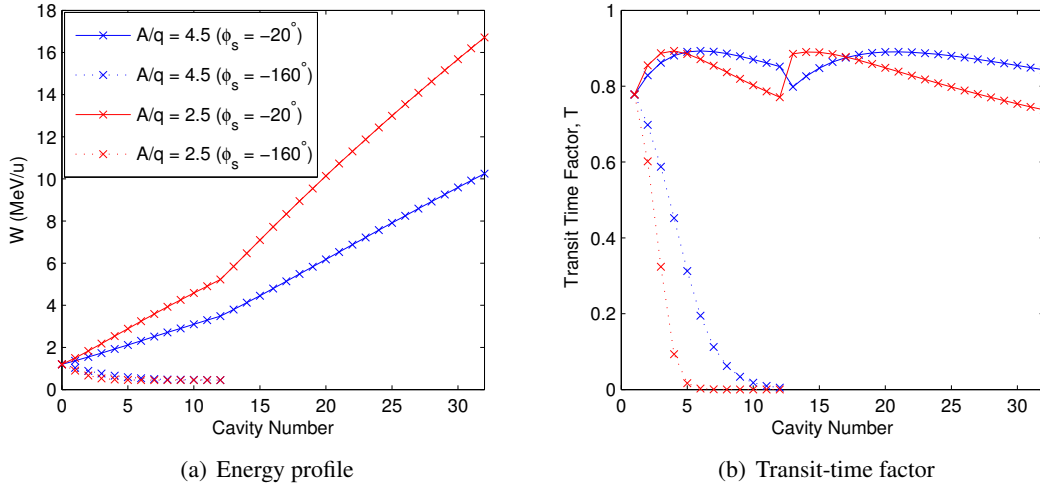
**Fig. 4.2:** The energy profiles and transit-time factors along the HIE-linac phased to accelerate and decelerate.

**Table 4.1:** HIE-linac cavity design parameters.

| Design parameter | Low-$\beta$ cavity | High-$\beta$ cavity |
|---|---|---|
| No. of cavities | 12 | 20 |
| No. of gaps | 2 | 2 |
| $f$ [MHz] | 101.28 | 101.28 |
| $\beta_g$ ($\beta_{\text{opt}}$) [%] | 6.3 (7.1) | 10.3 (11.3) |
| $L_g = \beta_g\lambda/2$ [mm] | 93 | 153 |
| $T_{\text{max}}(\beta_{\text{opt}})$ | 0.85 | 0.9 |
| $E_0$ [MV/m] | 6 | 6 |
| $L_{\text{a}}$ [mm] | 195 | 300 |
| Diameter of inner conductor [mm] | 50 | 90 |
| Mechanical length [mm] | 215 | 320 |
| Gap length ($g$) [mm] | 50 | 85 |
| Beam aperture diameter [mm] | 20 | 20 |
| $U/E_0^2 \left[\text{mJ}/(\text{MV/m})^2\right]$ | 73 | 207 |
| $E_{\text{pk}}/E_0$ | 5.4 | 5.6 |
| $B_{\text{pk}}/E_0$ [Oe/(MV/m)] | 80 | 100.7 |
| $R_{\text{max}}/Q$ [$\Omega$] | 564 | 554 |
| $\Gamma = R_{\text{s}}Q$ [$\Omega$] | 23 | 30 |
| $P$ [W] at $E_0$ | 7 | 10 |
| $Q_0$ for $E_{\text{acc}} = 6$ MV/m for $P$ at $E_0$ | $3.2 \cdot 10^8$ | $4.8 \cdot 10^8$ |
| Helium bath temperature [K] | 4.5 | 4.5 |

## 4.1 Nb/Cu coating

Two different technologies were considered for the production of the quarter wave resonators of the HIE-ISOLDE linac: bulk niobium and niobium coatings on copper. Both options would guarantee the required RF performance, however the Nb/Cu technology was selected as it was recognised to be more cost effective than bulk niobium in the temperature and frequency range (4.5 K, 100 MHz) of the HIE-ISOLDE linac.

Two mechanical designs were developed for the high-$\beta$ cavities [4]. Initial prototypes, shown

28

in Figure 4.3a, which were manufactured from two rolled copper sheets and contained a helium reservoir spread out over the shorting plate, were used to optimise manufacture and coating procedures. An improved cavity design was later produced, presented in Figure 4.3b, comprising inner and outer conductors that were shrink fitted and electron beam welded with a single weld on the RF side. The new design improved shape accuracy and repeatability and minimised sensitivity to fluctuations of helium pressure.
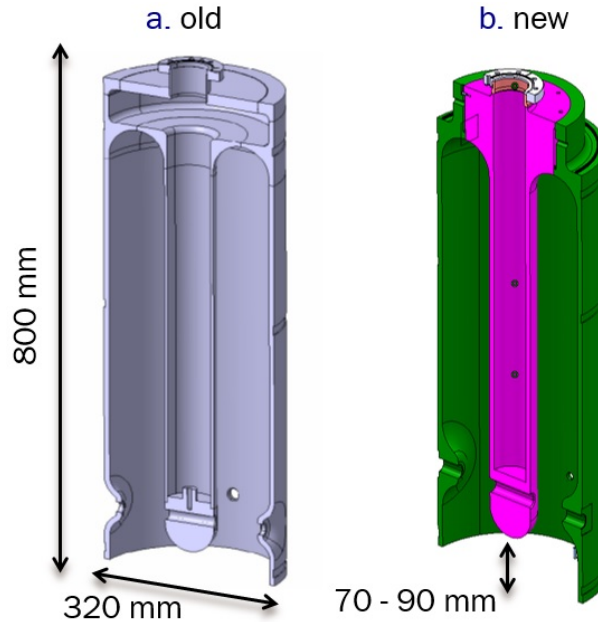


**Fig. 4.3:** Old and new design for the superconducting cavities. The original prototype from rolled copper sheets with the helium reservoir on top is presented in (a) and the machined copper cavity design is shown in (b).

Among the advantages of the Nb/Cu choice, are the high thermal and mechanical stability offered by the copper cavity substrates, which are less prone to quenches and to microphonics. This latter feature allows the operation of resonators at small bandwidths with consequent reduction in RF power requirements. Another known advantage is the relative insensitivity of Nb/Cu cavity to magnetic flux trapping, which allows the elimination of the magnetic shield from the cryomodule design.

The technology of Nb/Cu was invented at CERN and used for the LEP cavities and for the LHC cavities. These were elliptical cavities coated by magnetron sputtering. The method adopted to sputter coat the more complex shape of quarter wave resonators with high quality Nb films was developed at INFN Legnaro for the ALPI linac and it is based on DC bias sputtering [5].

The coating protocol, based on DC bias sputtering at high substrate temperatures, promotes the mobility of the sputtered atoms during growth and keeps film contamination low [6], in spite of a much lower deposition rate as compared to magnetron sputtering. The method was adapted to the size of the HIE-ISOLDE high beta cavity by using a mockup cavity, with the same thermal inertia as the real one, as a sample holder where up to 50 samples could be fixed. This was instrumental in optimising the thickness distribution on the cavity surface as well as the local material properties of the film, as shown for example in Figures 4.6 and 4.7. This experimental approach allowed to define the baseline recipe for the production coating, based on an iterative optimisation process.

The same setup was also used to investigate magnetron sputtering as an alternative coating method. Magnetron sputtering results in reduced impurity levels in the niobium layer, due to the high deposition rates and low working gas pressures. Moreover it was initially considered attractive as it requires less deposition time and thus allows to easily keep the process temperature relatively low. This was deemed important to prevent deformations of the cavity during coating. Subsequently, it was understood that

small deformations of the cavity during coating could be tolerated, when the latter were quantified and in parallel, mechanical tolerances were reassessed. Moreover, controlling the plasma distribution in the magnetron configuration was found to be challenging [7].

The sputtering setup, described in detail in [8], must be assembled in an ISO5 clean room to avoid dust contamination of the cavity surfaces before coating. The coating chamber itself is an ultra high vacuum system designed to reach base pressure after baking in the $10^{-8}$ mbar range at $300°$C (starting temperature of coating).

The sputtering cathode is a high RRR Nb cylinder, which is enclosed by two coaxial grids as shown in Figure 4.4. The grids are grounded, while the cathode and the cavity are set at different negative voltages to sustain the glow discharge and to promote ion bombardment of the growing film. Three infrared lamps providing up to 2 kW each are evenly positioned around the cavity and used for the bake out of the substrate.
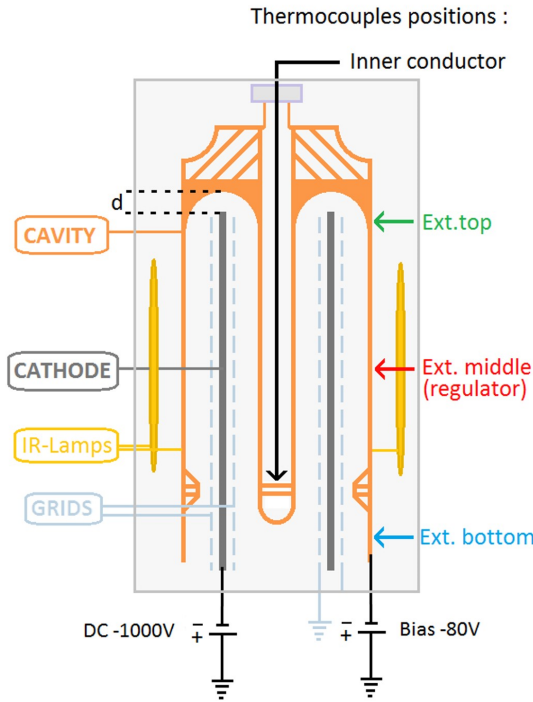


**Fig. 4.4:** DC bias diode sputtering setup.

Figure 4.5 presents the main steps of the baseline production process [8] for the superconducting cavities, which lasts for six weeks and requires a strict collaboration among different teams. First, the cavity is tuned and its copper surface undergoes chemical polishing and passivation. Then, it is rinsed with ultrapure water in an ISO5 clean room and mounted on the sputtering system for pump-down and bake-out at temperatures of $635 - 655°$C. The next step is niobium coating with the DC bias sputtering method at 8 kW discharge power, which is done in 14 runs of about 23 minutes each, with pauses in-between to allow the cavity to cool down before starting the next run, thus keeping the cavity temperature below the highest temperature reached during bake-out. Following niobium coating, cavities are rinsed with low pressure ultra pure water, they are equipped with a bottom plate made of Nb coated copper, and then undergo RF tests at 4.5 K.

It was found that, to reach their best performance, cavities had to be cooled down as homogeneously as possible to minimise the temperature differences across the resonator when the Nb layer crosses the superconducting transition. This is achieved by a second cool-down after full cavity thermalisation at 4.5 K, whereby the cavity is typically warmed up to $10 - 15$ K and then cooled down again.

The improvement in cavity performance for low thermal gradients upon cool-down is attributed to the presence of thermo-electric currents which cause magnetic flux to be trapped in the superconducting film, resulting in additional losses. However this is still not fully clarified and is an active field of research. The RF performance of series HIE-ISOLDE cavities at 4.5 K in the vertical test stand are shown in Figure 4.8. Initial prototypes entirely manufactured at CERN surpassed the design specification of 6 MV/m and 10 W power dissipation. In the course of the series production, however, the average performance was degrading.
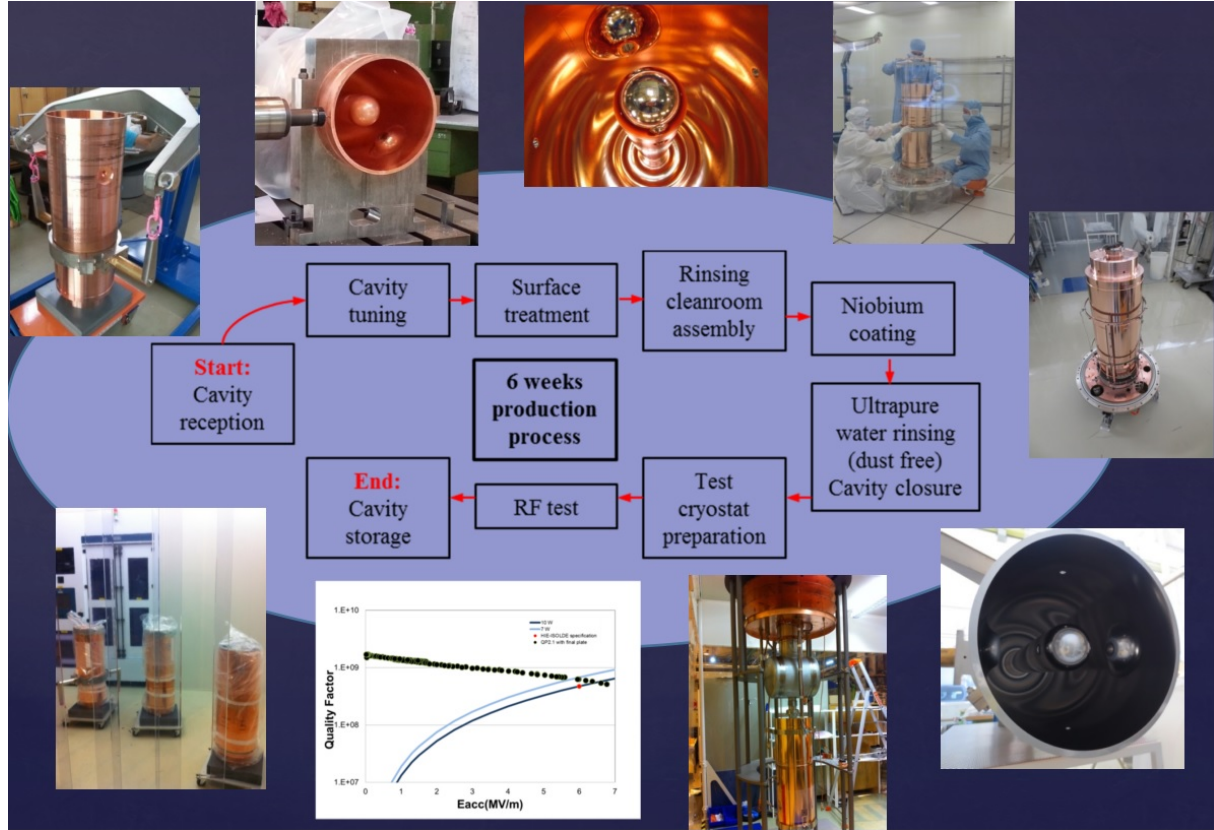


**Fig. 4.5:** Illustration of the superconducting cavity niobium coating procedure.

## 4.2   Seamless cavity design

Some cavities produced in industry were subject to defects on the RF surface, mostly located close to the electron beam weld. The most critical of these defects were in the form of cracks going deep into the material, predominantly along grain boundaries. The relative degradation of the Q values in the series cavities as compared to the prototypes has been correlated to the amount of defects observed.

A new cavity design [11] was developed with the aim of making it possible to machine them from a single copper billet, thus avoiding completely the electron beam weld. The main modification required was to reduce the protuberances of the RF surface at the beam ports (cavity noses). Removing the weld from the high magnetic field region would eliminate the main source of potential imperfections where sensitivity to RF losses is highest. The cross section for conduction cooling of the cavity is also much increased in the new design.

The new RF design started as a "perturbative" expansion of the already existing series production (QS) cavity, which is used as reference in the process of the new cavity design (QSS). The new seamless design consists of a rotational symmetric cavity with a double conical shape. This shape, with respect to a cylindrical one, will help reduce possible leakage through the beam ports, recovering the accelerating
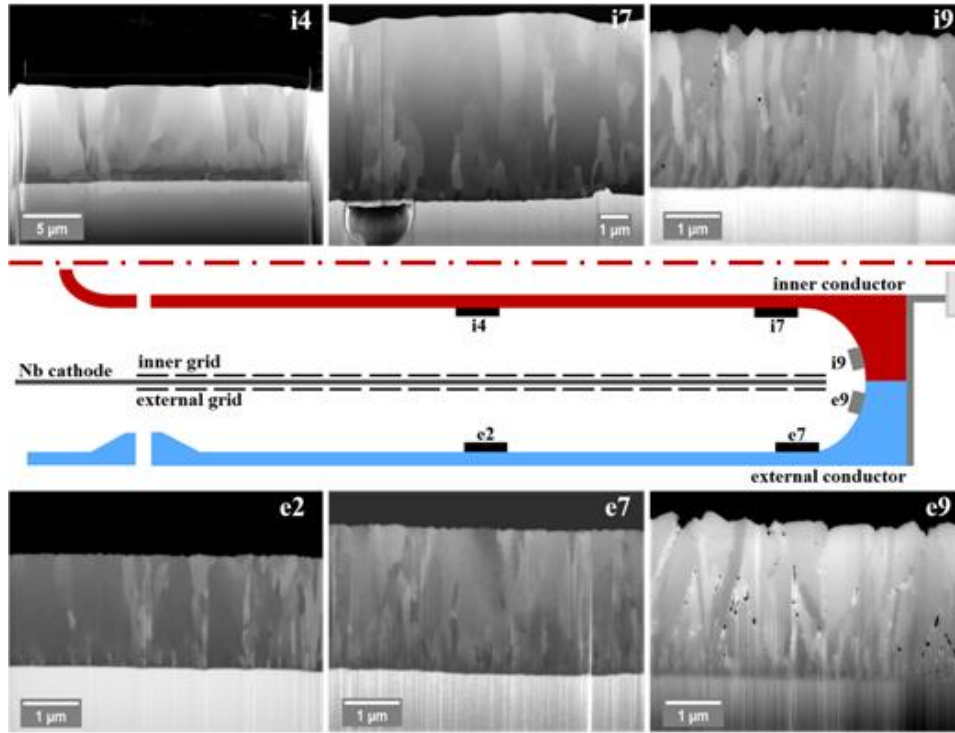
**Fig. 4.6:** Schema of the Q4.8 cavity. The black boxes represent the positions of the samples with deposited Nb coating along the inner and external conductor. The cross-section images from selected positions revealed the grain structure, in certain samples the presence of porosity. [9]
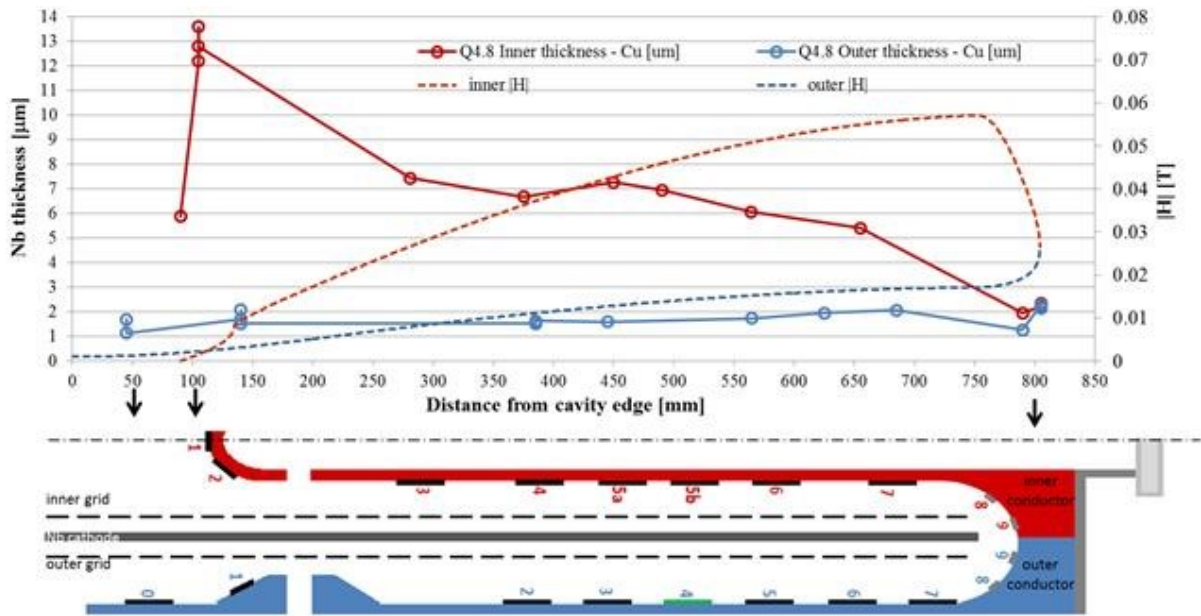


**Fig. 4.7:** Niobium film thickness profile along the cavity inner (solid red line) and outer (solid blue line) conductors, together with calculated surface magnetic field distribution on inner (dotted red line) and outer (dotted blue line) conductors. The sketch at the bottom represents the Q4 half cavity section with inner conductor (red), outer conductor (blue), and the schematic position of cathode, bias grids and samples on the cavity walls. [10]
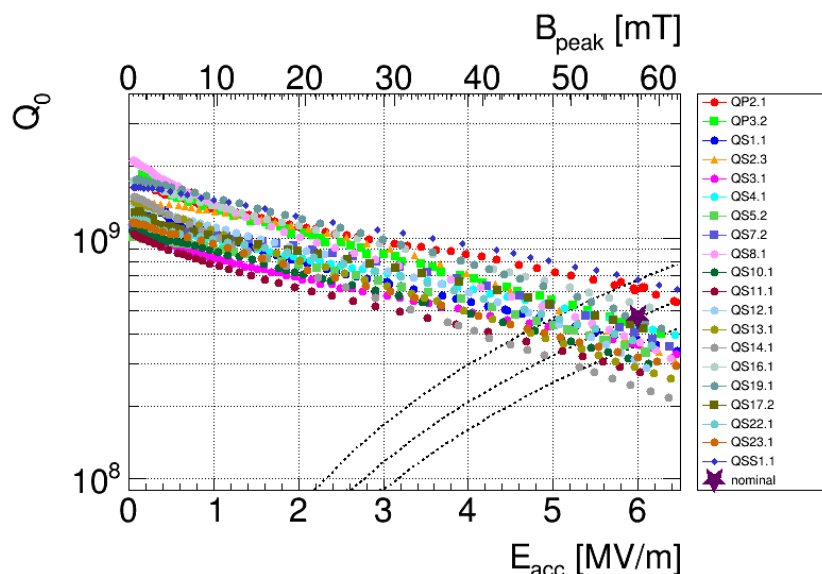
**Fig. 4.8:** Q vs $E_{acc}$ curves of bias diode coated cavities. [5].

efficiency, in terms of the shunt impedance over quality factor (R/Q), and staying within the required mechanical constrains for the cavity's outer shape. Some changes have also been made in the diameter of the inner conductor and the beam port size and shape to optimise efficiency.

Figure 4.9 shows the 3D model of the proposed design and in Figure 4.10 presents the fields' distribution. The parameters of the seamless high-$\beta$ cavity design are compared to the nominal design in Table 4.2.
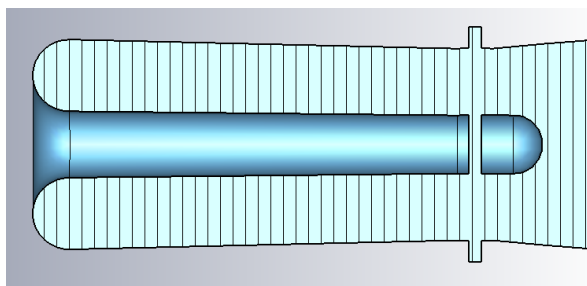


**Fig. 4.9:** 3D model of the seamless cavity.

## 4.3 Fundamental couplers

The fundamental power coupler for the HIE-ISOLDE cavity is variable and was designed to reach critical coupling conditions both in the superconducting and normal conducting states. This feature allows efficient conditioning of the multipacting levels and operation at low bandwidths to take advantage of low levels of microphonics. The operational bandwidth initially chosen was 16 Hz, implying a minimum of about 200 W RF average forward power for the nominal accelerating field of 6 MV/m. The first version of the coupler was optimised using a lumped model of the feed line to analyse the distribution of dissipated power and position the thermal intercepts (Figure 4.11). This design was qualified and used in the vertical tests during the cavity development phase.

During the 2015 commissioning campaign, a thermal instability, described in [6], was observed
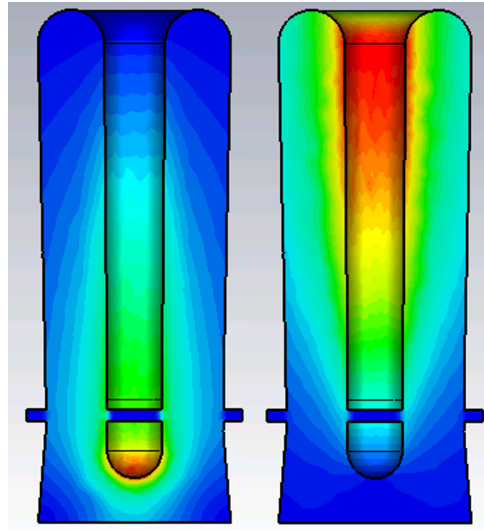
**Fig. 4.10:** E-Field (left) and H-Field (right) patterns for the seamless cavity.

**Table 4.2:** Parameters of the nominal and the new cavity design.

| Parameter | QS | QSS |
|---|---|---|
| $\beta_{opt}$ [%] | 10.9 | 12.2 |
| R/Q [$\Omega$] | 520 | 502 |
| $E_{peak}/E_{acc}$ | 5.4 | 5.2 |
| $B_{peak}/E_{acc}$ [Gs/(MV/m)] | 96 | 93 |
| $G = R_s \cdot Q$ [$\Omega$] | 30.34 | 30.71 |
| $U/E_{acc}^2$ [J/(MV/m)$^2$] | 0.207 | 0.214 |
| $P_c$ at 6 MV/m [W]* | 7.7 | 7.9 |

* calculated assuming $R_s = 50$ n$\Omega$
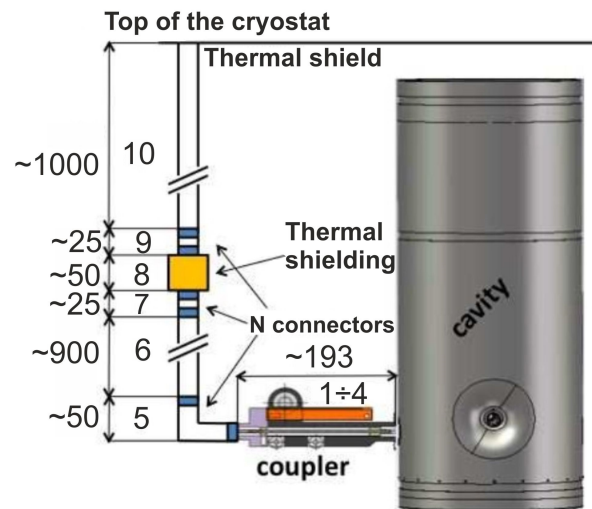


**Fig. 4.11:** Layout of the HIE-ISOLDE coupler.

34
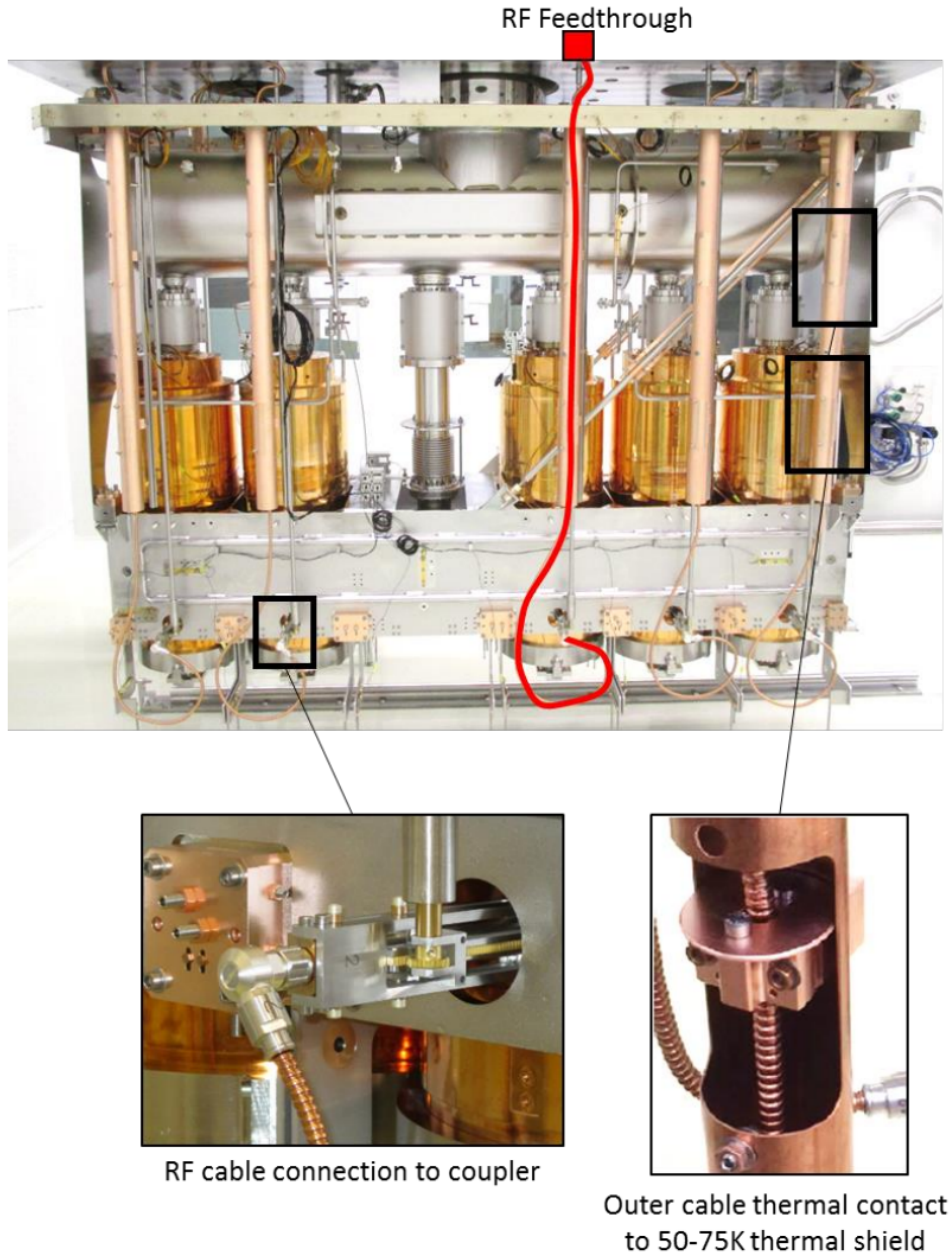
**Fig. 4.12:** Global layout of the RF coupler system in the HIE-ISOLDE cryomodule [12].

in the coupler lines. The RF signals were found to be drifting in a way which could be interpreted as the effect of a slow expansion of the coupler antenna. This was confirmed with offline tests in a vertical cryostat, highlighting a design flaw in the RF feed system, which would lead to thermal breakdown after a few hours of operation at nominal parameters. Following these findings, a crash program was launched to understand and solve the problem. A new design for the coupler lines was developed; it was installed in the second cryomodule and retrofitted to the first.

After benchmarking the numerical model by means of dedicated experiments in the vertical test stand, design modifications could be evaluated to improve the thermal stability of the coupling system. The most effective changes to the design parameters were the material of the coupler antenna, the contact between the antenna and the inner conductor of the RF line, and the location of the thermal anchors along the line. The antenna material was changed from a bronze alloy to OFE copper, which was directly

soldered on the cable, thus eliminating pressure contacts. A second thermal anchor was added very close to the coupler. The influence of these simple changes on the calculated temperature distribution is shown in Figure 4.13.
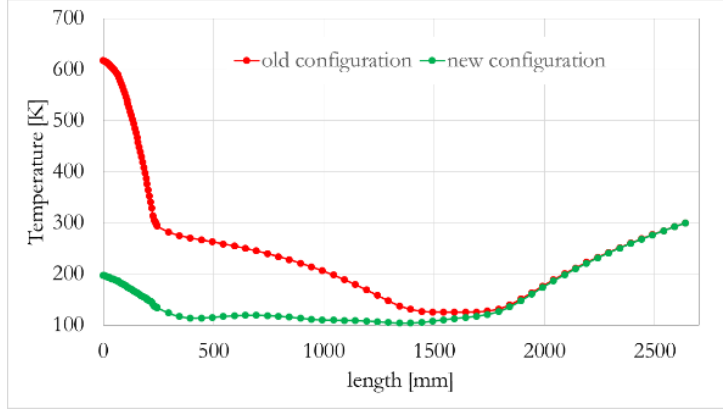


**Fig. 4.13:** Predictions of the thermal model at 200 W forward RF power, for the old and new configurations.

For each cavity two additional temperature sensors were implemented in order to monitor the temperatures of the coupler and of the RF cable. A prototype of the modified coupler was readily produced and extensively tested to validate the design. The result of four days running at nominal field (requiring less than 100 W) is shown in Figure 4.14.
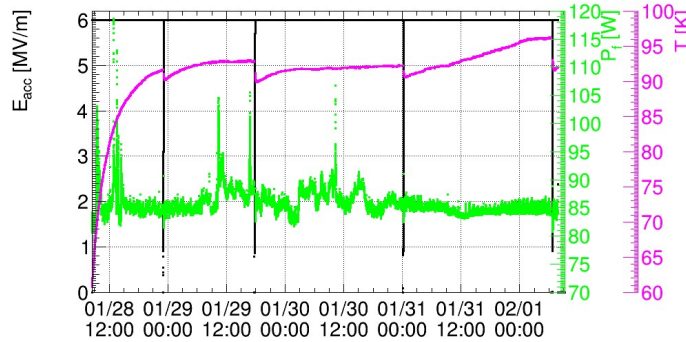


**Fig. 4.14:** Results of prototype validation, with RF power, accelerating field and coupler temperature during a 100-hour heat run in the vertical test stand.

## 4.4 Tuning system

The cavity tuning system has the function of bringing the cavity resonance frequency at the HIE-ISOLDE linac value of 101.28 MHz for beam acceleration. Small fluctuations of the cavity resonance are compensated by the low level RF system, which uses several loops to keep field amplitude and phase locked, at the linac frequency distributed by the master clock. Cavities are pre-tuned during the production process (see above) in order to reach close to the target frequency in the accelerator environment. The tuning system provides a coarse range of about 40 kHz to correct for the inevitable spread in the cavity frequency.

Tuning is achieved by deforming a 0.3 mm bottom plate made of OFE copper coated with Nb (by planar magnetron sputtering). A mechanical actuator, placed outside the cryogenic environment,

controls the plate deformation through a compact lever system, based on knife edge pivots and a flexural connection. The lever system is placed below the cavity as shown in Figure 4.15, and connected to the top plate by a stainless steel rod. All joints in the cryogenics environment are pinned to improve reliability on the long term, while the actuator can be changed without requiring transport and disassembly of the cryomodule. The tuner has a resolution of 0.1 Hz/step, which is largely sufficient to control the cavity even when operating at bandwidths of a few Hz. More information can be found in [13].



(a)  (b)
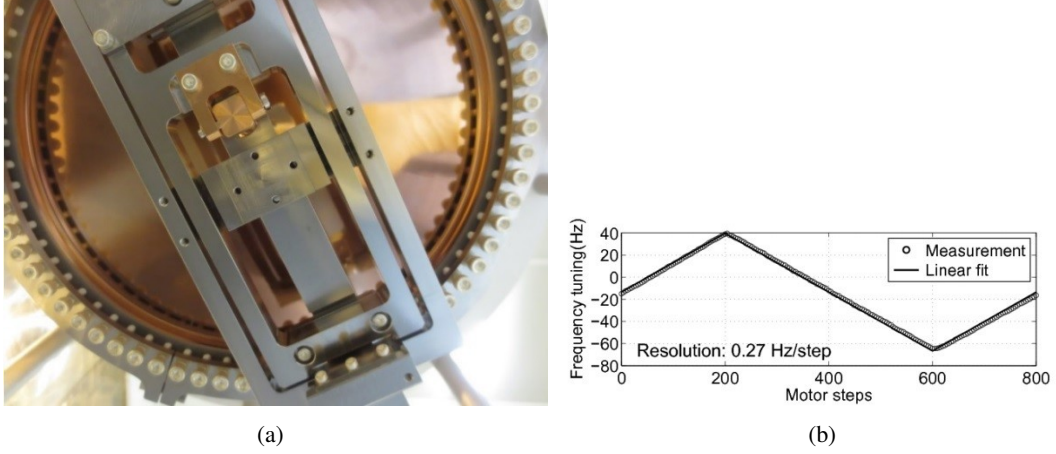
**Fig. 4.15:** (a) HIE-ISOLDE tuner plate and its lever mechanism and (b) measurement results of the frequency tuning vs motor steps.

## 4.5  Cold test facilities

To validate the RF performance of the cavity, an insert was designed and manufactured at CERN [14]. The insert is composed of a liquid helium reservoir to cool the cavity at $4.5$ K, horizontal thermal shields for radiation intercept and feedthroughs for the transmission of RF power, mechanical actuation of coupler and tuner and monitoring of environmental conditions such as temperature, pressure, magnetic field, and helium level. To avoid dust contamination, the cryostat insert with the test set up is prepared in an ISO5 clean room. Cavities are tested in a common vacuum, reproducing operating conditions in the cryomodule.

To keep the benefit of clean room assembly when connecting the insert to the heat screen and inserting the cavity into the cryostat, a metallic structure closed with PVC curtains was installed around the HIE-ISOLDE cryostat area, see Figure 4.16 for a 3D view [15].

A mobile laminar flow system is installed to improve the quality of the air in the cryostat area during the phases of test preparation. Measurements show an improvement of an order of magnitude of the particle concentration.

The cryostat is pumped by a primary pump to a level of $10^{-2}$ mbar and subsequently by a turbo-molecular pump. The test cryostat is equipped with an actively cooled thermal shield which is kept at $50$ K by circulation of helium gas. When the cool-down is complete, the pressure reaches the low $10^{-8}$ mbar range.

The cryogen is delivered to the cryostat, where the helium level is kept constant in a reservoir. From the reservoir, liquid helium fills the cavity and the heat exchange with the cavity is increased by a thermosyphon mechanism [14]. The evaporated helium gas is used to cool down the thermal shield and the cavity cool-down is done after the thermal shield and the tank reach their nominal cryogenic temperature. Then, residual gas is cryo-pumped on the thermal shield and the reservoir.

During cool-down, key temperatures are monitored: in particular two thermometers are placed on the cavity side to estimate the temperature gradient in the cavity during the superconducting transition.
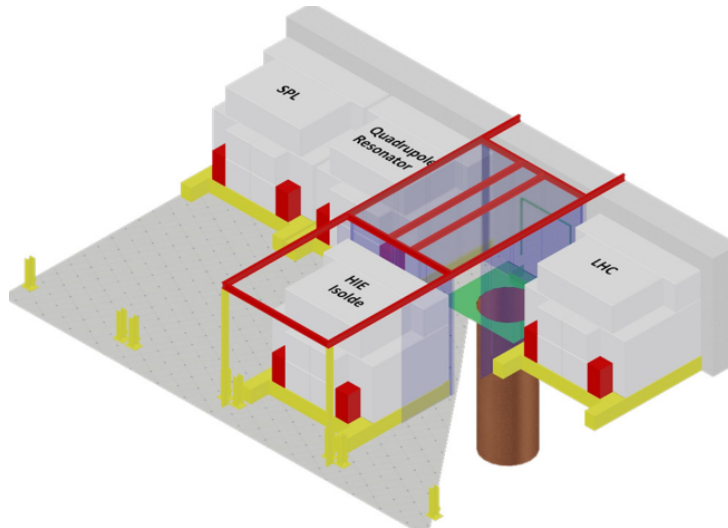
**Fig. 4.16:** Schematic view of the vertical cryostat area with the clean space.

The helium level is monitored by sensors installed inside the tank and in the cavity inner conductor.

The RF measurement system used a Phase Locked Loop to lock the cavity on the resonance during powering. A new, fully digital system, based on a self excited loop and developed for the linac operation, was also used to crosscheck the measurements.

The RF characterisation comprises the standard Q vs E curve and the measurement of the resonant frequency in operational conditions. The tuning plate is systematically tested to assess the tuning range, sensitivity and mechanical hysteresis. In some cases, the frequency shift and the surface resistance are also measured as a function of temperature between 2 and 9 K.

## References

[1] M. Kelly, Recent developments in low and medium beta SRF cavities, Proceedings of PAC'09, Vancouver, 2009, pp 699–703.

[2] Computer simulation technology - microwave studio (CST - MWS), Online, http://www.cst.com/, cited 2011.

[3] M. A. Fraser, R. M. Jones (dir) and M. Pasini (dir), PhD thesis, Manchester U., 2012, Presented 26 Jan 2012.

[4] L. Alberty et al., The copper substrate developments for the HIE-ISOLDE high-beta QWRs, 16th International Conference on RF Superconductivity, Paris, 2013, p tup069.

[5] W. Venturini Delsolaro et al., Nb Sputtered Quarter Wave Resonators for the HIE-ISOLDE, SRF2013, Paris, Paris, 2013, p weioa03.

[6] W. Venturini Delsolaro et al., HIE-ISOLDE: First Commissioning Experience, Proceedings of IPAC2016, Busan, 2016, pp 2230–2233.

[7] G. Lanza et al., The HIE-ISOLDE Superconducting Cavities : Surface Treatment and Niobium Thin Film Coating, Proceedings of SRF2009, Berlin, 2009, pp 801–805.

[8] N. Jecklin et al., Niobium Coatings for The HIE-ISOLDE QWR Superconducting Accelerating Cavities, 16th International Conference on RF Superconductivity, Paris, 2013, p tup073.

[9] B. Bártová et al., Characterization of Nb Coating in HIE-ISOLDE QWR Superconducting Accelerating Cavities by means of SEM-FIB and TEM, Proceedings of IPAC'15, Richmond, 2015, pp 3155–3158.

[10] A. Sublet et al., Nb Coated HIE-ISOLDE QWR Superconducting Accelerating Cavities: From Process Development to Series Production, Proceedings of IPAC'14, Dresden, 2014, pp 2571–2573.

[11] M. A. Fraser et al., A seamless RF cavity design for HIE-ISOLDE, EDMS 1651116 (CERN, Geneva, 2017).

[12] L. Valdarno and Y. Leclercq, Design of thermalisations for the RF coupler system for HIE-ISOLDE cryo-modules, EDMS 1608216 (CERN, Geneva, 2016).

[13] P. Zhang, W. Venturini Delsolaro, K. Artoos et al., *Nucl. Instrum. Methods Phys. Res., Sect. A* **797** (2015) 101.

[14] O. Capatina et al., Cryostat for Testing HIE-ISOLDE Superconducting RF Cavities, Proceedings of IPAC'11, San Sebastian, 2011, pp 313–315.

[15] J. Chambrillon et al., CERN SRF Assembling and Test Facilities, Proceedings SRF11, Chicago, Chicago, 2011, volume 5, pp 530–532.

# Chapter 5

# Focusing structures: SC solenoids

D. SMEKENS

As is common practice with low-energy superconducting linacs, a beam focusing system based on high-field compact superconducting solenoids was chosen and integrated inside the cryomodules alongside the cavities, reducing the overall length and cost of the machine. Less space is lost to the regions between the cryomodules and the longitudinal acceptance is increased as a consequence of the increased packing of the cavities. The single tuning knob makes the linac easier to operate when scaling to accelerate radioactive beams and solenoids have a higher tolerance to mismatch and acceptance to beams of multiple charge states [1]. Due to the stringent space restriction inside the cryomodules and to minimise the exposure of the RF cavities to the magnetic stray field, the magnets have been designed as compact as possible and equipped with an iron yoke.



(a) Cross-section

(b) 3D representation
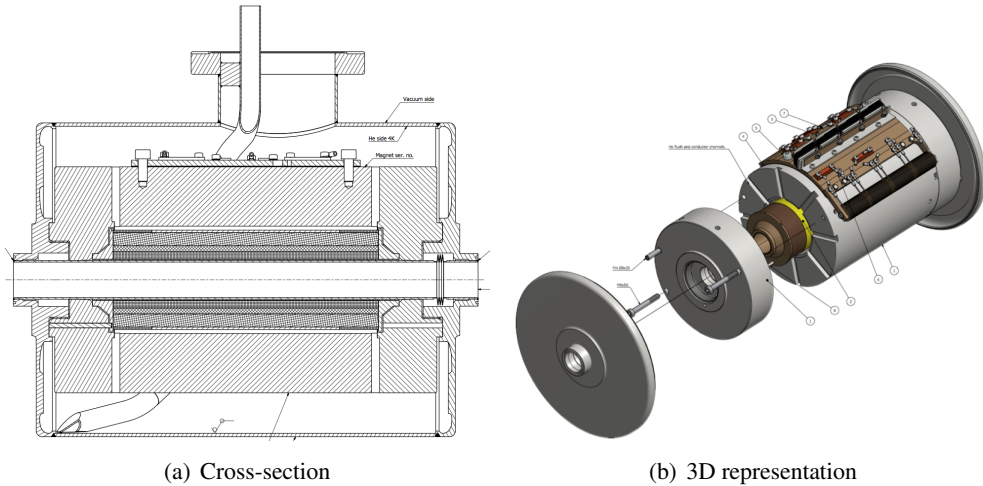
**Fig. 5.1:** Mechanical drawings of the SC solenoid in the HIE-linac.

The design and optimisation work was contracted at the end of 2012 to Danfysik A/S. Magnet production started in November 2013, with a first solenoid delivered fully tested in September 2014. Delivery of the series solenoids and of a fifth (spare) spanned over 2015–2016.

## 5.1 Magnetic design

The solenoid magnet, depicted in Figure 5.1, has been designed with graded coils using enamelled Nb-Ti wires. The bore diameter is 31 mm, the integrated square field reaches $13.5$ T$^2$m over $312$ mm magnetic length at a nominal current of $115.5$ A, with a field margin of $19\%$ at 4.5 K. The peak field at the centre is $7.86$ T, while magnetic yoke allows to significantly limit the stray field below $1.5$ mT, $230$ mm away from the centre. Figure 5.2 presents the field intensity map of the solenoid. The specification of the solenoid, which is based on the beam dynamics studies detailed in this thesis, is summarised in Table 5.1. The coil of the magnet is composed of $13,088$ turns divided in 4 sub coils using 3 different wires gradually smaller from the high field region of the bore toward the outside diameter of the coil. The superconducting wires are Nb-Ti/Copper matrix, enamelled with a PVA resin, available from OST. Description of the conductor and of the winding arrangements is given in Table 5.2.

**Table 5.1:** HIE solenoid design parameters.

| Magnet main parameters | Description/Value |
|---|---|
| Bore diameter [mm] | $31 \pm 0.3$ |
| Magnet length [mm] | 312 |
| Coil length [mm] | 232 |
| Field integral at nominal current [T$^2$.m] | 13.5 |
| Peak field at solenoid magnetic center [T] | 7.86 |
| Stray field at nominal current and at 230 mm from solenoid magnetic centre [T] | $< 1.81 \cdot 10^{-3}$ |
| Magnetic remanence at $I = 0$ and at 230 mm from solenoid magnetic centre [T] | $< 6.51 \cdot 10^{-5}$ |
| Nominal current [A] | 115.5 |
| Operating Temperature [K] | 4.5 |
| He bath operating pressure [MPa] | 0.13 |
| Inductance [H] | 2.37 |
| Stored energy [J] | $1.9E4$ |
| Working point at I$_{nom}$ [% B/Bc] | 81 |



(a)                                          (b)
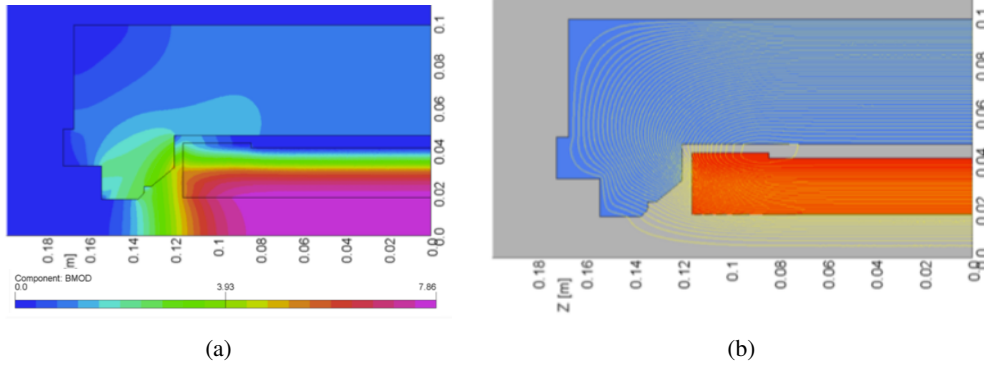
**Fig. 5.2:** Field intensity map (axisymmetric 2D model, ROXIE computation) is presented in (a); Field lines distribution (axisymmetric 2D model in red: coil in blue: iron yoke, ROXIE computation) in (b).

## 5.2 Magnet quench protection

The low stored magnet energy and the graded coil configuration of the solenoids allows for a passive quench protection. There is no quench detection system: the stored magnetic energy during a quench is dissipated through resistors connected in parallel with each coil subdivision, see Figure 5.3. To avoid losses in the parallel resistors during magnet ramping, anti-parallel diodes are connected in series with the resistors. These diodes have a forward voltage of about 1 V in cryogenic conditions. The resistors and diode stacks are placed outside the magnet yoke, in the helium bath.

## 5.3 Current leads

A high current Nb-Ti conductor (1200 A, 2 T at 4.22 K) with a large Cu/SC ratio (9 : 1) has been used for the powering leads to simplify the quench protection scheme. This solution prevents the need of monitoring the leads voltage. It also allows the use of a bolted resistive connection between the cryomodule powering circuit and the magnet leads in order to avoid fumes and risks of contamination from a soldered connection during assembly in the clean room. Bolted resistive connections have been preferred to soldered connections to avoid contamination from soldering inside the clean room during the installation of the magnet.

**Table 5.2:** Conductor and winding arrangements.

| Coil subdivision no. $\rightarrow$ | 1 | 2 | 3 | 4 |
|---|---|---|---|---|
| Sub-coil inner radius [mm] | 18 | 24.7 | 29.9 | 41.3 |
| Sub-coil outer radius [mm] | 24.7 | 29.9 | 41.3 | 43.5 |
| Sub-coil length [mm] | 232 | 232 | 232 | $2 \cdot 34$ |
| # of turns (/layer) | 180 | 308 | 428 | $2 \cdot 63$ |
| # of layers | 8 | 7 | 21 | 4 |
| Conductor manufacturer | OST | OST | OST | OST |
| Conductor shape | rectangular | round | round | round |
| Bare conductor dim. [mm] | $1.2 \cdot 0.75$ | $d : 0.7$ | $d : 0.5$ | $d : 0.5$ |
| Insul. conductor dim. [mm] | $1.28 \cdot 0.83$ | $d : 0.75$ | $d : 0.54$ | $d : 0.54$ |
| Cu/SC ratio | $1.35 : 1$ | $1.35 : 1$ | $1.35 : 1$ | $1.35 : 1$ |
| # of filaments / size [um] | 54/90 | 54/62 | 54/44 | 54/44 |
| Insulating material | Formvar | Formvar | Formvar | Formvar |
| Nominal current [A] | 115.5 | 115.5 | 115.5 | 115.5 |
| Current density $J_c$ [A/mm$^2$] | 336 | 607 | 1407 | 1407 |
| Working Point ($B/B_c$) [%] | 81 | 80 | 78 | 34 |
| Working Point ($I/I_c$) [%] | 30 | 44 | 62 | 37 |
| Peak field [T] | 7.9 | 7.0 | 5.8 | 2.5 |
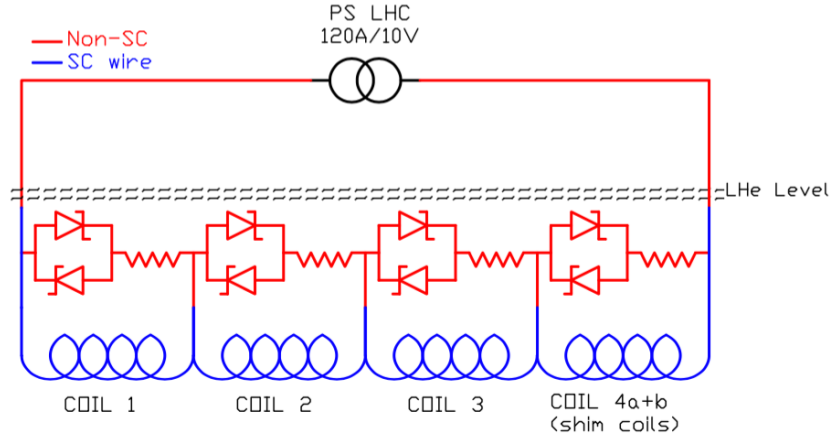


**Fig. 5.3:** Circuit diagram of HIE-ISOLDE passive quench protection.

## 5.4 Power supplies

During the magnet design phase, several iterations have allowed to decrease the operating nominal current from 180 A down to 115.5 A at the cost of a reduced integrated field (13.5 instead of 16.8) and a higher coil impedance. Operating below 120 A allows using compact air-cooled 10 V/120 A power supplies, already developed for the LHC corrector magnets [2].

## 5.5 Magnet production

During coil manufacture, pre-stressing of the coil layers is achieved by accumulating hoop stress during the winding by controlling the wire tension. After impregnation, the coil layers remain under compression. Following winding operations, the coil is impregnated under vacuum with an epoxy system. Two thermometers are cast inside the coil during the impregnation for process control by the cryogenic plant during operation. The terminals of the subcoils are routed outside the magnetic yoke and interconnected on a connection plate supporting the diode and resistor racks. In Figure 5.4, the four superconducting coils can be seen on the top of the solenoid during its assembly. The magnetic yoke is made of XC06 low carbon steel. After precision machining, the yoke components are nickel plated for corrosion resistance to avoid oxide particulate, incompatible with the cleanliness requirements during assembly and connection inside the cryomodule.
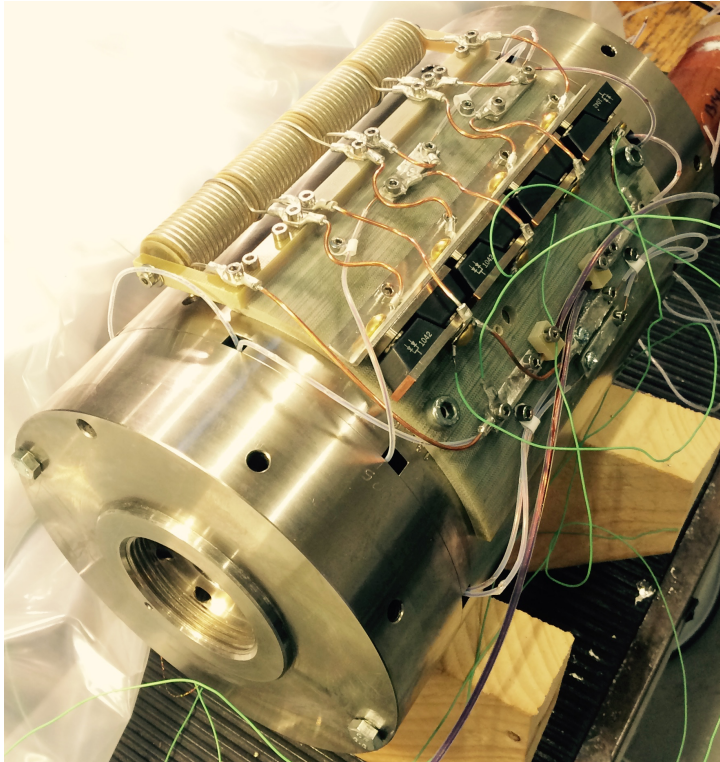


**Fig. 5.4:** Photograph of the solenoid during assembly.

## 5.6 Helium vessel

Each solenoid magnet is enclosed in a pressure vessel (helium vessel, see Figure 5.5 for a photo), connected to the common helium reservoir of the cryomodule. The vessel is an all-welded pressure tank made of austenitic steel (AISI 316L) designed with deformable end caps to sustain unbalance thermo-contraction during fast thermal cycling at 1.3 bars without permanent deformation. Such design shall also resist to an accidental loss of insulation vacuum followed by a pressure rise to 4.5 bars (max. pressure at which safety valves operate).

The vessel end caps are equipped with spherical fittings (fiducials) for alignment. The magnet is precisely positioned inside the helium vessel to guarantee that the magnet axis is coincident with the axis of the fiducials. All parts of the vessel have a mirror finish by electropolishing before magnet assembly. The welds and heat affected areas are mechanically polished after pressure testing of the vessel.

(a)                                        (b)
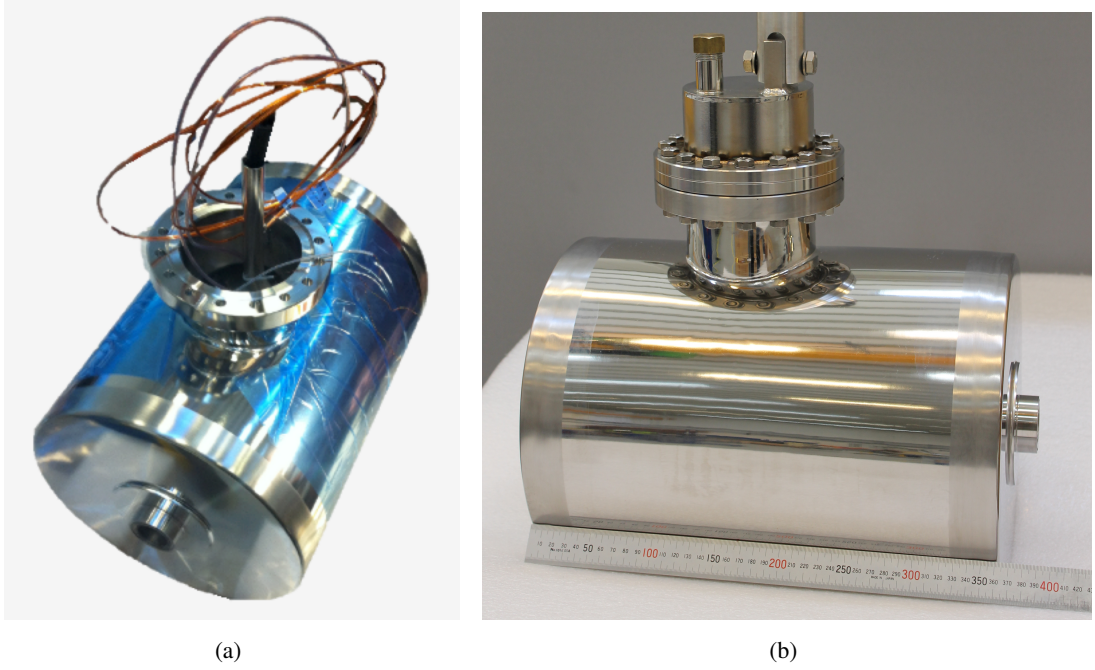
**Fig. 5.5:** The solenoid enclosed in its helium vessel.

## 5.7 Magnetic measurements

Results from magnetic measurements carried out by Danfysik A/S are presented in Figure 5.6, where the $B_z$ field profiles were measured at $r = 0$ mm, 5 mm and 10 mm by accurate Hall probe z-scans.
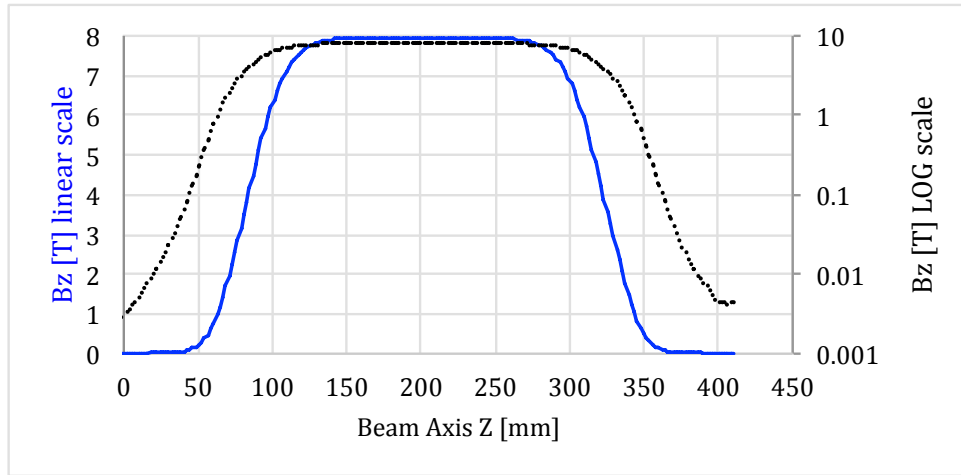


**Fig. 5.6:** Measured field profile along the beam axis (dotted line plotted according logarithmic scale to show the field decay at magnet extremities).

## 5.8 Transfer function

The relation between the integrated square field versus current can be fit with two polynomial functions (for low current $< 40$A, and above $40$A) with a deviation less than $0.5\%$. The measured transfer function is given in Figure 5.7. The variation of integrated field measured along an axis at $r = 5$ mm from the beam axis compared to the measure at beam axis ($r = 0$ mm) is less than $0.25\%$; at $r = 10$ mm the variation is less than $0.7\%$.
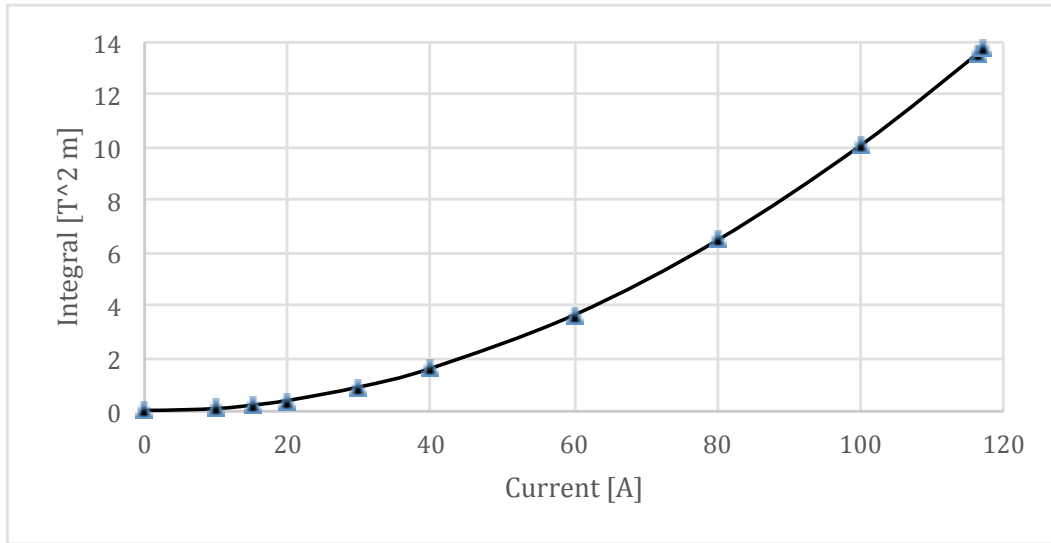
**Fig. 5.7:** Magnet Transfer Function: blue markers show measured $\int B^2 dz$ at fixed current.

## References

[1] M. Pasini and R. Laxdal, ISAC-II: Beam studies with multi-charge beams, TRI-DN-01-08 (TRI-UMF, 2001).

[2] Y. Thurel, D. Nisbet and B. Favre, Four quadrant 120 A, 10 V power converters for LHC, LHC-PROJECT-Report-1047. CERN-LHC-PROJECT-Report-1047 (CERN, Geneva, 2007).

# Chapter 6

# Cryomodule

V. Parma, L. Williams, Y. Leclercq

## 6.1 Introduction

The high-$\beta$ HIE-ISOLDE cryomodule comprises some $10,000$ parts from the smallest nut to the main vacuum vessel. The conceptual design, manufacturing choices and assembly procedure for each part are defined with the objective of fulfilling the specifications and ensuring the alignment of the cavities and solenoid, their steady temperature, cleanliness and the level of vacuum in which they operate.

Only the design of the cryomodule cryostat is detailed in this technical description; the cavities, solenoid and their layout are presented but not detailed. The assembly sequence, tooling and details are presented in the last section. A complete report of the detailed design is available in [1]. The cryomodule is designed under the GSI-M3 CERN rules (special equipment, see [2], and therefore does not require CE certified and marked equipment.

Following the directive EN 97/23/EC, the main volumes of the cryomodule are assessed to be in category II for the bi-phase helium volume. The other applied standards for the design and manufacturing are detailed in [1].

## 6.2 Technical description of the HIE-ISOLDE cryomodule

This section presents a general overview and the conceptual choices. The robustness and reliability of the design were considerably improved, thanks to advice and rules of good practice provided by the INFN and TRIUMF laboratories, which extensively contributed their experience of cryomodule design, assembly and operation.

### Overview

The design is built around the active components; five quarter wave superconducting cavities and one superconducting solenoid assembled in an environment offering the best performance of these components with respect to the specifications; temperature, pressure, vacuum level and alignment.

Five superconducting RF cavities and one superconducting solenoid are aligned on a common beam line and fixed to a rigid support frame. A helium reservoir connected via bellows to the RF cavities and solenoid reservoirs creates a common helium bath volume. The upper flange of the helium reservoir hosts the "chimney" providing the required temperature gradient in gaseous helium from 300 K and containing all interfaces for services between atmosphere and the bi-phase LHe-GHe volume; cryogenic bayonets, current leads, immersed instrumentation and pressure relief devices. This sub-assembly is suspended from the rectangular top plate of the vacuum vessel where all services into the vacuum volume are located; RF, thermal shield cooling, vacuum volume safety devices and position adjustment mechanisms. A parallelepiped thermal shield encloses the complete cold mass at 4.5 K (active components support frame and helium reservoir). The lower box of the vacuum vessel completes the common vacuum volume and provides the services for beam ports, vacuum and survey interfaces. See Figures 6.1 and 6.2 for a presentation of the main cryomodule components and their connections.
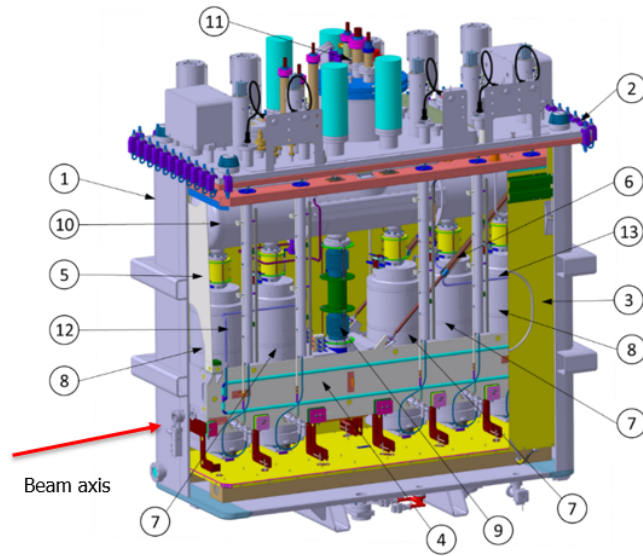
**Fig. 6.1:** Overview of the High-$\beta$ HIE-ISOLDE cryomodule main components.
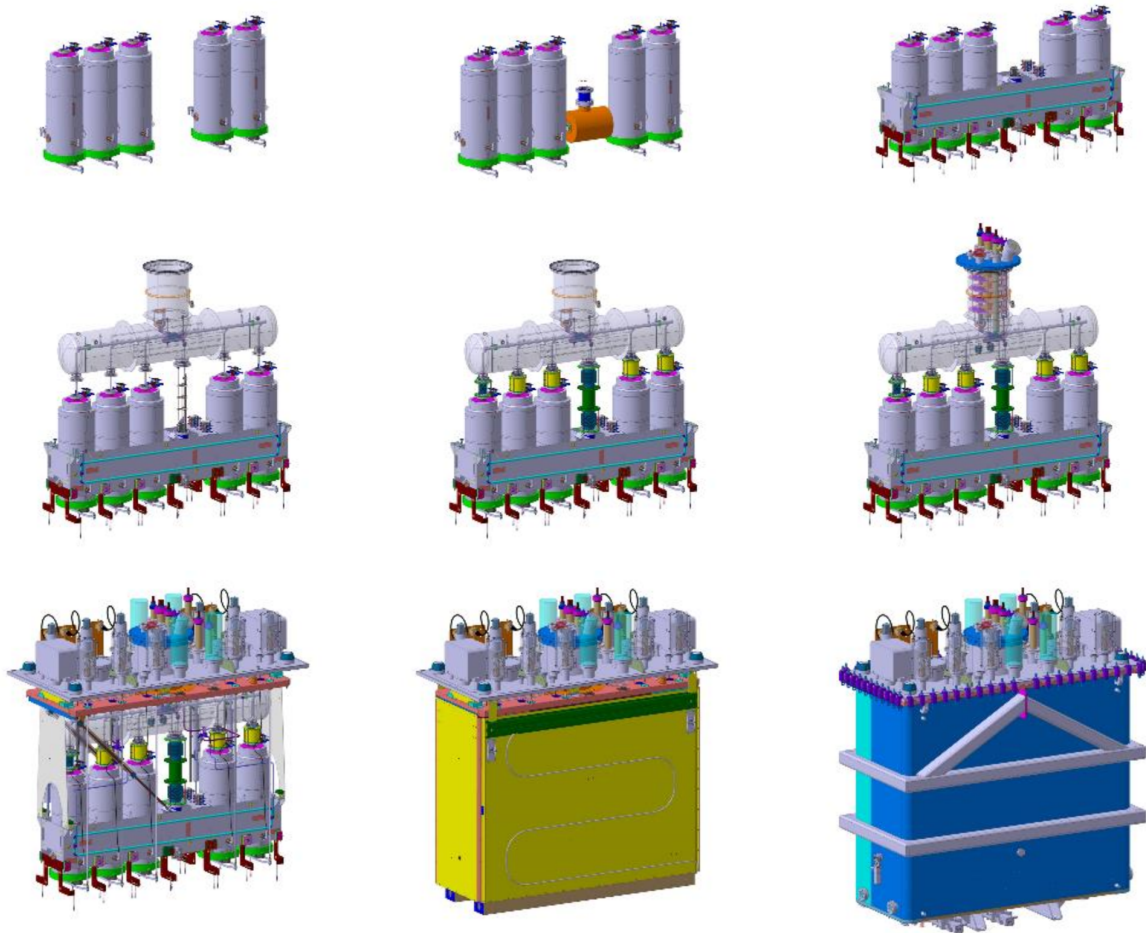


**Fig. 6.2:** Presentation of the connections of the main cryomodule components.

**Table 6.1:** Denomination of part numbers from Figure 6.1.

| Part number | Denomination | Part number | Denomination |
|---|---|---|---|
| 1 | Vacuum vessel lower box | 7, 8 | Cavities |
| 2 | Vacuum vessel top plate | 9 | Down tube to solenoid |
| 3 | Thermal shield lower box | 10 | Helium vessel |
| 4 | Support frame | 11 | Chimney assembly |
| 5 | Suspension end plate | 12, 13 | Support frame cooling |
| 6 | Tie-rod | | circuits supply, return |

**Pressures and temperatures**

The cryomodule comprises three distinct volumes; the common beam and insulation vacuum named "vacuum volume", the $55-70$ K gaseous helium circuit named "thermal shield circuit" and the bi-phase helium volume contained inside the reservoir, the RF-cavities and solenoid, and the piping supplying and welded onto the frame, named "helium bi-phase volume". The design takes into account the combination of the different possible relative pressures between the volumes.

Tables 6.2 and 6.3 present the temperature and pressure ranges respectively under steady-state and transient conditions.

**Table 6.2:** Pressure and temperature ranges for the three main volumes in steady-state conditions.

| | Temperature range [K] | Nominal pressure [bara] | Min-max design pressure [bara] | Volume [litre] | Fluid [-] |
|---|---|---|---|---|---|
| Helium bi-phase volume | $4.5-300$ | $1.3 \pm 0.01$ | $0-3.5$ | 250 | LHe-GHe |
| Vacuum volume | 300 | $1 \cdot 10^{-12}$ | $0-1.5$ | 5000 | Vacuum |
| Thermal shield circuit | $50-75$ | 10 | $0-16$ | 10 | GHe |

**Table 6.3:** Pressure and temperature ranges for the three main volumes in transient conditions.

| | Temperature range [K] | Pressure Range [bara] | Max design pressure [bara] | Volume [litre] | Fluid [-] |
|---|---|---|---|---|---|
| Helium bi-phase volume | $4.5-300$ | $0-2.5$ | 3.5 | 250 | LHe-GHe |
| Vacuum volume | 300 | $0-1$ | 1.5 | 5000 | Vacuum |
| Thermal shield circuit | $50-300$ | $0-16$ | 16 | 10 | GHe |

## 6.3 Alignment

Beam ports of the RF cavities and solenoids are first aligned with respect to a common theoretical beam line. There are then three different systems to adjust this common theoretical beam line with respect to the real beam line under vacuum and at cold as detailed in the following paragraphs.

**Specifications**

According to [3], the alignment specifications for cavities and solenoids are as follows:

- Solenoid aligned to $\sigma_{sol} = \pm 0.23$ mm.
- Cavities aligned to $\sigma_{cav} = \pm 0.45$ mm.

In order to fulfil the requirements, these specifications are translated into mechanical tolerances as follows (margins included), see Figure 6.3:

- The axis defined by the mechanical centres of the two beam ports of each solenoid must be co-axial to the beam line within a cylinder of diameter 0.3 mm.
- The axis defined by the mechanical upper centres of the two oblong beam ports of each cavity must be co-axial to the beam line within a cylinder of diameter 0.6 mm.

No formal specifications have been expressed neither for the angle of rotation of the cavities and solenoids around their beam axis nor for the longitudinal position on the beam axis of these superconducting components.
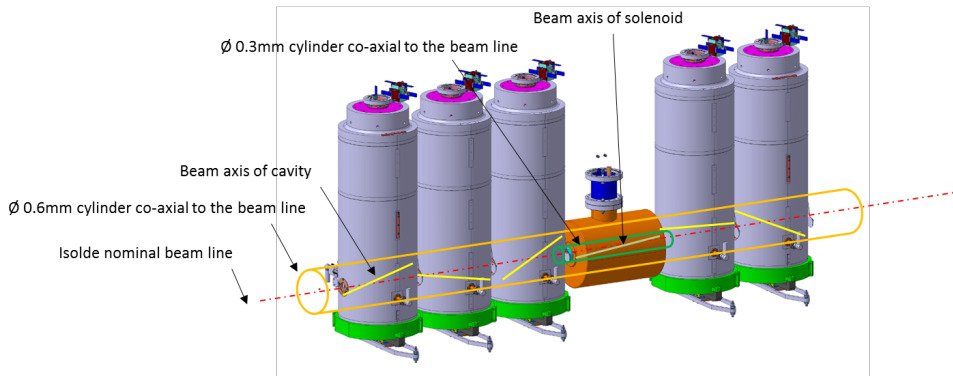


**Fig. 6.3:** Illustration of the alignment specifications. Each cavity beam port must be contained in a cylinder of diameter 0.6 mm centred onto the beam line, 0.3 mm for the solenoid.

**Alignment procedure and adjustment systems**

A sequence of alignment operations is foreseen and is carried out at stages during the assembly. At each stage, an offset with tolerance is defined in order to reach the required specified position once at stable operating temperature and in the presence of cryogenic pressure.

To position the solenoid and cavities beam ports onto the beam line within specifications, the alignment is performed in three main steps during assembly and installation. A fourth adjustment step allows a correction of the position of the active components' common axis at cold if needed, see Figure 6.4. In operation, the monitoring of the position of the active components is performed using BCAMs devices and reflective targets as presented in [4] and [5].

Alignment sequence:

- Alignment onto a best-fit line within 0.05 mm and fixing of the beam ports' positions to the supporting frame.
- Alignment of the best-fit line between the beam ports to the top plate within 0.5 mm to nominal position.
- Alignment of the best-fit line between the beam ports to the nominal beam line within 0.1 mm.
- Adjustment of the common best-fit line position at cold if needed.

(a) Alignment of components to a common best-fit line.  (b) Alignment of the best-fit line between components to the top plate referential.  (c) Alignment of the best-fit line to the beam line.
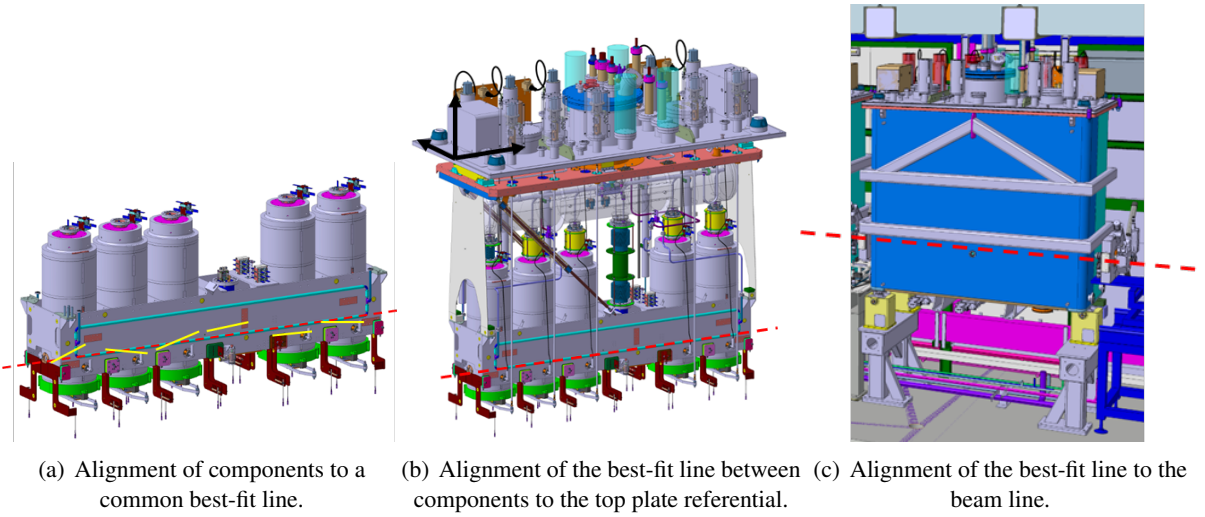
**Fig. 6.4:** The three main steps of the components alignment.

## 6.4 Vacuum design

**Specifications**

The vacuum requirements are specified in [6].

As an overview, Table 6.4 presents some of the key values from [6].

**Table 6.4:** Key values for vacuum specifications from [6] version 4.1.

| Parameter | Value |
|---|---|
| Operation pressure at warm | $1 \cdot 10^{-7}$ mbar |
| Ultimate operation pressure | $1 \cdot +10^{-8}$ mbar |
| Outgassing rate, $H_2O$ | $< 3 \cdot 10^{-9}$ mbar.l.s$^{-1}$.cm$^{-2}$ after 1 h pumping |
| Upper limit of RGA signal for $M > 28$ | 1/100 of the $H_2O$ peak after 10 h pumping |

In addition to the vacuum level and quality, the sensitivity of internal RF surfaces of the cavities to dust particle contamination requires an assembly performed in a clean room providing an ISO5 air quality level.

In addition to the pressure level, the total leak flow rate due to outgassing, permeation and possible leaks must remain low (target: $1 \cdot 10^{-9}$ mbar.l.s$^{-1}$) to avoid creating a significant gas condensation layer on internal cold surfaces, in particular on superconducting surfaces of RF cavities, that would deteriorate their performance. Moreover, significant gas condensation may adversely affect the emissivity level of the thermal shield surfaces and release large amounts of gas during cryomodule warm-up.

The cryomodule contains one common insulation and beam vacuum, as detailed in [7]. The vacuum equipment and layout is presented in [8]. In steady-state operation, two 700 l/s turbo pumps are running continuously. The total cold surface area ($< 80$ K) is above $30$ m$^2$, which then provides a powerful cryopumping capacity to reach the operating pressure in a $4$ m$^3$ volume.

**Sealing design**

To limit permeation, ease leak testing and reduce the possibility of leaks, the general approach is to apply copper gasket between ConFlat type flanges wherever possible; either for vacuum or helium (gas or liquid). All flanges are, therefore, (from design) CF type. For flanges of dimensions above DN250,

Helicoflex metal seals are used to ensure the tightness between the helium volume and vacuum or atmosphere.

The vacuum vessel top-plate to box seal is a double elastomer seal design with interseal pumping to provide flexibility and redundancy where a limited leak rate on one of the two seals may be containable in operation, see Figure 6.5.
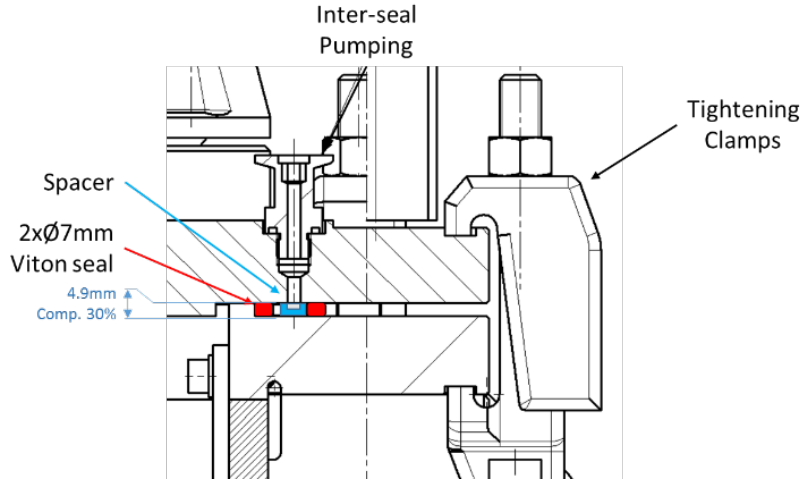


**Fig. 6.5:** Sealing design of the vacuum vessel.

The sealing design takes into account the restrictions imposed by the clean room assembly where the use of vacuum grease is prohibited and no welding nor brazing may be carried out. The sealing interface between the reservoir and the vacuum volume is made with a double Helicoflex-Viton seal as presented in Figure 6.6.
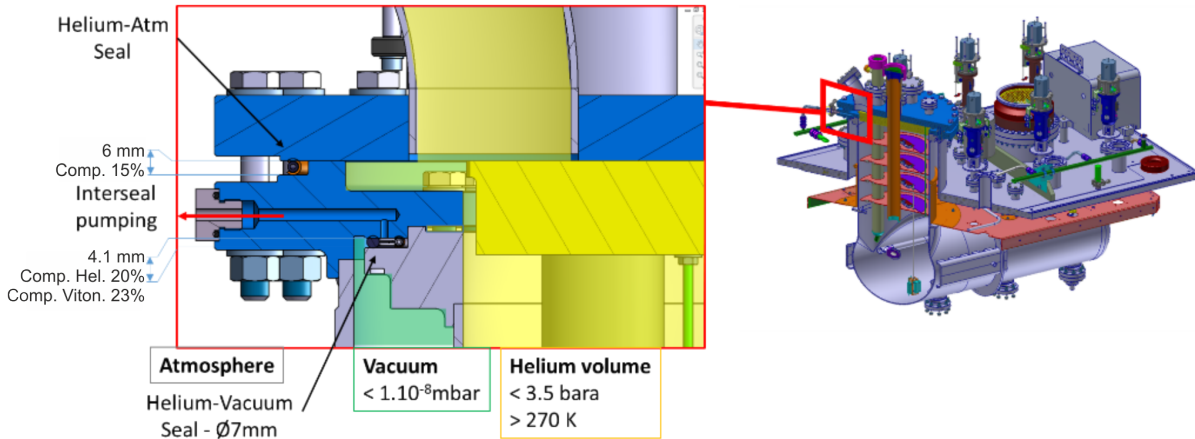


**Fig. 6.6:** Sealing design of the chimney to top plate interface.

Details on the sealing design of the bayonets, current leads, and instrumentation feedthroughs are available in [1].

## 6.5 Cryogenic design

The cryogenic design of the cryomodule together with its interfaces to the supply of cryogens ensures that it can be cooled down and warmed up in reasonable time and can be maintained at sufficiently

constant temperature and pressure during steady state operation. The PID of the complete installation is referred in [9].

**Specifications**

The cryostat design aims at ensuring at reasonable cost a stable temperature of the superconducting cavities of 4.5 K $\pm$0.5 K. In nominal operation, the static bath pressure is stabilised within a $\pm$10 mbar range in order not to substantially change the tuned frequency of the RF cavities by deforming their structures.

In operation, the solenoids must remain completely immersed in liquid helium at all times and allow their stored energy to be locally transferred to the liquid helium during quenches (19 kJ of stored energy equivalent to nine evaporated litres of liquid helium at 1.3 bara).

Heat loads must be minimised to fall within the cryogenic plant capacities while operating with four cryomodules, see [10].

Operating procedures must ensure the RF cavities continuously remain the warmest components during cryomodule cool-down to minimise residual gas cryopumping onto RF cavity surfaces and performance deterioration.

**Cool-down and warm-up procedures**

In order to fulfil the requirements, the following procedure was decided at the start of the design, see [11] for details:

- Standstill cryomodule at room temperature ready for cool-down.
- Shield cool-down 300 K $\rightarrow$ 75 K.
- Vessel and frame cool-down 300 K $\rightarrow$ 75 K.
- Cavities and solenoid cool-down 300 K $\rightarrow$ 75 K.
- Vessel and frame cool-down 75 K $\rightarrow$ 4.5 K.
- Cavities and solenoid cool-down 75 K $\rightarrow$ 4.5 K.
- Steady-state all active components at 4.5 K.
- Helium vessel emptying.
- Cavities and solenoid warm-up 4.5 K $\rightarrow$ 75 K.
- Helium vessel warm-up 4.5 K $\rightarrow$ 75 K.
- Global warm-up 75 K $\rightarrow$ 300 K.

**Description**

The active components (cavities and solenoid) have their own liquid helium volumes linked to a 350 l reservoir located above. In steady-state, the pressure of the bi-phase volume is regulated with the outlet valve in the jumper box. The reservoir is half filled with liquid (125 l) and the other half plus the chimney with gas (225 l) offering 4.5 K bi-phase volume stable in temperature and pressure. To reduce the heat loads to the cold mass and to ensure the stability and homogeneity of the active components in this temperature, the cold mass is surrounded by a thermal shield, actively cooled to $55 - 70$ K (nominal values). The solenoid is equipped with resistive vapour-cooled current leads equipped with a warm gas recuperation line. An overview of the circuits and pressure relief devices is presented in Figure 6.7.

Thermalisations for locally improving heat transfer and promoting heat extraction to intermediate temperatures are integrated in the design.
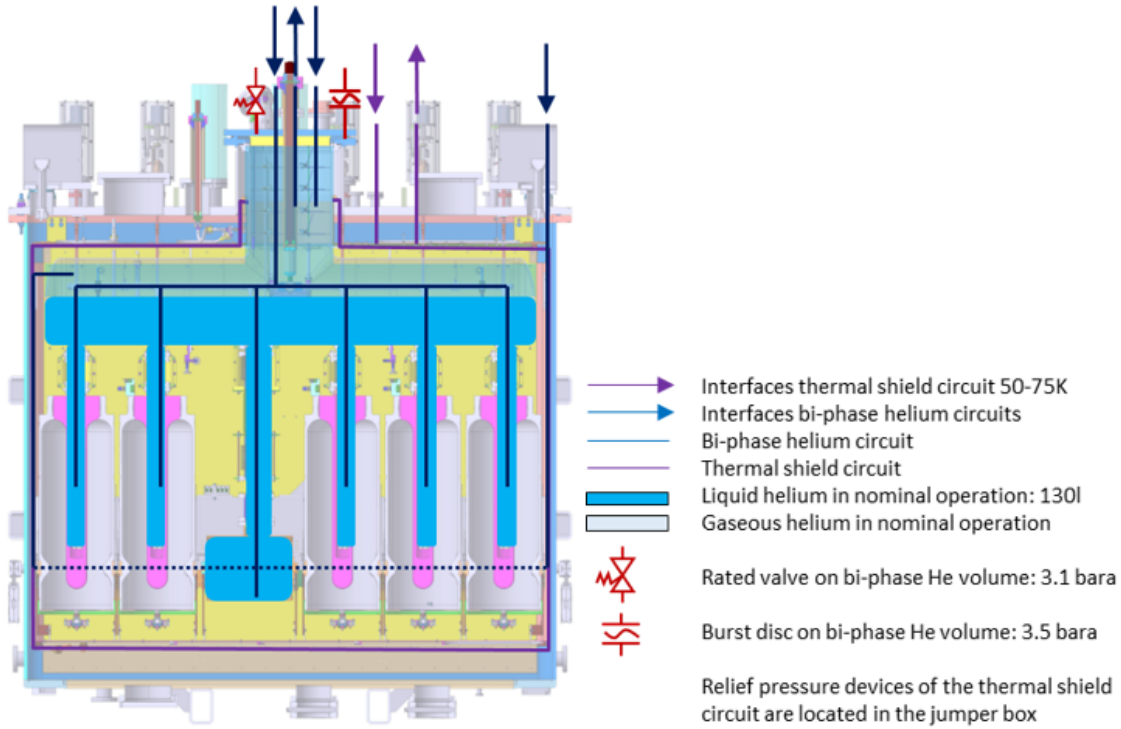
**Fig. 6.7:** Overview of the cryogenic circuits and pressure relief devices.

**Table 6.5:** Heat loads estimation as presented in [12].

| Heat loads | Nominal [W] |
|---|---|
| To GHE circuit $50 - 75$ K | 362 |
| To LHE circuit $4.5$ K + liquefaction load $0.03$ g/s | 70 |

**Heat loads**

Figure 6.8 presents the heat transfer layout in the cryomodule in steady-state. Heat loads to the $50 - 75$ K circuit are dominated by radiation, as MLI cannot be used due to cleanliness requirements, see Figure 6.9. Heat loads to the $4.5$ K circuit are dominated by dynamic loads from the cavities in operation ($> 70\%$ of the total load based on nominal full load dissipation of 10 W per cavity), see Figure 6.10.

As detailed in [12], the calculated heat loads from the design are presented in Table 6.5.

## 6.6 Safety design

The design for the safety of the cryomodule covers the protection against excessive pressure generated in the internal volumes and the safe behaviour of the linac structures when shaken by seismic events.

A dedicated report [15] details the standards, study and sizing of the protective devices for the vacuum vessel ($< 1.5$ bara), the thermal shield circuit ($< 16$ bara in the jumper box) and the bi-phase GHe-LHe volume ($< 3.5$ bara). HSE validation is available in [16]. Figure 6.11 presents the general layout.

For both volumes, an undersized subsidiary pressure relief device is added, rated to open at lower pressures and relieve pressure spikes before the safety relief device opens, but this is not considered safety equipment. To prevent a dangerous decrease of oxygen content in the HIE-ISOLDE shielding tunnel, the exhaust of all devices is routed outside the tunnel and into the experimental hall.
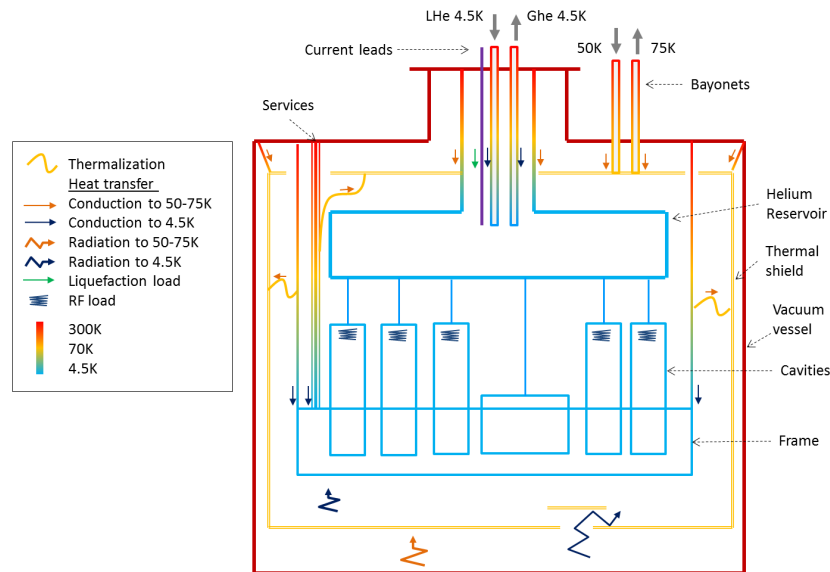
**Fig. 6.8:** Layout of heat transfer in steady state.
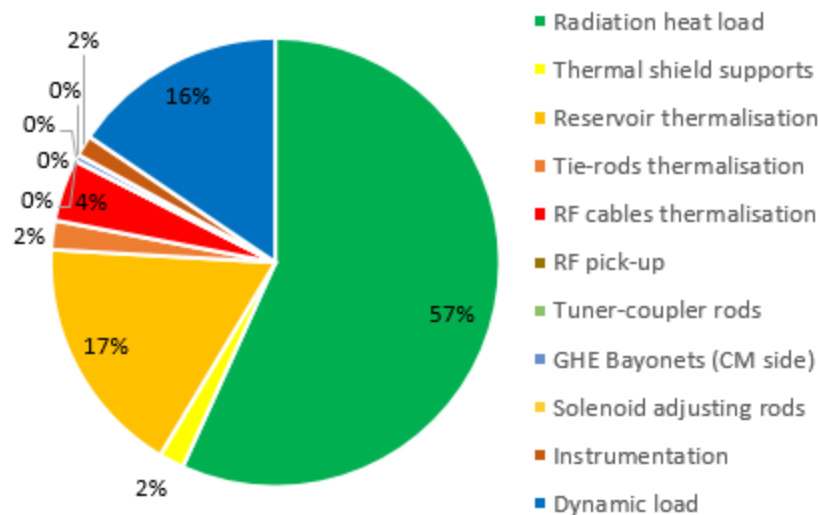


**Fig. 6.9:** Overview of heat loads repartition to $50 - 75$ K GHe circuit, see [13] for details.

Two cases are studied in case of a seismic event:

– Rupture of internal parts.
 The internal parts of the cryomodule get damaged, leading to the full rupture of the biggest bellow. Consequently, a high flow of liquid helium spreads into the vacuum vessel and gets released to the atmosphere via the main burst disc, see Figure 6.11.

– Instability of the whole cryomodule.
 The typical expected magnitude of seismic events in the CERN region can be found in [17]. In case of a serious seismic event, the jacks are designed with additional retainers to prevent the cryomodule falling from its jacks. In addition, M16 holes were foreseen in the lower side of the vacuum vessel for the attachment of tie-rods to the ground but these were not deemed needed.
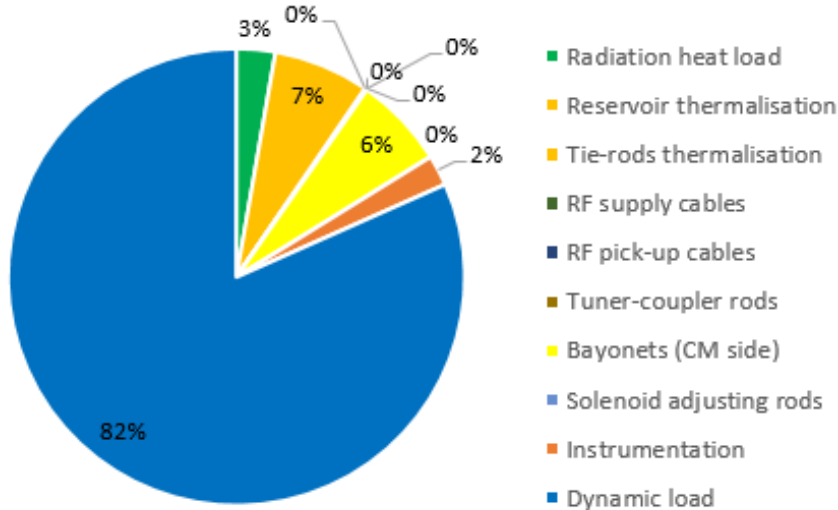
**Fig. 6.10:** Overview of heat loads repartition to $4.5$ K, from [14].
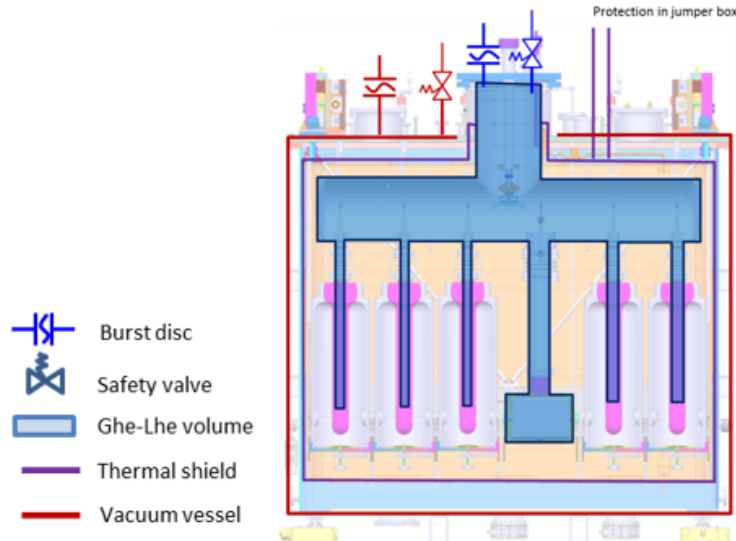


**Fig. 6.11:** Schematic of the safety devices' numbers and location. Safety valves are used for operation purposes and sized for non-critical events. Burst discs are sized for critical events.

## 6.7 Splice and current leads design

The design is performed for a nominal current of 120 A. Before operation, the solenoid supply line is instrumented and tested in SM18. Details are available in [18], [12] and [19].

Commercially available vapour-cooled resistive current leads have been chosen: 200 A nominal. Extra length is included in the design to allow up to three new splices assembly in the future. Figure 6.12 presents the layout of the supply of the solenoid.

A mechanical resistive splice assembly is designed and presented in [20]. The design offers a 40 mm contact between the superconducting bus-bar leads coming from the upper current leads and the identical section superconducting leads of the solenoid. Once assembled, the splice is covered with

Current leads external interface (xxxx.MJL.0400)

Vapor-cooled current leads

Brazed CL-bus bar interface

Bus-bar

Splice

Leads from solenoid

Adapted current leads
Procurement in progress
Shipped to CERN from CH on 2 July 14

Bus bar Cu/Sc >9
Type : 600A Spool piece bus
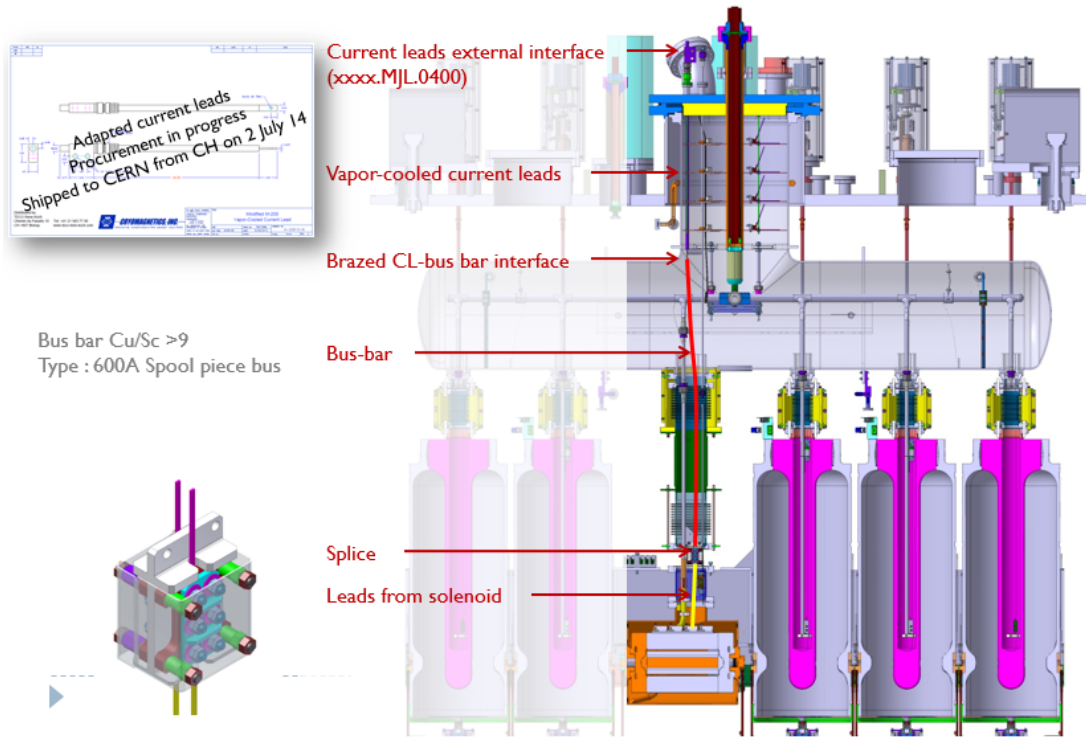
**Fig. 6.12:** Layout of the solenoid supply, details in [18]. The bus-bar is in two parts, an upper part in OFE copper tapering to a cross section where it is US welded to an 1 m length of 600 A capacity rectangular section superconducting wire.

PE insulator parts to shield against electric arcs to earth (in gaseous helium) connected surrounding components. Figure 6.13 presents the key parts of the splice assembly.

## 6.8   New coupler thermalisation

During the commissioning phase of CM1 on the beam line in August 2015, an anomalous decrease of efficiency of the RF system, built for a maximum continuous RF power of 250 W, has been observed. This situation has caused overheating and damage of the couplers of CM1 leading to severe limitations on RF powering. After a brief period of operation and physics at reduced power, CM1 was returned to the assembly facility for maintenance and a newly designed coupler was installed in the second cryomodule and retrofitted in the first.

To limit downtime in the refurbishment of the assembled cryomodules, the free parameters available to the final design are limited by the existing equipment, interfaces and available space. Two thermalisation positions are designed: one to the thermal shield cold source to extract the heat from the RF cable at an intermediate point between the existing thermalisation and the coupler and the other on the coupler itself to extract heat from its antenna, see Figure 6.14.

A thermalisation between the cable and the radiative tube is designed based on bolted connections and copper sheets. The contact to the corrugated RF cable outer conductor or sheath is made, as elsewhere in the cryo-module design, by a block with a machined profile ensuring contact to the corrugations and an optimized thermal contact with the RF cable. The long edge of the copper sheet is set perpendicular to the direction of coupler displacement to minimise loads applied to the tuning mechanism. A thermalisation between the coupler and the frame is designed to thermalise both the outer conductor of the coupler and the outer conductor of the RF cable. For monitoring the cable and coupler temperatures,
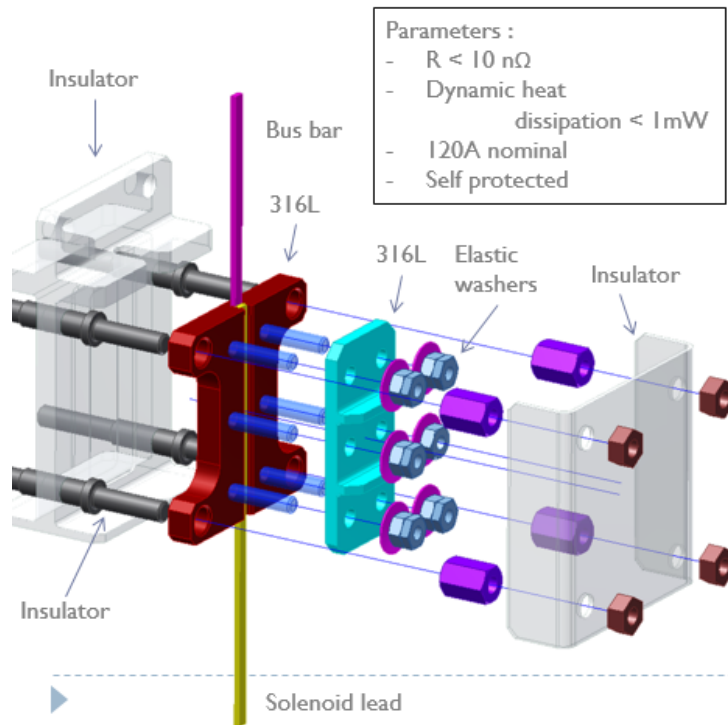
**Fig. 6.13:** Key components of the mechanical resistive splice assembly.
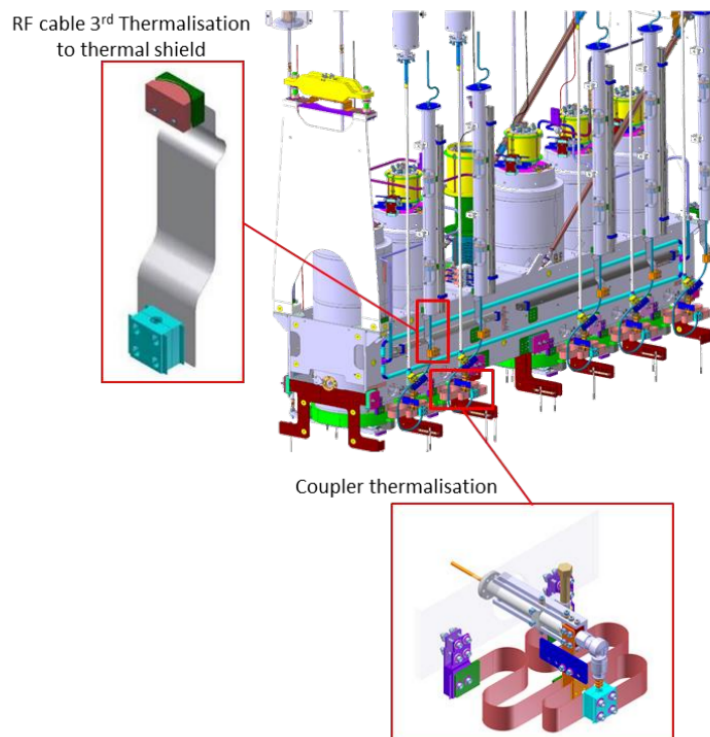


**Fig. 6.14:** Layout of the additional thermalisations.

two additional sensors are installed.

The outer conductor of the coupler and the external conductor of the RF cable are thermalised to a common temperature. For each cable/coupler thermalisation, four surfaces of thermal contact with the support frame are foreseen to compensate for uncertain bolted thermalisation effectiveness to rough surfaces for a total of $2500$ mm$^2$ area. Bolted connections are limited to extremities. Wherever possible, electron beam welding is used to weld the extremities of the $0.4$ mm thick copper strips to their intermediate attachment blocks.

The internal conductor of the RF cable is brazed at its lower end to the rear extremity of the antenna. This provides an all-metal path for the extraction of heat from the tip of the antenna into the RF cable and from there into the thermalisation system. The antenna and the copper blocks are manufactured in OFE copper, the sheets are made of OF copper, that was readily available and where the difference in thermal conductivity (when compared to OFE) is negligible. Retainers are installed so not to induce bending stresses directly into the EB welds joining the sheets to the blocks, stresses that may lead to a fatigue failure of the assembly, see Figure 6.15.
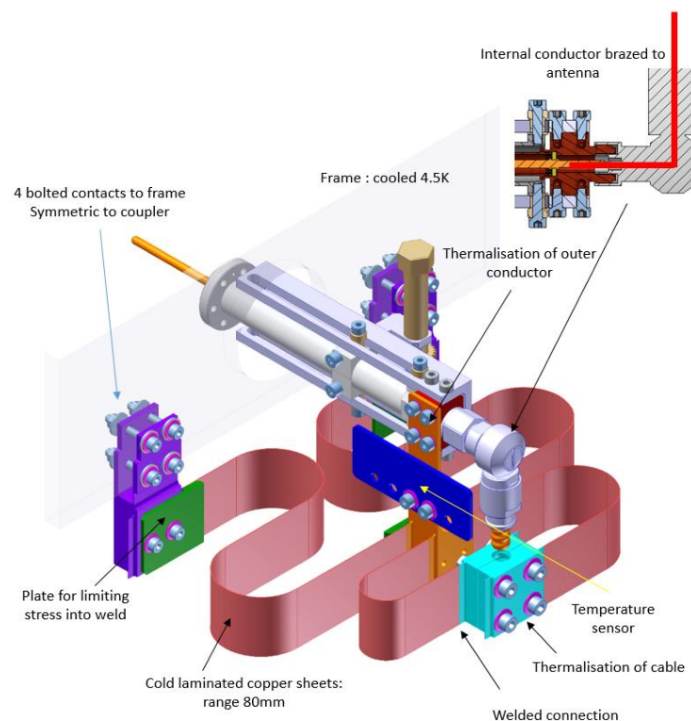


**Fig. 6.15:** Detailed design of the thermalisation of the coupler to the support frame.

## 6.9 Instrumentation design

Instrumentation, cabling, connectors and sensors allow the monitoring of temperature distribution of the cooled structures, the level of liquid helium in the different volumes, cryogenic and vacuum pressures and includes electrical supply to cryo-heaters.

In vacuum, a first set of cables connects the main instrumentation flange to smaller patch panels into which individual connectors serving sensors (or pairs of sensors) can be assembled. Routing instrumentation wires is dust producing. These intermediate patch panels allow the cavities to be installed after the cabling and thus reduces the level of dust produced in presence of sensitive cavities. This also allows quick partial replacement of cabling if damaged (no fixing inside the clean room) and safe pre-assembly of the sensors onto the components. Cables are routed in dedicated guiderails to limit dust release to

vacuum.

In the helium volume, sensors are directly connected to the set of cables connected to the instrumentation flange, except for connections performed in the clean room (temperature sensors and level gauges in cavities-solenoid). Cables are routed along the distribution manifold during manufacturing of the helium vessel.

The instrumentation layout in vacuum and in the helium volumes, covering more than 60 temperature sensors, 5 level gauges and 12 heaters, is presented in Figure 6.16 and in [1].
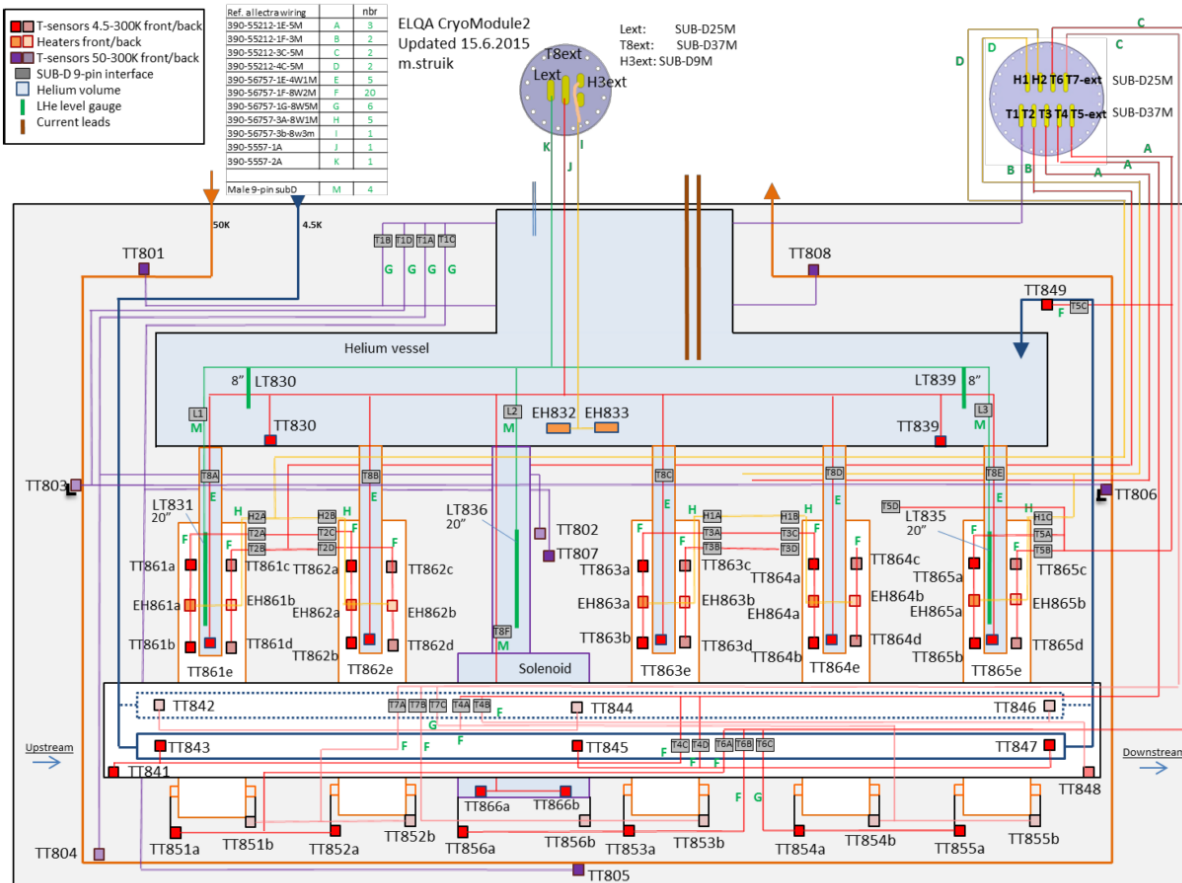


**Fig. 6.16:** Layout of the instrumentation sensors and wires. Connectors are presented in grey. More than 60 temperature sensors, 5 level gauges, 12 heaters.

## 6.10 Assembly

All individual drawings used for manufacturing and assembly can be traced from the master assembly drawing in [21]. The assembly is carried out according to instructions contained in twelve main assembly procedures, see [22]. Information on tooling, specific and general can be found in [23]. Organisation and logistics for the support to the assembly is presented in [24].

The complete high-$\beta$ cryomodule assembly is done vertically, suspended to a mobile frame, as can be seen in Figure 6.18. The assembly process, described in [25] can be divided in 14 main steps:

– Vacuum vessel top plate separation and storage.
– Vacuum vessel (VV) preparation.
– Thermal shield (TS) assembly and insertion into VV.
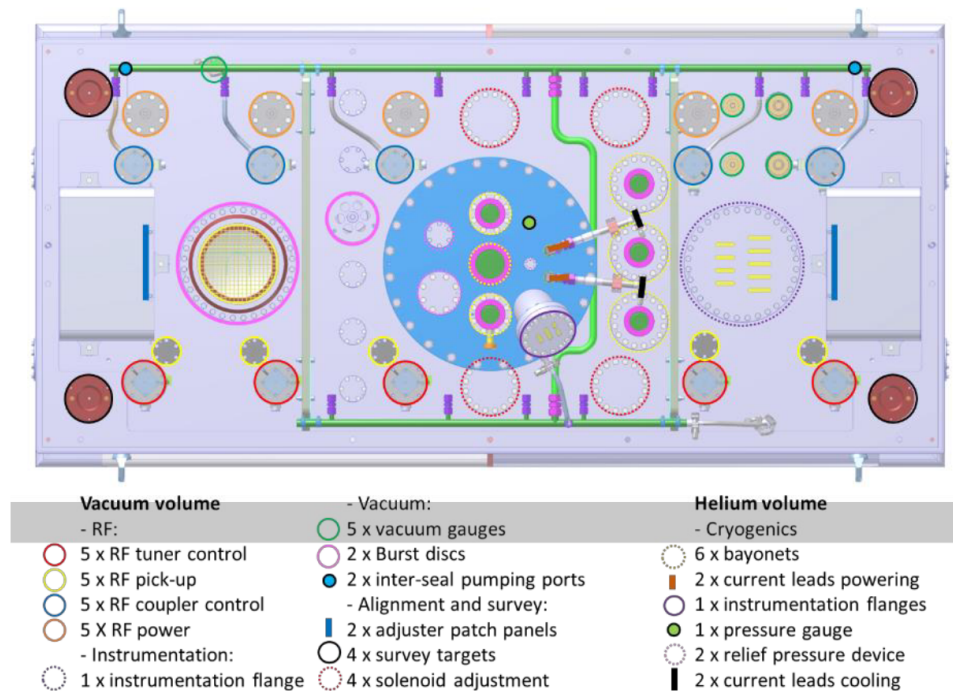
**Fig. 6.17:** Cryomodule top plate interfaces.

- Chimney assembly and installation on the frame.
- Top plate assembly.
- Chimney insertion in the top plate.
- Support frame installation.
- Solenoid and cryogenics instrumentation interfaces installation.
- Cavity insertion test.
- Intermediate vacuum testing.
- Cavities installation.
- RF ancillaries' installation and test.
- Cryo-module vessel closure.
- Final assembly and qualification tests.

One cryomodule contains more than $10,000$ parts under more than $500$ references, going in size from sub-millimetre dimensions to four cubic meters, and weighing up to $2.5$ tonnes. The assembly of CM1 showed that a full blank assembly of the complete cryomodule would have been necessary to identify problems at the earliest opportunity, but this was not entirely done because of time constraints. After their reception, all parts were controlled before cleaning and conditioning to ISO5 standards. For the CM1 assembly, a database was put in place and improved for CM2 according to our needs. The database permitted to follow up the stock and the status of each part (reception, quantity, quality control, cleaning, and conditioning).

The common vacuum design required a specific assembly environment, to avoid dust contamination and ensure cavity performances. The conditioning, the preparation of sub-assemblies, and the CM assembly proper are all done in ISO5 soft-wall clean rooms.

During the design and assembly of the first HIE-ISOLDE cryomodule, it was realised that to build these large, heavy, precisely machined and clean cryomodules, specialised tooling would be needed. A

(a) Installation of instrumentation on the rinsed superconductive cavity before assembly into CM1.

(b) Final verifications on CM2 before closure and transport to the ISOLDE facility.

**Fig. 6.18:** Cryomodule assembly in the SM18 clean room.

lifting device was used to lift and position the components during assembly, while specially designed trolleys were used for the installation of the cavities and solenoid and for the transport of the helium tank, thermal shield and top plate. More information on tooling can be found in [23].

# References

[1] Y. Leclercq, Design of the HIE-ISOLDE HighB cryomodule, EDMS 1605095 (CERN, 2017).

[2] C. Parente, Conformity assessment and documentation of the HIE-ISOLDE cryomodules, EDMS 1227928 (CERN, 2015).

[3] M. Fraser, Notes on the relaxation of the HIE-ISOLDE linac alignment tolerances, EDMS 1304103 (CERN, 2014).

[4] G. Kautzmann et al., HIE-ISOLDE – general presentation of MATHILDE, ACC-2015-0084 (CERN, 2014).

[5] G. Kautzmann et al., The HIE-ISOLDE alignment and monitoring system software and test mock up, CERN-ATS-2012-273 (CERN, 2012).

[6] G. Vandoni, Vacuum system for HIE-ISOLDE, EDMS 1209352 (CERN, 2014).

[7] L. Williams et al., Design of the high beta cryomodule for the HIE-ISOLDE upgrade at CERN, ATS-2011-247 (CERN, 2011).

[8] S. Blanchard, HIE-ISOLDE SC linac stg1b vacuum control layout, EDMS 1465628 (CERN, 2015).

[9] C. Wach, ISOLDE cryo distribution system – QHIS P&I diagram, EDMS 1553657 (CERN, 2016).

[10] N. Delruelle et al., *AIP Conference Proceedings* **1573** (2014) 811.

[11] W. Venturini Delsolaro, Hardware commissioning procedure for the HIE-ISOLDE cryomodules, EDMS 1511269 (CERN, 2016).

[12] L. Valdarno et al., *IOP Conference Series: Materials Science and Engineering* **101** (2015) 012045.

[13] P. Zhang, Cooling-down: Temperature range limits, EDMS 1513867 (CERN, 2015).

[14] L. Valdarno and Y. Leclercq, Heat load estimation for the HIE-ISOLDE cryomodule, EDMS 1274821 (CERN, 2016).

[15] Y. Leclercq, Sizing of the safety relief pressure devices protecting the HIE-ISOLDE cryomodule from over pressure, EDMS 1289883 (CERN, 2014).

[16] HSE Unit, Safety validation – HIE ISOLDE safety devices, EDMS 1336808 (CERN, 2013).

[17] J. Lopes, Seismic action at CERN, EDMS 1158454 (CERN, 2016).

[18] J. Dequaire, Current lead assembly, EDMS 1448990 (CERN, 2016).

[19] L. Valdarno, HIE-ISOLDE cryomodule, current leads tests, EDMS 1608070 (CERN, 2016).

[20] J. Dequaire, Connexion équipée, EDMS 1388123 (CERN, 2014).

[21] J. Dequaire, HIE-ISOLDE cryomodule complet, CDD drawing EDMS 1503456 (CERN, 2016).

[22] G. Barlow, HIE-ISOLDE cryomodule assembly procedure list, EDMS 1560484 (CERN, 2015).

[23] G. Barlow, HIE-ISOLDE cryomodule list of tooling, EDMS 1560196 (CERN, 2016).

[24] J. B. Deschamps and A. Vande Craen, Organisation logistique pour l'assemblage des cryomodules HIE-ISOLDE, EDMS 1568957 (CERN, 2016).

[25] Y. Leclercq et al., The Assembly Experience of the First Cryo-module for HIE-ISOLDE at CERN, Proceedings of IPAC2015, Richmond, 2015, pp 3131–3133.

# Chapter 7

# Transport and handling of the cryomodule

C. BERTONE

The development of a method to transport the cryomodules from the clean room in SM18 to the final installation in ISOLDE (CERN, Meyrin site) has been driven by two factors:

- Transport constraints dictated by the cryomodule design (to ensure safe transfer).
- Surrounding infrastructure constraints dictated by the buildings and roads to be followed.

## 7.1 Cryomodule constraints

Because of its design, the cryomodule can be roughly represented as a bell. The cavities and solenoid are suspended inside the cryostat and can have free oscillations in both directions. The vicinity of the cavities to the thermal screen (fixed inside the cryostat) allows tiny angular oscillations of the inner parts [1].The transport constraints are then the following:

- Relative angular limit (cryostat to cavities): 0.5 degrees in in the length (longitudinal) and 1 degree in the width (transversally).
- Maximum acceleration: 0.5 g vertically and 0.1 g horizontally both sides.
- Centre of gravity not centred with respect to the geometrical centre of the piece [1].

## 7.2 Infrastructure constraints

The cryomodule path from the clean room to the destination (see Figure 7.1 should cover the transfer to the test bunker (inside SM18 as well) and finally to the HIE-ISOLDE installation site (building 170).The main concerns over the path from SM18 to building 170 were:

- The door height (4.3 m in SM18 and 4.5 m in building 170).
- The slope and the tilt of the road (up to 8.6%) along the way.
- The need to use national roads.

## 7.3 Transport proposal

After studies, it has been concluded that the only way to guarantee the verticality of gravity during transport was to profit from gravity so that the cryostats have to travel suspended on a special metallic frame.

This frame should be able to correct $\sim 10$ degrees of road tilt on both rotational axes. As the oscillation of the external inner cavities is not in phase with the oscillation of the cryostat, it was decided to realise the maximum angle of the cryomodule to 1 degree (dynamically).

No dumping system was installed to avoid a potential phase delay between the two oscillating parts during transport and to avoid the horizontal forces to be applied on the cryostat by such a system.

**Fig. 7.1:** Route of the cryomodule from the SM18 clean room, where it was assembled, to building 170.

**Table 7.1:** Summary of tilt values during the transport of CM3.

| Stage | Max roll tilt ($\circ$) | Min roll tilt ($\circ$) | Max pan tilt ($\circ$) | Min pan tilt ($\circ$) |
|---|---|---|---|---|
| Loading – SM18 | 2.20 | −0.89 | 0.79 | −1.62 |
| Transport 170>BA7 | 1.88 | −1.55 | 2.13 | −2.63 |
| Unloading – 170 | 3.44 | −2.89 | 1.54 | −1.70 |
| Positioning – 170 | 1.94 | −1.47 | 1.99 | −1.20 |

The transport frame [2] is very compact in height to allow passage under the doors and it includes a spreader to be used in the departure and destination buildings. A special interface permits direct insertion of both hooks of the crane to diminish the interposition of elastic layers between the frame and the crane that can create further oscillation with different frequencies. The spreader is equipped with a registering system in both directions so that it is possible to statically correct the position of the centre of gravity to minimise the static suspension angle before the first lifting ($< 0.1$ degrees).

To limit the angles during transport, it was decided to limit the speed of the truck to 0.5 km/h and ask two persons standing on the truck to manually correct free oscillations. To allow this, the public road was closed by the police during transport. No transport was allowed on windy days, but rain was not considered a problem since the cryostat was well protected.

Tilting and acceleration values during transport were measured online and recorded along the way to permit immediate action in case of need. To validate all these parameters and ensure that all constraints were respected, a double testing campaign (including monitoring) has been conducted with the final frame and tooling: one with real mass but incorrect shape (steel block of small dimensions) and one with real shape but incorrect mass (cryostat of CM2 empty).

The third cryomodule was transported to the ISOLDE hall (building 170) on 24 January 2017. Tilt values during loading, transport, unloading and positioning were recorded and are summarised in Table 7.1.

**Fig. 7.2:** Three-tier control system.

## 7.4 Transport inside the building

Concerning the bunker, the limited height of its door (70 mm higher than the net overall height of the CM1) and the need of unloading the cryomodule inside it with no handling means and no possibility to raise it of more than 5 cm during unloading were the driving factors of the tooling design. The transport frame had to be loaded by the crane from the top.

A separate frame [3] has been developed without tilting correction (floor of SM18 is flat) with soft wheels. This frame is supporting the modules from underneath on the two long sides by a range of silent blocks. It is then closed on the fourth side. There is no added layer below or above the cryomodule to leave the $5 + 2$ cm room to floor and to door.

The frame is opened on the small side once in the bunker and the cryomodules are lifted from below by mechanical jacks that are situated in positions corresponding to the final supports during tests. The frame is retracted backwards and the cryomodule is simply lowered in position.

## References

[1]  Y. Leclercq, Transport limits for HIE-ISOLDE cryomodules, EDMS 1539646 (CERN, 2015).

[2]  F. Delsaux, Assemblage cryomodule + chassis, CDD Drawing EDMS 1409270 (CERN, 2015).

[3]  F. Delsaux, Chassis transport cryomodule equi, EDMS ISLHHJ__0002 (CERN, 2015).

# Chapter 8

# MATHILDE: Monitoring and Alignment Tracking for Hie-IsoLDE

J-C. GAYDE, G. KAUTZMANN, F. KLUMB

According to beam physics simulations [1] the main axes of the active components, located inside the cryostats, require alignment to within a precision of $0.3$ mm for the superconducting RF cavities and $0.15$ mm for the superconducting solenoids at one sigma level along directions perpendicular to the beam axis. It was chosen to actively monitor the alignment with respect to the HIE-ISOLDE Nominal Beam Line (NBL). Once the linac is fully installed, a total number of 40 active elements will be monitored, six in each of the four high-$\beta$ cryomodules (five RF cavities and one solenoid), eight in each of the two low-$\beta$ cryomodules (six RF cavities and two solenoids).
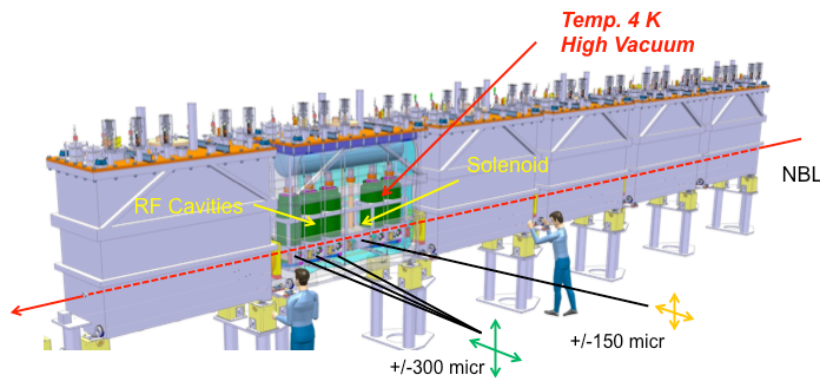


**Fig. 8.1:** Alignment needs.

To perform the alignment at the requested level of precision, a permanent system is integrated to the linac equipment. The system must:

- Provide the relative alignment parameters of the superconducting RF cavities and solenoid(s) inside a cryomodule.
- Allow the alignment follow-up of the RF cavities and solenoid(s) during the adjustment steps as well as during vacuum pumping and cooling down.
- Create a geometrical link between the monitored elements inside the different cryomodules and the NBL datum in order to provide their positions with respect to the NBL along the full linac and in a single coordinate system.
- Be able to run during stop and operation phases.

The Monitoring and Alignment Tracking for HIE-ISOLDE (MATHILDE) system has been developed and is based on opto-electronic sensors, precise optical components, metrological tables and mechanical elements. Some of them, situated inside the cryomodules, are exposed to non-standard environmental conditions such as high vacuum and cryogenic temperatures.

## 8.1   The alignment system concept

The basic concept of the MATHILDE [2] alignment system is the creation of a closed geometrical network continuously measured and linked to an external reference datum defined in the NBL coordinate system.
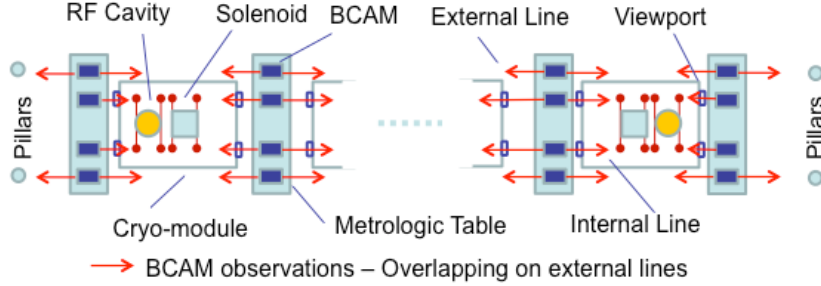


**Fig. 8.2:** Sketch of the alignment system — top view.

The positions of the cryomodule, RF cavities and solenoids are measured in this geometrical frame. Double-sided HIE-ISOLDE Brandeis CCD Angle Monitor (HBCAM) [3] cameras installed on precise metrological tables inserted in the inter-tank space observe each other and four end-pillars fixed to the floor. The locations of the pillars, determined via survey in the NBL coordinate system, are used as datum points.
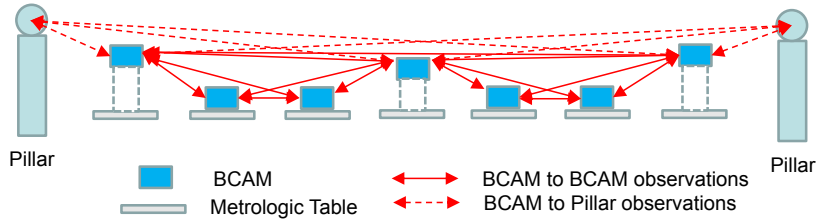


**Fig. 8.3:** Overlapping external line — side view.

As is shown in Figure 8.2, the HBCAM arrangement creates four lines of devices roughly parallel to the NBL. The apparatuses placed on the metrologic table's outer areas create two external lines of sight, one on each side of the cryomodule, allowing the reconstruction of the position of the inter-tank metrological tables. The double-sided HBCAMs of the external lines are placed in such a way that overlapping observations are possible, presented in Figure 8.3.

Two internal lines-of-sight are formed by a second set of double-sided HBCAMs, symmetrically placed on the same inter-tank metrological tables. They are used to observe the reference targets on the active components, RF cavities and solenoids through precise glass viewports. Each RF cavity and each solenoid is equipped, via the component supports (Omega plates), with four reference targets fixed at precisely known positions with respect to the component geometry. The MATHILDE system measures their positions and therefore determines the principal axis location and orientation of each active component with respect to the NBL.

In order to make the system more robust, redundancy is also introduced in the internal lines. Each target support is equipped with two glass ball reflectors kept at a known relative distance by a spacer made of precise ceramic balls. Most of the targets are visible independently from the two HBCAMs placed respectively on the upstream and downstream metrological tables. In addition, these two HBCAMs observe each other.

The geometrical frame and the position of each RF cavity and solenoid are calculated from the

redundant observations using MATHIS (Monitoring and Alignment Tracking of HIE-ISOLDE Software), a specifically developed pre-processing and 3D adjustment software. The calculation takes into account the HBCAM to HBCAM observations, the image coordinates of the targets on the HBCAM sensors, the mechanical dimensions of the metrological tables and the different supports, the HBCAM calibration parameters, the effects due to temperature changes and the distortions induced by the orientation of the optical ports situated between atmosphere and high-vacuum media.

The target movement measurement range is of $\pm 3$ mm for horizontal direction and of $-6/+11$ mm in vertical direction relatively to the surrounding targets. This range is only limited by the fact that a target can be hidden by the other one's shadow. It is not limited by the HBCAM field of view which is large enough to see a full set of targets. Nevertheless, a special spatial arrangement of the targets is required to cover the HBCAM field of view, to avoid shadowing effects and cope with integration issues into the cryomodule. The cool-down, which induces approximately the same shift for all the targets of a same set, does not significantly modify the measurement range.

## 8.2 HBCAMs

The HBCAM is a metrology opto-electronic device developed in collaboration with the Brandeis University from the original BCAM (Brandeis CCD Angle Monitor). It contains two cameras facing in opposite directions, two pairs of laser diode light sources, and two sets of four white LED flash arrays. The cameras, lasers, and flash arrays are assembled in one anodized aluminium chassis that sits on a cone/slot/plane kinematic mount, which allows a unique and constraint-free positioning and orientation of the device on a three-ball support plate. In a metrology system, the HBCAMs are arranged so that they can view one another's sources. They may also view sources that have no cameras associated with them, such as ends of flashing optical fibers, retroreflectors, and internally lit ceramic spheres. In the HIE-ISOLDE application, the HBCAMs flash each other and some of them also observe the image of their own lasers in retro-reflecting glass spheres.



(a)                                        (b)
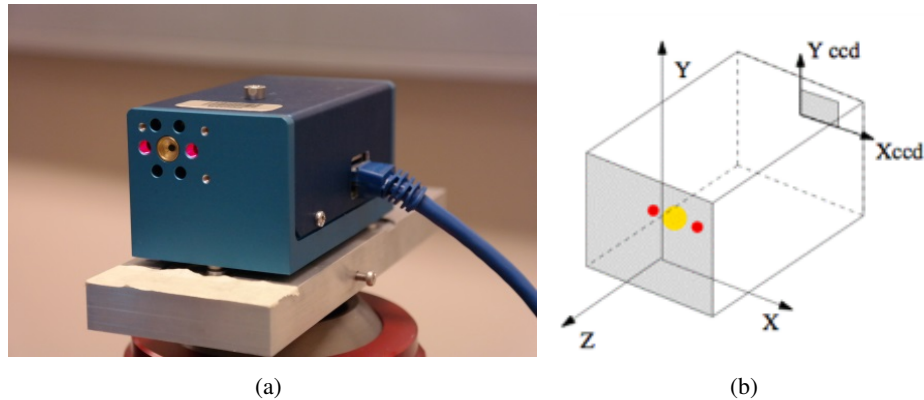
**Fig. 8.4:** Picture of a HBCAM flashing its lasers.

The LWDAQ (Long Wire Data Acquisition) system can read out the image either as $520 \cdot 700$ pixels each 7.4 $\mu$m square, or as $260 \cdot 350$ pixels each 14.8 $\mu$m square. The 7.4 $\mu$m pixel readout provides better measurement precision for sharply-focused spots. The 14.8 $\mu$m pixel readout provides 3 image/s readout rate with the LWDAQ Driver (A2071E). The HBCAM measurement precision is proved to be at the level of 5 $\mu$rad across the entire field of view. Note that no image sensor irregularities were observed so far with the used CCD. Figure 8.5 shows the changes in the measured value of the offset between two laser sources separated by a constant distance and moved across the field of view of a HBCAM. The camera is focused at a range of 1.5 m. The obtained precision for the separation is at the 4 $\mu$rad

**Table 8.1:** HBCAM specifications.

| HBCAM | HIE-ISOLDE Brandeis CCD Angle Monitor | |
|---|---|---|
| **Type** | Double sided | Blue and black symmetrical models exist |
| **CCD** | $520x700$ — $7.4\mu$m square pixel | Sony ICX424AL Monochrome — $5.2X3.8$mm$^2$ |
| **Laser** | Two diodes per side, $\lambda = 650$nm | Calibrated output 5mW$\pm$0.5mW |
| **Flash** | Two sets of four white light LEDs | One set each side around the lenses |
| **Lens** | $f = 48$mm, plano-convex lens | At 50mm from CCD, sharpest focus at 1.5m |
| **Field of view** | 100mrad ·75mrad | |
| **Kinematic mount** | Cone/slot/plane under the chassis | Define the Mount Coordinate System |
| | | Specific mounting torque |
| **Geometrical calibration** | Delivered calibrated | Done with a roll cage |
| **Relative precision** | 5 micro radians | Laser diode image location on a same CCD |
| **Absolute accuracy** | 50 micro radians in mount system | All calibration taken in account |

level ($\sim$ 3 $\mu$rad for individual spot · $\sqrt{2}$), which is consistent with the expected 7 $\mu$rad ($\sim$ 5 $\mu$rad for individual spot · $\sqrt{2}$).
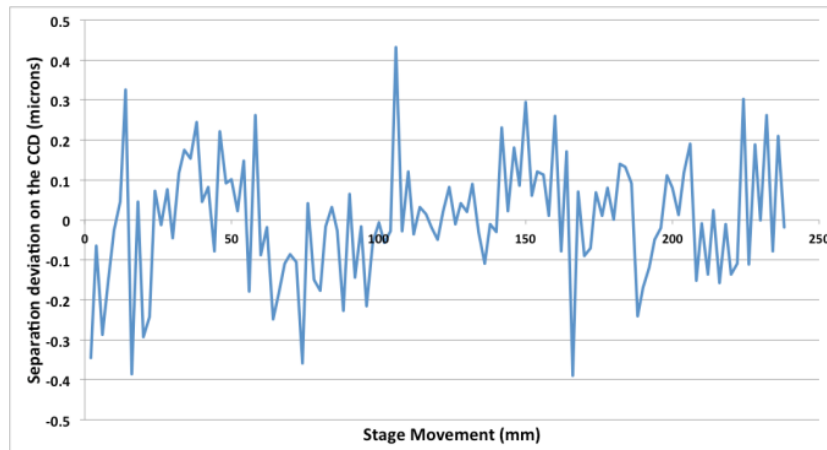


**Fig. 8.5:** Image separation deviation.

In the same conditions, Figure 8.6 shows the residuals from a straight line fit to the position of two lasers moving across the field of view. The achieved precision is about 4 $\mu$rad for the lateral movement.

The HBCAM is delivered calibrated. The calibration is done in a roll-cage. It guarantees accuracies with respect to the kinematic mount system of about 50 $\mu$rad in source bearing, 20 $\mu$m in pivot point position, and 20 $\mu$m in source position. Once fully installed to cover the six cryomodules of the linac in the tunnel, the opto-electronic part of the MATHILDE system [3] will be made of: 28 HBCAMs, seven temperature sensors connected to one RTD head, seven Multiplexers (MUX) and one LWDAQ Driver. Figure 8.7 shows a sketch of the cabling and connection configuration.

## 8.3 Targets

As shown in Figure 8.8, the cavities and solenoids have hollow half-spheres centred and attached to their beam entry and exit point. For each active element, the two half-spheres are sitting in V-slots machined on two omega shaped plates. The targets are attached to the Omega plates and guided by V-grooves, blocked in height by a pin and fixed by a screw. Each Omega plate is geometrically characterised with a CMM in a metrology laboratory. Therefore, the metrology results are used in the MATHIS 3D reconstruction
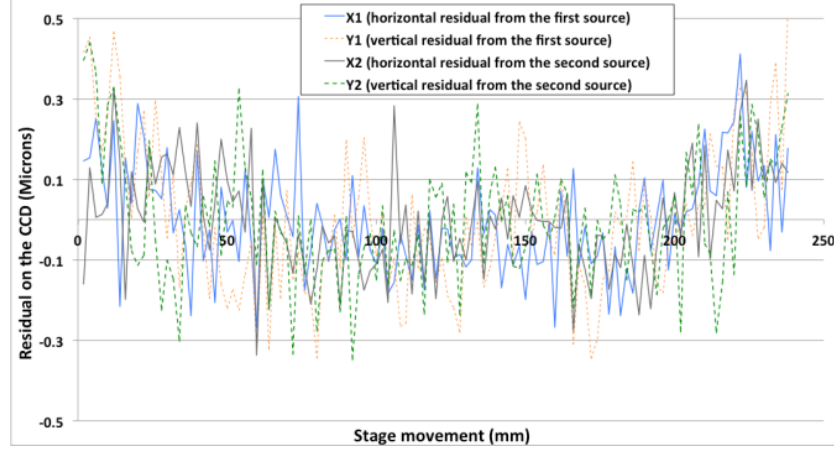
**Fig. 8.6:** Non-linearity across entire field of view. Residuals in microns on the image sensor, plotted against stage position.
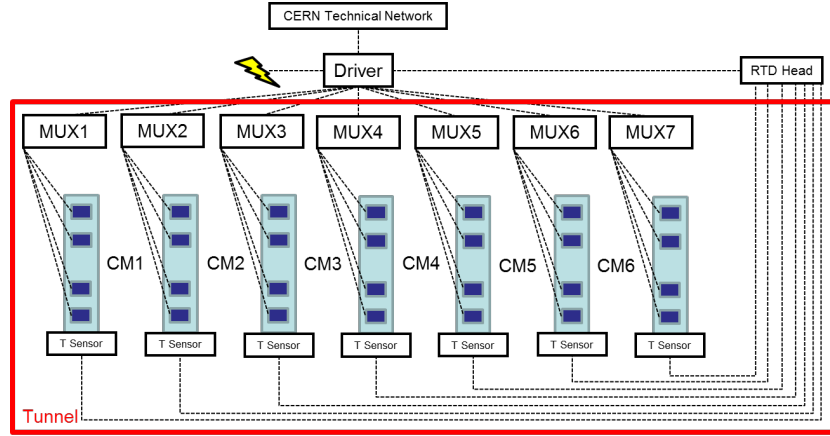


**Fig. 8.7:** Sketch of the cabling and hardware connection for MATHILDE.

process to calculate the position of the beam port from observations done at the level of the targets. The process takes into account the thermal contraction of the plates.

Inside the cryomodule two lines of targets are present; each one comprises 12 or 16 targets to be measured, respectively for high-$\beta$ and low-$\beta$ cryomodules. They are placed in a special spatial distribution in order to be visible in the field of view of the HBCAMs and to stay in their allowed envelope without shadowing each other, see Figure 8.9.

The targets must sustain the linac operating conditions and the main constraints are to be vacuum compatible, to work at $4.5\,\mathrm{K}$ and to withstand a radiation cumulated dose estimated of $150\,\mathrm{Sv/year}$. In addition, they have to be measurable from opposite directions and to have a narrow shape (6 mm max) to stay in their allocated envelope.

The targets developed for the project are based on the optical properties of high-index glass ball lenses [4]. Those lenses are made from S-LAH79 material, produced by OHARA Inc [5]. This glass offers a refracting index of about 1.993 for the HBCAM laser wavelength (650 nm). The high refractive index glass balls can partially reflect light backwards to the light source and are acting as pseudo retro-reflector mirrors. This opens the possibility to observe with an HBCAM the image of its own laser spots and therefore to measure the relative position between the HBCAM and the target ball. Once pre-processed, these observations are used in the global 3D reconstruction software MATHIS.

73

(a)              (b)              (c)
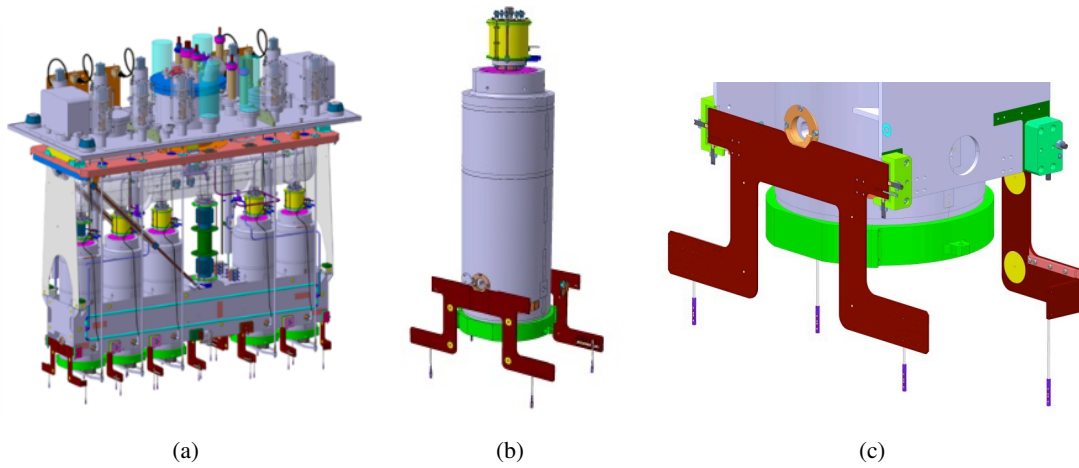
**Fig. 8.8:** (a) View of an opened cryomodule, (b) one cavity on its supporting plates and monitoring targets hanging on the bottom and (c) supporting principle of the cavities and solenoids, targets hanging to the Omega plate.



(a)



(b)
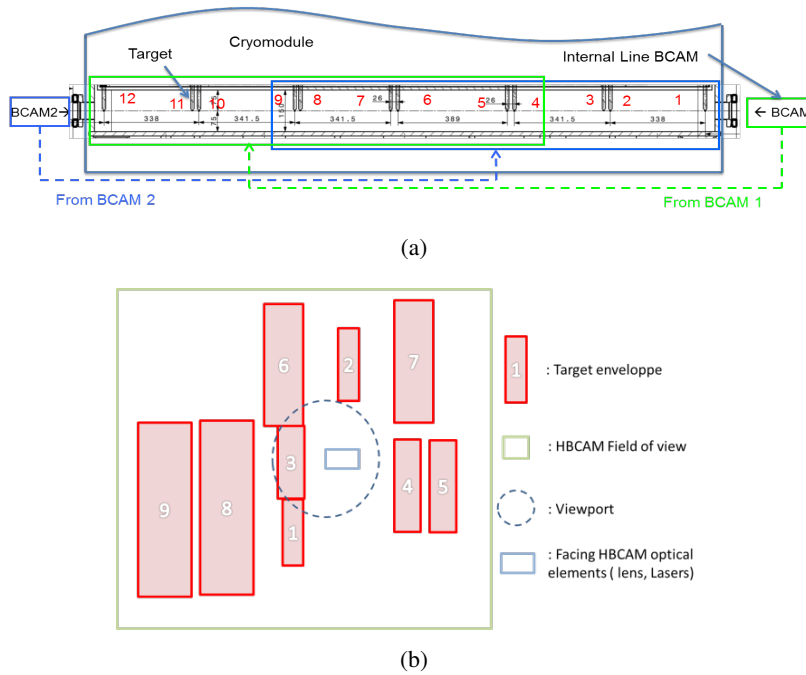
**Fig. 8.9:** View of what a device sees inside the high-$\beta$ cryomodule: 9 targets (out of 12).

Figure 8.10 shows the final design of the target. The 4 mm diameter balls are encapsulated in a precise 6 mm diameter titanium body. The spring, the glass and ceramic balls are loaded from the bottom. Once those elements are inserted, the target is closed by a plug held in place by a 2 mm diameter pin. The design allows housing several glass balls in one support. As sketched in Figure 8.10, a configuration with two glass balls spaced by two precise ceramic balls is the standard target placed inside the cryomodule. To increase the redundancy of the system, the targets allow multidirectional observations: most of the glass balls can be observed from the two HBCAMs, placed upstream and downstream on the same internal line of one cryomodule. For the high-$\beta$ cryomodule, the target comes into five different well-known lengths between the middle pin, which is the centring pin in the Omega plates, and the last glass
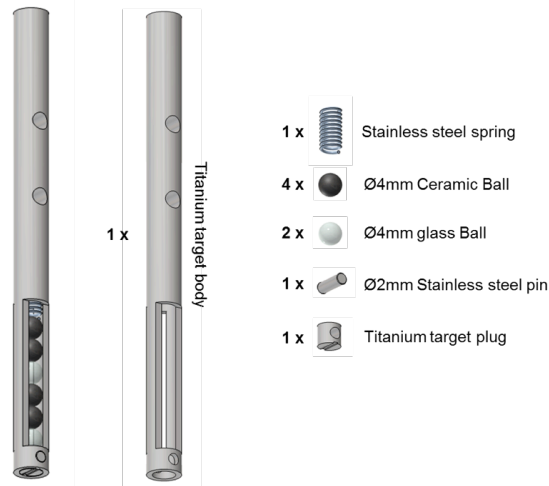
**Fig. 8.10:** Pictures of the final target design.

balls in order to maximise the number of targets measurable. The same principle will be followed for the target integration into the low-$\beta$ cryomodules, the HBCAM field of view will permit to maximise the number of targets seen by one device.

The target has been designed to be vacuum compatible. The outgassing rate of the high index glass has been tested for an amount of glass spheres sufficient to equip one full high-$\beta$ cryomodule. It stays at the sensitivity limit of the used outgassing system (below $3.8 \cdot 10^{-8}$ mbar l/s) and therefore is negligible compared to the total gas load budget of $2 \cdot 10^{-4}$ mbar l/s of a cryomodule. See Figure 8.11 for the outgassing test results.
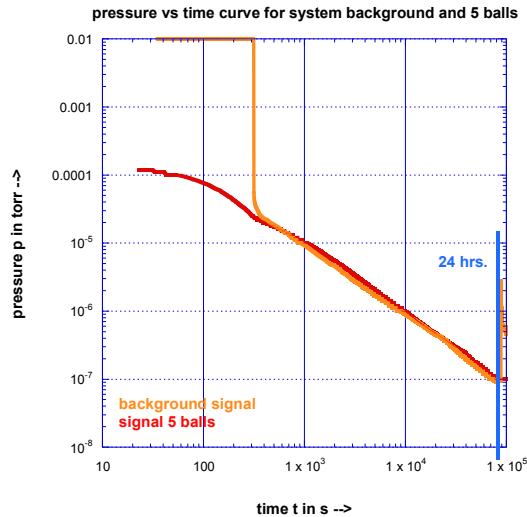


**Fig. 8.11:** High index glass ball outgassing tests results, courtesy of M. Herrmann.

Cryogenic tests have been performed using an HBCAM observing glass ball targets sitting inside a cryostat, shown in Figure 8.12, through an inclined viewport. Neither specific behavior nor damage was observed down to $5\,\text{K}$ and $40 \cdot 10^{-6}$ mbar.

The radiation hardness of the high index ball has been tested on samples having received doses

(a)　　　　　　　　　　　　　　　　(b)
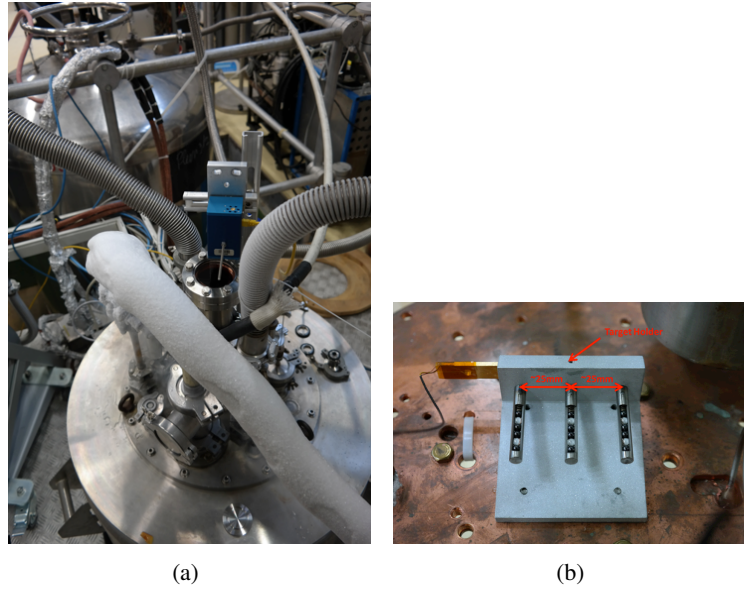
**Fig. 8.12:** (a) Set up on a Cryostat and (b) detail on the targets.

from $0.1$ to $5\,\text{kGy}$. The retroreflective behaviour of the balls and their position detection with an HBCAM are not significantly different before and after the irradiation.

**High index glass balls position detection**

Each HBCAM laser diode spot observed in the imaging system is not in the centre of the ball, shown in Figure 8.13. This effect is due to the offset between the observing point and the flashing laser source. The observed spot intensity profile is asymmetrical due to reflexions in the glass balls. For two laser diodes, symmetrically placed on the both sides of HBCAM lens, two spots on the ball surface are observable with a symmetrical intensity profile. The left spot corresponds to the left source, and vice versa. The centres of gravity of these two spot images correspond to the centre of the ball image. Variations due to lateral ball movement within the HBCAM field-of-view boundaries are negligible and the average value of the two spots is still valid.
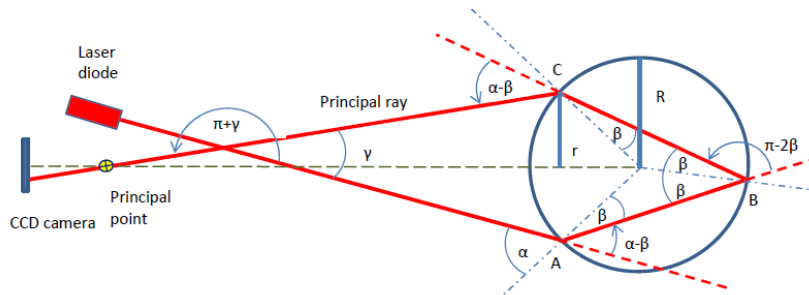


**Fig. 8.13:** Light path inside a high-index glass ball shined by a HBCAM Laser.

The precision of the reconstruction of a lateral movement (with respect to the HBCAM optical axis) has been tested by taking measurements on two 4 mm diameter high index glass balls encapsulated in one of the target prototypes. The movement is done by a micrometer stand and controlled by an AT401 Laser Tracker. The average offset observed between the HBCAM reconstructed movement and the one from the Laser Tracker is within a few microns, with a precision at one sigma level of 10 $\mu$m in object

space, see Figure 8.14. These tests have been done for a lateral translation covering 40% of the field of view starting from one of the CCD edge. Those values are consistent with other tests performed.
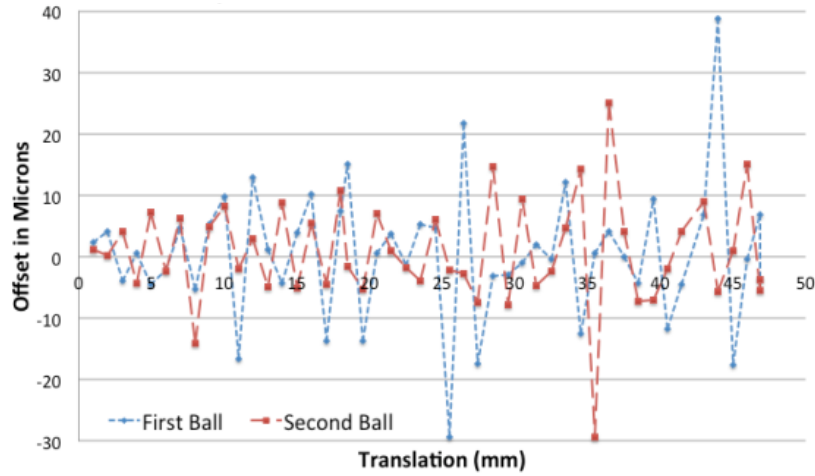


**Fig. 8.14:** Graph of the offset in object space between a nominal movement and the one reconstructed by HBCAM measurements. The figure displays two sets of measurements done with two different glass balls.

## 8.4 Viewports

Each cryomodule is equipped with four viewports, through which the targets placed on the RF cavities and solenoid Omega plates can be observed from the HBCAMs standing in the intertank region at atmospheric conditions. A 6.55 mm thick fused silica viewport mounted in a CF63 has been selected. It is vacuum compatible and is of high optical quality to minimise optical degradation effects. The studies and tests [2, 4] show that:

– The wedge angle needs to be limited to 10 arc/second for MATHILDE.
– The parallel plate effect is tested and validated.
– The glass deformation due to vacuum pumping is simulated and tested. The effect is negligible for the HIE-ISOLDE application.

To avoid parasitic reflections, viewports, presented in Figure 8.15 c, mounted onto the CF63 flange with a 5 degree angle (with respect to the external surface of the flange) have been developed in collaboration with industry and CERN's vacuum experts. The validation tests have been successfully performed in order to, amongst other things, control the inclination of each viewport in its flange ($5 \pm 0.5$ degrees) and the glass wedge angle ($< 10$ arc/second).

In the final assembly, the angle of the viewports are measured by survey means and introduced as a parameter in the 3D reconstruction process to compensate the deviation of the observations due to window crossing effects. The orientation of the viewport must be known and remain stable within 1 degree in the HIE-ISOLDE reference datum. This value is reasonably achievable by precise standard survey means and periodic controls are foreseen.

## 8.5 Metrological tables

At the end of the linac and between the cryomodules, a metrological table housing four HBCAMs is inserted. The metrological table includes:

– A base plate fixed to the same foot on which the diagnostic boxes and the steerers are installed.
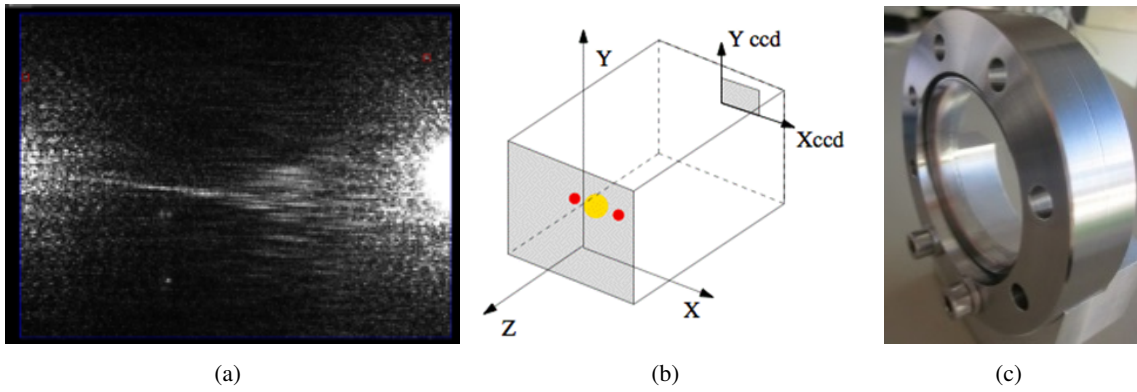
**Fig. 8.15:** HBCAM image showing the parasitic reflection in the glass (a), definition of the axis [3] (b), picture of a tilted window in its flange (c).

- An intermediate tilt plate, placed on top of the base plate, that can be levelled and moved in height.
- A metrological plate fixed in a kinematic way to the tilt plate which supports the HBCAM interfaces and can be shifted radially and rotated around a vertical axis.
- Four interfaces housing the HBCAM mounting balls fixed on the metrological table, the outer pieces being differently elevated with three rods on some table in order to stage the HBCAMs in height and make overlapping measurements possible. The setup is depicted in Figure 8.16.
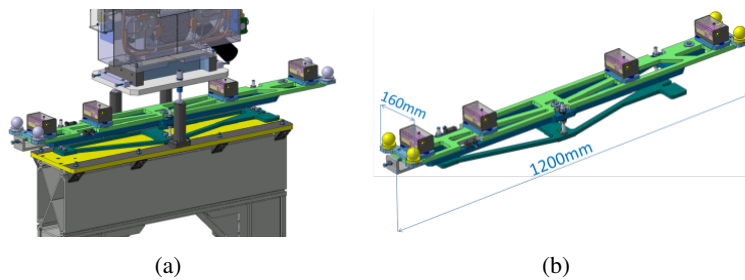


**Fig. 8.16:** Picture of a metrological table prototype (light green) on its adjustable support (dark green) (b), integrated in its inter-cryomodule region (a).

The plates are pierced with openings in order to decrease their own weight whilst keeping most of their rigidity. The full ensemble weighs only around 11 kg. The set-up has been optimised to attenuate as much as possible the impact of vibrations potentially induced by the vacuum turbo pumps of the diagnostic boxes sitting in the vicinity.

The assembled metrological tables are passing through metrology in order to get the geometrical relations between the $4 \times 3$ HBCAMs supporting balls and the link to the four fiducial marks sitting at the ends of the table. The critical values are the relative orientations between each device; a special adapter reproducing the HBCAM supporting interface is used to improve the relative angle observations. The tables are inserted as an ensemble in the intertank region in order to keep the calibration measurements. Once installed in the linac and aligned by precise standard survey means using the fiducial marks, the tables are considered as "floating rigid bodies" in the MATHILDE system. Their fine position with respect to the NBL, and consequently the one of the HBCAMs, is re-measured and re-calculated by the MATHIS software each time a whole set of observations is acquired. In addition, the metrological plates are equipped with temperature sensors, run as the HBCAMs by the LWDAQ system, in order to

compensate the variations of temperature in the 3D reconstruction.

## 8.6 Integration in the cryomodule

Alignment dedicated corridors have been introduced in the design of the thermal shielding. They allow the targets to cross them with a minimal addition to the heat load of the cavities and solenoids, whilst keeping them visible from the HBCAMs. Anodised aluminium plates cover the inner part of the corridor to minimise potential parasitic reflection on the HBCAM images.



(a)                                                                 (b)
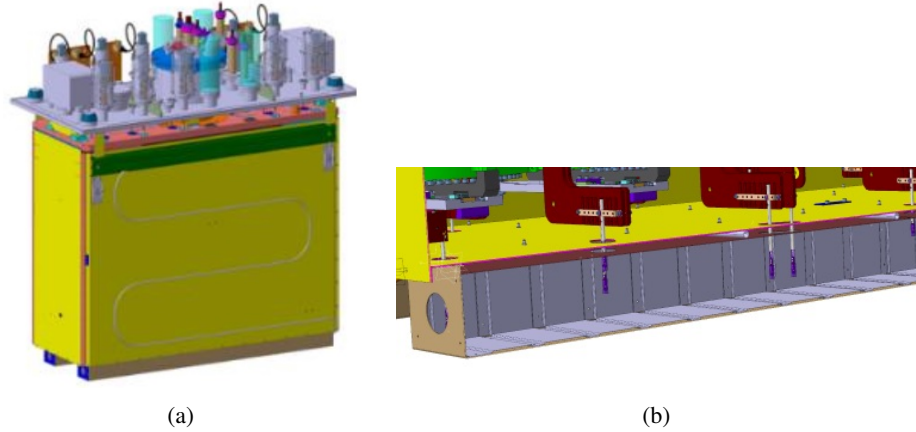
**Fig. 8.17:** Thermal shield with the two alignment corridors on the bottom (a), cut away detail view (b).

## 8.7 Datum pillars

At both extremities of the linac, four pillars are placed, one at each end of the external lines. On top of them, an adjustable plate supports a target measured in the NBL coordinate system using survey methods. These pillars define the datum for the 3D reconstruction. When the four high-$\beta$ and the two low-$\beta$ cryomodules will have been installed for the linac phase 3 configuration, the two upstream pillars will be moved to an upward position.
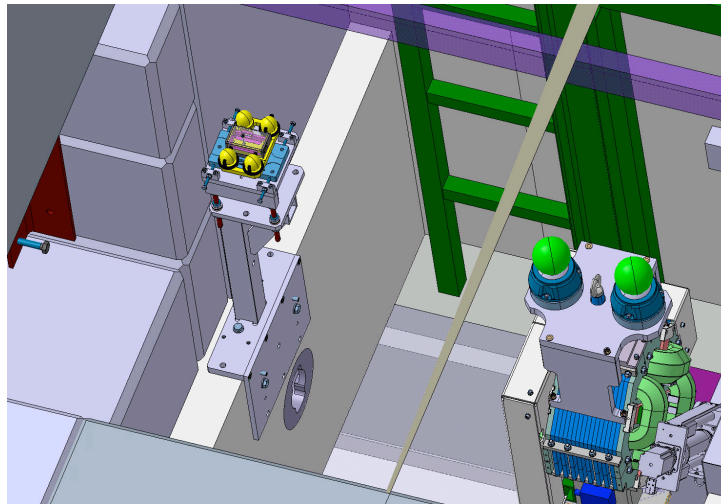


**Fig. 8.18:** View of a downstream pillar.

## 8.8   MATHIS - Monitoring and Alignment Tracking for HIE-ISOLDE Software

The general Monitoring and Alignment Tracking for HIE-ISOLDE Software (MATHIS) is inspired by ARAMyS software [6]. To sum up, every element, even a point, has a coordinate system attached to it. All the frames are placed in a hierarchical order, in which one frame can only have one parent but several child systems. The geometrical link between frames is described by six transformation parameters (three translations, three rotations). Each of them can be constrained or not and can be parametrised by a formula depending on temperature and, if needed, pressure in order to cope with the deformation of the mechanical pieces due to changes of these environmental parameters. Each frame can have some options depending on their type (active/passive targets, viewport, etc.) allocated to them. For instance, the additional options for a glass ball target are its refractive index and diameter. The goal is to recalculate each free parameter by a 3D adjustment, taking into account the HBCAMs measurement done between themselves, on the targets and on the datum points. This highly versatile and flexible principle allows virtually to create any kind of system configuration using BCAM or HBCAM.
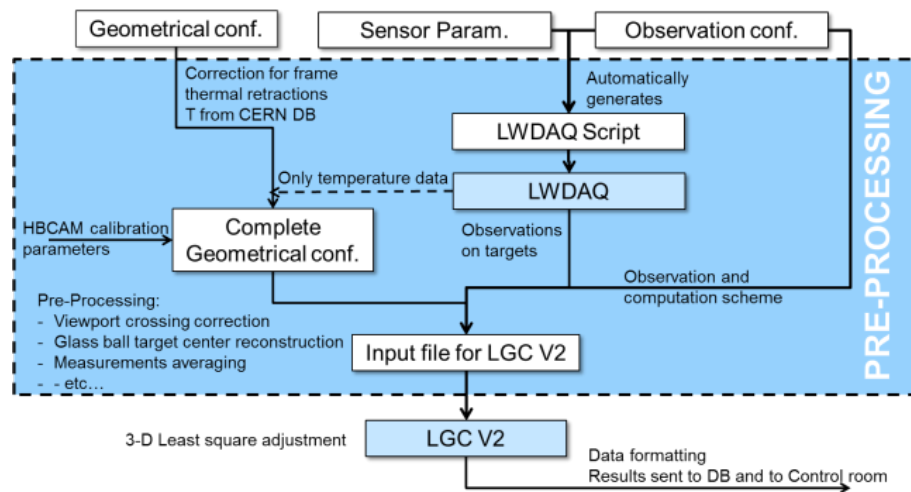


**Fig. 8.19:** MATHIS data flow.

From a practical point of view, a whole system is described by three XML files:

– The geometrical file declaring all the coordinate frames and describing all their links and associated parameters.
– The sensor file defining each type of sensor allowed into MATHIS.
– The observation configuration file which declares which device is installed on which coordinate frame; how to address each sensor; which targets are measured by which device and what is the chosen computation scheme.

Those three files are going through a pre-processing routine. By retrieving the temperature of mechanical pieces, the Omega plates inside the cryomodule and the metrological tables outside the cryomodule, the geometrical configuration file is corrected for the thermal expansion with the formulas expressed in this same file. A change of temperature acts on the transition between frames. This step also includes the automated creation of several frames related to the HBCAM calibration file. Each component (pivot point, laser sources, etc.) of a HBCAM is transformed in a coordinate frame. By combining the sensor and geometrical observation files, MATHIS automatically creates an LWDAQ script making the observations. LWDAQ is the software managing the HBCAM measurement, as well as all other devices developed by Brandeis University.

With the observations, the corrected geometrical configuration and the observation configuration file, MATHIS is able to calculate the viewport crossing effect and compute the corrected observation

at the high index glass ball centre. In the case of observations crossing two viewports, an equivalent viewport is determined. Once this step is finished, the pre-processing ends by creating entry data to be processed by the LGC V2 CERN 3D adjustment software.

LGC V2 is being updated in order to be run by MATHIS and cope with a hierarchical set of frames and laser tracker observations not linked to gravity. The HBCAM type sensors are considered laser trackers with distance measurements loosely weighted and determined from the a priori positions. One laser tracker-like instrument is automatically created on each device pivot point and the CCD measurements are transformed in two angles. The LGC V2 result is formatted and sent to the LOGGING Database and to the control room.

Simulations of a first version of the computation shell have shown that the position of the HBCAMs on a six-cryomodule configuration can be done within 20 microns at one sigma level [7]. The positions of the active element beam port centers can be reconstructed —in most cases— within a precision of 0.05 mm at one sigma level and with respect to the common datum. A precision degradation to $0.1 - 0.2$ mm can occur at the first and last beam port centres within a cryomodule due to a change of the Omega plate design, initiated by integration issues

## References

[1] M. A. Fraser, R. M. Jones and M. Pasini, *Phys. Rev. ST Accel. Beams* **14** (2011) 020102.

[2] J. C. Gayde et al., *eConf* **C1209102** (Sep 2012) 25. 6 p.

[3] BCAM, online, http://alignment.hep.brandeis.edu/.

[4] G. Kautzmann et al., HIE ISOLDE – General Presentation of MATHILDE, CERN-ACC-2015-0084 (CERN, 2014).

[5] Ohara inc., online, http://www.ohara-inc.co.jp.

[6] C. Amelung, *Nucl. Phys. B Proc. Suppl.* **172** (2007) 132 .

[7] G. Kautzmann et al., The HIE-ISOLDE alignment and monitoring system software and test mock up, CERN-ATS-2012-273 (CERN, 2012).

# Chapter 9

# Cryogenics system

N. DELRUELLE

The cryogenics system provides the required cooling capacity at all temperature levels between 300 K and 4.5 K (including helium liquefaction) plus a cryogenic distribution system to feed the six cryomodules. An overhead six-port cryogenic line is installed to link a single helium refrigerator to all six cryomodules. Each port has six different transfer lines (see Figure 9.1). The installed refrigeration capacity allows cooling of the complete six-module chain from ambient to operational temperature in about one week, and a single module in 24 hours.
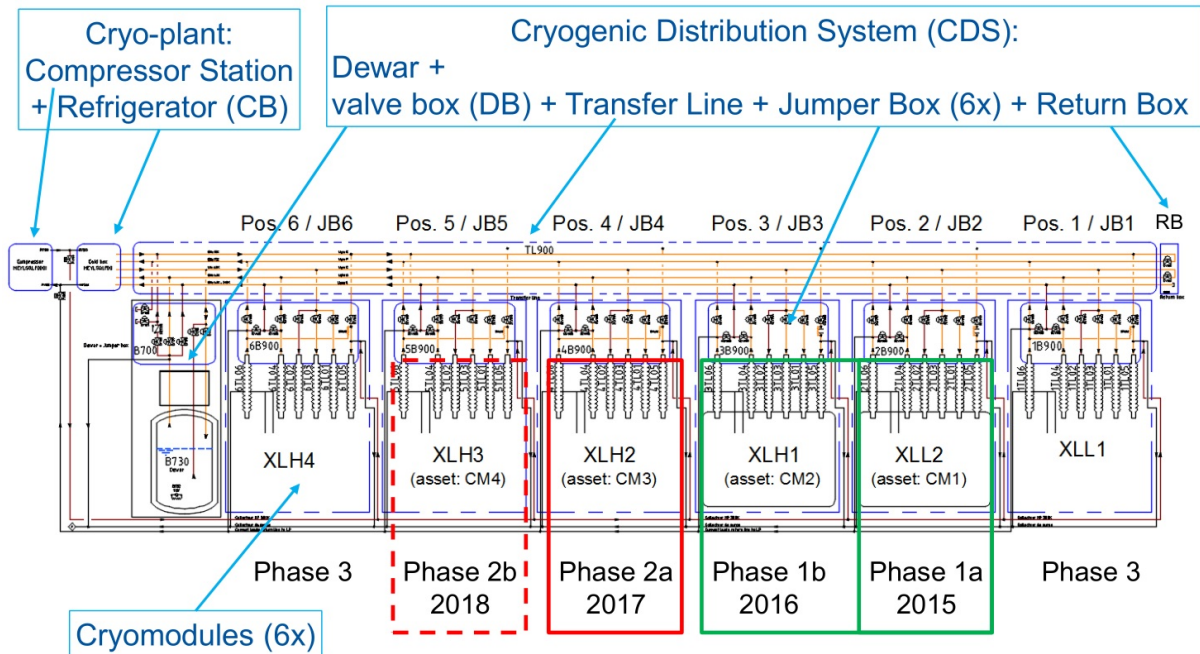


**Fig. 9.1:** Cryogenic system scheme.

The cryogenics system consists of:

– A helium compressor station.
– A single refrigerator cold box.
– A liquid helium storage dewar.
– A cryogenic transfer line.
– Six interconnecting cryogenic boxes (one per cryomodule).

## 9.1 Cryogenic plant and thermal performance of the cryomodule

The static and dynamic heat loads for one cryomodule operating at steady state conditions were calculated for 75 K and 4.5 K temperatures. The results are summarised in Table 9.1; the minimum values

do not include contingency, while the maxima allow for uncertainties. The static heat load at 4.5 K is depicted in Figure 9.2.

**Table 9.1:** Estimated static and dynamic steady state heat loads for one high-$\beta$ cryomodule.

| Source | Nominal heat load to 75 K Min/Max [W] | Nominal heat load to 4.5 K Min/Max [W] |
|---|---|---|
| **Static heat loads** | | |
| Radiation | 188/347 | 1.9/2.4 |
| Conduction | 127/157 | 16/25 |
| Total: Static | 315/504 | 17.9/27.4 |
| **Dynamic heat loads** | | |
| Conduction | 52/52 | 52/55 |
| Total: Static and Dynamic | 367/556 | 70/83 |
| Liquefaction load | - | 0.025/0.025 g/s |
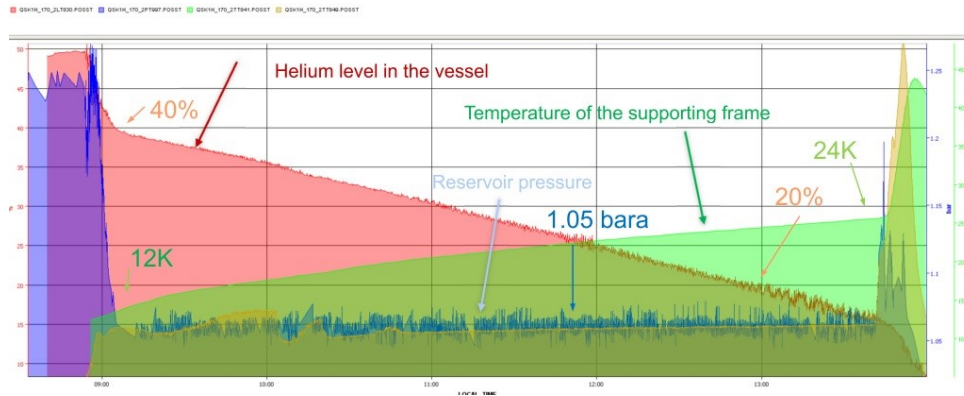


**Fig. 9.2:** Static heat load at 4.5 K (boil-off test).

## 9.2  Helium compressor station

The compressor station provides the flow of gaseous helium at the required pressures to achieve the required performance of the cryogenic system, as specified in [1]. Figure 9.3 presents the layout for the compressor station inside building 198. The compressor station houses the equipment needed to compress the required mass-flow of pure helium, cool it back to ambient temperature and restore it to its original purity. It is based on the use of oil-lubricated screw compressors and provides high-purity compressed helium suitable for liquid helium production. The compressor station includes:

– Two identical screw-compressors, each of them with dedicated motor and mechanical coupling.
– Oil-storage, cooling and circulation equipment.
– Helium cooling equipment.
– A set of minimum three coalescing filters for the continuous separation of oil mist from the helium.
– A charcoal adsorber to adsorb oil aerosols (i.e. to complete helium purification).
– A dryer to trap the humidity hold in the helium.
– Oil and gas filters.
– All interconnecting pipework and valves between the skids.

– All the equipment (valves, vacuum pumps, heaters, etc.) needed for the relief of overpressures, for the purging of all circuits, for the regeneration of the charcoal adsorber and of the dryer, the connection of gas-analysis equipment and the connection to the gas-storage tanks.

– One main electric cabinet and two local cabinets (one for each compressor skid).

– All measuring and actuating devices up to the main electric cabinet.

– All safety devices necessary to protect the operating personnel and the expensive components (compressors, motors) by means completely independent of the Process Control System.

– All hardware interlocks and incorporated control logic.
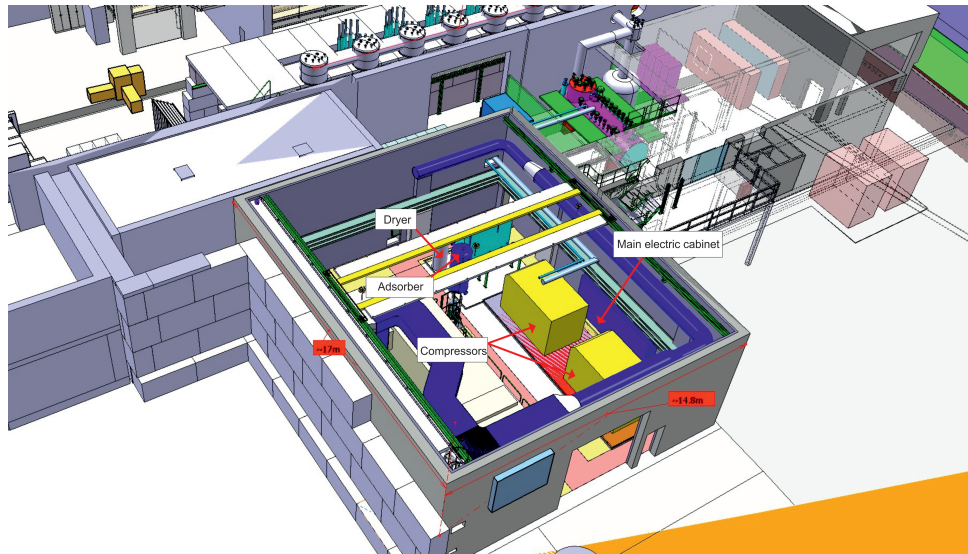


**Fig. 9.3:** Layout of the compressor station.

The gas discharged by the two compressors passes successively through an oil separator equipped with rough filter elements, a water-cooled helium cooler, a minimum of three coalescing filters, the charcoal adsorber, the dryer and a fine dust filter before leaving the compressor station towards the cold box.

## 9.3 Helium refrigerator

One helium refrigerator is used to supply to the cryomodules with the required cooling capacity at all temperature levels between 300 K and 4.5 K. This refrigerator provides for the three main operational modes of the cryomodules; namely, the cool-down from ambient temperature, the steady-state operation at 4.5 K and the warm-up. To reduce the HIE-ISOLDE project's overall cost, an existing helium refrigerator, manufactured by Linde Kryotechnik in the late 1980s and connected to the ALEPH magnet during LEP operation from 1989 to 2000, was reinstalled in 2014 in a dedicated building located next to the HIE-ISOLDE experimental hall. This refrigerator cold box was capable in 1989 [2] of providing simultaneously an isothermal refrigeration power of 630 W at 4.5 K, a shield cooling of 2700 W between 50 K and 75 K and a helium liquefaction rate of 1.5 g/s. Two screw compressors provide a total mass flow of 0.156 kg/s (156 g/s) compressed from 0.104 MPa (1.04 bara) up to 1.59 MPa (15.9 bara).

The cold box is based on a two-pressure Claude cycle and is equipped with two turbines in series which successively expand the cycle helium from 1.47 MPa (14.7 bara) to 0.545 MPa (5.45 bara) and then from 0.519 MPa (5.19 bara) down to 0.125 MPa (1.25 bara). The discharge temperature of these turbines is respectively 51 K and 11 K. The final expansion is performed in a J-T valve, producing two-phase saturated helium at 0.130 MPa (1.30 bara).

## 9.4 Cryogenic distribution system

The cryogenic distribution system, presented in Figure 9.4, consists of a 30-meter long transfer line, a 2000 l storage dewar and six interconnecting valve boxes. The design of this transfer line housing five cold pipes in the same vacuum vessel allows very low-loss liquid helium transfer — typically a heat load on the 4.5 K pipe less than 0.3 W/m$^2$, whereas each interconnecting valve box provides independent feeding of the cryomodules and operational flexibility, allowing warm-up, disconnection via bayonet connections and removal of individual modules in case of need. Figure 9.5 presents an estimation of the heat load in the cryogenics distribution system. An interconnecting valve box allows a cryomodule cool-down sequence to be split into four phases. The first one involves thermal shield cooling from ambient temperature to about 75 K to ensure cryo-pumping onto the shield of a maximum of residual gas away from the inner surfaces of the RF cavities. In the second phase, the exhaust of the thermal shield already at 75 K is injected into the horizontal reservoir and into the supporting frame to cool them also towards 75 K. During the third phase the RF cavities and the solenoid are cooled down to 75 K. Once at 75 K, the fourth and final phase starts with the supply of liquid helium directly into the horizontal reservoir and into the supporting frame until they reach 4.5 K. As long as the gaseous helium produced during the transient phases has a temperature above 10 K, it is recovered by a dedicated line. The complete technical specification can be found in [3].



(a)          (b)

**Fig. 9.4:** The cryogenics distribution system (a) and the cold box housed in the new building next to the ISOLDE experimental hall (b).
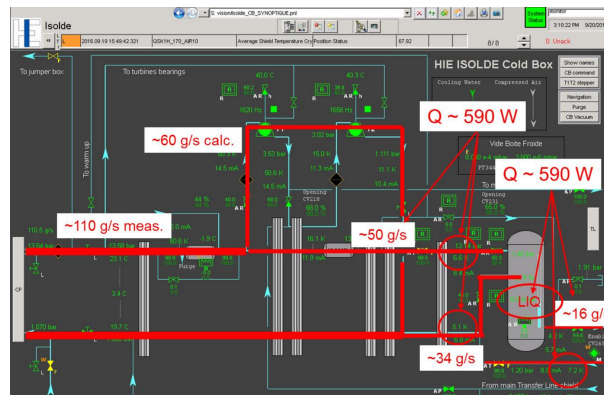


**Fig. 9.5:** Estimations of the heat load in the cryogenics distribution system and the cryomodules, made from the refrigerator balance.

## References

[1] N. Delruelle, Technical specification for the cryogenic system of the HIE-ISOLDE project, EDMS 1146908 (CERN, 2012).

[2] J. P. Dauvergne et al., *Adv. Cryog. Eng., B* **35** (Jul 1989) 901.

[3] N. Delruelle, IT 3777 The cryogenic system of the HIE-ISOLDE experiment, Technical Specification EDMS 1211948 (CERN, 2016).

# Chapter 10

# Vacuum

J. A. FERREIRA SOMOZA

## 10.1 Vacuum requirements of HIE-ISOLDE superconducting linac and beam transfer lines

The vacuum requirements of HIE-ISOLDE have been defined in [1]. The values are $< 10^{-8}$ mbar and leak rate $< 10^{-10}$ mbar·l/s for all the vacuum system. HIE-ISOLDE can be divided into three main different domains from a vacuum point of view:

- Intertanks (including the first D-box, XLN2).
- Cryomodules.
- Tranfer lines.

### Cryomodule vacuum requirements

The vacuum system of the cryomodule has two main functions: to provide insulation vacuum for cryogenics and a pressure compatible with the operation of superconducting cavities.The main risk of the combination of insulation and beam vacuum is a leak from the cryogenic circuits that could be incompatible with beam operation. Because the cryomodule will operate under cryogenic (4 K) conditions, all the gases except helium will be pumped by the cold surfaces. The pumps installed on the cryomodule could allow the operation with a maximum helium leak rate of $10^{-6}$ mbar·l/s from the cryogenic circuits. The vacuum layout of one cryomodule is shown in Figure 10.1. Each cryomodule is equipped with:

- Two redundant Penning and Pirani gauges to monitor the pressure.
- One membrane gauge to follow pumpdown and venting of the main volume.
- One membrane gauge to monitor the pressure in secondary volumes (interspace between seals and rotary feedthroughs).
- Two DN40CF elastomer sealed valves for sectorization.
- One nitrogen line equipped with a calibrated orifice for venting.
- One helium injection line to inject a controlled amount of He for conditioning.
- One roughing line connected to a dry primary pump (ACP28).
- Two turbopumps with 700 l/s nominal speed, each sharing same backing dry pump.

The cryomodule is assembled in ISO5 clean room. Each step of the assembly process is validated with a leak detection. At the end of the assembly process, the cryomodule exits the clean room with all the valves closed and it is temporally equipped with the pumping system (roughing and high vacuum pumping lines). During the final validation test, the cryomodule is under vacuum and all the cryogenic circuits with He are pressurised to nominal pressure. If no leak is observed, the cryomodule is considered valid for transport to the tunnel.

### *Slow pumpdown of the cryomodule*

The cryomodule has to be pumped slowly to avoid the movement of dust particles that could contaminate the superconducting cavity surface, thus impairing its performance [2].The flow speed inside the
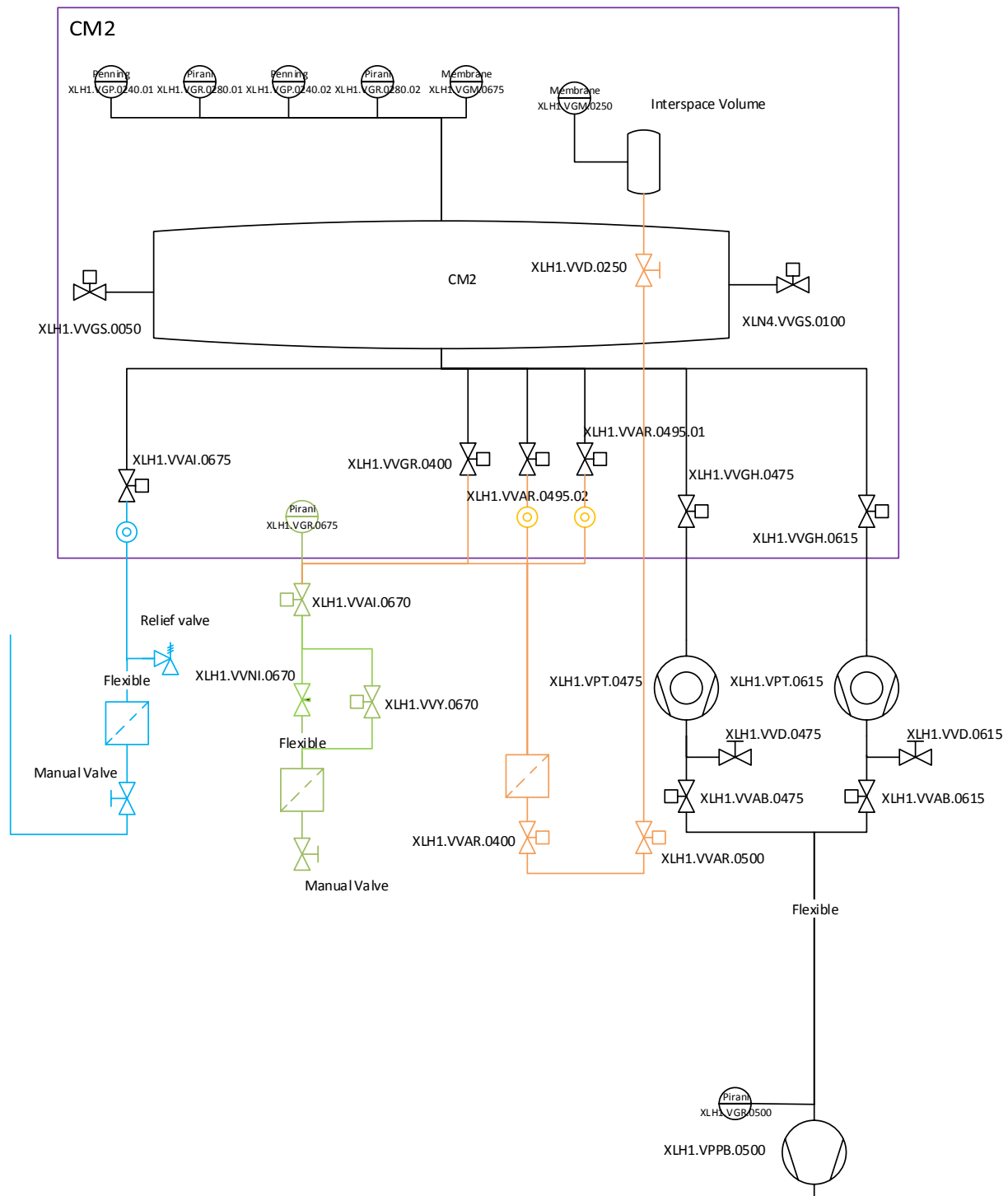
**Fig. 10.1:** Cryomodule vacuum layout.

cryomodule is defined by the size of the primary pump used. An ACP15 (max. pumping speed 15 m$^3$/h) ensures the flow speed will be lower than 1 m/s at the opening of a DNCF63 flange (connection of valve XLH1.VVAR.0495 in Figure 10.1). At this speed, the Reynolds number value is approximately 3000, thus the flow can only be turbulent downstream this position. The big cross section of the cryomodule ensures the flow speed inside will be much smaller and hence laminar. To confirm that the flow speed is low and the regime is laminar, the system was simulated using COMSOL$^\circledR$ [2]. The flow speed inside the thermal shield of the cryomodule is always lower than 0.01 m/s. The comparison of the experimental pumpdown with the simulation, shown in Figure 10.2, shows good agreement for an internal volume of 3.25 m$^3$. The pumpdown time to reach 1 mbar was in the order of 1.5 h.
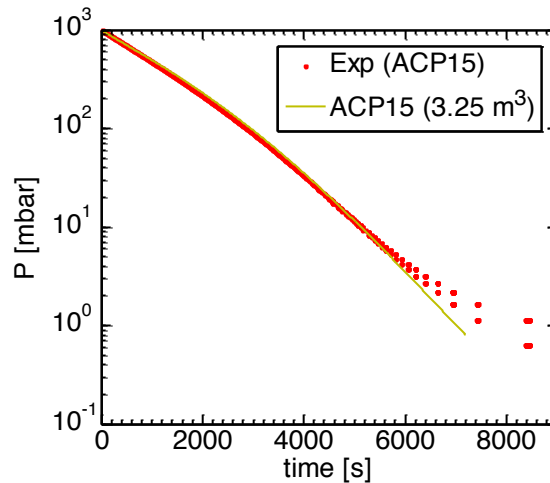


**Fig. 10.2:** Pumpdown curve of the cryomodule (simulation in yellow, experimental values in red dots).

### *Venting of the cryomodule and helium injection system*

In the event the cryomodule needs to be vented, it was equipped with one valve (XLH1.VVAI.0675 in Figure 10.1) limited by a 3 mm orifice that ensures a maximum speed at the aperture of a DN40CF flange of 1 m/s and supersonic flow at the entrance. The nitrogen line is also filtered with a 0.5 micron filter that also restricts the flow. The minimum time required to complete the venting will be in the order of 2 hours.

The cryomodule is equipped with a helium injection system through a dosing valve (XLH1.VVNI.0650 in Figure 10.1). This valve can be bypassed and all of the helium line can be flushed with helium and pumped using the roughing system to clean the lines before injection. The injection system (including flushing) is automatic and only requires the pressure value desired. Owing to the complexity and risks associated with this operation, it should be carried out only by trained personnel. Both the venting and the helium injection systems have to be activated with a specific key in the vicinity of the cryomodule to avoid accidental activation. The information about slow pumpdown and venting is summarised in [2].

### Transfer lines vacuum requirements

The operational pressure of the transfer lines is $10^{-8}$ mbar [1]. The vacuum system in the transfer lines consists of turbomolecular pumps 80 l/s nominal speed, all of them backed by one common backing line. The lines are pumped from atmospheric to $10^{-1}$ mbar through a common roughing line. The XT00, XT01 and XT02 transfer lines are separated by sector valves. The layout of the transfer lines is shown in Figure 10.3.
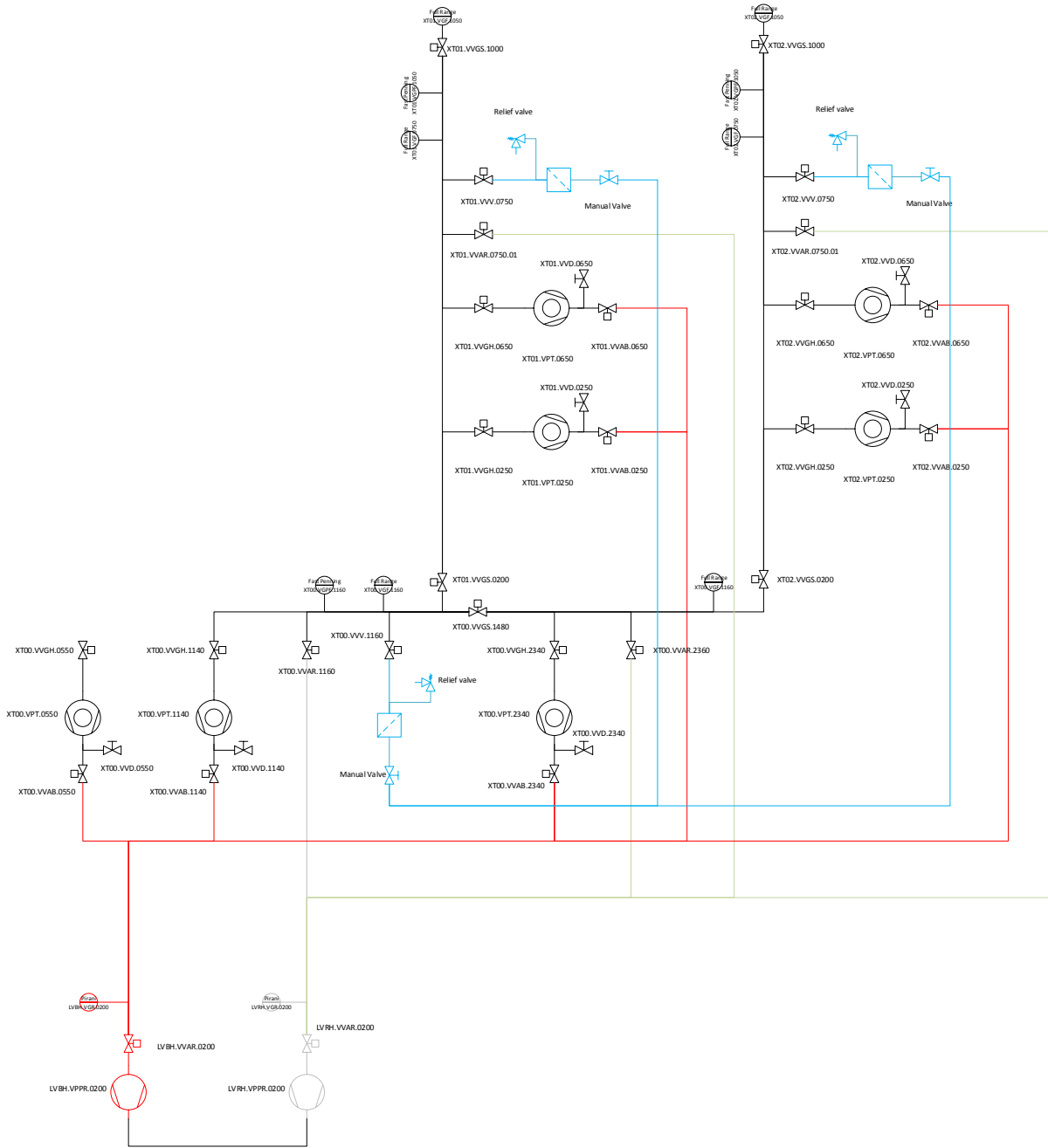
**Fig. 10.3:** Vacuum layout of the transfer lines XT01 and XT02 of HIE-ISOLDE.

## Intertank vacuum system

The intertank consists of a diagnostic box (DB) equipped with different beam instrumentation, pumping and gauges. The pressure objective of the intertank is $< 10^{-8}$ mbar [1, 3]. To achieve this objective, all the intertanks are equipped with one turbomolecular pump (TMP) with nominal pumping speed of 80 l/s (HiPace 80). The pumping layout of the intertank vacuum system is shown in Figure 10.4. Each intertank is equipped with one TMP pump isolated with one gate valve and equipped with one venting line. The intertank is instrumented with one Penning and one Pirani Gauge.

The intertank is limited by the sector valves of the nearby cryomodules, except for those on the extremities that are limited on one side by one cryomodule and on the other by a fast valve that protects the superconducting linac.
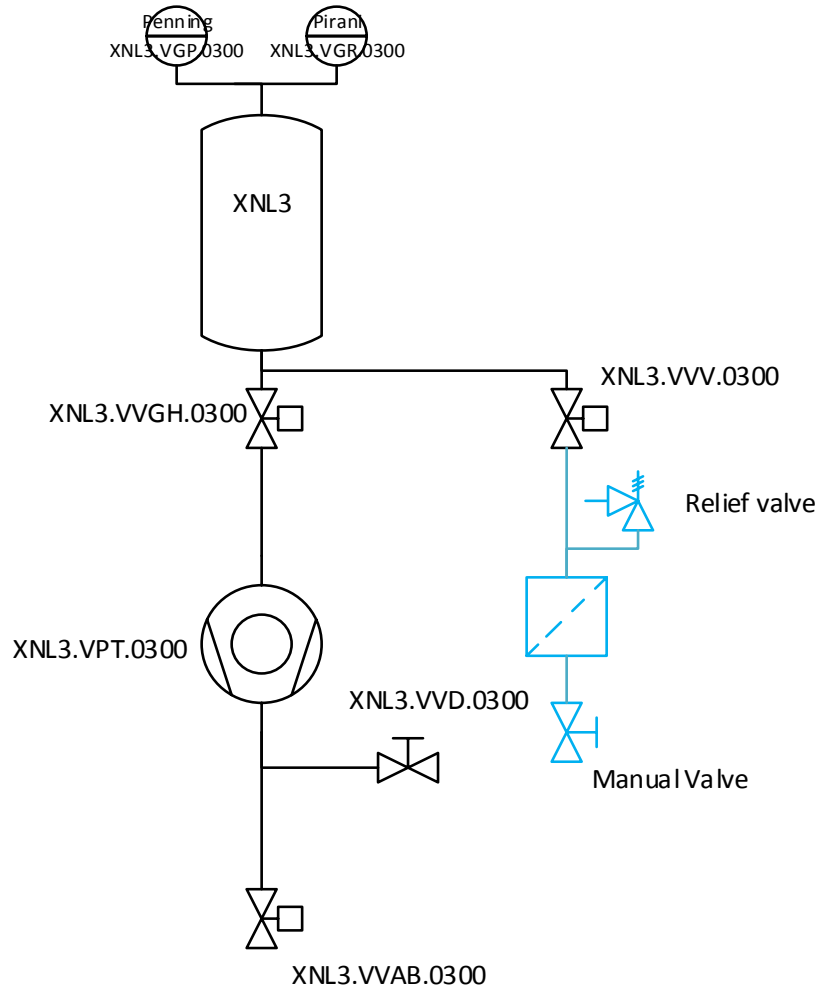
**Fig. 10.4:** Intertank vacuum layout.

All the intertanks share the same primary dry pump (ACP15) for roughing and backing of the turbopump. The control process of all the turbopumps is driven by a master process (VPG_XLN). In case one pump has to be stopped or exchanged during maintenance, this process allows to isolate the rest of operational turbos while the concerned turbo is being pumped, preventing any air inrush on the other intertanks through the backing lines. The control system layout of the intertanks is shown in Figure 10.5.

The effect of the intertank corrector magnet on the performance of the turbopump was studied in detail [4]. The recommendation was to shield the turbopump or keep it at a safe distance ($> 305$ mm from the beam axis). In the final configuration, the distance from the beam axis is $585$ mm for short DBs and $835$ mm for long DBs, ensuring the magnetic field is compatible with the operation of the turbopump.

During the validation of the DBs [5], an abnormally high outgassing rate was observed. It was linked to the use of Vespel® for insulation of the Faraday cups (i.e. CDD drawing [6]). The Vespel® components were replaced by ceramic (Macor®). The DBs meet the outgassing specification after the replacement.

## 10.2 Vacuum layout

The complete vacuum layout of HIE-ISOLDE at the end of phase 1 can be found in [7] and is shown in Figure 10.6. The main domains of the vacuum layout are the cryomodules, intertanks and transfer
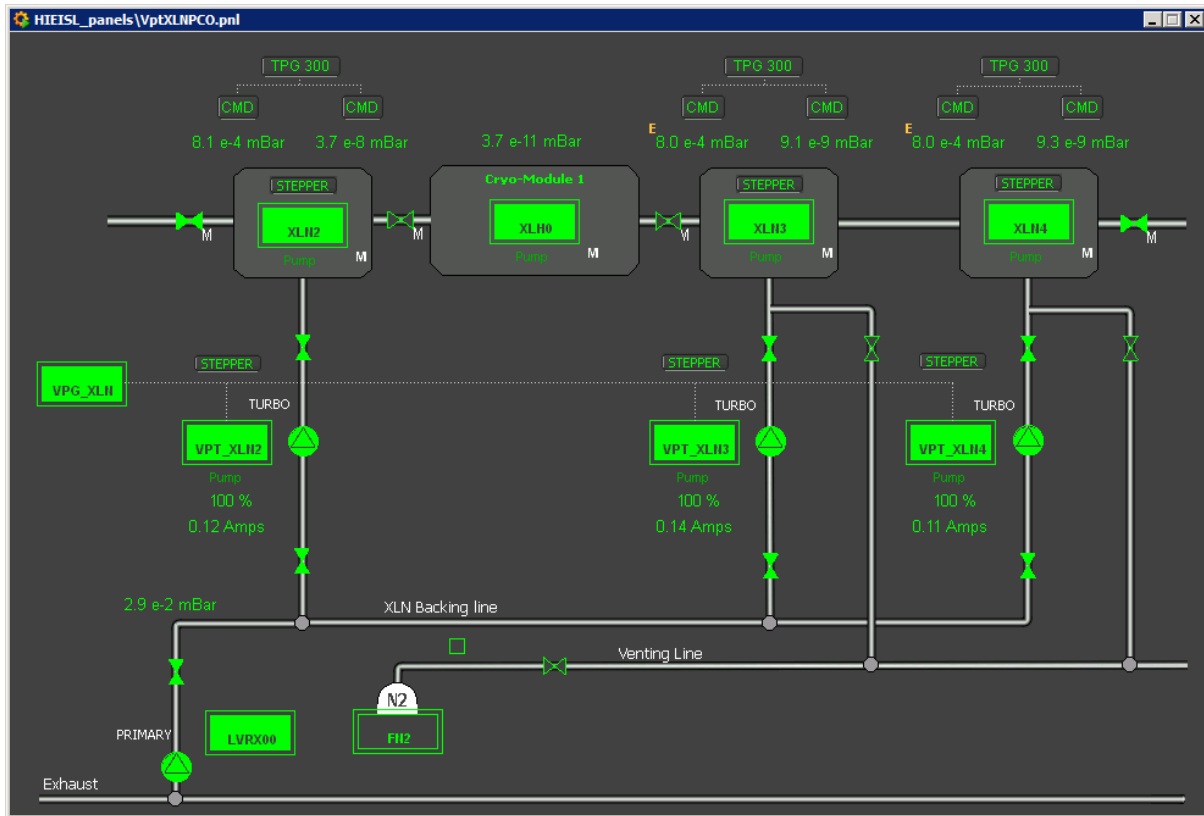
**Fig. 10.5:** Vacuum control system of intertanks.

lines. All the vacuum chambers and vacuum vessels of HIE-ISOLDE are made of stainless steel. All the flanges are either CF type (ISO/TS 3669-2:2007) or ISO-KF (ISO 2861:2013), using metallic seals (copper for CF flanges and aluminium lip for KF) for all the connection of the beam vacuum and viton O-rings for the connections on the backing lines. The mechanical layout of HIE-ISOLDE is shown in [8].
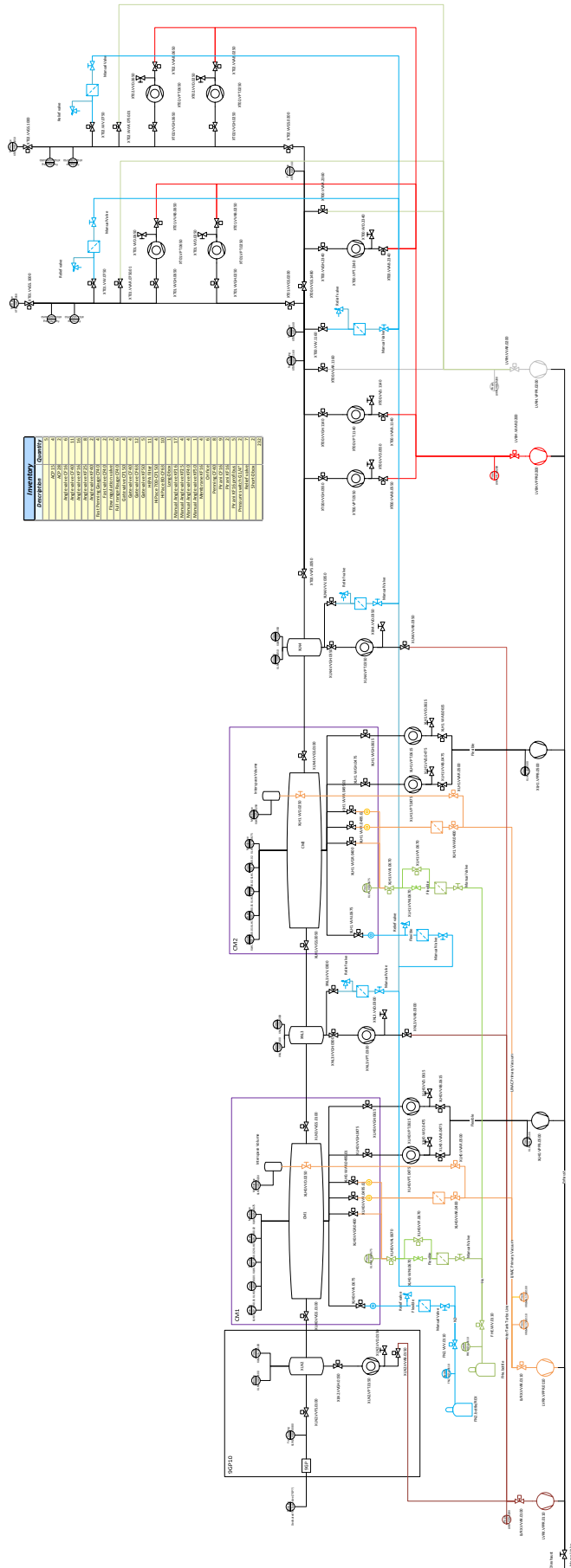
**Fig. 10.6:** Vacuum layout of HIE-ISOLDE.

## 10.3   Vacuum control system

The architecture of the vacuum control system consists on one PLC that controls the different layers of active and passive instruments through a profibus network. The hardware architecture is shown in Figure 10.7. The vacuum control layout at the end of phase 1 is available in [9] and [10]. All the operations in HIE-ISOLDE are highly automated. Each vacuum sector can be pumped or vented. The control system operates different pumps and valves following a predefined logic. The logic of all the processes running on the HIE-ISOLDE vacuum control system can be found in [11].
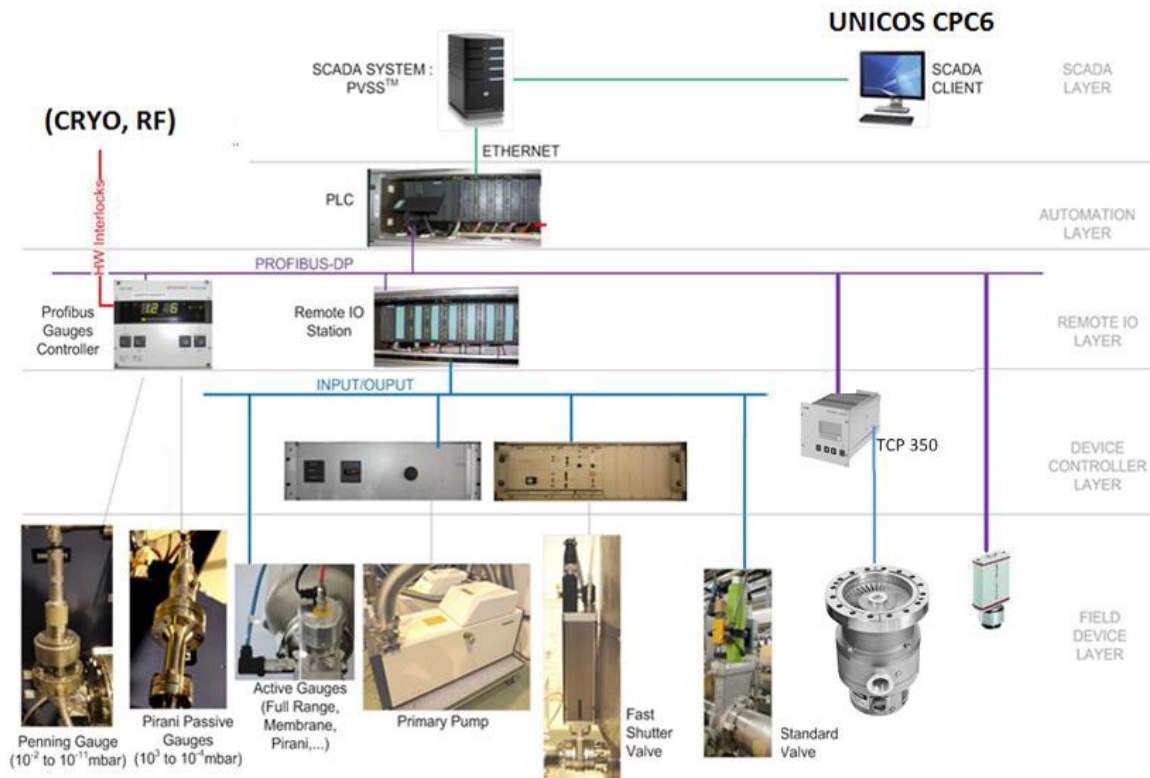


**Fig. 10.7:** Hardware architecture of the vacuum control system.

## References

[1] G. Vandoni, Vacuum system for HIE-ISOLDE, EDMS 1209352 (CERN, 2014).

[2] J. A. Ferreira Somoza, Pumpdown and venting of HIE-ISOLDE cryomodule, EDMS 1485142 (CERN, 2014).

[3] M. A. Fraser et al., Beam diagnostic boxes for HIE-ISOLDE, Functional specification EDMS 1213401 (CERN, 2014).

[4] P. Farantatos, Magnetic compatibility assessment and magnetic shielding proposal for turbo-molecular pump operating under HIE-ISOLDE steerer's stray magnetic field region through magnetic modeling, EDMS 1468590 (CERN, 2015).

[5] A. Harrison, Pumpdown and outgassing measurements of HIE-ISOLDE D-Box, EDMS 1434542 (CERN, 2014).

[6] A. Demougeot, Extended FC assembly, CDD Drawing EDMS 1344625 (CERN, 2015).

[7] J. A. Ferreira Somoza, Vacuum layout of HIE-ISOLDE, EDMS 1471645 (CERN, 2014).

[8] N. Favre, Vacuum overall layout, EDMS ISLLVH__0001 v.0 (CERN, 2014).

[9] S. Blanchard, HIE-ISOLDE HEBT vacuum control layout, EDMS 1465636 (CERN, 2015).

[10] S. Blanchard, HIE-ISOLDE SC Linac Stg1B Vacuum Control Layout, EDMS 1465628 (CERN, 2015).

[11] S. Blanchard, HIE-ISOLDE vacuum control process specifications, EDMS 1466287 (CERN, 2015).

# Part III

# Beam Dynamics

# Introduction

A wide range of accelerating cavities are used for post-acceleration at ISOLDE and each requires particular treatment in terms of the simulation of beam dynamics. These accelerating structures include the RFQ, interdigital IH-DTL structures, multi-gap split-ring cavities and superconducting quarter-wave resonators. The codes used throughout the beam dynamics design studies are outlined in Table 10.1 along with references for further details. For more specific design work, custom written scripts were used and benchmarked where possible with at least one of the codes in Table 10.1. The reference document, where more details can be looked up for the technical summary that follows is [1].

**Table 10.1:** Summary of beam dynamics codes.

| Simulation code | Developers | Comments |
|---|---|---|
| PARMTEQM | LANL [2] | RFQ design code with multi-particle beam dynamics |
| TRACE 3-D | LANL [2] | first-order beam dynamics design and matching code |
| LANA | INR [3] | first-order beam dynamics code with multi-particle tracking |
| LORASR | IAP [4] | KONUS multi-particle beam dynamics design code |
| TRAVEL (PATH Manager) | CERN [5] | numerical tracking of multi-particle beams in field maps[a] |
| TRACK | ANL [6] | numerical tracking of multi-particle beams in field maps[a] |

[a] Hard-edge elements also can be implemented.

# Chapter 11

# REX linac

M.A. FRASER

During the design phase of the HIE-linac, an investigation of REX was undertaken to review the available literature [7–26] and the working points of the machine, with the objective of creating benchmarked beam dynamics simulations tested with beam measurements. The results of the investigation were important for providing reliable input to simulations of HIE-linac. See Chapter 2 for the acronyms used to describe the REX accelerating cavities. The RFQ beam dynamics simulations were benchmarked and bead-pull measurements of the IHS were undertaken in order to benchmark the different codes used to simulate it. Models of the 7GX cavities and the 9GP cavity were also implemented into a single end-to-end `LANA` simulation that was benchmarked with measurement. The longitudinal beam parameters were measured both after the RFQ and before the 7G3, along with transverse emittance measurements.

## 11.1  Transverse emittance measurements

During shutdown periods in 2006 and 2008, the transverse emittance was measured at various energies behind the RFQ, IHS, 7G3 and 9GP structures using a dedicated emittance rig. The measurement campaign is discussed in [27]. The results are summarised and compared to other measurements made during commissioning [23, 24] in Figure 11.1.
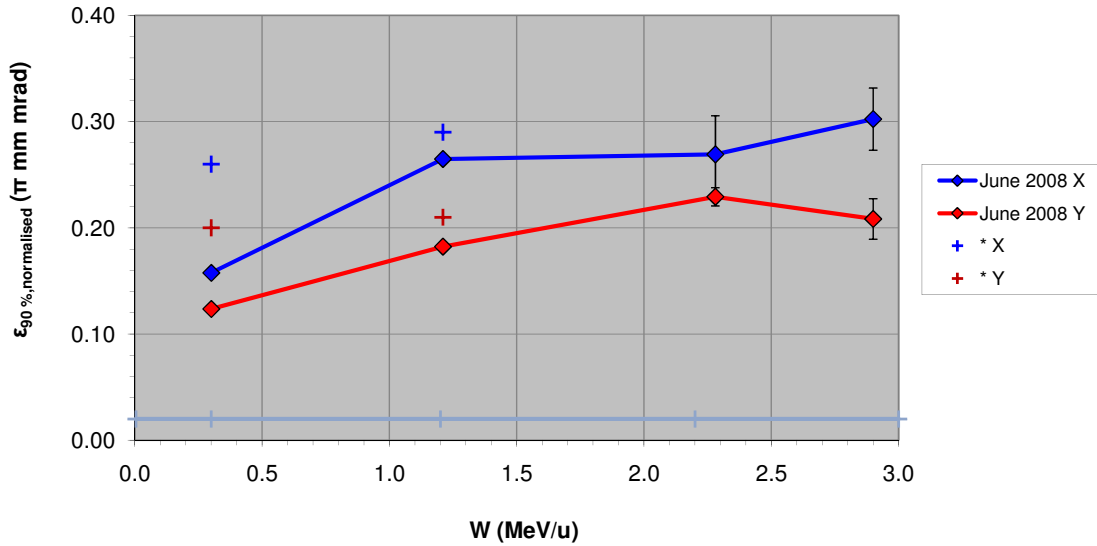


**Fig. 11.1:** Summary of the transverse emittance measurements at REX (Data from [23, 24])(Reproduced from Figure 4 of [27]).

The emittance was measured to be larger in the horizontal projection, which was most likely because of the horizontal slit used after the $A/q$ separator that bends the beam vertically down from the REXEBIS to the REX beam line [8]. The IHS appears to be the dominant source of emittance growth, increasing the emittance by approximately $50\%$. This observation supports a recommissioning of the IHS accompanying the upgrade of the linac. The measured $90\%$ normalised emittance of $0.3\ \pi$ mm

mrad was used as input for the end-to-end beam dynamics studies.

## 11.2  Longitudinal emittance measurements

Longitudinal beam measurements were made at the test stand at the Maier-Leibnitz Laboratory during the initial testing period of the REX front end before commissioning at CERN [9–11]. The measured energy spread and bunch length were consistent with beam dynamics simulations of the RFQ.

The HIE-ISOLDE upgrade will be staged with the high-energy section arriving before the low-energy section, thus it was important to investigate the beam properties at both low and high energies. In 2010 and 2011 the longitudinal emittance was measured at REX for the first time at opportune moments during pauses in the nuclear physics programme to ensure its compatibility with the acceptance of the new superconducting linac. The longitudinal emittance was measured using the three-gradient technique before and after the IHS at $0.3$ MeV/$u$ and $1.92$ MeV/$u$ as shown in Figure 11.2. The three-gradient technique uses an RF device operating at non-accelerating phases to vary the energy spread of the beam as a function of the RF voltage. The response of the energy spread to the RF voltage can then be measured and the emittance extracted by fitting the data using the Courant-Snyder formalism. The rms longitudinal emittance at output from the RFQ was measured as $0.34 \pm 0.08$ $\pi$ ns keV/$u$ and at entry to the 7G3 as $0.36 \pm 0.04$ $\pi$ ns keV/$u$, indicating a small growth of emittance in the IHS.



(a)  Re-buncher at 0.3 MeV/$u$.

(b)  7G3 at 1.9 MeV/$u$.
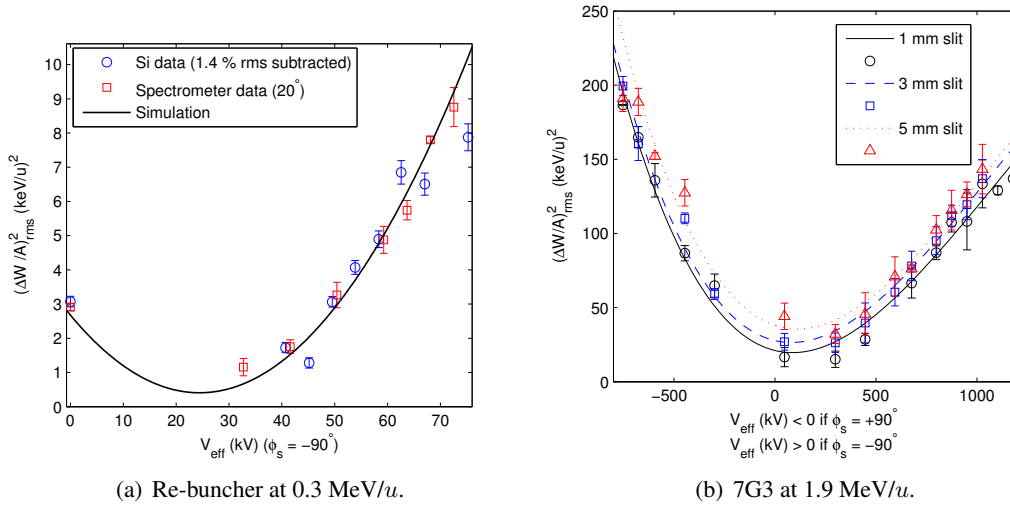
**Fig. 11.2:** Energy spread measured as a function of the (a) ReB or (b) 7G3 voltage used to reconstruct the longitudinal emittance.

## 11.3  End-to-end simulations of REX

The investigation of REX was concluded with end-to-end beam dynamics simulations of the linac using the realistic particle distribution from the RFQ simulations to provide the beam parameters at the exit of the IHS and 9GP cavities, which were required to design the matching sections for the superconducting upgrade. The beam envelopes were matched using a `TRACE 3-D` model before end-to-end `LANA` simulations were carried out, as summarised in Figure 11.3. The relevant simulated beam parameters are collected in Tables 11.1, 11.2 and 11.3. The simulations identified three main regions of emittance growth:

- The internal re-bunching section of the IHS introduces emittance growth in all three phase space planes.

- Matching from a triplet focusing channel to a doublet across the 7G1 introduces emittance growth in the vertical phase space projection.
- Operating the 9GP close to the crest of the RF introduces significant longitudinal emittance growth.

The transverse emittance is increased in the internal re-bunching section of the IHS, where the synchronous phase is lowered and the transverse beam size is large due to its proximity to the internal quadrupole triplet magnet. The large phase spread of the beam in the 7G1 combined with the vertical beam size, which has to be increased to match the beam through the quadrupole doublet magnet, causes emittance growth in predominantly the vertical projection. The 9GP is operated at a synchronous phase of $0°$ to attain the maximum possible energy gain requested by the experiments at ISOLDE, which introduces strong non-linearity in the longitudinal dynamics. The emittance growth is made worse by the long drift preceding it after the 7G3 and the doubling of the RF frequency.
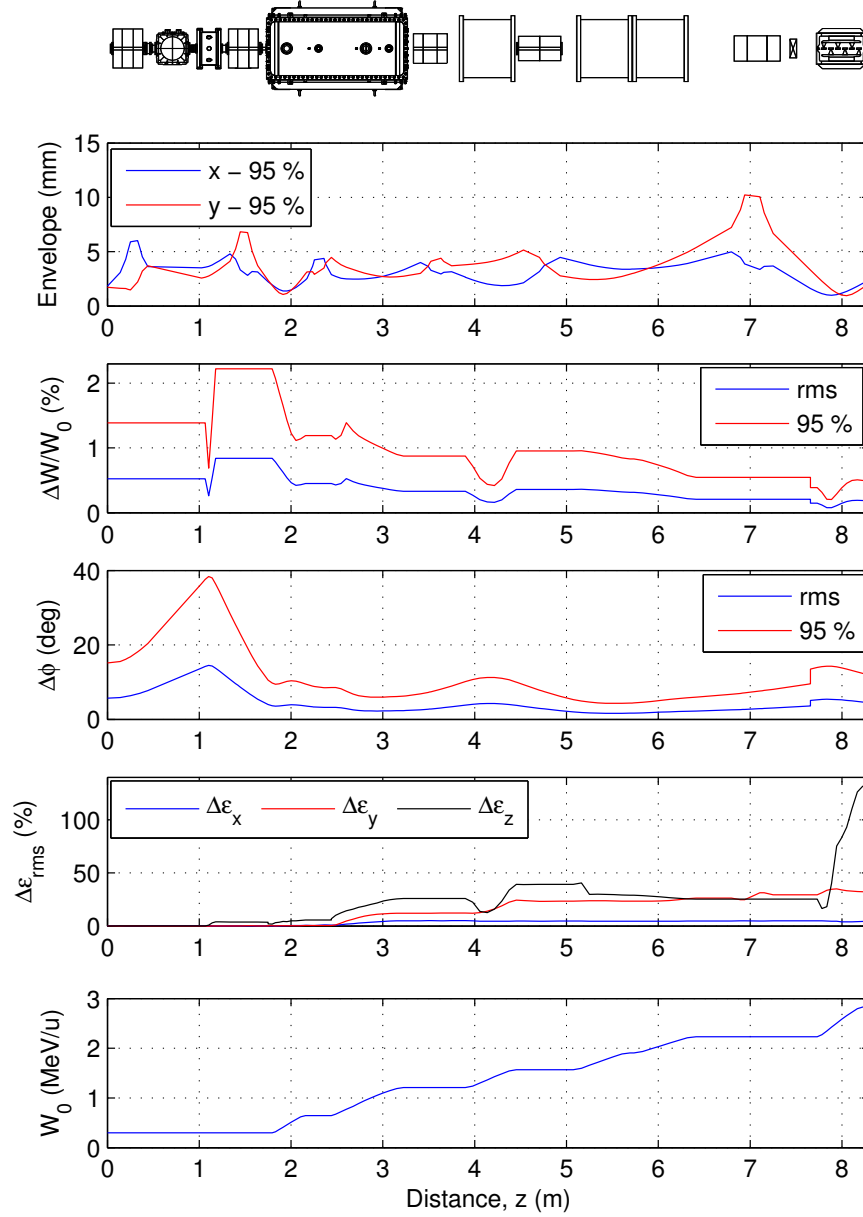


**Fig. 11.3:** Summary of end-to-end multi-particle LANA simulations of REX ($A/q = 4.5$).

105

**Table 11.1:** Summary of the simulated horizontal REX beam parameters[a].

| Position | Simulation code | Energy [MeV/u] | $\tilde{\alpha}_x$ | $\tilde{\beta}_x$ [mm/mrad] | $\epsilon_x^{geom\,rms}$ [π mm mrad] | $\epsilon_x^{geom\,95\%}$ [π mm mrad] | $\epsilon_x^{norm\,rms}$ [π mm mrad] | $\epsilon_x^{norm\,95\%}$ [π mm mrad] |
|---|---|---|---|---|---|---|---|---|
| RFQ exit | PARMTEQM | 0.30 | −0.93 | 0.23 | 2.92 | 13.6 | 0.07 | 0.35 |
| IHS exit | Tracking code | 1.20 | −1.72 | 2.06 | 1.66 | 8.47 | 0.08 | 0.43 |
| 9GP exit | LANA | 2.82 | −2.44 | 1.25 | 0.99 | 4.78 | 0.08 | 0.37 |

**Table 11.2:** Summary of the simulated vertical REX beam parameters[a].

| Position | Simulation code | Energy [MeV/u] | $\tilde{\alpha}_y$ | $\tilde{\beta}_y$ [mm/mrad] | $\epsilon_y^{geom\,rms}$ [π mm mrad] | $\epsilon_y^{geom\,95\%}$ [π mm mrad] | $\epsilon_y^{norm\,rms}$ [π mm mrad] | $\epsilon_y^{norm\,95\%}$ [π mm mrad] |
|---|---|---|---|---|---|---|---|---|
| RFQ exit | PARMTEQM | 0.30 | 0.52 | 0.20 | 2.90 | 13.6 | 0.07 | 0.35 |
| IHS exit | Tracking code | 1.20 | −0.83 | 1.30 | 1.64 | 8.45 | 0.08 | 0.43 |
| 9GP exit | LANA | 2.82 | −2.23 | 0.74 | 1.25 | 7.37 | 0.10 | 0.58 |

**Table 11.3:** Summary of the simulated longitudinal REX beam parameters[a].

| Position | Simulation code | Energy [MeV/u] | $\tilde{\alpha}_z$ | $\tilde{\beta}_z$ [ns/(keV/u)] | $\epsilon_z^{rms}$ [π ns keV/u] | $\epsilon_z^{95\%}$ [π ns keV/u] | $\epsilon_z^{rms}$ [π°%][b] | $\epsilon_z^{95\%}$ [π°%][b] |
|---|---|---|---|---|---|---|---|---|
| RFQ exit | PARMTEQM | 0.30 | −0.06 | 0.10 | 0.26 | 1.79 | 3.12 | 21.8 |
| IHS exit | Tracking code | 1.20 | 0.32 | 0.03 | 0.32 | 2.11 | 0.96 | 6.41 |
| 9GP entry | LANA | 2.23 | 1.26 | 0.07 | 0.32 | 1.96 | 0.52 | 3.20 |
| 9GP exit | LANA | 2.82 | −0.59 | 0.03 | 0.64 | 4.18 | 0.82 | 5.4 |

[a] The input files to all the simulation codes can be found on the CERN Engineering and Equipment Data Management Service (EDMS) under the HIE-ISOLDE project.
[b] At 101.28 Hz.

## 11.4 Beam parameters for phases 1 and 2

The realistic phase space distribution at the output of REX is shown in Figure 11.4, using `LANA`. The 7GX resonators were set at a synchronous phase of $-20°$ and the 9GP at $-10°$. The non-linearity in the dynamics of the longitudinal and vertical planes is clearly observed in the phase space distributions. In particular, the longitudinal phase space is shown both before and after the 9GP to show the non-linearity developed inside the structure.



(a) Horizontal phase space – after 9GP, $W_0 = 2.82$ MeV/$u$

(b) Vertical phase space – after 9GP, $W_0 = 2.82$ MeV/$u$

(c) Longitudinal phase space – before 9GP, $W_0 = 2.23$ MeV/$u$

(d) Longitudinal phase space – after 9GP, $W_0 = 2.82$ MeV/$u$
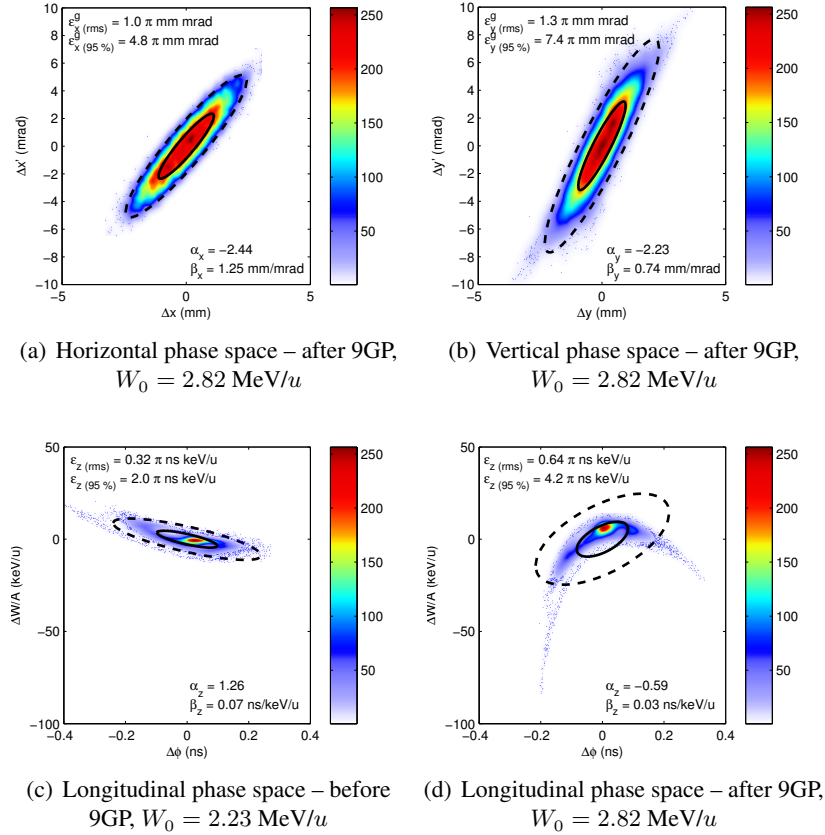
**Fig. 11.4:** Beam phase space distribution at exit to REX, simulated with `LANA`.

## 11.5 Beam parameters for phase 3

The beam parameters at output from the IHS were calculated by tracking through the realistic fields of the ReB and IHS. The phase space distribution of the beam at exit from the IHS is shown in Figure 11.5, in which a horizontal displacement caused by the dipole kick in the IHS is noticeable. The beam parameters are also summarised in Tables 11.1, 11.2 and 11.3.

(a) Horizontal phase space      (b) Vertical phase space      (c) Longitudinal phase space
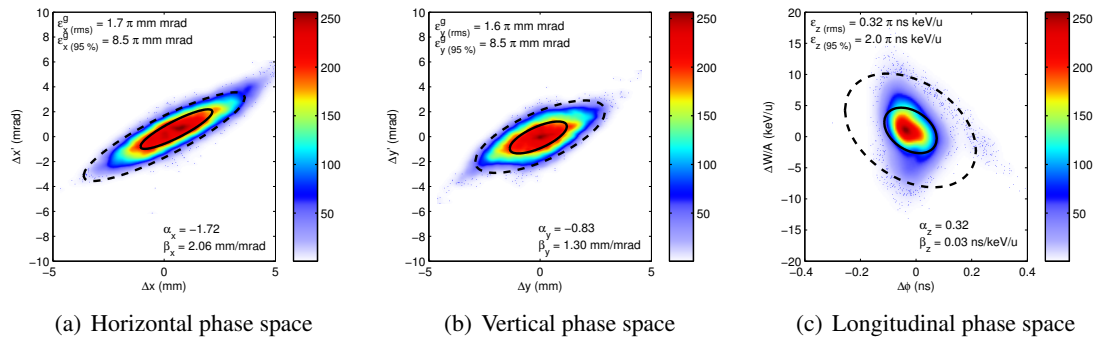
**Fig. 11.5:** Beam phase space distribution at the exit to the IHS, simulated by tracking in the realistic fields of both the ReB and IHS.

# References

[1] M. A. Fraser, R. M. Jones (dir) and M. Pasini (dir), PhD thesis, Manchester U., 2012, Presented 26 Jan 2012.

[2] Los Alamos Accelerator Code Group, LAACG design codes, http://laacg1.lanl.gov/, cited 26 December 2011.

[3] D. V. Gorelov and P. N. Ostroumov, The LANA computer code for beam dynamic simulation in a multi cavity linac, 1995.

[4] R. Tiede et al., LORASR code development, Proceedings of EPAC'10, Edinburgh, 2006, pp 2194–2196.

[5] A. Perrin, J. F. Amand et al., *Travel v4.07 User Manual*, CERN, April 2007.

[6] V. N. Aseev, P. N. Ostroumov, E. S. Lessner and B. Mustapha, TRACK: The new beam dynamics code, Proceedings of PAC'05, Knoxville, 2005, pp 2053–2055.

[7] D. Habs et al., *Nucl. Instrum. Methods Phys. Res. B* **139** (1998) 128.

[8] R. Rao et al., *Nucl. Instrum. Methods Phys. Res. A* **427** (1999) 170.

[9] T. Sieber et al., *Nucl. Phys. A* **701** (2002) 656.

[10] T. Sieber, PhD thesis, Ludwig-Maximilians University Munich, 2001.

[11] T. Sieber et al., Test of the REX-RFQ and status of the front part of the REX-ISOLDE linac, Proceedings of PAC'99, New York, 1999, pp 3516–3518.

[12] K. U. Kühnel, Master's thesis, Institute for Applied Physics, Goethe University Frankfurt, 1999.

[13] S. Emhofer et al., Status of the IH-structure for REX-ISOLDE, Maier-Leibnitz-Laboratorium Annual Report, p 74. MLL, Munich, 1999.

[14] S. Emhofer, Master's thesis, Ludwig-Maximilians University Munich, 1999.

[15] S. Emhofer, PhD thesis, Ludwig-Maximilians University Munich, 2004, Unpublished.

[16] T. Sieber, Master's thesis, Heidelberg University, 1999.

[17] O. Kester et al., Test measurements with the REX-ISOLDE linac structures, Proceedings LINAC'00, Monterey, 2000, pp 351–355.

[18] T. Sieber et al., Acceleration of radioactive ions at REX-ISOLDE, Proceedings of LINAC'02, Gyeongju, 2002, pp 291–295.

[19] S. Emhofer, Commissioning results of the REX-ISOLDE linac, Proceedings of PAC'03, Portland, 2003, pp 2869–2871.

[20] O. Kester et al., An energy upgrade of the REX-ISOLDE linac, Proceedings of PAC'03, SLAC, California, 2003, pp 2872–2874.

[21] T. Sieber, D. Habs and O. Kester, Test and first experiments with the new REX-ISOLDE 200 MHz IH structure, Proceedings of LINAC'04, Lubeck, 2004, pp 318–320.

[22] H. Bongers, Master's thesis, Ludwig-Maximilians University Munich, 2003.

[23] O. Kester et al., Status of REX-ISOLDE, Proceedings of LINAC'04, Lubeck, 2004, pp 18–22.

[24] F. Ames, J. Cederkäll, T. Sieber and F. Wenander, *The REX-ISOLDE Facility: Design and Commissioning Report* (CERN, Geneva, 2005).

[25] O. Kester et al., *Nucl. Instrum. Methods Phys. Res. B* **204** (2003) 20.

[26] R. von Hahn et al., The 7-gap-resonators for REX-ISOLDE, Proceedings of EPAC'02, Paris, 2002, pp 975–977.

[27] D. Voulot, REX-linac emittance measurements, Internal Note CERN-BE-Note-2009-012 (CERN, Geneva, 2009).

# Chapter 12

# HIE-ISOLDE linac

M.A. Fraser

## 12.1 Suppression of longitudinal-transverse coupling

The coupling of the transverse and longitudinal dynamics through the phase dependence of the transverse RF (de)focusing force in the accelerating cavities is a source of transverse emittance growth in the HIE-linac. The perturbation of the beam envelope is driven by the phase spread of the beam in the cavities and the moderately large longitudinal emittance of $2-4\,\pi$ ns keV/$u$ delivered by the REX linac. The coupling is suppressed with stronger transverse focusing and, at higher phase advances, the transverse emittance growth depends only very weakly on the longitudinal emittance. At phase advances close to $90^\circ$ per focusing period, the emittance growth is minimised, hence why the focusing system was specified at a phase advance close to $90^\circ$ per period.

LANA simulations were validated with particle tracking in 3D field maps of the high-energy section in phase 2 of the upgrade, using TRACK, as shown in Figure 12.1. After the beam-steering in the cavities is compensated, as described in Section 12.3, the parametric excitation of the transverse motion by the cavities is the dominant source of emittance growth remaining.
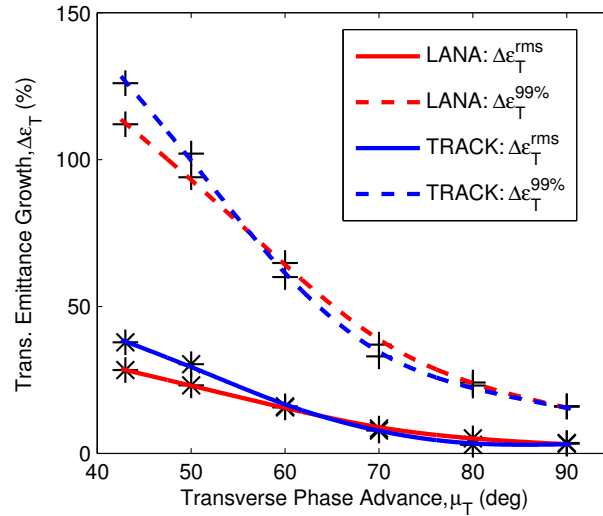


**Fig. 12.1:** Transverse emittance growth calculated with LANA and TRACK as a function of focusing strength in Phase 2 of the HIE-linac ($\epsilon_{L,0}^{tot} = 2\,\pi$ns keV/$u$).

The first-order beam dynamics studies for phase 3 of the superconducting linac are summarised with a beam of $A/q = 4.5$ in Figure 12.2. The study was carried out by tracking $50,000$ particles in the LANA model without imperfections and no particles were lost. A small growth of the transverse emittance arises in the first cavity, which acts as a rebuncher, because of the increased phase spread of the beam after the drift from the IHS. The focusing strength is sufficient that the parametric resonance of the transverse motion is suppressed, even though the phase advance in the second low-energy cryomodule is relaxed to match the beam into a focusing strength of $90^\circ$ per period in the high-energy section. The growth of the

normalised rms emittances is at the level of just a few percent and the adiabatic damping of the transverse beam size is observable. The longitudinal emittance growth arises from the non-linear nature of the phase space gymnastics in the low-energy section and across the transition region into the high-energy section. However, the non-linear effects do not grow and are largely cancelled out. The absence of a dedicated matching section between the two sections of the the linac does not have a significant effect on beam quality.
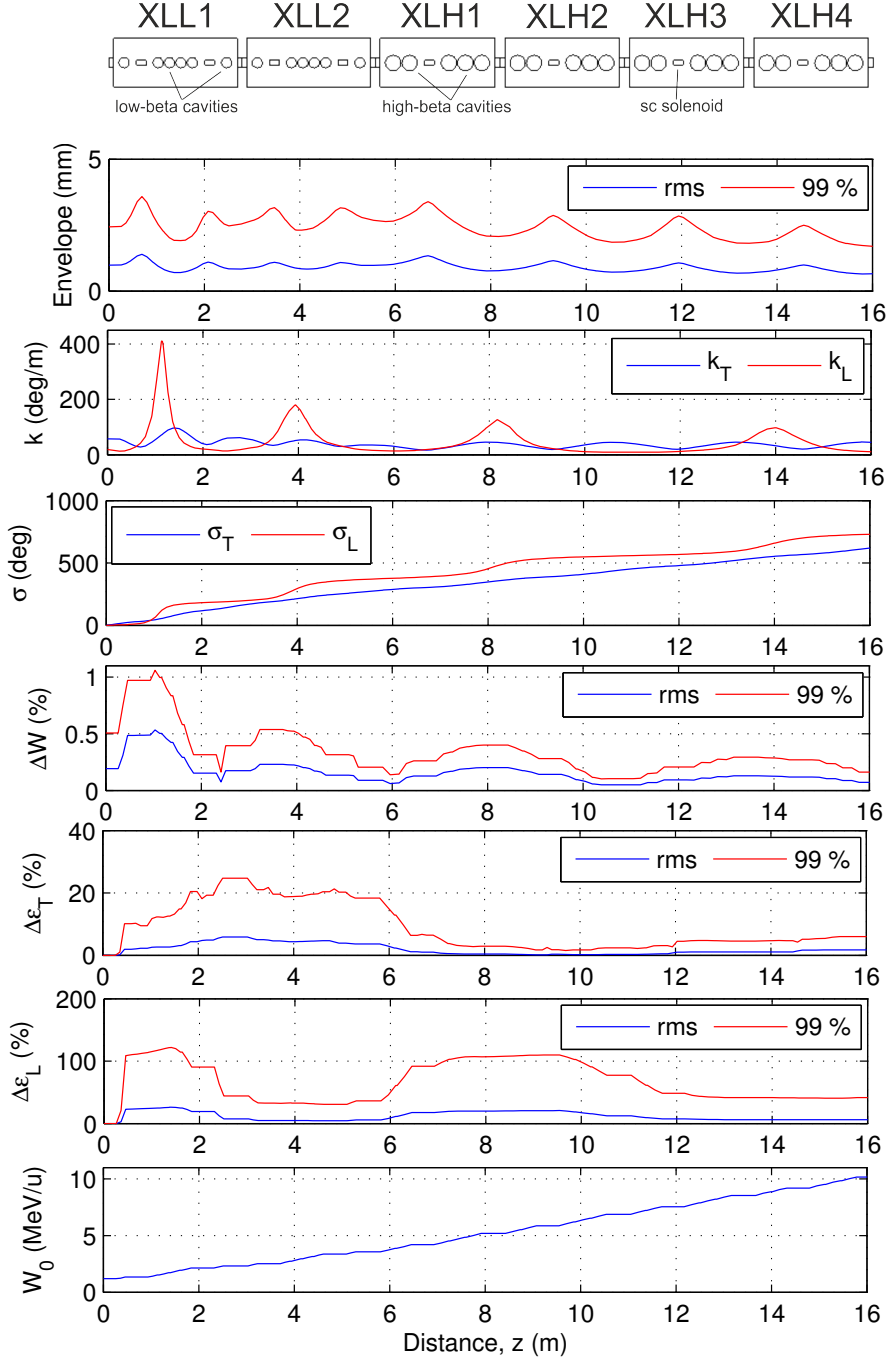


**Fig. 12.2:** Summary of multi-particle LANA simulations of the HIE linac, $\mu_T = 90°$ and $A/q = 4.5$.

## 12.2 Matching REX to the HIE-linac

The normalised transverse acceptance of the HIE-linac is $2.8\ \pi$ mm mrad with a circular aperture of radius 10 mm in the cavities and 15 mm in the solenoids, which is a factor of ten larger than the measured $90\%$ beam emittance of $0.3\ \pi$ mm mrad. The strength of the transverse-longitudinal coupling is reduced as the packing factor and the longitudinal acceptance is increased because the bunch can be constrained tighter in its phase extent. Only a small increase in acceptance is achieved by reducing the spacing between cryomodules below 50 cm because of the longitudinal space already taken up by the solenoids inside the cryomodules. The longitudinal acceptance is close to a factor of five times larger than the nominal emittance of $2\ \pi$ ns keV/$u$, defined by a matched beam ellipse enlarged to touch the edge of the acceptance region shown bounded by blue in Figure 12.3.



(a) $\phi_s = -20^\circ$: large energy spread causes filamentation.

(b) $\phi_s = -10^\circ$: optimum solution, no further emittance growth.

(c) $\phi_s = 0^\circ$: large phase spread causes filamentation.
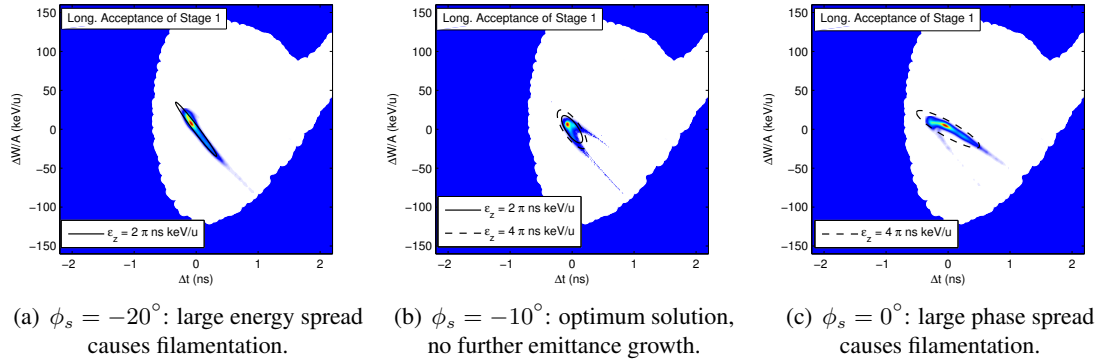
**Fig. 12.3:** Longitudinal acceptance of phase 1 of the HIE linac and the beam at its entrance for different 9GP synchronous phases ($\phi_s$).

### Phases 1 and 2

The first high-energy cryomodule is installed at a position 1.59 m downstream of the 9GP, which is compatible with its position in phase 3 and prevents it having to be moved when the low-energy superconducting section is installed.[1] The REX beam is shown against the longitudinal acceptance of Phase 1 at entry to the first superconducting cavity in Figure 12.3, with the 9GP operating at three different synchronous phases. The longitudinal matching is optimised with the 9GP operating at $-10^\circ$; the emittance grows by over a factor of two in the 9GP but no more growth occurs in the superconducting machine. The $4\ \pi$ ns keV/$u$ emittance is best accepted when the synchronous phases of the first two high-$\beta$ cavities are lowered to $-30^\circ$. When the 9GP is operated at higher synchronous phases, the phase spread of the beam is too large, and at lower phases the energy spread is too large, to be efficiently captured by the superconducting linac and filamentation ensues. The transverse matching to the solenoid channel can be achieved with four quadrupoles characterised by gradients below 50 T/m, each with an effective length of 200 mm and a radial aperture of at least 15 mm, which was specified at a little over twice the $95\%$ beam size, see Figure 12.4.

### Phase 3

The matching section was made as compact as possible with only 1 m between the output of the IHS and the first low-$\beta$ cavity. To this end, a triplet was chosen because the beam is closely round on exit from the IHS and only small additional adjustments to the last quadrupole of the triplet internal to the IHS are

---

[1]If a chopper line is installed with phase 3, the REX front end could be extended by the length of one high energy cryomodule such that only the first high energy cryomodule will require moving to the end of the linac, leaving the other three cryomodules and the cryogenic distribution line undisturbed.

needed to provide the four matching parameters for the solenoid channel. As described in [1], a pole tip radius of 15 mm is adequate to keep 95% of the beam within half the aperture and demanding up to 0.9 T on the pole tip, see Figure 12.5.
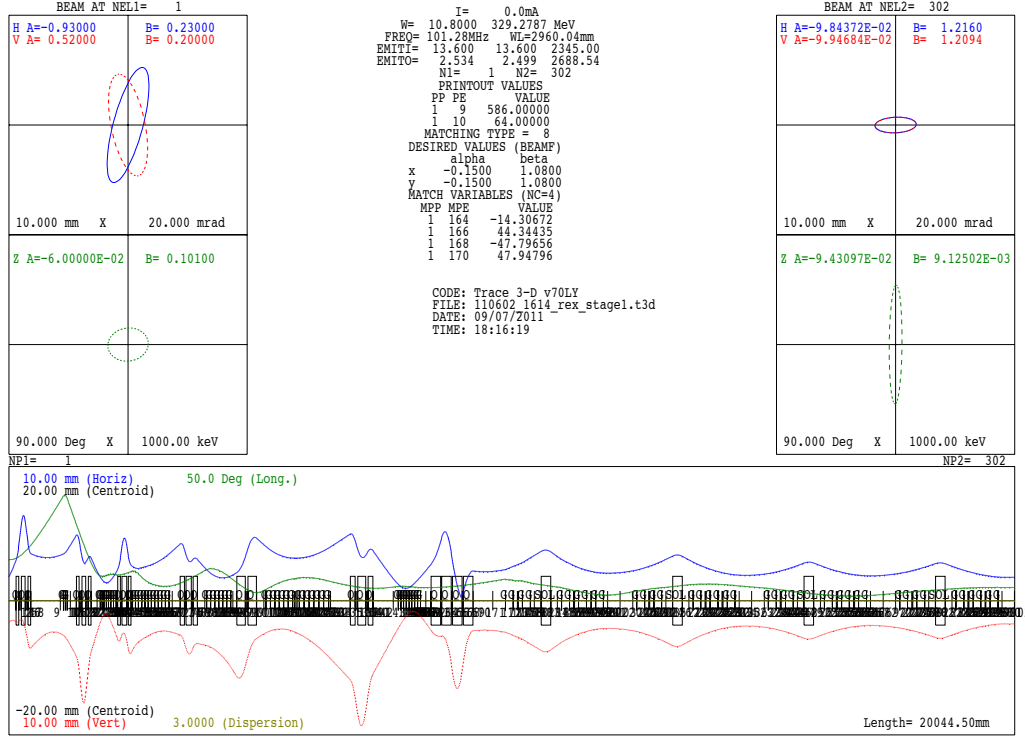


**Fig. 12.4:** `TRACE 3-D` model for matching REX to phase 1 and 2 of the HIE-linac ($A/q = 4.5$).

## 12.3 Compensation of beam-steering in the QWR

For 101.28 MHz quarter-wave resonators, the steering forces are moderate and can be compensated using the RF (de)focusing force by deliberately offsetting the beam inside the aperture. The beam-steering due to RF (de)focusing can be written as,

$$\Delta y'_{\text{steering}} = -\frac{qE_0(y_0)L_a T(\beta)}{A\gamma u c} \underbrace{\delta\frac{\pi}{\lambda}\frac{1}{c\gamma^2\beta^3}}_{\text{RF (de)focusing}} \sin\phi_s,$$ 
(12.1)

where $\delta$ is the offset of the beam centroid with respect to the centre of the aperture. The beam-steering can be compensated by adjusting $\delta$ as a function of $\beta$ such that,

$$\delta_{\text{comp}} = \frac{\lambda c}{\pi}\left[\beta^2\kappa_B(y_0) - \frac{\beta\kappa_E(y_0)}{c}\cot\frac{\pi\beta_g}{2\beta}\right].$$ 
(12.2)

The $1/\beta^3$ dependence of the RF (de)focusing force makes the compensation very effective at low velocity and requires only small offsets of the beam inside the aperture. At higher velocity, the offset becomes larger and limits the application of this technique. The offset allows for an effective compensation over a wide range of velocities, as is shown in Figure 12.6 for the high-$\beta$ cavity in normal operating conditions with $\delta_{\text{comp}} = 2.5$ mm. The compensation ability of the RF (de)focusing force is only effective for $\beta \gtrsim \beta_g/2$ because the RF (de)focusing force in each gap cancels in the limit that $\beta \to \beta_g/2$. Below
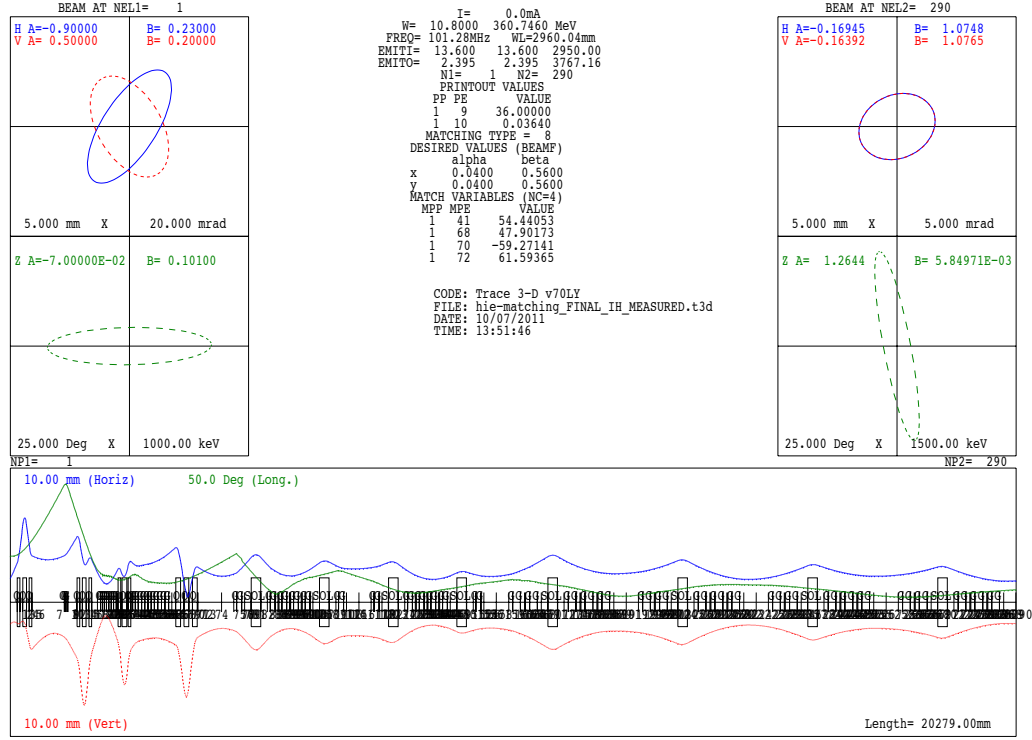
**Fig. 12.5:** `TRACE 3-D` model for matching REX to phase 3 of the HIE-linac ($A/q = 4.5$).



(a) $A/q = 2.5$

(b) $A/q = 4.5$
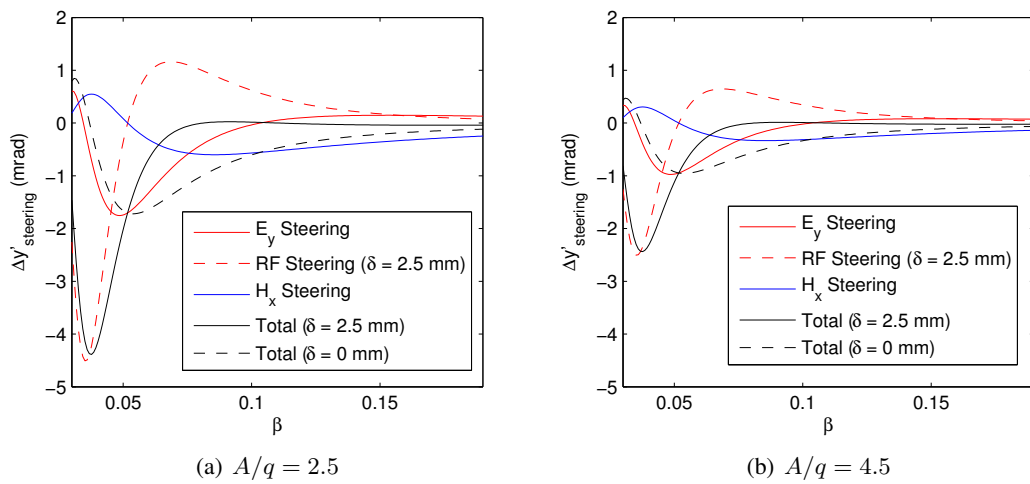
**Fig. 12.6:** An analytic calculation showing the compensation of beam-steering using the RF (de)focusing force in the high-$\beta$ cavity ($\beta_g = 10.3$ %).

$\beta \approx \beta_g/2$ the $1/\beta^3$ of the RF defocusing force causes the compensation offset to become inhibitive, as is shown by the comparison with and without an offset in Figure 12.6.

A $\delta_{\text{comp}}$ of approximately $0.5$ mm is required in the low-$\beta$ cavity whereas, in the high-$\beta$ cavity, the offset necessary is five times larger at closer to $2.5$ mm, which represents a quarter of the radial aperture. The compensation of the beam-steering by modifying the cavity geometry in the vicinity of the beam axis was ruled out to avoid complications in sputtering the copper substrate with niobium. Instead, an elongated aperture in the direction of the offset was used to reduce the loss in aperture arising from the offset, see Figure 12.7.
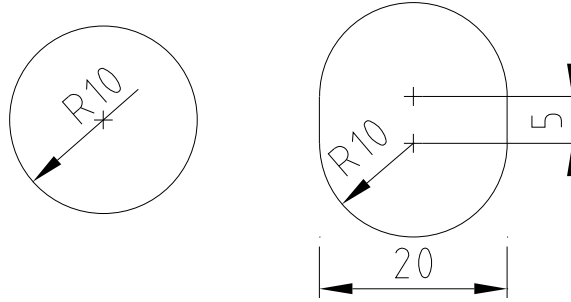


**Fig. 12.7:** Schematic of the circular and racetrack apertures (dimensions in mm).

## 12.4  Optimisation of cavity geometry

To keep the design of the cryomodules as simple as possible, it was decided to apply the same compensation offset ($\delta_{\text{comp}}$) to all cavities of a given family. The cavity geometry was optimised using the computed rms deviation from zero of the ensemble of kicks in $N$ cavities,

$$\sigma_{\Delta y'} = \frac{\sqrt{\sum_{i=1}^{N} \Delta y_{i,\text{steering}}'^2}}{N}, \tag{12.3}$$

and used as a figure of merit to assess the quality of the compensation of the beam-steering as a function of the height of the beam axis and $\delta$. A survey of $\sigma_{\Delta y'}$ as a function of $y_0$ and $\delta$ in the high-energy section of phase 2 is shown in Figure 12.8.

The beam-steering is minimised when the height of the centre of the beam port is located approximately 50 mm above the end of the straight part of the internal conductor with $\delta \approx 2.5$ mm; the steering becomes rapidly difficult to compensate close to the end of the internal resonator because the $\kappa_E$ term rises significantly in this region.

## 12.5  Offset of the beam port noses

The magnitude of $\delta_{\text{opt}}$ was reduced by placing the beam port asymmetrically on the nose of the cavity by a distance $\Delta$, as is demonstrated in Figure 12.9. The asymmetry introduces a small additional vertical dipole component of electric field on the beam axis that modifies the intrinsic electric dipole. The modification introduces higher harmonic terms in the Fourier expansion for $E_y(z)$ that results in a force with the correct phase to compensate the magnetic steering, as is discussed in [2]. The dipole component that is introduced on to the beam axis in the presence of a racetrack shaped aperture by shifting the position of the noses upwards by 2 mm ($\Delta = +2$ mm) is shown in Figure 12.10 alongside a survey of $\sigma_{\Delta y'}$ for

(a) $A/q = 2.5$

(b) $A/q = 4.5$
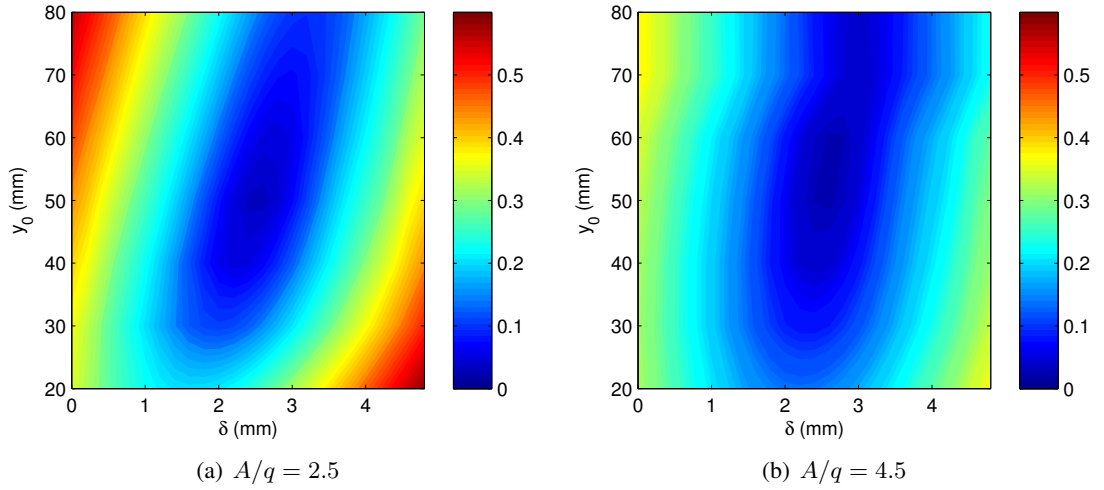
**Fig. 12.8:** Contours of $\sigma_{\Delta y'}$ (mrad) in the high-energy section for 3 2a ($\phi_s = -20^\circ$).



(a) $\Delta > 0$

(b) $\Delta = 0$

(c) $\Delta < 0$
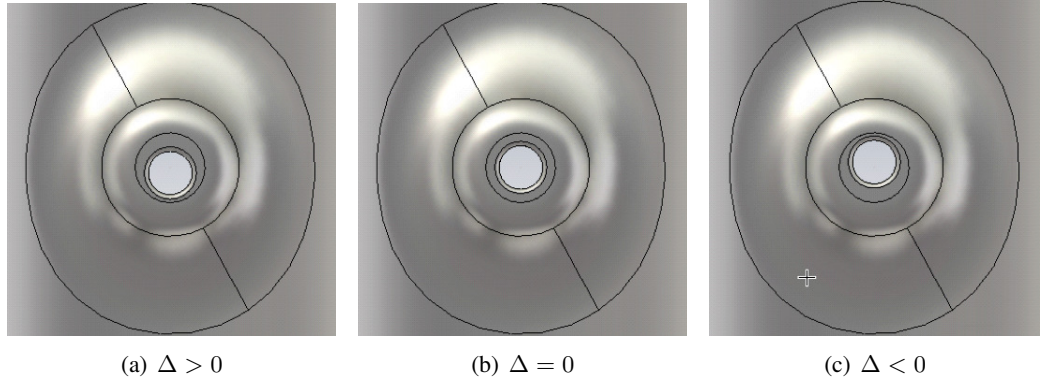
**Fig. 12.9:** The position of the centre of the noses relative to the centre of the beam port, parameterised by $\Delta$.

$\Delta = \pm 2$ mm at $y_0 = 40$ mm. If the offset is made in the correct direction, not only is $\delta_{\text{opt}}$ reduced but so is the magnitude of $\sigma_{\Delta y'}$ at the optimum.

The results of the beam-steering study are summarised in Table 12.1. The optimisation routine was also carried out in the low-energy section for the linac accelerating with $\phi_s = -20^\circ$.

**Table 12.1:** Summary of the results of the beam-steering optimisation study.

| Cavity family | Beam port geometry | $\Delta$ [mm] | $\delta_{\text{opt}}$ [mm] | $y_0$ [mm] |
|---|---|---|---|---|
| Low-$\beta$ | circular | 0 | +0.6 | 35 |
| High-$\beta$ | racetrack | +2.5 | +2.5 | 40 |

## 12.6 Compensation of transverse asymmetry in the QWR

The cylindrical geometry of the quarter-wave resonator introduces a quadrupole component to the transverse electric fields in the vicinity of the beam axis, which breaks the radial symmetry of the electromagnetic fields in the linac. The asymmetry splits the horizontal and vertical phase advances, mismatching the focusing channel and causing the horizontal and vertical emittance projections to oscillate as the

(a) The additional dipole component of electric field compared to the nominal field

(b) $y_0 = 40$ mm and $A/q = 4.5$
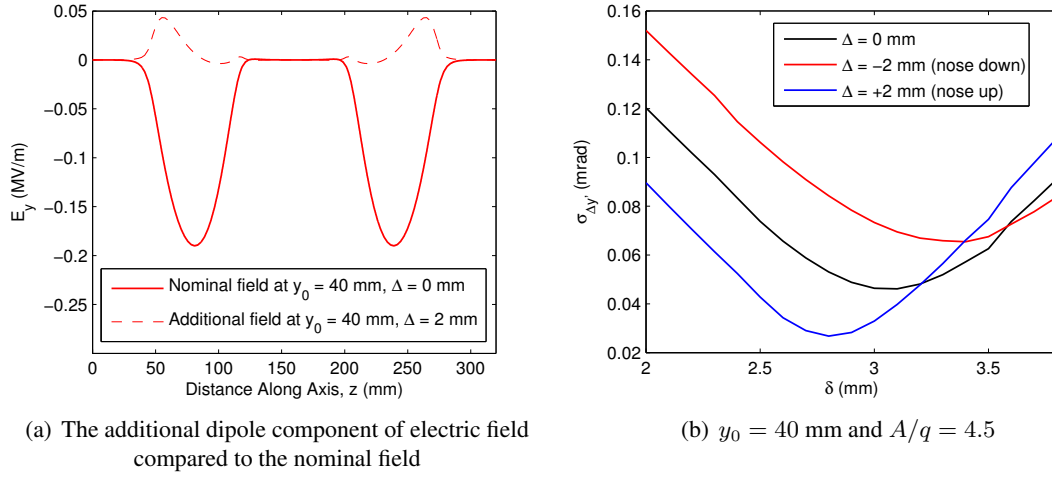
**Fig. 12.10:** The consequence of positioning a racetrack shaped beam port 2 mm above and below the centre of the noses ($\Delta = \pm 2$ mm).

beam is rotated in the solenoids [3]. The asymmetry is summarised in Figure 12.11, which also includes a cavity in which the field symmetry was much improved by modifying the geometry of the end of the internal conductor. This cavity is described in more detail in [4]. The racetrack aperture reduces the
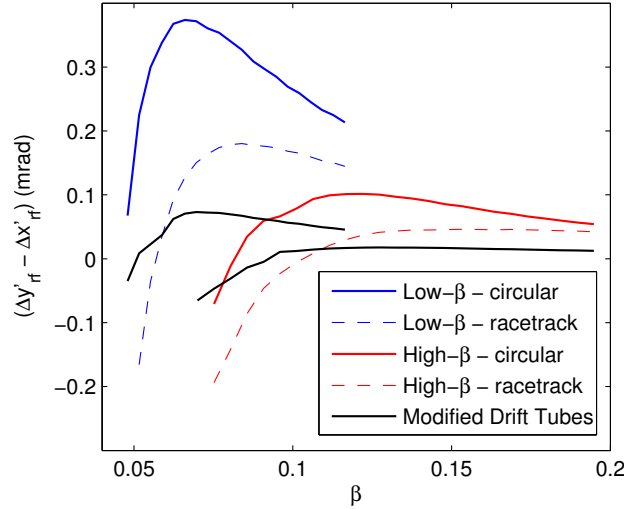


**Fig. 12.11:** Asymmetry of the RF (de)focusing in the cavities at $\pm 1$ mm from the beam axis ($A/q = 2.5$ and $\phi_s = -20°$).

asymmetry of the (de)focusing fields considerably over a wide velocity range, which includes the range of beam velocities in each section after the completion of the upgrade: $\beta > 0.051$ and $> 0.088$ in the low and high-energy sections, respectively.

## 12.7  Removal of cavity noses

The feasibility of removing the beam port noses on some of the high-$\beta$ cavities was investigated with the objective of simplifying and reducing the cost of manufacturing the cavity. If necessary, the noses could be removed from the high-$\beta$ cavities in the final cryomodule with a negligible effect on the beam quality

and an increase in accelerating efficiency.

## 12.8 Deceleration in low-energy section

At REX, beam energies in the range of $0.3-1.2\,\text{MeV}/u$ cannot be delivered to experiments because of the fixed velocity profile of the IHS. Although the IHS was originally designed with flexibility in its output energy, from $1.2-1.1\,\text{MeV}/u$, which would permit further deceleration in the 7G1 down to $0.8\,\text{MeV}/u$, manufacturing problems of its drift-tubes prevented the tilting of the gap voltage profile and variability in its output energy. The low-energy section of the superconducting linac can decelerate beams after the IHS into an energy range that was never previously available at ISOLDE and has particular relevance for the investigation of certain nuclear astrophysics reactions that demand beam energies close to $0.5\,\text{MeV}/u$, see e.g. [5,6]. The commonly used expression,

$$\Delta W \approx q\Delta V_0 T(\beta)\cos\phi, \tag{12.4}$$

cannot be applied to accurately calculate the energy gained or lost by a charged particle interacting with the electromagnetic fields of the cavity at velocities significantly below the geometry velocity of the cavity. A semi-numerical approach was employed using two extra second-order transit time factors, which take into account a small change in velocity inside the cavity and permit the separation of the variables of phase and velocity,

$$\Delta W \approx q\Delta V_0 T(\beta)\cos\phi + \frac{(q\Delta V_0)^2}{W}(T^{(2)}(\beta) + T_s^{(2)}(\beta)\sin 2\phi). \tag{12.5}$$

More details of this formalism can be found in [7].

Phase-stable deceleration through the zero of the first-order transit-time factor is possible by smoothly varying the synchronous phase from the within the range $-\pi < \phi < -\pi/2$ to the range $-5\pi/4 < \phi < -\pi$. The phase must then be switched rapidly by $\pi$ into the range $-\pi/2 < \phi < 0$ and eventually into the range $0 < \phi < \pi/2$ as the sign of the first-order transit-time factor switches and starts to dominate again below $\beta_g/2$. The above listed regions of phase stability that are compatible with deceleration are shown in bold in Figure 12.12 (a) and the shifting phase of the minimum of the energy gain is shown in Figure 12.12 (b).



(a) Schematic

(b) Phase of the minimum of $\Delta W$
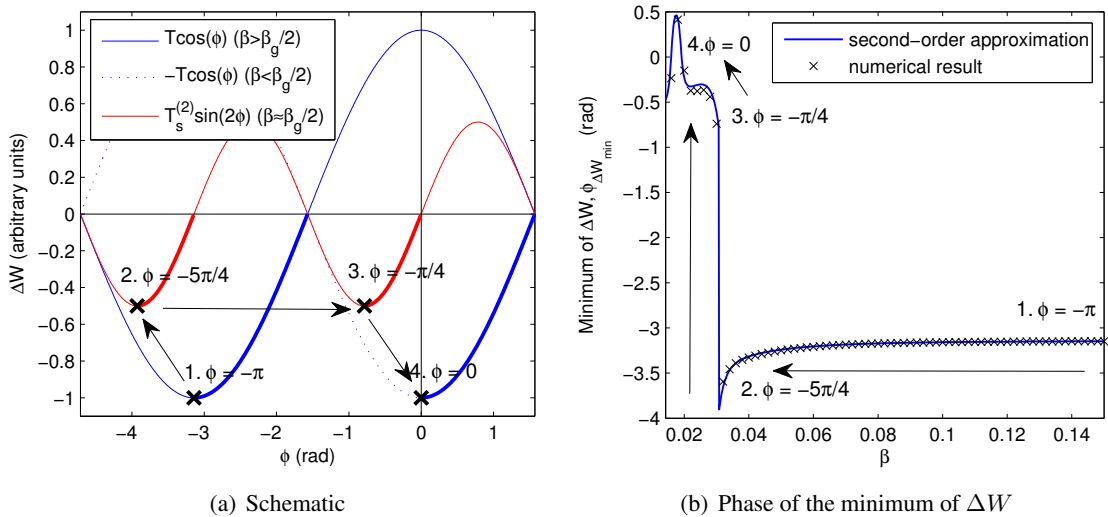
**Fig. 12.12:** Phasing the low-$\beta$ cavity for deceleration ($A/q = 4.5$ and $E_0 = 6$ MV/m).

The heaviest beams with $A/q = 4.5$ can be decelerated down to $0.45$ MeV/$u$, close to the zero of the transit time factor, $T$. The deceleration in this case is limited by the number of low-$\beta$ cavities.

In principle, lighter beams can be decelerated though the zero of $T$ to close the gap in energy between 1.2 MeV/$u$ and 0.3 MeV/$u$, however severe deterioration of the beam quality is expected as the zero of $T$ is traversed. The 12 superconducting low-$\beta$ cavities provide an effective deceleration potential of 3.4 MV for $A/q = 4.5$ and 3.0 MV for $A/q = 3$, as opposed to 10.8 MV for acceleration. The beam energy after each cavity is shown in Figure 12.13 using the first and second-order approximations with a comparison made to the numerical result and the TRACK code for two beams with $A/q = 4.5$ and 3.



(a) $A/q = 4.5$  (b) $A/q = 3$
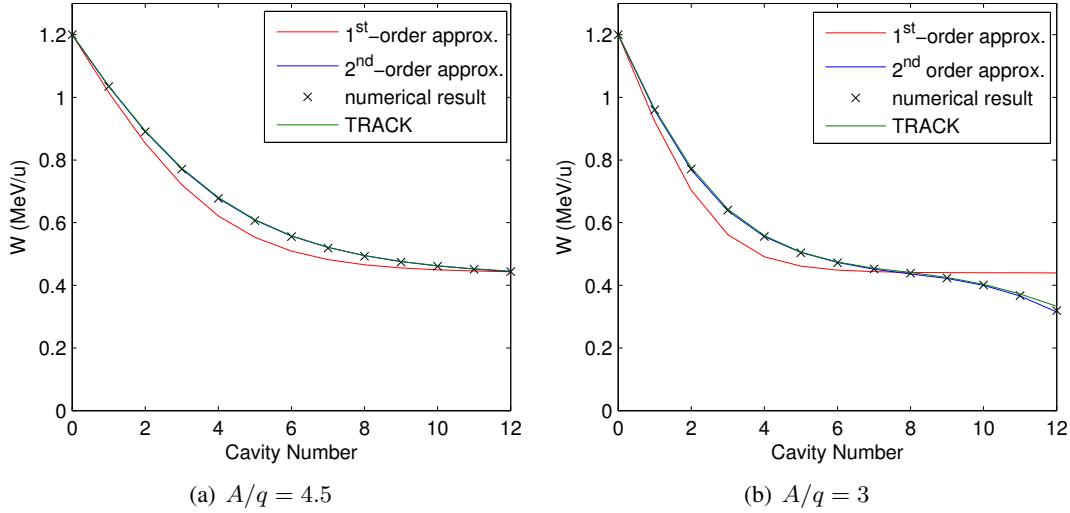
**Fig. 12.13:** Deceleration in the low-energy section ($E_{\mathrm{acc}} = 6$ MV/m and $\phi_s = +20°$).

## 12.9 Misalignment and error studies

The sensitivity of the beam to misalignment and RF instabilities was investigated in order to understand the robustness of the design to imperfections. The following imperfections were investigated:

– Transverse misalignment of the cavities and solenoids: $\sigma_{x,y,\mathrm{cav}}$ and $\sigma_{x,y,\mathrm{sol}}$.
– Longitudinal misalignment of the cavities: $\sigma_{z,\mathrm{cav}}$.
– Phase and voltage instability in the cavities: $\sigma_{\Delta\phi}$ and $\sigma_{\Delta V}$.

The beam is about five times more sensitive to the misalignment of the solenoids than to the misalignment of the cavities, see the results presented in [8]; owing to this dominance and the axial symmetry of the solenoid, skew errors (rotations about the beam axis) were neglected. The effect of a variation in the longitudinal position of the cavities was investigated to understand the tolerance to which the cavities must be aligned to avoid having to re-phase the linac. Static field errors and longitudinal misalignment of the solenoids were ignored.

Unlike in a fixed-velocity linac, where the fields are scaled and the effect of misalignment is independent of $A/q$, in a superconducting linac the full accelerating voltage is delivered to all beams and those with lower $A/q$ are usually more sensitive to misalignment; beams with $A/q = 2.5$ were shown to be 15% more sensitive than $A/q = 4.5$ to misalignment [9]. The high-energy section of the linac in phase 2a was simulated with $A/q = 2.5$ to provide the specification of the alignment tolerances for the development of the high-energy cryomodule.

### Correction routine

Warm steerer magnets and beam position monitors (BPMs) will be installed in the spaces between the cryomodules. The correction routine is bracketed over each cryomodule, with a corrector located before

and a BPM after each cryomodule. A phase advance of close to $\pi/2$ between the corrector and BPM is optimum for an orbit correction system [10]. As a result of the coupled motion in the solenoid focusing channel, the corrector strength in each orthogonal plane is coupled to the dynamics in the other plane.

**Transverse cavity misalignment**

The effect of cavity misalignment on the likely centroid trajectory is shown in Figure 12.14, with and without correction, for 1000 linac error seeds and a tolerance on the alignment of $\sigma_{x,y,\mathrm{cav}} = \pm 0.5$ mm. There is no error in the BPM or misalignment of the solenoids.
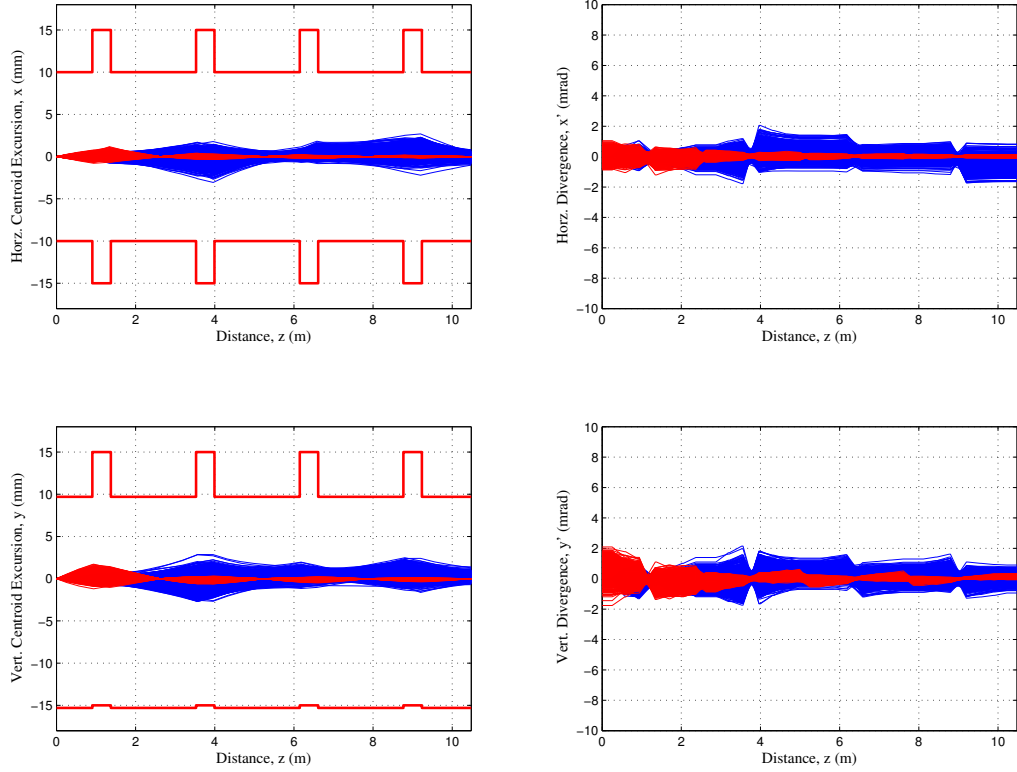


**Fig. 12.14:** The centroid trajectory and divergence for 1000 linac error seeds with (red) and without correction (blue) for $\sigma_{x,y,\mathrm{cav}} = \pm 0.5$ mm. The physical aperture of the beam pipe is shown as a solid red line on the plots.

**Transverse solenoid misalignment**

In a similar fashion, the centroid trajectories in 1000 randomly misaligned linacs are presented in Figure 12.15 for a solenoid alignment tolerance of $\sigma_{x,y,\mathrm{sol}} = \pm 0.5$ mm.

**Transverse acceptance**

The transverse acceptance of the linac is determined by both the physical aperture and the strength of the focusing channel, and is strongly affected by the machine alignment and correction procedure. Enveloping the rms spatial extent of the centroid trajectories with $\sigma_c$, one can express the loss in acceptance $\Delta A/A$. The loss in acceptance is surveyed in phase 2a operating at a transverse phase advance of $\pi/2$ per focusing period for different solenoid and cavity misalignments and accuracies on the BPM in Figure 12.16. As discussed above, a phase advance of $\pi/2$ or $90°$ per focusing period is preferred for beam quality concerns and, in order to optimise the acceptance at this focusing strength, the alignment of the solenoids should be achieved to better than $\sigma_{x,y,\mathrm{sol}} = \pm 0.1$ mm. The alignment tolerances
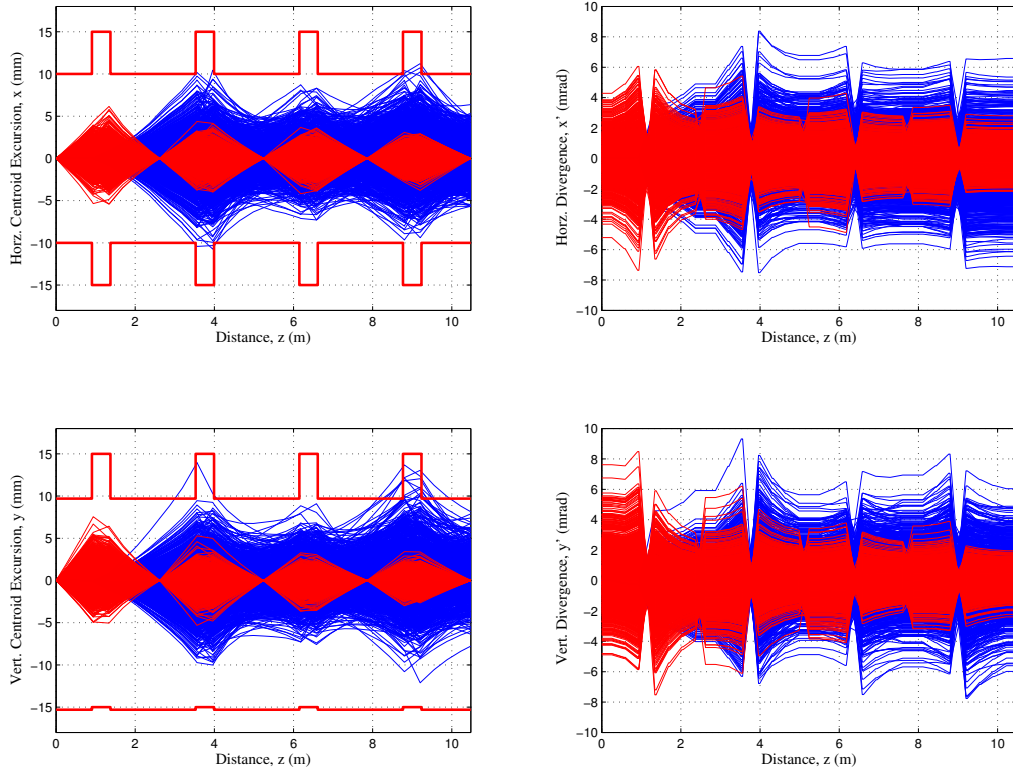
**Fig. 12.15:** The centroid trajectory and divergence for 1000 error seeds with correction, in red, and without correction, in blue, for $\sigma_{x,y,\text{sol}} = \pm 0.5$ mm.

for the linac were specified such that in the worst case the loss in acceptance will not exceed 25% (at a certainty of 99.7%), demanding the tolerances $\sigma_{x,y,\text{sol}} = \pm 0.15$ mm, $\sigma_{x,y,\text{cav}} = \pm 0.30$ mm and $\sigma_{x,y,\text{BPM}} = \pm 0.20$ mm. This can be contrasted to the loss of 20% of the acceptance used at ISAC II, see [11]. The centroid should remain within 15% of the aperture, i.e. $3\sigma_c/R_{\text{ap}} \lesssim 15\%$.

### 12.9.1 Emittance growth

The likelihood of emittance growth caused by misalignment was investigated using the error module in TRACK. An ensemble of 250 error seeds was used with each seed containing 2000 particles in the bunch. The emittance growth relative to the nominal case, with and without orbit correction, for a transverse cavity alignment tolerance of $\Sigma_{x,y,\text{cav}} = \pm 2.0$ mm is shown in Figure 12.17 in the horizontal plane. The growth of the longitudinal emittance, which mainly arises from the radial dependence of the transit-time factor, is an order of magnitude lower than the transverse emittance growth.

*Cavity: transverse misalignment*

The probability of transverse emittance growth relative to the nominal case is shown in Figure 12.18, with and without correction using warm steerers. The probability of the emittance growth exceeding 10% is less than 1 in 100 with correction, for a tolerance as large as $\Sigma_{x,y,\text{cav}} = \pm 2.0$ mm on the exit and entry position of the cavity.

*Cavity: longitudinal misalignment*

The stability of the longitudinal alignment of the cavities is important to ensure that the linac does not need re-phasing. The most likely cause of changes to the longitudinal position of the cavities will be
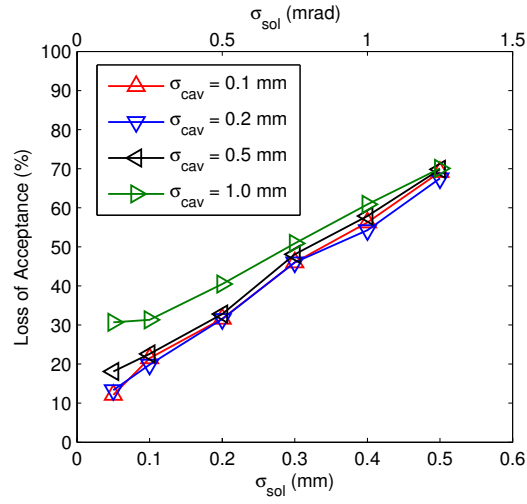
(a) $\sigma_{x,y,\text{BPM}} = \pm 0.1$ mm
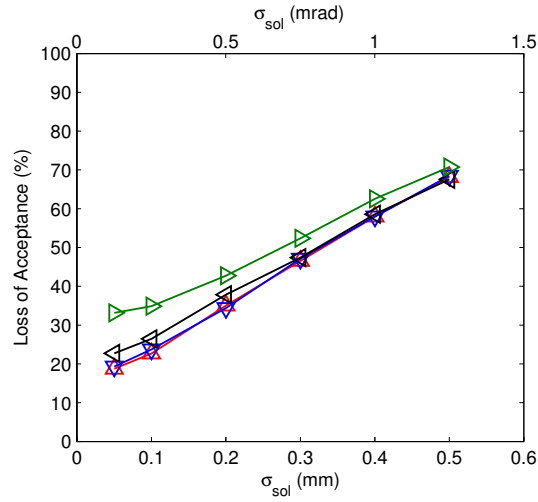


(b) $\sigma_{x,y,\text{BPM}} = \pm 0.2$ mm
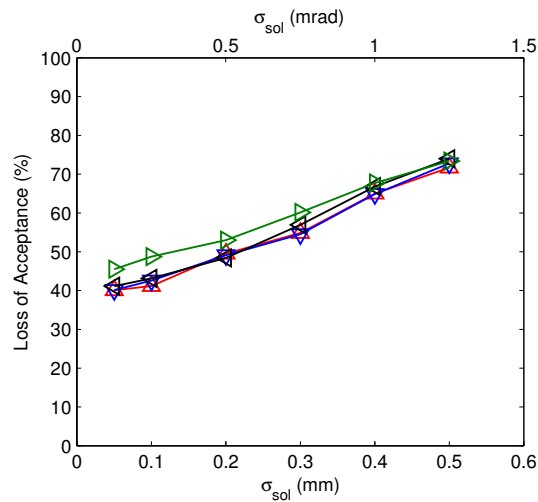


(c) $\sigma_{x,y,\text{BPM}} = \pm 0.5$ mm

**Fig. 12.16:** A survey of the loss in acceptance ($\Delta A/A$) as a function of the solenoid alignment tolerance, for BPM error tolerances in the range $\pm 0.1 - 0.5$ mm and cavity alignment tolerances in the range $\pm 0.1 - 1.0$ mm.

(a) Horizontal emittance growth

(b) Longitudinal emittance growth
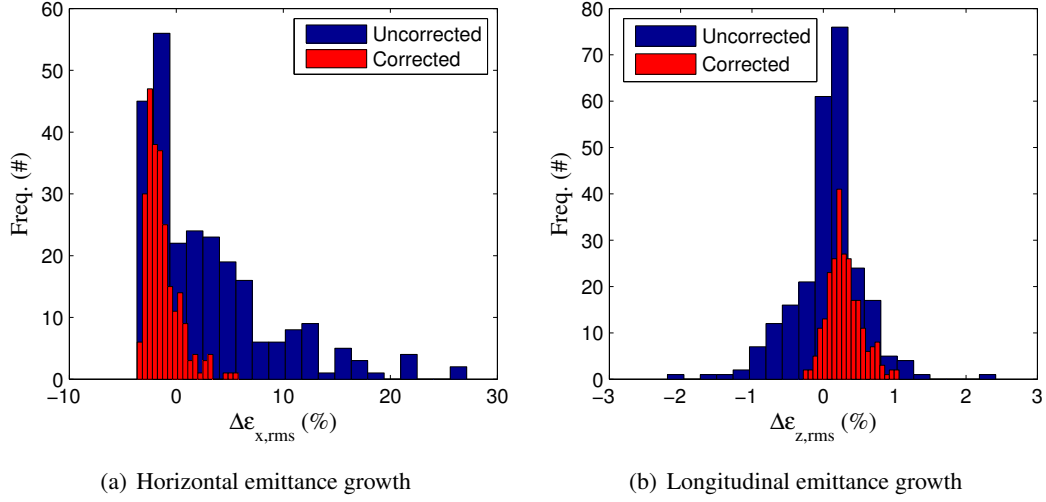
**Fig. 12.17:** The emittance growth from 250 error seeds of the phase 2 linac with $\Sigma_{x,y,\mathtt{cav}} = \pm 2.0$ mm.



(a) Uncorrected

(b) Corrected with warm steerers
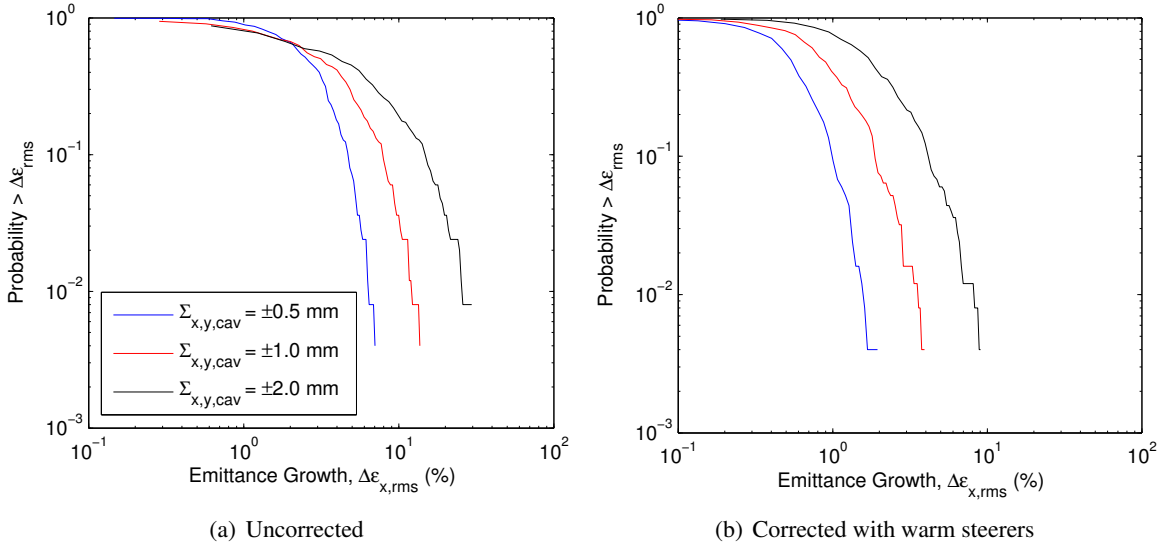
**Fig. 12.18:** The probability of emittance growth in phase 2 with transverse misalignment of the cavities.

the mechanical stresses involved in the thermal cycling of the cryomodule during shutdown and maintenance periods. As shown in Figure 12.19, the longitudinal emittance is only significantly affected if the longitudinal position of the cavities cannot be controlled to better than $\Sigma_{z,\mathtt{cav}} = \pm 2.0$ mm.

### Solenoid: transverse misalignment

The probability of transverse emittance growth relative to the nominal case is shown in Figure 12.20, with and without correction using warm steerers. The probability of the emittance growth exceeding 10% is less than 1 in 100 with the orbit corrected for a tolerance as large as $\Sigma_{x,y,\mathtt{sol}} = \pm 0.5$ mm on the exit and entry position of the solenoid.
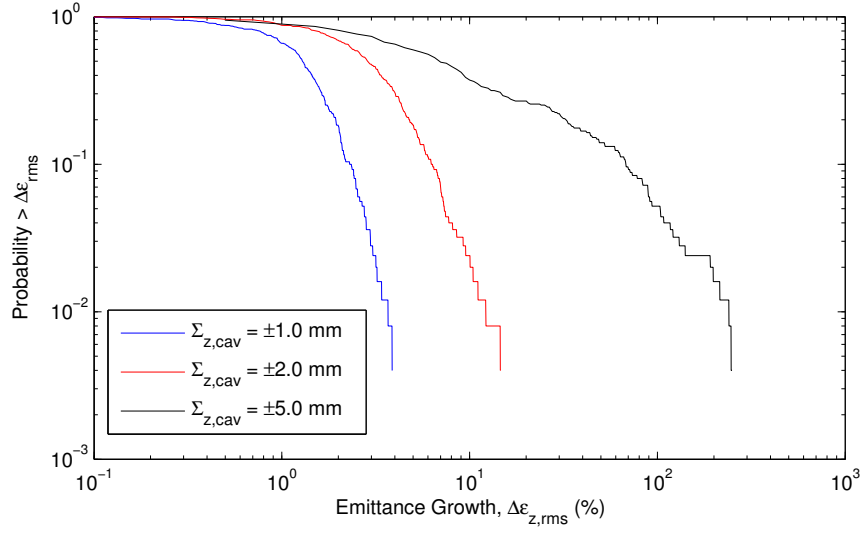
**Fig. 12.19:** The probability of emittance growth in phase 2 with longitudinal misalignment of the cavities.



(a) Uncorrected



(b) Corrected with warm steerers
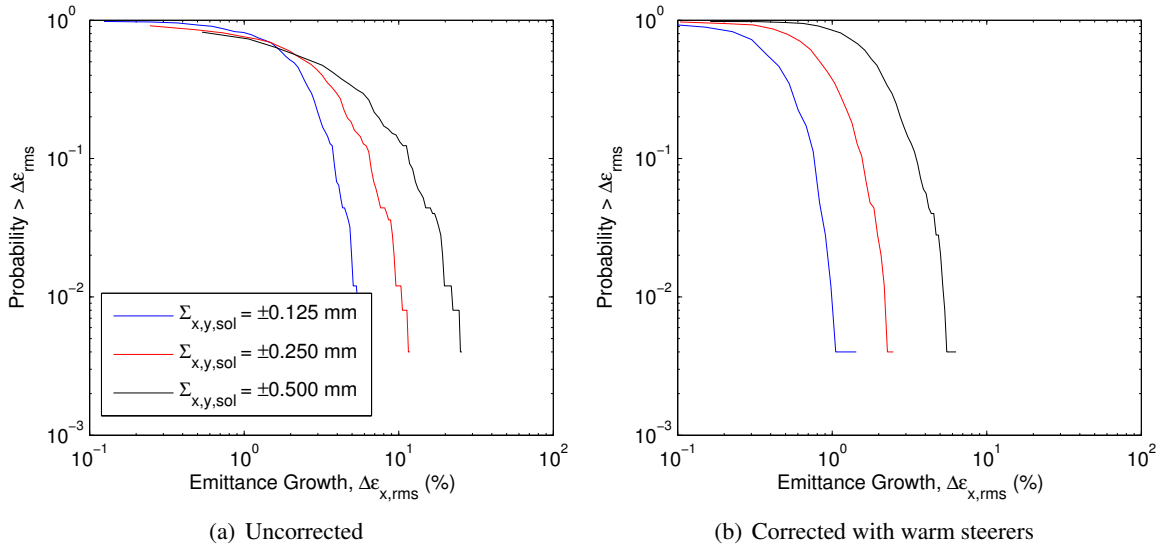
**Fig. 12.20:** The probability of emittance growth in phase 2 with transverse misalignment of the solenoids.

### *RF jitter*

The stability of the RF power sources in independently phased superconducting linacs has already been shown to be one of the most significant causes of effective longitudinal emittance growth, even in linacs with high beam currents that also experience the disruptive effects of beam-induced higher-order cavity modes [12]. The effect of fast jitter of the RF amplitude ($\sigma_{\Delta V}$) and phase ($\sigma_{\Delta \phi}$) of the cavities on the time-averaged longitudinal beam emittance was surveyed using TRACK for beams with $A/q = 2.5$ and 4.5, as shown in Figure 12.21. The plot shows the factor ($f_{\mathrm{rms}}$) by which the time-averaged rms emittance grows in the presence of jitter, i.e.,

$$f_{\mathrm{rms}} = \frac{\epsilon_{\mathrm{rms,jittered}}}{\epsilon_{\mathrm{rms,nominal}}}. \tag{12.6}$$

The effect of RF instability is strong and has most impact on beams with low $A/q$. In order to keep the time-averaged emittance growth below $50\%$ for all beams, the rms phase and amplitude stability must be

(a) Contours of $f_{\text{rms}}$, $A/q = 2.5$

(b) Contours of $f_{\text{rms}}$, $A/q = 4.5$
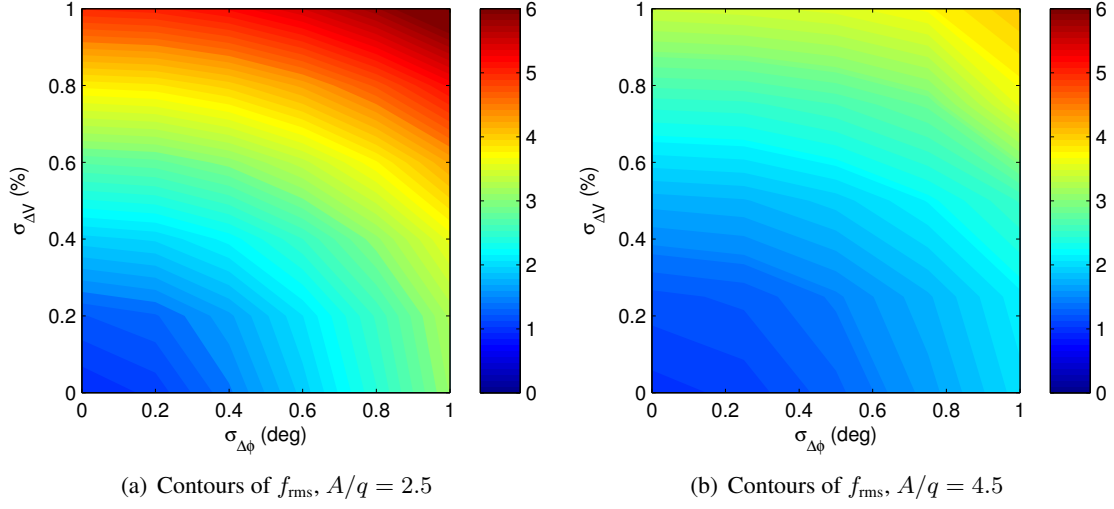
**Fig. 12.21:** The time-averaged longitudinal emittance growth factor ($f_{\text{rms}}$) at output from phase 2 as a function of the rms voltage ($\sigma_{\Delta V}$) and rms phase ($\sigma_{\Delta\phi}$) stability.

controlled to better than $0.2°$ and $0.2\%$. The evolution of the time-averaged longitudinal emittance along the linac is closely linear with cavity number as shown in Figure 12.22.
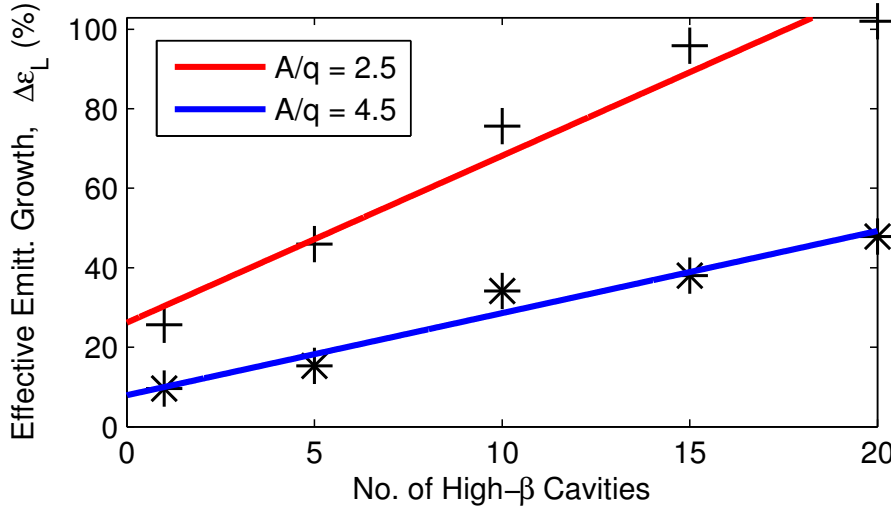


**Fig. 12.22:** The time-averaged rms longitudinal emittance growth in phase 2 as a function of cavity number for $\sigma_{\Delta\phi} = \pm0.33°$ and $\sigma_{\Delta V} = \pm0.33\%$.

### 12.9.2    Summary and end-to-end beam dynamics simulations

End-to-end simulations were carried out for the complete linac in phase 3 with all the errors discussed above also applied to the low-energy section:

– Transverse solenoid misalignment of $\pm0.15$ mm ($\pm\sigma$, truncated at $\Sigma = \pm3\sigma$).
– Transverse cavity misalignment of $\pm0.30$ mm ($\pm\sigma$, truncated at $\Sigma = \pm3\sigma$).
– RF jitter of $\pm0.2°$ and $\pm0.2\%$ ($\pm\sigma$, truncated at $\Sigma = \pm3\sigma$).

The realistic particle distribution was used with a beam of $A/q = 4.5$ after tracking it through the IHS. Over 9000 particles were simulated in each of 250 error seeds. The focusing strength in the low-energy section was relaxed to $70°$ per period and, as a consequence, the average transverse emittance growth is $10\%$ larger than if the focusing strength was kept at $90°$. The transverse emittance growth with correction using warm steerers is on average $18\%$, with just over $1\%$ rms variation in the presence of the errors simulated, see Table 12.2. The time-averaged longitudinal emittance in this scenario grows by just $22\%$. No particles were lost in any of the 250 runs, even with the orbit correction procedure turned off. A doubling of the error tolerances showed rare cases of particle losses in the absence of orbit correction.

**Table 12.2:** The rms emittance growth in end-to-end simulations of phase 3 in the presence of misalignment and RF jitter.

| $\Delta\epsilon^{\mathbf{nominal}}_{x,\mathbf{rms}} \pm \langle\Delta\epsilon_{x,\mathbf{rms}}\rangle$ [%] | $\Delta\epsilon^{\mathbf{nominal}}_{y,\mathbf{rms}} \pm \langle\Delta\epsilon_{y,\mathbf{rms}}\rangle$ [%] | $\langle\Delta\epsilon_{z,\mathbf{rms}}\rangle_{\mathbf{time\ avg.}}$ [%] |
|---|---|---|
| $15.8 \pm 1.4$ | $20.5 \pm 1.3$ | $21.6$ |

## 12.10 Summary of beam parameters

The beam parameters from realistic field `TRACK` simulations of the superconducting linac are presented here at the output of the last cryomodule at $5.9$ MeV/$u$ for phase 1, and at $0.45$ MeV/$u$ and $10$ MeV/$u$ for phase 3. The realistic particle distribution from the RFQ was used and initially either tracked through the realistic fields of the IHS or through a `LANA` model of REX with $A/q = 4.5$ and without the imperfections discussed in Section 12.9. The input parameters can be found in Tables 11.1, 11.2 and 11.3, which are consistent with a $90\%$ normalised transverse emittance of $0.3\ \pi$ mm mrad and the measured longitudinal emittance. The beam parameters at the exit to the linac are summarised in Tables 12.3, 12.4 and 12.5.

### 12.10.1 Phase 1: 5.9 MeV/$u$

The non-linearity in the longitudinal phase space, which is introduced by the 9GP, noticeably increases the energy spread of the beam at output, see Figure 12.23. The energy spread at output is $\pm 0.6\%$ ($\approx \pm\sqrt{6}\sigma$, where FWHM $\approx \sqrt{6}\sigma$). The $95\%$ longitudinal emittance is approximately $4\ \pi$ ns keV/$u$, but the normalised transverse emittance remains largely unaffected.



(a) Horizontal phase space          (b) Vertical phase space          (c) Longitudinal phase space
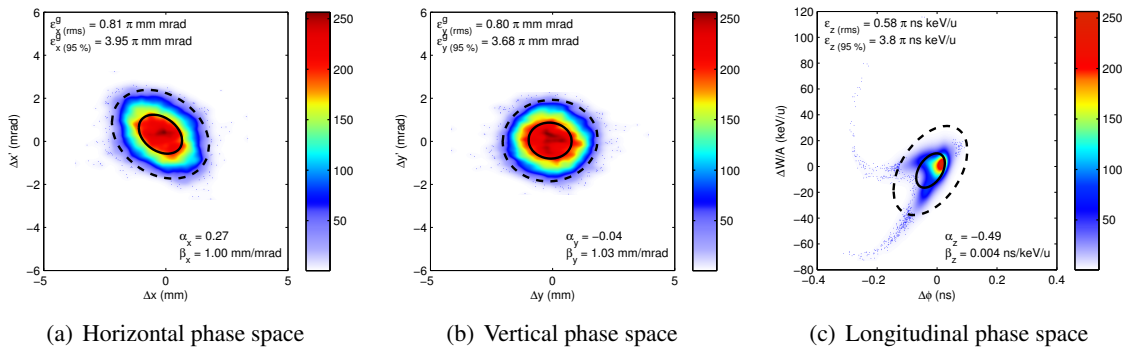
**Fig. 12.23:** Beam phase space distribution at exit to the second high-energy cryomodule in Phase 1 at $5.9$ MeV/$u$, simulated with `TRACK` ($A/q = 4.5$).

**Table 12.3:** Summary of the simulated horizontal HIE beam parameters[a].

| Phase | Simulation code | Energy [MeV/u] | $\tilde{\alpha}_x$ | $\tilde{\beta}_x$ [mm/mrad] | $\epsilon_{x\,rms}^{geom}$ [π mm mrad] | $\epsilon_{x\,95\%}^{geom}$ [π mm mrad] | $\epsilon_{x\,rms}^{norm}$ [π mm mrad] | $\epsilon_{x\,95\%}^{norm}$ [π mm mrad] |
|---|---|---|---|---|---|---|---|---|
| Phase 1 | TRACK | 5.9 | 0.27 | 1.00 | 0.81 | 3.95 | 0.09 | 0.45 |
| Phase 2 | TRACK | 10.2 | 0.30 | 1.55 | 0.60 | 3.14 | 0.09 | 0.46 |
| Phase 3 | TRACK | 0.45 | −0.32 | 0.51 | 3.40 | 20.2 | 0.11 | 0.62 |

**Table 12.4:** Summary of the simulated vertical HIE beam parameters[a].

| Phase | Simulation code | Energy [MeV/u] | $\tilde{\alpha}_y$ | $\tilde{\beta}_y$ [mm/mrad] | $\epsilon_{y\,rms}^{geom}$ [π mm mrad] | $\epsilon_{y\,95\%}^{geom}$ [π mm mrad] | $\epsilon_{y\,rms}^{norm}$ [π mm mrad] | $\epsilon_{y\,95\%}^{norm}$ [π mm mrad] |
|---|---|---|---|---|---|---|---|---|
| Phase 1 | TRACK | 5.9 | −0.04 | 1.03 | 0.80 | 3.68 | 0.09 | 0.42 |
| Phase 2 | TRACK | 10.2 | 0.00 | 1.21 | 0.60 | 3.16 | 0.09 | 0.47 |
| Phase 3 | TRACK | 0.45 | −0.37 | 0.80 | 3.56 | 19.6 | 0.11 | 0.61 |

**Table 12.5:** Summary of the simulated longitudinal HIE beam parameters[a].

| Phase | Simulation code | Energy [MeV/u] | $\tilde{\alpha}_z$ | $\tilde{\beta}_z$ [ns/(keV/u)] | $\tilde{\beta}_z$ [°/%][b] | $\epsilon_{z\,rms}$ [π ns keV/u] | $\epsilon_{z\,95\%}$ [π ns keV/u] | $\epsilon_{z\,rms}$ [π °%][b] | $\epsilon_{z\,95\%}$ [π °%][b] |
|---|---|---|---|---|---|---|---|---|---|
| Phase 1 | TRACK | 5.9 | −0.49 | 0.004 | 8.7 | 0.58 | 3.8 | 0.36 | 2.34 |
| Phase 2 | TRACK | 10.2 | 0.88 | 0.003 | 12.0 | 0.30 | 2.12 | 0.11 | 0.76 |
| Phase 3 | TRACK | 0.45 | 11.9 | 14.9 | 2450 | 0.35 | 2.60 | 2.84 | 21.1 |

[a] The input files to all the simulation codes can be found on the CERN Engineering and Equipment Data Management Service (EDMS) under the HIE-ISOLDE project.
[b] At 101.28 MHz.

### 12.10.2 Phase 2: 10.2 MeV/$u$

The installation of the low-energy superconducting section significantly reduces the tails of the longitudinal phase space distribution and the energy spread at output can be expected as $\pm 0.3\%$ ($\approx \pm\sqrt{6}\sigma$), see Figure 12.24. The $95\%$ longitudinal emittance is approximately $2\,\pi$ ns keV/$u$.



| (a) Horizontal phase space | (b) Vertical phase space | (c) Longitudinal phase space |
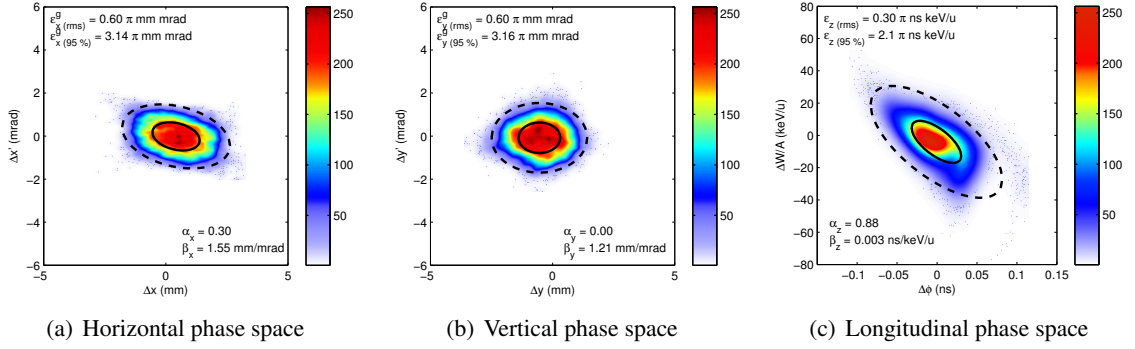
**Fig. 12.24:** Beam phase space distribution at exit to the final high-energy cryomodule in Phase 2 at 10.2 MeV/$u$, simulated with TRACK ($A/q = 4.5$).

### 12.10.3 Phase 3: 0.45 MeV/$u$

The energy spread at output will be close to $\pm 1.1\%$ ($\approx \pm\sqrt{6}\sigma$) and bunches at 101.28 MHz will have started to coalesce, see Figure 12.25. There is significant growth in the geometric transverse emittance.



| (a) Horizontal phase space | (b) Vertical phase space | (c) Longitudinal phase space |
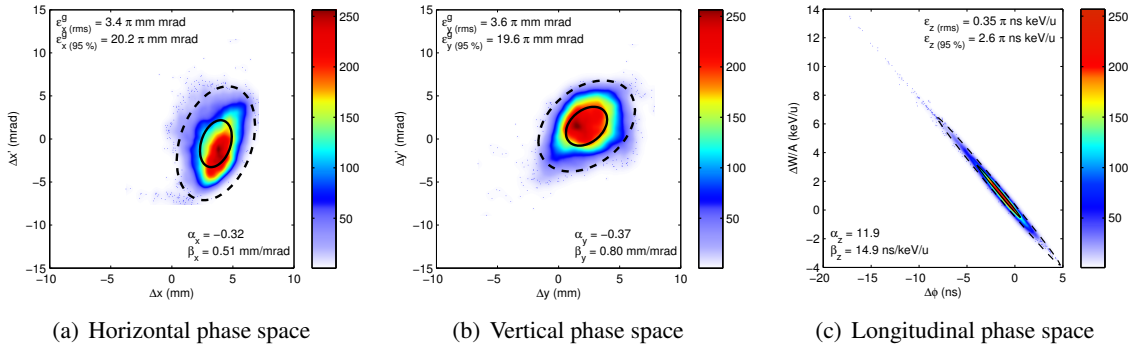
**Fig. 12.25:** Beam phase space distribution at exit to the final high-energy cryomodule in Phase 3 at 0.45 MeV/$u$, with the low-energy section phased to decelerate, simulated with TRACK ($A/q = 4.5$).

### References

[1] M. A. Fraser et al., Beam dynamics studies of the REX-ISOLDE linac in preparation for its role as injector for the HIE-ISOLDE SC linac at CERN, Proceedings of LINAC'10, Tsukuba, 2010, pp 950–952.

[2] P. N. Ostroumov and K.W. Shepard, *Phys. Rev. ST Accel. Beams* **4** (2001) 110101.

[3] P. N. Ostroumov and K. W. Shepard, Minimising transverse field effects in superconducting quarter-wave cavities, Proceedings of LINAC'02, Gyeongju, 2002, pp 473–475.

[4] M. A. Fraser, M. Pasini, A. D'Elia and R. M. Jones, Compensation of Transverse Field Asymmetry in the High-beta Quarter-wave Resonator of the HIE-ISOLDE Linac at CERN, Proceedings of SRF2009, Berlin, 2009.

[5] P. Decrock et al., *Phys. Rev. Lett.* **67** (1991) 808.

[6] M. Huyse and R. Raabe, *J. Phys. G* **38** (2011) 024001.

[7] M. A. Fraser, R. M. Jones (dir) and M. Pasini (dir), PhD thesis, Manchester U., 2012, Presented 26 Jan 2012.

[8] M. A. Fraser, R. M. Jones and M. Pasini, Beam dynamics studies for the HIE-ISOLDE linac at CERN, Proceedings of PAC'09, Vancouver, 2009, pp 3753–3755.

[9] M. Fraser and M. Pasini, Misalignment and Error Studies of the High Energy Section of the HIE-ISOLDE Linac, HIE-ISOLDE-PROJECT-Note-0006 (CERN, 2009).

[10] K. Wille, *The physics of particle accelerators: An introduction*, chapter 10.4.2, pp 281–287, Oxford University Press, Oxford, 2000.

[11] M. Pasini, R. Laxdal and A. Bandyopadhyay, Misalignment studies of the medium beta section of the ISAC-II superconducting linac, TRI-DN-03-03 (TRIUMF, 2003).

[12] M. Schuh, F. Gerigk, J. Tückmantel and C. P. Welsch, *Phys. Rev. ST Accel. Beams* **14** (2011) 051001.

# Chapter 13

# High Energy Beam Transfer (HEBT)

M.A. Fraser, B. Goddard

The network of HEBT lines was designed and installed to transport the beam accelerated by the HIE-ISOLDE linac to multiple experimental stations over a wide range of energies and mass-to-charge states. The design of the HEBT is based on modular units of doublet cells, achromatic $90°$ bends and final focusing triplets upstream of the experimental stations as shown in Figure 3.4. The requirements placed challenging demands on the dynamic range and aperture of the transfer line magnets and their power supplies, especially as it was chosen to standardise as much as possible the equipment to be procured. Nevertheless, a single type of dipole, quadrupole and steerer magnet and beam diagnostic box could be used throughout the HEBT. A detailed description of the instrumentation and transfer line magnets is given in Chapters 16 and 17, respectively.

## 13.1   Beam parameters

The beam parameters delivered by the linac vary with energy, although in all cases the beam exits the linac's solenoid focusing channel at a waist and with reasonable symmetry in the vertical and horizontal phase space planes. The transverse beam parameters damp adiabatically with increasing energy and the longitudinal beam emittance will reduce significantly on completion of the upgrade and installation of the low energy superconducting section. The energy of the beams at output from the linac depends on the experiment's request, and depending on the $A/q$ will range from between 0.3 to 17 MeV/$u$. The maximum rigidity specified for the HEBT is 2 Tm, covering the entire range deliverable from the linac. The requested beam parameters are summarised in Table 1.1 and the beam parameters used as input to design the transfer lines were presented in the previous chapter, at output from the final cryomodule, in each stage. Although the energy and time structure of the beam is very important for the experiments, a dedicated RF cavity for longitudinal manipulation of the bunch length or momentum spread was not considered as the parameters deliverable by the linac RF were deemed acceptable.

## 13.2   Beam optics

In order to match the beam from the linac into the periodic doublet structure of the HEBT, four quadrupoles are arranged in a quadruplet structure with each magnet equipped with a bi-polar power supply. Although the magnets are laminated and can pulse rapidly, the sharing of a given radioactive beam between experimental stations is not foreseen and operational set-up time is required to switch. In the long drift sections of the HEBT, two dipole magnets bend the beam to each experimental station. All the quadrupoles, even those located in the doublet channel, are powered independently to provide the required flexibility. The beam is focused into a tight spot at the experimental target by a triplet of quadrupole magnets located directly in front of the experimental setup.

An example optics calculation for the longest line, XT03, is shown in Figure 13.1. The lattice functions are matched into the periodic doublet channel, before being matched through the achromat and focused at the experimental station's target. The dispersion at the target is designed to vanish. A phase advance of $\pi/2$ results in quadrupole gradients of 11.1 Tm$^{-1}$ at 10 MeV/$u$ with a quadrupoles of an effective length of 200 mm. The gradients in certain matching quadrupoles can be twice as high as this value, and for this reason a specification of 25 Tm$^{-1}$ was made with an aperture diameter of 40 mm being acceptable for all beam energies; importance was placed on the delivery of higher energy beams

and some transmission loss may occur for the lowest rigidity beams.



(a)



(b)
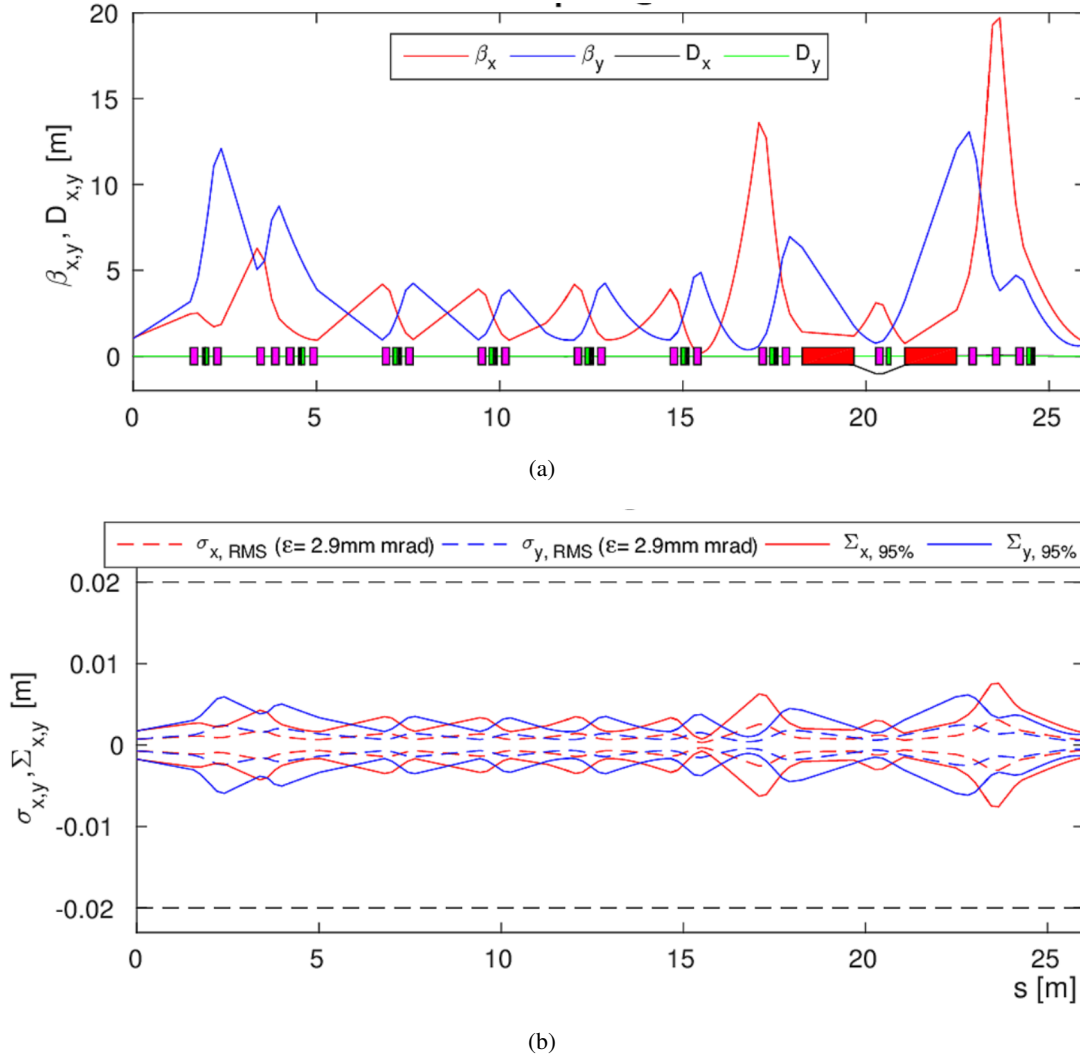
**Fig. 13.1:** Optical functions and beam sizes along XT03 of the HEBT.

## 13.3  Error studies

Once the first order design and integration was completed, error studies involving particle tracking were carried out to verify the robustness of the design to imperfections. The impact and sensitivity of the beam to magnet field errors, both static and dynamic, and alignment imperfections in the HEBT were studied in detail using MADX [1]. Standard, achievable design tolerances for the equipment were used, as outlined in Table 13.1, and simulations carried out to validate the design choices on power supply ripple, alignment tolerances, magnet field quality, instrument resolution, physical apertures and steering power. The tolerances outlined in Table 13.1 were shown to be acceptable. The piecewise orbit correction routine (threading from one diagnostic box to the next) was validated and specified in the presence of all imperfections, and orthogonal steering limits checked to ensure the beam can be steered onto the experimental targets.

Dipole power ripple is the main sources of dynamic error: accepted tolerances for $\Delta I/I$ are of the order $10^{-4}$ at 5.9 MeV/$u$ (and higher energies) and of the order $10^{-3}$ at 0.3 MeV/$u$. At 0.3 MeV/$u$ dynamic errors introduce a dilution to the horizontal spot size at the target of $\sigma = 0.3$ mm.

**Table 13.1:** Accepted tolerances for static error sources.

| Error Source | Value | Distribution |
|---|---|---|
| Dipole field, $\Delta Bdl/Bdl$ | $1.0 \cdot 10^{-3}$ | uniform |
| Roll angle $d\psi$, rad | $2.0 \cdot 10^{-4}$ | uniform |
| Longitudinal position dS, m | $1.0 \cdot 10^{-3}$ | uniform |
| Quadrupole field, $\Delta K/K$ | $1.0 \cdot 10^{-3}$ | uniform |
| Shift dX, dY, m | $2.5 \cdot 10^{-4}$ | Gauss($\sigma$) |
| Initial conditions dX, dY, m | $5.0 \cdot 10^{-4}$ | Gauss($\sigma$) |
| dpx, dpy, mrad | $5.0 \cdot 10^{-4}$ | Gauss($\sigma$) |
| Monitor shift dX, dY, m | $2.5 \cdot 10^{-4}$ | Gauss($\sigma$) |
| Resolution X, Y, m | $2.0 \cdot 10^{-4}$ | uniform |

## 13.4   Impact of stray fields

In some cases, the users' experimental apparatus proposed for physics at HIE-ISOLDE will introduce significant levels of stray magnetic field into the experimental hall and surrounding beam lines. A first analytic study placed a conservative stray field limit of 5 G at the beam lines [2] before a detailed study validated a realistic stray field of the ISS [3] magnet, which was computed using the real magnet geometry in a 3D electromagnetic field solver code. The effect on the beam transport of ISS was shown to be negligible at most beam rigidities. A small perturbation is expected for low energy and can be controlled by procedure, e.g. ensuring no change of the ISS magnet status during low energy beam operation. The stray field will be further reduced with the installation of shielding around the ISS magnet.

## References

[1] A. Parfenova et al., HIE-ISOLDE HEBT beam optics studies with MADX, ACC-NOTE-2014-0021 (CERN, 2014).

[2] M. A. Fraser, Limits for Stray Magnetic Fields of Experiments at HIE-ISOLDE, EDMS 1289865 (CERN, 2015).

[3] J. Mertens et al., Beam dynamics studies of the hie-isolde transfer lines in the presence of magnetic stray fields, Proceedings of IPAC2017, Copenhagen, 2017, pp 768–770.

# Chapter 14

# Design Study for 10 MHz beams: increased bunch spacing

M.A. FRASER

A comprehensive beam dynamics study was carried out to assess the performance of a proposed bunching system to increase the bunch spacing of post-accelerated radioactive ion beams by a factor of 10 to approximately 100 ns. Different layout options were assessed and their relative performance compared, each based on a multi-harmonic buncher (MHB) with a fundamental sub-harmonic frequency of 10.128 MHz placed upstream of the REX-ISOLDE RFQ.

## 14.1 Pre-RFQ bunching

A single-gap, grid-less MHB similar to those employed at ANL and TRIUMF was studied to avoid the transmission losses ($\sim 20\,\%$) associated with gridded bunchers that are unacceptable for the acceleration of rare RIBs. The feasibility of the MHB-RFQ bunching system at HIE-ISOLDE has been validated with an MHB mixing the first four harmonics of 10.128 MHz. The transmission and rms longitudinal emittance is shown in Figure 14.1 as a function of the upstream distance ($L$) of the MHB and the effective voltage ($V_0$) of its first harmonic. The iso-contour lines of transmission in Figure 14.1(a) indicate that the optimum focal point of the buncher is located 29 cm inside the RFQ at the position on the electrodes where the adiabatic bunching section starts. The longitudinal emittance delivered by the RFQ can be significantly reduced as the drift distance between the RFQ and MHB is increased. Transmissions of up to $\sim 80\,\%$ can be expected with $\sim 15\,\%$ of the beam spilling out of the main bunch and populating the nine 101.28 MHz satellite bunches. A chopper structure after the RFQ will be required to meet the specification made by the experiments on the population of satellite bunches.[1]



(a) Transmission [%] after RFQ.

(b) Longitudinal emittance: ratio with dc injection, $\epsilon_{MHB}^{rms}/\epsilon_{dc}^{rms}$.
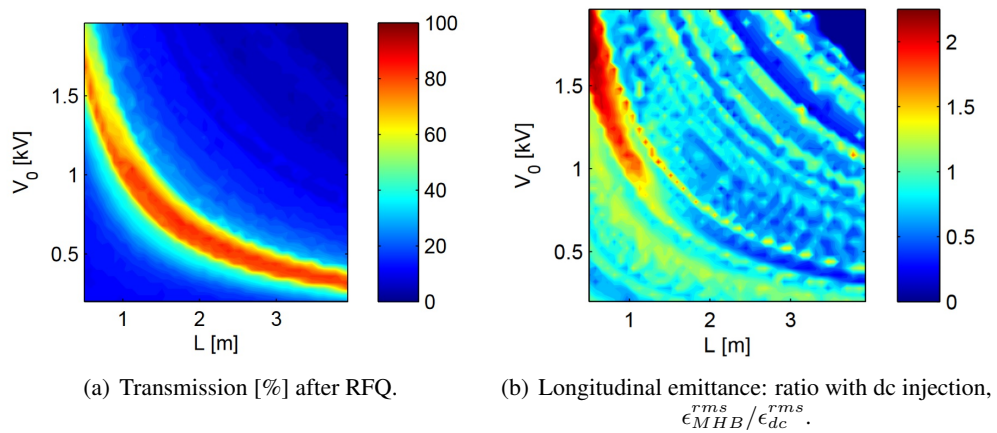
**Fig. 14.1:** Survey of $L$ and $V_0$ for a four-harmonic MHB.

---

[1] In principle, chopping could also take place before the RFQ. However, this was discounted because of the need to 'grid' the chopper plates and the concomitant loss of transmission; the aperture is far larger than the permitted longitudinal extent of the chopper fields, which must be $\ll \beta\lambda_{\mathrm{MHB}} = 97\,\mathrm{mm}$.

## 14.2 MHB optimisation studies

The main design considerations for the MHB involve maximising the transit-time efficiency from each harmonic component whilst minimising the coupling between the transverse and longitudinal motions, which drives emittance dilution. The transit-time efficiency (on-axis) for any given harmonic of the fundamental frequency $\lambda_0$ can then be expressed,

$$T_n(\beta) = \frac{\sin \frac{\pi g}{\beta \lambda_n}}{\frac{\pi g}{\beta \lambda_n}}, \qquad \text{where} \qquad \lambda_n = \lambda_0/n. \tag{14.1}$$

Thereby, the efficiency of a single-gap buncher drops rapidly close to the first zero of the sinc $\frac{n\pi g}{\beta \lambda_0}$ function where $g$ is the gap length, i.e. when $\frac{g}{\beta \lambda_0} = \frac{1}{n}$, shown in Figure 14.2 for the first 4 harmonics. It can thus be stated that for efficient bunching with a single-gap MHB mixing $n$ harmonic components,

$$g \ll \frac{\beta \lambda_0}{n}. \tag{14.2}$$



(a) $T_n$ with normalised $g$.

(b) $T_n$ with $g$.
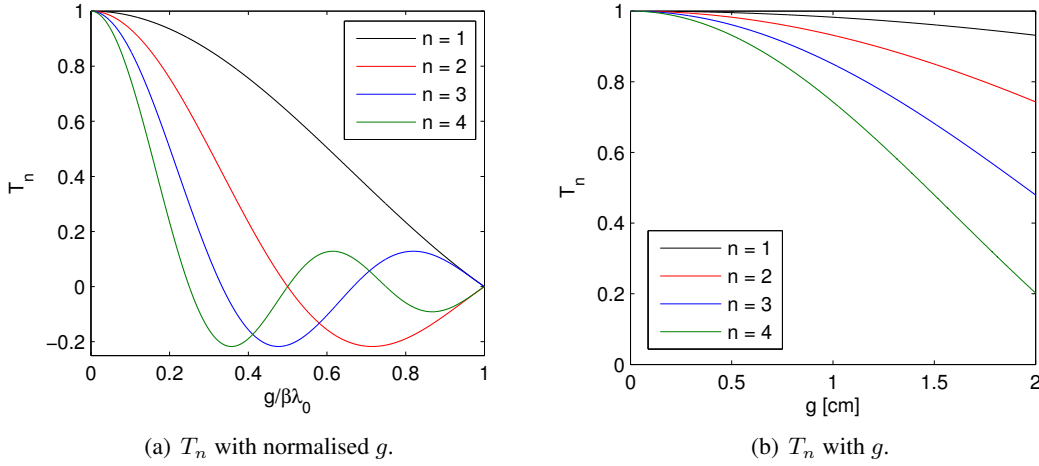
**Fig. 14.2:** Transit-time efficiency with a simplified field shape as a function of gap size $g$ and the harmonic component $n$ for HIE-ISOLDE parameters: $\beta = 0.00328$ and $\lambda_0 = 10.128$ MHz.

The injection energy per nucleon for the REX-ISOLDE RFQ is 5 keV/$u$, which corresponds to $\beta = 0.00328$; for $\lambda_0 = 10.128$ MHz and for $n = 4$ the gap length must be $g \ll 2.4$ cm. One cannot keep adding harmonics as the gap would become impractically small for efficient transfer of energy to the beam. Fortunately, it is the lowest-order harmonic components that are needed to transfer the most energy to the beam and one can truncate the number of harmonics in the system to 3 or 4 with little impact on the bunching efficiency.

In reality, the aperture needed to allow the passage of the beam causes the field to leak into the drift tubes; the effective gap length $g_{\text{eff}}$ increases and the transit time function develops a radial dependence. The single-gap MHB drift-tube geometry should be designed such that (i) the aperture is minimised but specified by transverse beam size, (ii) the gap length is minimised such that $T_n$ is optimised but the axial dependence of $T_n$ is not too strong and (iii) the beam size extends no further than $\sim 0.25R$ to minimise the effect of the radial variation of $T_n$.

A single-gap buncher was studied in detail, consisting of two drift-tubes driven in 'push-pull' mode, i.e. $-V/2$ and $+V/2$, housed inside a grounded vacuum chamber, as shown in Figure. 14.3 rendered using the numerical 3D electromagnetic field solver code CST EM Studio®. The bunching field

should leak to ground over a distance $\sim \beta\lambda$ such that the energy gain experienced by the beam outside of the drift-tubes is somewhat 'averaged-out' to zero. The vacuum chamber of such a buncher then has typical dimension of $\sim 2\beta\lambda_0 \approx 20\,\text{cm}$ in the HIE-ISOLDE case. More compact structures can be realised with double-gap bunchers but one has to be much more careful with the phase variation of the voltage signal delivered to the drift-tube in order to avoid cancellation of the bunching effect for certain harmonics.
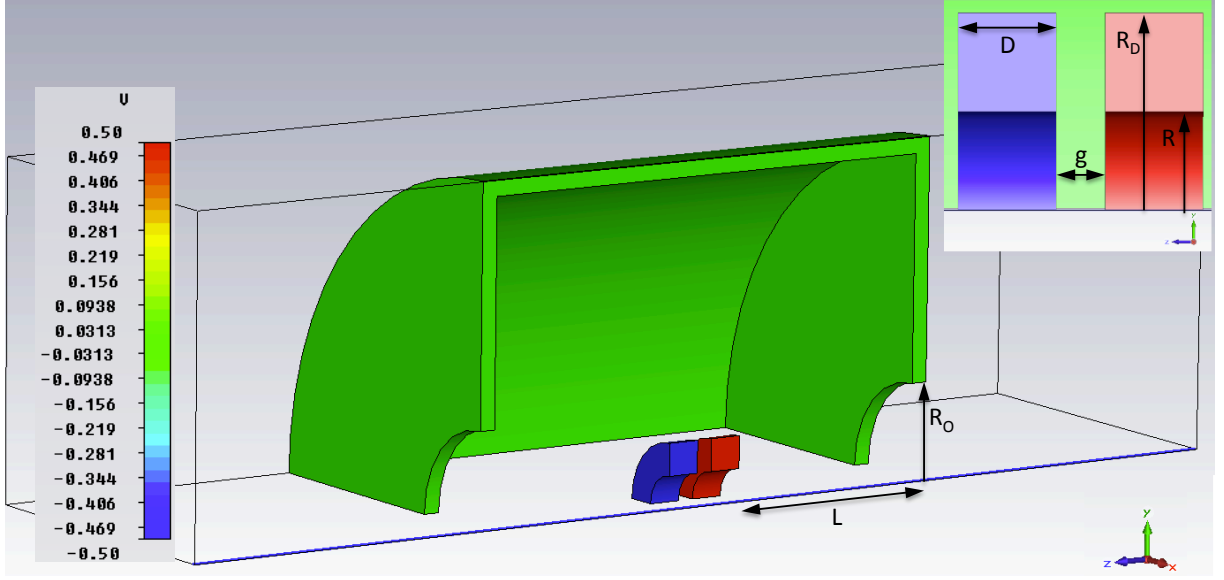


**Fig. 14.3:** MHB geometry modelled in CST EM Studio® ($V = 1\,\text{V}$).

For the optimised structure, the bunching field leaks to ground over a distance $\sim \beta\lambda_0 = 97\,\text{mm}$ outside of the drift-tubes, as shown in Figure 14.4(a), and the field profile resembles that of a three-gap buncher. Indeed, the transit-time factor has the characteristic shape of a short multi-gap accelerating structure, as shown in Figure 14.4(b).



(a) $E_z(r, z)$, $V = 1\,\text{V}$.

(b) $T(\beta\lambda_n)$ on and off-axis.
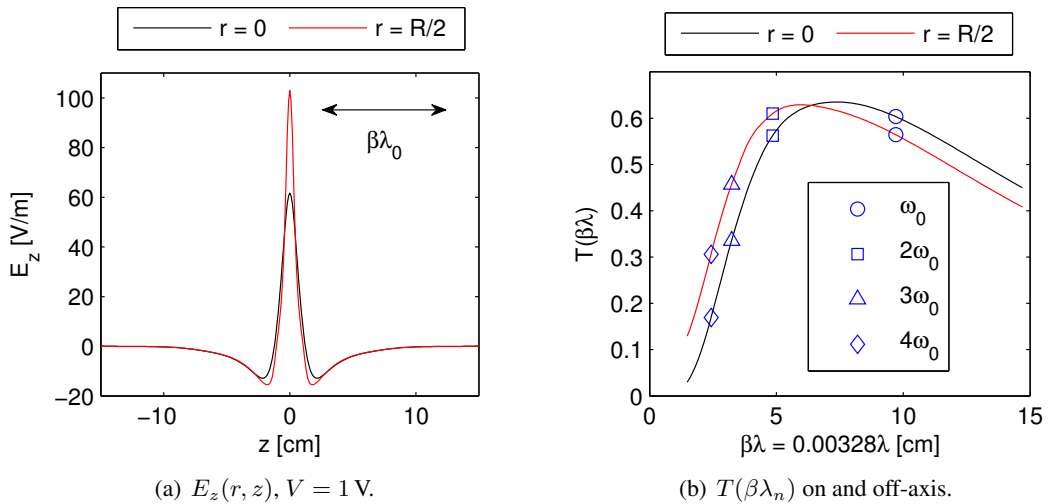
**Fig. 14.4:** Transit-time factor $T(r, \beta\lambda_n)$ for the optimised MHB.

Systematic parameter sweeps of the important geometric parameters of the drift tubes were undertaken and the transit-time factors for each harmonic component calculated numerically from the com-

puted field profiles $E_z(r, z)$,

$$T_n(r, \beta) = \frac{\int_{-\infty}^{\infty} E_z(r, z) \cos \frac{2\pi z}{\beta \lambda_n} \, dz}{\int_{-\infty}^{\infty} |E_z(r, z)| \, dz}. \tag{14.3}$$

The geometry of the drift-tubes was optimised over four harmonic components to minimise the power dissipated,

$$P \propto \frac{1}{\tau_0} \int_{-\tau_0/2}^{+\tau_0/2} V^2(\tau) \, d\tau, \tag{14.4}$$

where the potential difference between the drift-tubes is given by,

$$V(\tau) = \frac{V_{\text{eff}}(\tau)}{T} = V_0 \left( \frac{\sin \omega_0 \tau}{T_1} - \frac{0.428 \sin 2\omega_0 \tau}{T_2} + \frac{0.215 \sin 3\omega_0 \tau}{T_3} - \frac{0.101 \sin 4\omega_0 \tau}{T_4} \right), \tag{14.5}$$

and $V > V_{\text{eff}}$ because of the transit-time effects.[2] If the structure had a perfect transit-time efficiency then the figure of merit $P$ would equal unity, i.e. $P = P_0 = 1$. Therefore, the figure of merit compares the power dissipated with an ideal structure. The use of this figure of merit assumes that the RF impedance of the structure does not change significantly over the frequency range in question. The 3D field map of the MHB was computed around the beam axis of the structure with a 1 mm mesh density totalling $21 \cdot 21 \cdot 301$ points. Particles were tracked through the field map to study the dynamics of the structure specified in Table 14.1. The tracking was benchmarked with the TRACK code [1]. More details on the parametric optimisation studies of the MHB electrode geometry can be found in [2].

**Table 14.1:** HIE-ISOLDE MHB dimensions.

| Parameter | Value |
|---|---|
| Drift-tube aperture (inner diameter), $2R$ [mm] | 20 |
| Drift-tube length, $D$ [mm] | 10 |
| Drift-tube outer diameter, $2R_D$ [mm] | 40 |
| Gap length, $g$ [mm] | 5 |
| Vacuum tank length, $2L$ [mm] | 250 |
| Aperture in vacuum tank, $2R_T$ [mm] | 60 |

## 14.3 Beam dynamics studies

In order to characterise the beam dynamics in the Low Energy Beam Transfer (LEBT) line between the REXEBIS and RFQ, the entire system was simulated by tracking particles through the 3D field maps of each active component, including the RFQ [2], using the TRACK code [3]. The tracking simulations were matched using a COSY-∞ model [4] that incorporated fringe field effects and a benchmarking of the two codes showed that Taylor maps computed to third-order were adequate to describe the non-linear transverse beam dynamics [5]. TRACK was required for a complete understanding of the non-linear longitudinal dynamics in the LEBT and RFQ. The results of the study are summarised in Table 14.2 and in sections 14.3.5, 14.3.6 and 14.3.7; the different layouts are shown in Figure 14.6. The transmission and time structure of the bunch train is shown in Figure 14.5.

The study identified geometric aberrations induced by the existing electrostatic quadrupoles before the RFQ as a source of emittance growth. This motivated the design of a new LEBT employing solenoids, which is more tolerant to the increase in energy spread introduced by the MHB because the beam size

---

[2]One can show that $P \propto \frac{1}{\tau_0} \int_{-\tau_0/2}^{+\tau_0/2} V^2(\tau) \, d\tau \propto \frac{V_0^2}{2} \left( \frac{1}{T_1^2} + \frac{0.43^2}{T_2^2} + \frac{0.21^2}{T_3^2} + \frac{0.10^2}{T_4^2} \right)$.
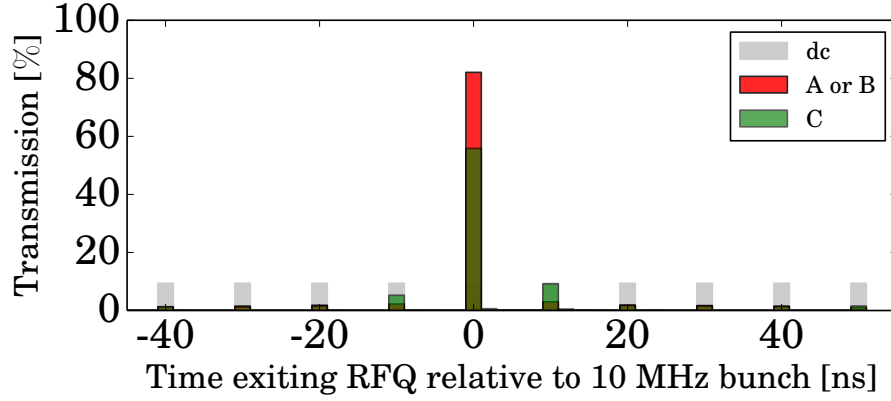
**Fig. 14.5:** Bunch intensity distribution at the RFQ exit. Results for options A and B are similar and plotted together.

can be kept compact in both orthogonal phase space planes. In addition, this helps to minimise the non-isochronous effects that introduce phase-lagging and cause the bunch length to increase at the focal point inside the RFQ.

The MHB can also improve beam purity by time-of-flight filtering of nearby $A/q$ contaminants into the satellite bunches, which are chopped and thus removed from the bunch train [6].

### 14.3.1   Option A

Option A provides a relatively simple integration solution with the MHB placed directly before the RFQ. However, large voltages must be applied to the electrostatic triplet to realise a beam waist in the MHB and as a result geometric aberrations cause transverse emittance growth. The beam size in the triplet is large because of the tight waist made at the mass selection slit in the upstream diagnostic box directly after the separator. The beam dynamics is summarised in sub-Chapter 14.3.5. This option is flexible should the MHB need moving closer to the RFQ, as demonstrated by Option C.

### 14.3.2   Option B

The large drift distance between the MHB and RFQ in option B provides a solution that offers a significant reduction of the longitudinal emittance. The MHB is placed at a position on the beam line after the ion source that will require careful integration into a crowded region. The $A/q$-separator is not completely achromatic and as a consequence a small amount of transverse emittance growth occurs in the vertical plane where the dispersion function is non-zero downstream. Nonetheless, the emittance growth is less than that induced by the aberrations of option A. In addition, the time-of-flight filtering by the bunching system would increase the resolution of the existing mass separator by a factor of $\sim 3$. The beam dynamics is summarised in sub-Chapter 14.3.6.

### 14.3.3   Option C

An increased beam energy spread is expected from a proposed upgrade of the REXEBIS [7] will affect the bunching efficiency. In this scenario the only reasonable solution is to place the MHB closer to the RFQ. The effect of a large (order of magnitude) increase in the beam energy spread from the ion source was simulated with the MHB located just 0.9 m before the RFQ. The results are collected as option C in Table 14.2. An increased beam energy spread from the EBIS limits the performance of the system. The beam dynamics is summarised in sub-Chapter 14.3.7.

### 14.3.4 Performance without chopper or final phase of upgrade

It should be emphasised that a reasonable bunching performance and reduction of longitudinal emittance can be achieved even without the final stage of the linac upgrade being completed, i.e. without extension of the linac and without chopper. Full details of the performance and layout options can be found in [8].
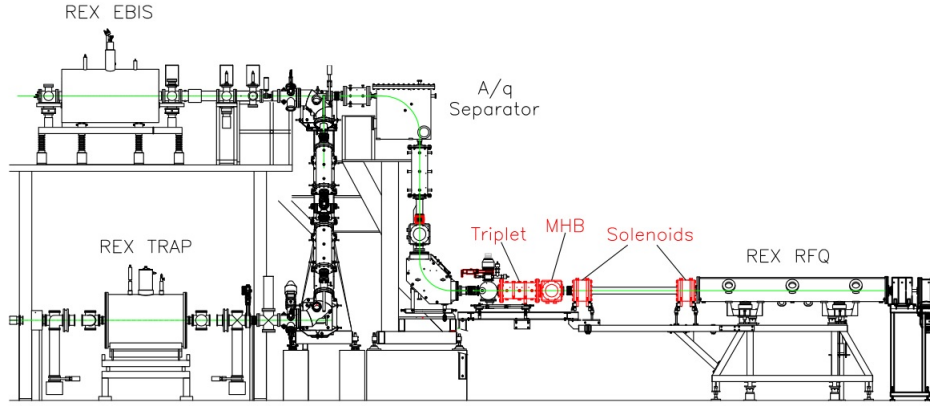


(a) Option A: MHB placed after the REX $A/q$-separator.
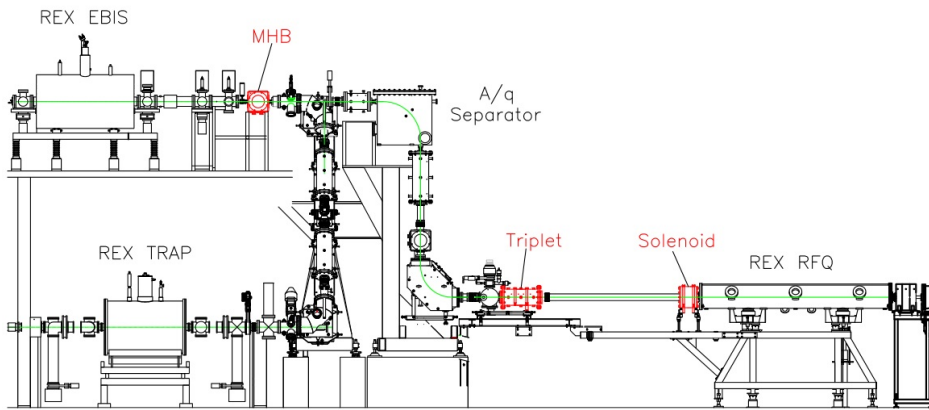


(b) Option B: MHB placed before the REX $A/q$-separator.
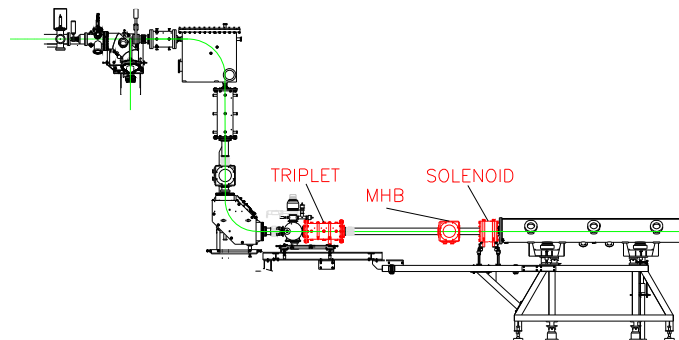


(c) Option C: MHB placed close to RFQ, triplet and solenoid installed.

**Fig. 14.6:** Pre-buncher layout options: new components highlighted in red.

**Table 14.2:** Summary of the simulated beam dynamics performance of the different MHB layout options.

| Upgrade Option | MHB Status | $V_0$ [a] [V] | L [m] | $\frac{\Delta A/q}{A/q}$ | $\Delta\phi$ [b] [deg] | $\frac{\Delta W}{W}$ source [%] | $T_{\text{total}}$ [%] | $T_{\text{10 MHz}}$ [%] | $T_{\text{sat}}$ [%] | $\epsilon_x$ rms, $\epsilon_y$ rms [mm mrad] | $\epsilon_z$ rms [ns keV/u] |
|---|---|---|---|---|---|---|---|---|---|---|---|
| A | ON | 465 | 2.32 | $\sim \frac{1}{150}$ | $-30$ | 0.1 | 98.6 | 82.4 | 16.2 | 0.93, 0.72 | 0.15 |
|   | OFF | 0 | - | - | - | 0.1 | 94.3 | - | - | 0.95, 0.74 | 0.26 |
| B | ON | 175 | 9.49 | $\sim \frac{1}{500}$ | $-70$ | 0.1 | 98.5 | 83.2 | 15.3 | 0.70, 0.79 | 0.08 |
|   | OFF | 0 | - | - | - | 0.1 | 93.9 | - | - | 0.60, 0.63 | 0.27 |
| C | ON | 1150 | 0.87 | - | $-30$ | 1.0 | 76.9 | 54.2 | 22.7 | 0.74, 0.76 | 0.59 |
|   | OFF | 0 | - | - | - | 1.0 | 93.4 | - | - | 0.72, 0.78 | 0.27 |

[a] The effective voltage experienced by the beam: $V_{eff} = V_0(sin\omega_0 t - 0.43sin2\omega_0 t + 0.21sin3\omega_0 t - 0.10sin4\omega_0 t)$.
[b] RFQ phase shift relative to MHB at 101.28 MHz to compensate for the phase-lagging of non-isochronous particles.

### 14.3.5   Beam dynamics summary for option A
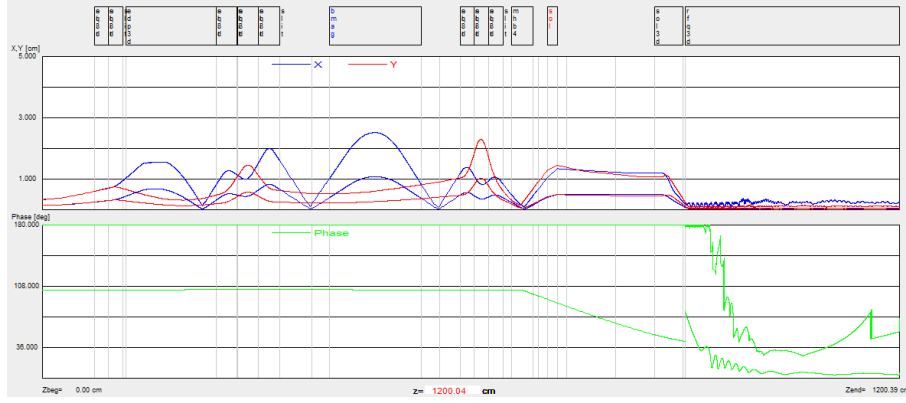


**Fig. 14.7:** Stage 3: option A, TRACK envelopes from REXEBIS to RFQ exit.



(a) Horizontal phase space.  (b) Vertical phase space.  (c) Longitudinal phase space.
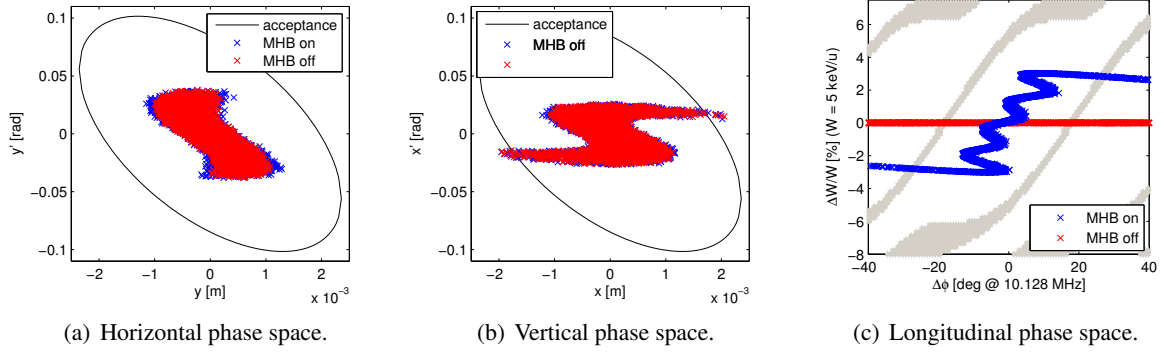
**Fig. 14.8:** Stage 3: option A, phase space at RFQ entrance.



(a) Horizontal phase space.  (b) Vertical phase space.  (c) Longitudinal phase space.
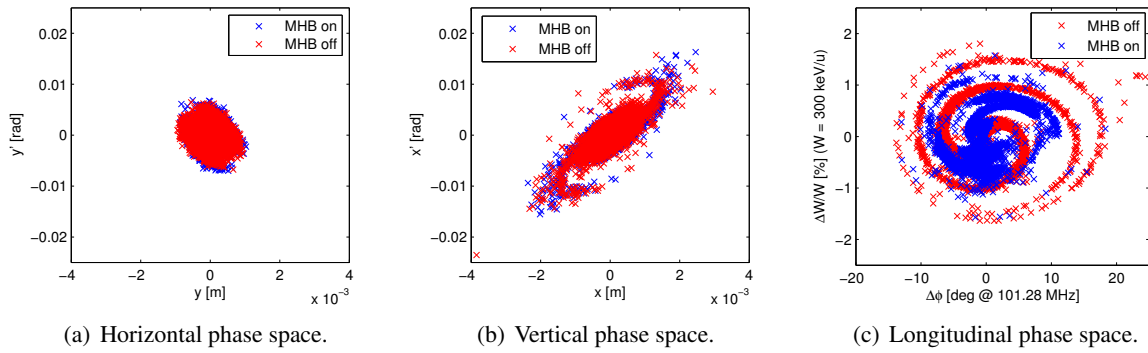
**Fig. 14.9:** Stage 3: option A, phase space at RFQ exit.

### 14.3.6 Beam dynamics summary for option B
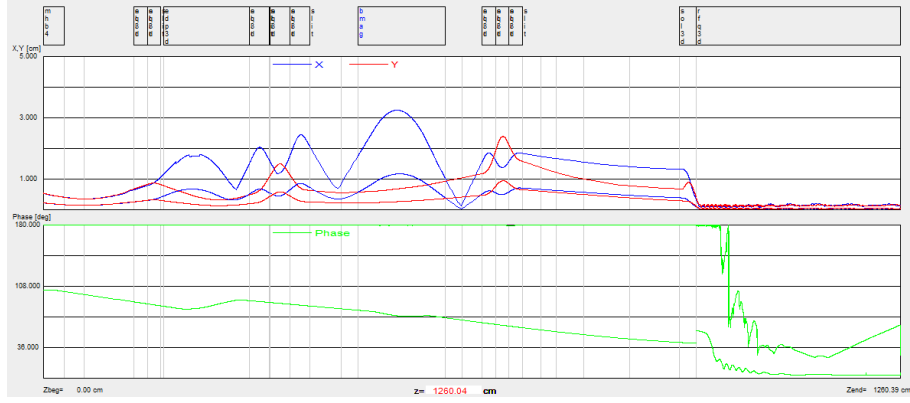


**Fig. 14.10:** Stage 3: option B, TRACK envelopes from REXEBIS to RFQ exit.



(a) Horizontal phase space.

(b) Vertical phase space.

(c) Longitudinal phase space.
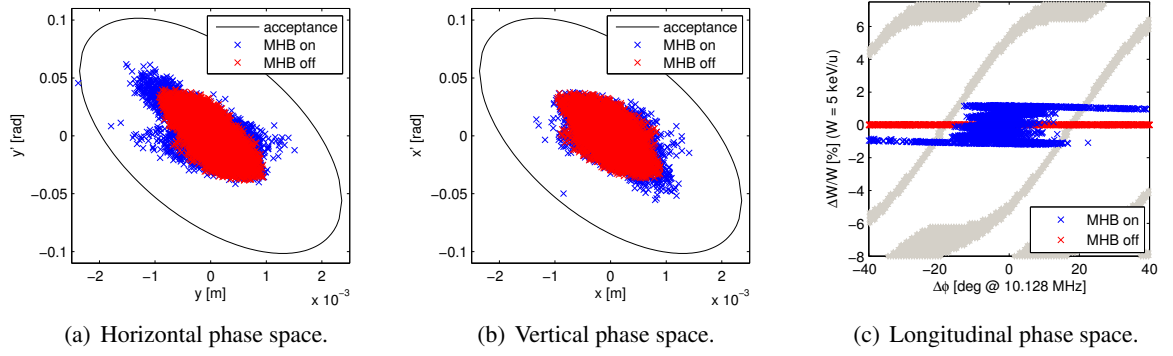
**Fig. 14.11:** Stage 3: option B, phase space at RFQ entrance.



(a) Horizontal phase space.

(b) Vertical phase space.

(c) Longitudinal phase space.
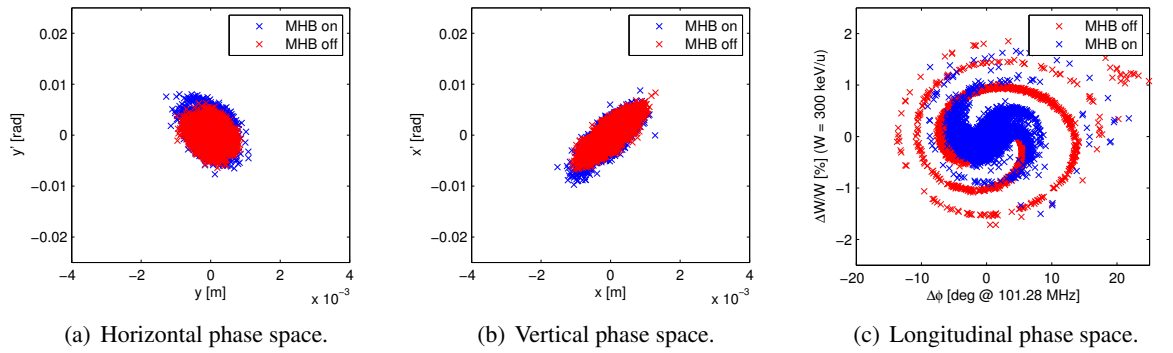
**Fig. 14.12:** Stage 3: option B, phase space at RFQ exit.

### 14.3.7 Beam dynamics summary for option C
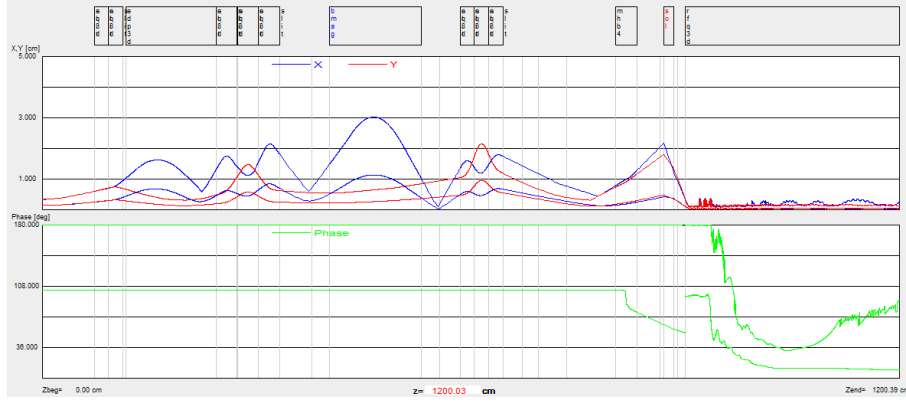


**Fig. 14.13:** Stage 3: option C, TRACK envelopes from REXEBIS to RFQ exit.



(a) Horizontal phase space.

(b) Vertical phase space.

(c) Longitudinal phase space.
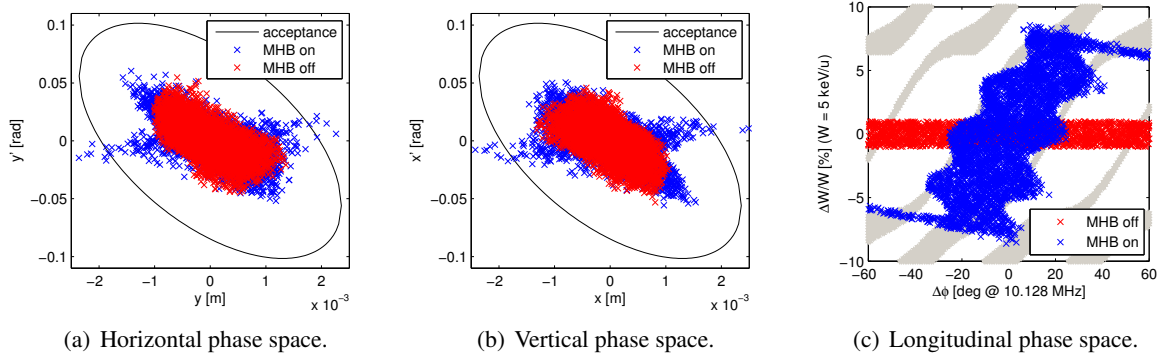
**Fig. 14.14:** Stage 3: option C, phase space at RFQ entrance.



(a) Horizontal phase space.

(b) Vertical phase space.

(c) Longitudinal phase space.
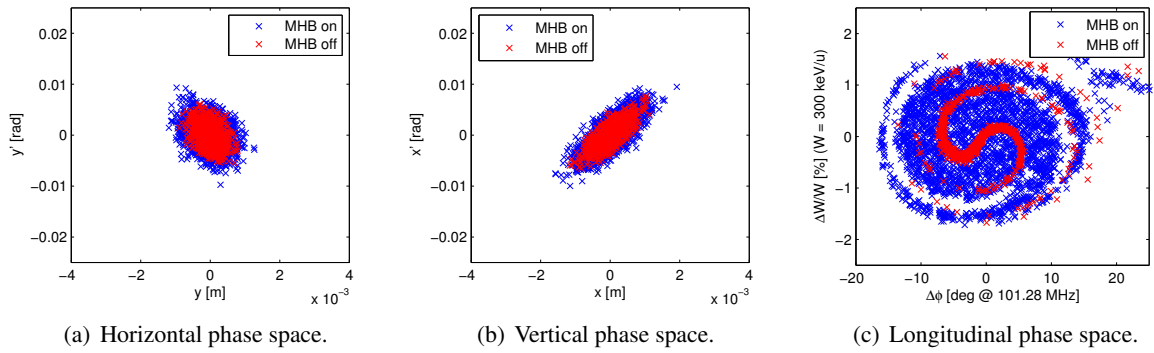
**Fig. 14.15:** Stage 3: option C, phase space at RFQ exit.

## 14.4 Post-RFQ chopping

The feasibility of cleanly removing the satellite bunches from the bunch train with a travelling-wave type chopper placed after the RFQ was demonstrated using a quasi-static model comprising a chain of synchronised capacitors pulsed at high-voltage [9]. The travelling-wave option was preferred over a two-frequency resonant chopper, e.g. the ISAC system at TRIUMF [10], because the proximity of the satellite bunches ($\beta\lambda_{\mathrm{RFQ}} = 75$ mm) demands shorter electrodes, and consequently larger voltages, to avoid significantly perturbing the main 10.128 MHz bunches. The power requirements of the structure are less of a concern because of the duty factor ($< 10\,\%$) of the injector. In addition, the travelling-wave chopper can be programmed to remove an arbitrary number of 10.128 MHz pulses to extend even further the dead-time. A classic chopper line design, shown in Figure 14.16 is employed in the Medium Energy Beam Transfer (MEBT) line [11] demanding 4 mrad of deflection from the chopper, which can be kept shorter than 0.5 m with a voltage of 1.2 kV.
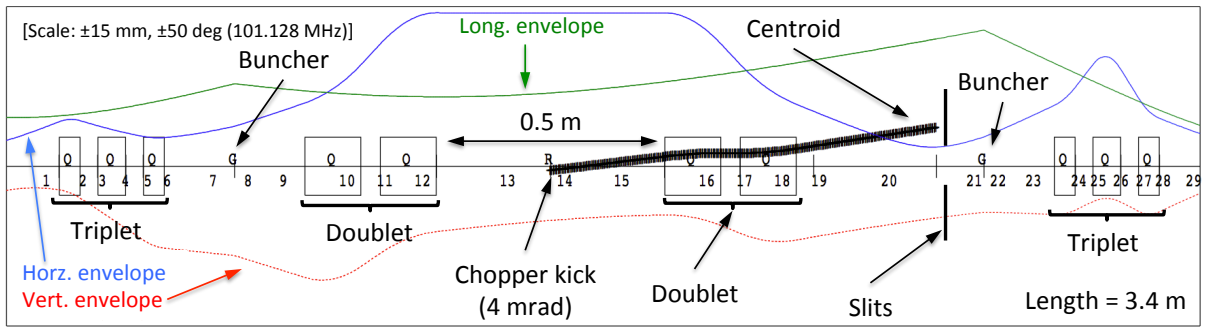


**Fig. 14.16:** MEBT optics design, $\epsilon_t^{\mathrm{n}} = 0.66$ mm mrad.

The MEBT maintains the acceptance of the machine whilst the predicted transverse emittance growth is negligible provided the rise/fall time of the chopper is $< 5$ ns. The specification of the chopper is similar to the double meander strip-line chopper developed at CERN for Linac4 [12]. Although the chopper would require scaling to match the beam velocity after the REX RFQ ($\beta = 0.0254$), the demands on the power amplifiers in terms of burst repetition rate ($< 50$ Hz), burst length ($< 2$ ms), pulse rise/fall time ($< 5$ ns), pulse length ($\sim 90$ ns) and voltage ($\pm 0.6$ kV) are also similar.

## References

[1] V. N. Aseev, P. N. Ostroumov, E. S. Lessner and B. Mustapha, TRACK: The new beam dynamics code, Proceedings of PAC'05, Knoxville, 2005, pp 2053–2055.

[2] M. A. Fraser and R. Calaga, REX-ISOLDE RFQ Beam Dynamics Studies using CST EM Studio, CERN-ACC-NOTE-2014-0015 (CERN, 2014).

[3] TRACK, http://www.phy.anl.gov/atlas/TRACK.

[4] COSY INFINITY, http://bt.pa.msu.edu/cosy.

[5] M. A. Fraser, D. Voulot and F. Wenander, Beam Dynamics Simulations of the REX-ISOLDE A/q-separator, CERN-ACC-NOTE-2014-0017 (CERN, 2014).

[6] M. Marchetto, Progress and plans for high mass beam delivery at TRIUMF, Proceedings of HIAT'12, Chicago, 2012, pp 33–39.

[7] A. Shornikov, A. Pikin, R. Scrivens and F. Wenander, *Nucl. Instrum. Methods Phys. Res. B* **317** (2013) 395.

[8] M. A. Fraser, CERN-HIE-ISOLDE-PROJECT-Note-0035 (CERN), to be published.

[9] A. Mukhopadhyay et al., Investigating the Feasibility of a Travelling-wave Chopper for the Clean Separation of 10 MHz Bunches at HIE-ISOLDE, CERN-ACC-NOTE-2014-0016 (CERN, 2014).

[10] R. E. Laxdal, ISAC-I and ISAC-II at TRIUMF: Achieved Performance and New Construction, Proceedings LINAC'02, Gyeongju, 2002.

[11] M. A. Fraser, R. Calaga and I. B. Magdau, Design Study for 10 MHz Beam Frequency of Post-accelerated RIBs at HIE-ISOLDE, Proceedings of IPAC2013, Shanghai, 2013, p 3933.

[12] M. Paoluzzi, F. Caspers and T. Kroyer, CERN Chopper final report, CERN-AB-Note-2008-040-RF. CARE-Report-2008-020-HIPPI (CERN, 2008).

# Part IV

# General Services and Systems

# Chapter 15

# Radiofrequency

D. VALUCH, M. ELIAS

## 15.1 Accelerating field quality and cavity RF power requirement

The impact of the accelerating field quality to the beam quality, mainly the longitudinal emittance growth, has been thoroughly studied in [1]. In order to keep emittance growth below 50% in the time-averaged emittance for $A/q = 2.5$, the maximal uncorrelated noise of the accelerating field in each cavity should be below 0.2% rms in amplitude and 0.2 degrees rms in phase [1]. The accelerating field quality is controlled by the Low Level RF system (LLRF).

The aforementioned constraints are relatively comfortable to be achieved by a modern digital LLRF system. The quarter-wave resonator (cavity) design parameters relevant to the required RF generator power need are summarised in the Table 15.1.

**Table 15.1:** HIE-ISOLDE cavity parameters relevant to the RF system design [2].

| Parameter | Value | Unit |
|---|---|---|
| Frequency | 101.28 | MHz |
| Accelerating field | 6 | MV/m |
| Gap length | 300 | mm |
| $\frac{R}{Q}$ | 554 | Ohm |
| Gap voltage V | 1.8 | MV |
| Typical beam current | $\sim 100$ | pA |
| Cavity $Q_0$ at operating field | $6.6 \cdot 10^8$ | - |

As beam loading is negligible in the case of the HIE-ISOLDE machine, the accelerating structures can be run at relatively high values of the external $Q$. The upper limit is imposed only by ability to control the resonator by the LLRF system. High-$Q_{ext}$ operation allows for a very low RF power need. Table 15.2 summarises static RF power required to obtain an accelerating gradient of 6 MV/m in a cavity which is at resonance and in absence of external perturbations (e.g. vibrations, microphonics etc.).

Considering the expected microphonics level, Lorentz force detuning sensitivity and the mechanical tuner resolution, the preferred operating bandwidth lies in the interval of 5 to 10 Hz.

## 15.2 RF system overview

The HIE-ISOLDE radiofrequency system is relatively simple in number of components, however the challenges are presented by very complex dynamics of the quarter-wave resonator with strong Lorentz force detuning sensitivity and presence of external perturbations.

One RF power source directly drives one cavity, controlled by a dedicated LLRF system. Thanks to the linac operating frequency, which lies within the FM broadcasting band, standard, off the shelf, commercially available FM transmitters are the choice to power the HIE-linac.

A separate chassis housing a ferrite circulator and power RF load provides separation of the power amplifier output from the fully reflecting superconducting cavity.

A variable fundamental power coupler allows to set a large range of the cavity $Q_{EXT}$, from very

**Table 15.2:** Required cavity RF forward power for various operating conditions [3].

| Desired operating bandwidth (Hz) | $Q_{ext}$ | Forward power $P_g$ (W) at resonance | Reflected power $P_r$ (W) at resonance | Dissipated power (W) at resonance | Forward power $P_g$(W) 1BW from resonance | Forward power $P_g$(W) 2BW from resonance |
|---|---|---|---|---|---|---|
| 1 | $1.012 \cdot 10^8$ | 19.22 | 10.36 | 8.86 | 33.67 | 77.00 |
| 2 | $5.060 \cdot 10^7$ | 33.49 | 24.63 | 8.86 | 62.39 | 149.1 |
| 5 | $2.024 \cdot 10^7$ | 76.74 | 67.87 | 8.86 | 148.9 | 365.7 |
| 10 | $1.012 \cdot 10^7$ | 148.9 | 140.1 | 8.86 | 293.4 | 726.8 |
| 15 | $6.747 \cdot 10^6$ | 221.2 | 212.3 | 8.86 | 438.0 | 1088 |
| 20 | $5.060 \cdot 10^6$ | 293.4 | 284.5 | 8.86 | 582.3 | 1449 |
| 30 | $3.373 \cdot 10^6$ | 437.9 | 429.0 | 8.86 | 871.3 | 2172 |
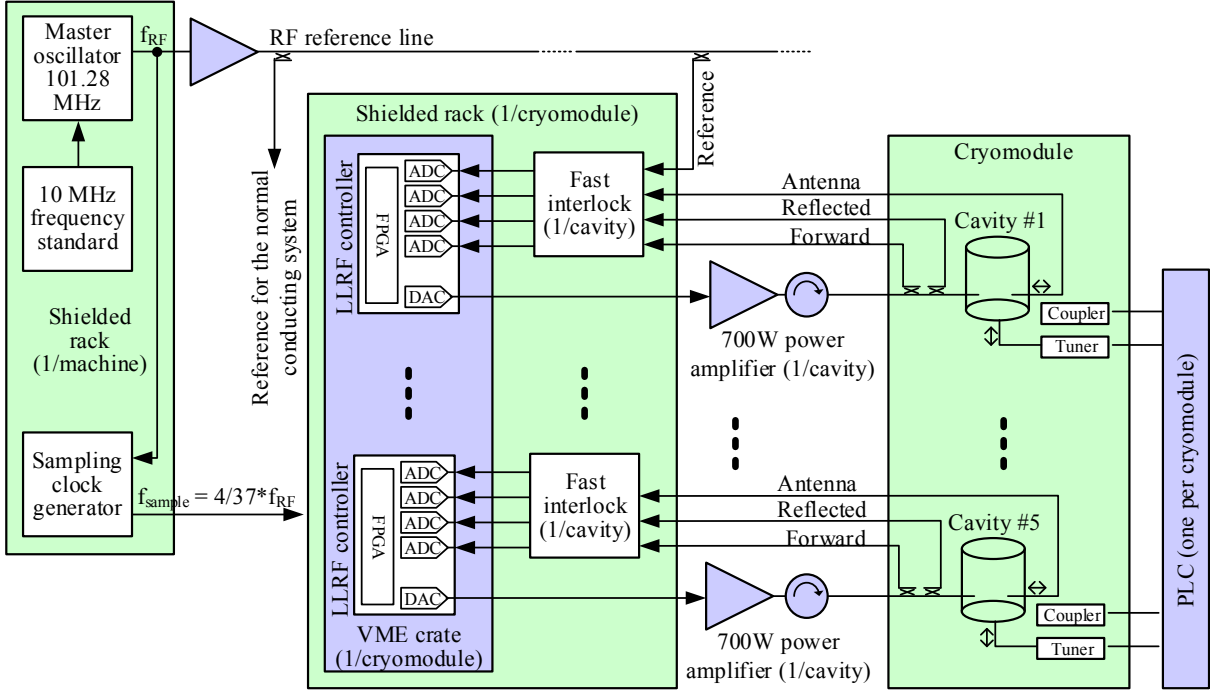


**Fig. 15.1:** Simplified diagram of the HIE-ISOLDE RF system.

high values close to the intrinsic Q, down to values close to the normal conducting condition. There is a very different RF power requirement to cover such range of $Q_{EXT}$, which may lead to dangerous over-powering or over-field conditions. The system is therefore protected by an additional, independent fast RF interlock, based on analogue circuitry with no software or variable parameters involved.

## 15.3 LLRF system

The purpose of the LLRF system is to control a field with a given quality in the accelerating structure. The three foreseen fundamental modes of operation are the self excited mode, the generator driven mode and the feedback mode.

The self excited mode sends a defined generator power to the cavity, while there is a positive feedback on the cavity phase. The positive feedback oscillates at the natural frequency of the external

resonator (the cavity), so the LLRF system is capable of exciting a field in the cavity, which can be in any tune state and any value of the $Q_{EXT}$. The loop is able not only to find the cavity resonant frequency, but also to follow any changes of the resonant frequency, e.g. those caused by Lorentz force detuning or microphonics. This mode is foreseen to be used for cavity conditioning and to bring the cavity up to the desired accelerating field, maintain the accelerating field during action of the mechanical tuner and prepare the cavity before the feedback loops can be locked.

The generator driven mode is an open-loop mode of operation, in which the LLRF system sends an RF vector defined by the set-point (amplitude and phase) at the nominal linac frequency to the power system, regardless of the cavity tune state. This mode is used e.g. for system tests, power amplifier heat runs or as a transition between the self excited mode and the fully locked mode. The generator driven mode is also very useful for measurements of external perturbation to the cavity.

The feedback mode, or "locked mode", is a closed loop operation mode, in which the cavity return signal vector is locked to the set-point and kept constant by means of feedback loops. The set-point phase in this mode of operation is dynamically normalised by the reference line phase to provide the required distribution of the absolute phase over the linac to achieve the desired acceleration.

## 15.4   High-Q resonator dynamics and control strategy

The HIE-ISOLDE machine runs in a very different mode than the other accelerators using superconducting cavities at CERN. While lower $Q_{EXT}$ (tens of thousands) is typical, a high beam loading is present. It is easy to bring the resonator to the nominal accelerating field, using hundreds of kW of RF power, but subsequently a whole set of very sophisticated feedback loops need to fight the beam loading effects. The RF amplifiers run close to the saturation and typically only few percent of power reserve is available for the LLRF regulation.

The working point of the HIE-ISOLDE machine lies in exactly the opposite side of parameter space. As already mentioned in the introduction, beam loading is negligible, so the superconducting resonators can be operated at high values of $Q_{EXT}$. The intended operating point falls in the interval $1 \cdot 10^7 \ldots 3 \cdot 10^7$, with corresponding cavity bandwidth $10 \ldots 3$ Hz. The fundamental RF power requirement for an unperturbed cavity lies in the range of $50 \ldots 150$ W. Due to a need of cavity surface conditioning already at warm, the RF power system is capable of delivering 700 W of RF power, leaving an unusually large power margin for LLRF regulation.

There are no hard limitations to the system presented by technology, therefore the working point choice is defined mainly by the level and nature of the external perturbations. The expected microphonics level for the LLRF controller design is $< 1$ Hz$_{pk}$ with important spectral components up to $\sim 300$ Hz.

The second most important perturbation, relevant to the resonator control strategy, will be the sensitivity of the cavity tuning plate to Lorentz force detuning. Cold tests performed in SM18 indicate relatively high Lorentz coefficient $|k| \sim 3.5$ Hz/MV$^2$. The cavity resonant frequency shifts by $\sim 75$ Hz between the low accelerating field and the nominal accelerating field operation. In the case of the intended 3 Hz operating bandwidth, the Lorentz force will cause a cavity detuning by 25 operating bandwidths. Such behaviour is extremely tricky to control, especially in the high field operation. For example, a 5% change in the set-point can lead to detuning by a full operating bandwidth. The same applies to the detuning caused by microphonics. A sudden microphonics "surge" can detune the cavity by a fraction of bandwidth. When not immediately compensated by a large amount of extra RF regulation power to keep the field stable, the cavity can easily unlock and the field collapses completely.

A MATLAB Simulink model had been developed to thoroughly study the various dynamic effects of the resonator operation. Taking into account all particularities of the system, the following controls strategy, which further developed into the nominal cavity operating sequence, was established.

A standard P-I feedback loop topology is sufficient to provide the requested accelerating field quality. The cavity should be first powered up in the self excited loop mode with a low RF power

injected ($\lesssim$ 2 W) to find the resonant frequency and calculate the cavity operating bandwidth. If the cavity operating bandwidth is outside of the intended set-point, the operator has to manually correct it. If the bandwidth is correct, the power roughly corresponding to the initial locking field (e.g. 1 MV/m) is injected. The cavity is tuned to the nominal linac RF frequency of 101.28 MHz. The set-point rate of change limiters is enabled to allow only well defined, very adiabatic changes in the cavity set-point. The tuner loop is enabled and the LLRF controller is switched over to the generator driven mode. It keeps the same amplitude, but transfers the field phase from the last point left behind the free-running cavity in the self excited mode to a constant value defined by the control system. The tuner loop is enabled to keep the cavity in resonance at the linac frequency, regardless of the accelerating field magnitude. The tuner loop also compensates for all detunings caused by the slow liquid helium pressure variations.

The next step is to switch over to the feedback mode, starting with gains GINTEGRAL = 0 and GPROPORTIONAL = 0. The magnitude set-point is still set to a low, initial value, while the phase is already locked to the reference phase. The feedback gains are increased to their nominal values and the cavity is locked to the intermediate (low) set-point. The feedback gain is also regulated by rate of change limiters in order to avoid large field transients which, due to high Lorentz force detuning sensitivity, can lead to loss of the accelerating field.

Once both P and I feedback loops are fully locked, the nominal machine values of the accelerating field phase and magnitude are programmed and the LLRF, together with the tuner loop, slowly increases the field. The process is very delicate and it can take up to two minutes to power up the cavity from an idle state to the nominal 6 MV/m condition.

A block diagram of the LLRF controller internal functionality is shown in Figure 15.2.
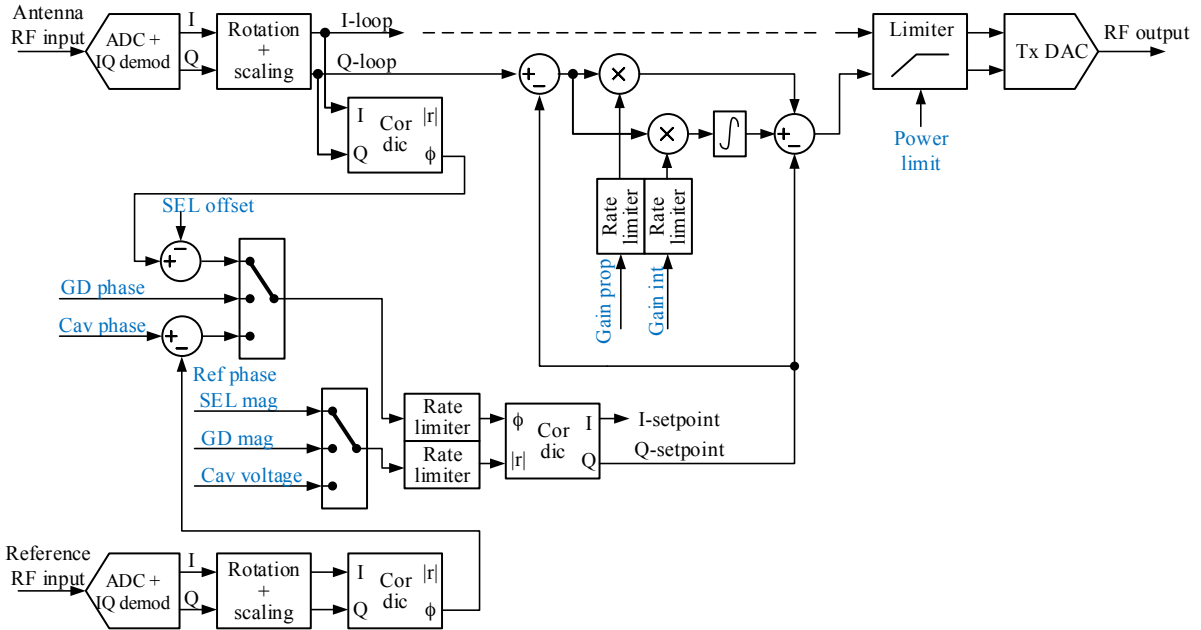


**Fig. 15.2:** A block diagram of the LLRF controller. Legend: SEL - self excited loop, GD - generator driven, Prop - proportional loop, Int - integral loop. Blue are parameters programmed by the control system.

## 15.5  LLRF system hardware

The HIE-ISOLDE LLRF system is a fully digital system, based on the customised LHC RF VME architecture. Complete LLRF functionality for one cavity is implemented on a single VME card. Five or six VME LLRF controller cards are then housed in one VME crate, providing functionality for a whole

cryomodule. One VME crate, together with a fast interlock crate and auxiliary devices, is installed in an RF shielded rack, mimicking the function of a Faraday cage, often used at CERN to house the sensitive LLRF systems.

The GPS disciplined 10 MHz frequency standard with all clock generation circuitry is housed in a dedicated shielded rack, same as the 230 V distribution and an Ethernet network star point. As all equipment is designed to be remotely controlled without a need of local interventions, even during the commissioning period, the elimination of a Faraday cage offers significant savings to the project.

In order to save development efforts, the HIE-ISOLDE LLRF controller design re-uses hardware of the SPS 800 MHz cavity loops controller. However, as the HIE-linac frequency lies well within the capabilities of modern analogue to digital converters a direct RF sampling was proposed for the HIE-ISOLDE LLRF system. Equally, modern digital to analogue converters are capable of directly generating vector modulated signals up to hundreds of MHz, which allows for a direct digital RF generation [4]. The whole LLRF controller hardware then shrinks to a set of ADCs, a powerful FPGA for signal processing and a so-called TxDAC. A photo of the original SPS 800 MHz cavity loops controller is shown in Figure 15.3.
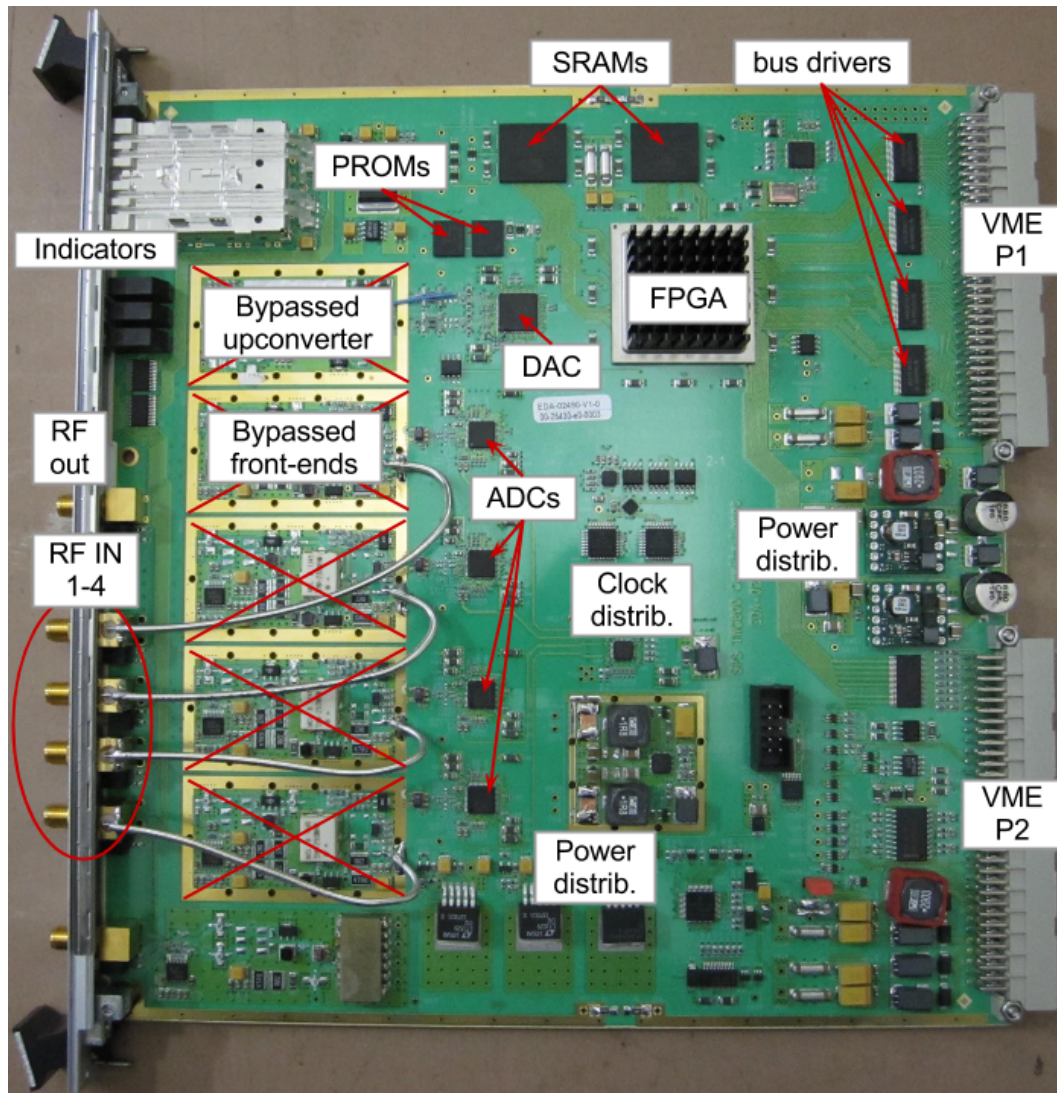


**Fig. 15.3:** Photo of the original SPS 800 MHz cavity loops controller showing all important blocks, including the hardware which was eliminated by using the direct RF sampling and direct RF generation.

As the cavity operating bandwidth, including all expected perturbation signals, is very low (max. a few kHz), one can profit from the direct RF sampling and by undersampling and a clever choice of the sampling frequency also achieve a direct digital quadrature demodulation. Such condition is achieved if the sampling frequency $f_S$ is in a relation to the sampled frequency $f_{RF}$ defined by

$$f_S = \frac{4}{n+1} f_{RF}, \tag{15.1}$$

where n is a positive integer. In LLRF systems, where an IF frequency is sampled, the $n$ is typically 0, however using $n \ggg 0$ brings the system to the undersampling mode.

For the proper function of the feedback loops, the total system electrical delay has to be kept under control to allow the high gain loop required to achieve the desired accelerating field quality regulation. Minimum sampling frequency in this case is hundreds of kHz. However, the LLRF system is used to measure and condition the quarter-wave resonators already in their normal conducting state, where large bandwidth is necessary. The exact sampling frequency needs to be determined based on the tests with real system, but it lies in the range 10 to 40 MHz ($n = 12 \ldots 40$).The feedback loops and certain time critical control automation are implemented in fully digital domain in the FPGA.

Slow control is performed by the standard CERN controls infrastructure based on FESA middleware. The FESA classes house all calibration parameters and translate the machine level parameters, e.g. request for a given magnitude and phase of the accelerating gradient to binary values corresponding to the required set-point and individual calibration factors of each accelerating structure/LLRF system.

The fully digital LLRF systems offer an intrinsic observation capability, which is extremely useful for the system set up, tuning and fault diagnostics. All external signals (cavity antenna, Fwd, Rfl, RF drive signals) and internal signals (set-points, loop regulation signals etc.) can be stored into long digital buffers. The signals are time-aligned at the sample level, giving invaluable information about what is happening within the system. The LLRF controller features memories similar to the "post mortem buffers" available in large machines.

## 15.6   RF power system

Power rating of the HIE-ISOLDE RF system is defined mainly by the RF power required for the warm cavity conditioning. The fundamental RF power couplers are designed to support 500 W of CW power at full reflection, which is sufficient to treat the first multipacting barrier at low field, while the cavity surface is still in a normal conducting state. Conditioning at warm later saves a significant amount of time during the linac machine commissioning.

The RF system is cabled using 3/8" corrugated coaxial cables for the low-level signals (attenuation 3.5 dB/ 100 m at 100 MHz) and 7/8" smoothwall coaxial cables (attenuation 1 dB/ 100 m at 100 MHz). The LLRF and RF power racks are located relatively close to the linac tunnel, therefore no high RF losses are expected in the RF cable distribution network.

RF amplifiers were selected as standard, off the shelf FM broadcasting transmitters. Built on the current fifth generation RF power MOSFETs, a unit with one single transistor delivers typically 700 W of output power, which fits with the HIE-ISOLDE machine parameters.

In order to protect the RF power amplifier from the superconducting cavity reflected power, a ferrite circulator with sufficiently rated RF load has to be inserted into the RF chain. The circulator and load should rather be installed in a separate 3U chassis than integrated into the RF power amplifier. This simplified the tendering and later maintenance of the system. Both devices, the power amplifier and the circulator chassis, are cooled by demineralised water.

## 15.7   RF reference line

Based on the required beam parameters, different energies of different ion species, the individual cavities are re-phased on the fly by the high level control system [5]. A robust absolute phase reference has to be established in the linac to support this kind of operation.

A linac RF frequency signal from the master oscillator at a power level of 100 W is distributed over a full length of the linac. A set of directional couplers are installed at the position of each cryomodule sampling the reference line. The reference signals are also distributed to the normal conducting system, beam instrumentation system and the future TSR.

## References

[1] M. A. Fraser, R. M. Jones (dir) and M. Pasini (dir), PhD thesis, Manchester U., 2012, Presented 26 Jan 2012.

[2] A. D'Elia, Design and characterization of the power coupler line for HIE-ISOLDE high beta cavity, HIE-ISOLDE-PROJECT-Note-0011 (CERN, 2011).

[3] D. Valuch,  RF power requirements for the HIE-ISOLDE cavity and the power amplifier,  HIE-ISOLDE-PROJECT-Note (CERN, 2011), unpublished.

[4] M. Elias, PhD thesis, Czech Technical University in Prague, 2013.

[5] S. Haastrup and M. A. Fraser,  An Automatic Cavity Phasing Routine for HIE-ISOLDE,  CERN-ACC-NOTE-2014-0097 (CERN, 2014).

# Chapter 16

# Beam instrumentation

E. BRAVIN, E. D. CANTERO

## 16.1  Diagnostic boxes

### General description

The beam instrumentation devices of the REX accelerator for the HIE-ISOLDE project are installed in several diagnostic boxes (DB) both in the linac and the HEBT sections. The main structure of the HIE-DB is an octagonal-shaped tank with six ports available for the insertion of instruments, stripping foils and collimators. One port includes an adaptation piece for the connection to the vacuum pumping system, if required. The functional requirements for the diagnostics system can be found in [1].

The aim of the diagnostic boxes is to measure the current, profile and position of the particle beams of the post-accelerator. The beam current is measured by means of Faraday cups (FC). The transverse profiles are measured by reading the beam current passing through a thin slit as a function of the slit position. Both horizontal and vertical profiles are measured by cutting a V-shaped slit in a blade that moves at 45 degrees. The position of the beam is calculated from the beam profiles. Longitudinal beam parameters are measured using solid state detectors (silicon detectors).

### Beams used for diagnostics

The diagnostic system monitors the stable pilot beams of HIE-ISOLDE post-accelerator, which are used for the normal set-up procedures while tuning the accelerator and its transfer lines. Typical values for the stable beam intensities are in the range of 1 to 50 pA, with values rising up to 1 nA only in the exceptional case of the transverse emittance measurements. More details about typical beam parameters at the different locations can be found in Part III.

### Instruments and devices for the HIE-ISOLDE diagnostic box

The modular design of the DBs can house several of the following devices, which have been designed or adapted for the HIE-ISOLDE post-accelerator instrumentation [1]:

- Faraday cup (detector), in two different versions: short (for HIE-linac) and long (for the HEBT).
- Silicon detector.
- Scanning slit, which consists of a blade with two slits for scanning the beam in vertical and horizontal directions.
- Collimators type I, which consist of a blade with four circular collimators.
- Collimators type II, which consist of a blade with four vertical slits.
- Stripping foils, which consist of a blade with up to three light-weight carbon thin foils that are used for charge-state cleaning of the beam.

### Types and position of diagnostic boxes

In order to preserve beam emittances, the drift space between the accelerating cavities is reduced. As a consequence, the longitudinal space available for diagnostics in the linac region is severely limited. That problem is not present in the beam transfer lines. The conceptual design of the boxes and instruments

for the entire HIE-ISOLDE post-accelerator is similar, but the implementation has been separated in two DBs of different sizes:

- Short diagnostic boxes for the Linac region (referred hereafter as short DBs or Linac DBs). The total longitudinal length from wall to wall of the box is 58 mm.
- Long diagnostic boxes for the HEBT region (referred hereafter as long DBs or HEBT DBs). The total longitudinal length from wall to wall of the box is 93 mm.

The limited longitudinal space available on the short DBs does not affect the design of the devices enumerated in the previous subsection, except in the case of the Faraday cup, for which two detectors have been designed, both of them having the same aperture but different overall longitudinal dimensions.

Depending on the requirements in terms of instruments, collimators and other devices to be included in the DBs, different types of diagnostic box modules is assembled [1].

- DB type I: includes FC, scanning slit, and collimators type I.
- DB type II: includes FC, scanning slit, collimators type II and stripping foils.
- DB type III: includes FC, scanning slit, collimators type I and Si detector.
- DB type IV: includes FC, scanning slit, collimators type II, stripping foils and Si detector.

The positioning of the DBs follows the guidelines presented in [1].

**Other general considerations**

The tanks of the diagnostic boxes have been manufactured of stainless steel 316L. The beam diagnostic instruments are operated with linear motion feedthroughs. The Faraday cup and the Si detector instruments have only one working position, aligned with the beam axis. The linear actuators for the scanning slit, collimators and stripping foils have several working positions. The movement of the devices is performed by means of stepper motors or brushless DC motors.

The diagnostic boxes are installed and operated in an UHV environment. Vacuum tightness is obtained using UHV rated materials and seals. More details about the vacuum aspects of the instrumentation are described in Chapter 10.

## 16.2   Beam intensity measurement

The measurement of beam current is essential in order to measure and optimise transmission. It is done with the Faraday cup detector. Two different FCs have been designed for HIE-ISOLDE, one for the short DBs and one for the Long DBs.

The main body of the Faraday cup is made of stainless steel (304L), while the repeller cylinder and the signal cup (collector) is made of aluminium (Aldural 6082). The insulating parts is made of Vespel. Layouts of the geometrical design and pictures of the FCs are presented in Figures 16.1 and 16.2.

The precision and accuracy of the FCs for determining beam currents (in the range 1 pA to 1 nA) have been checked during experimental measurements [2] performed on prototype FCs tested with stable ion beams at REX-ISOLDE and TRIUMF [1]. Some results of these measurements are shown in Figure 16.3; the reference beam current was obtained with an FC from REX-ISOLDE with an applied repeller voltage of $-V_{\text{rep}} \geq 60$ V.

The Faraday cup is mounted on a movable support in order to allow its insertion and extraction from the beam path. The positioning tolerance is of the order of $\pm 0.5$ mm in both transverse planes. The Faraday cup is able to be in beam at the same time as either the scanning slit or the collimator slit.

---

[1]Canada's national laboratory for particle and nuclear physics and accelerator-based science

(a) Cross section of the HEBT (long) FC. Dimensions in mm.

(b) Picture of the HEBT (long) FC.
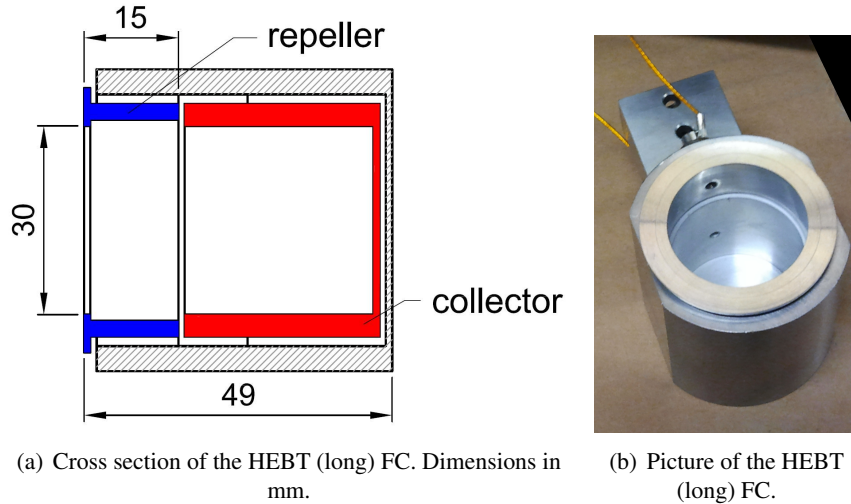
**Fig. 16.1:** Faraday cup for the transfer lines of HIE-ISOLDE.



(a) Cross section of the linac (short) FC. Dimensions in mm.

(b) Picture of the linac (short) FC.
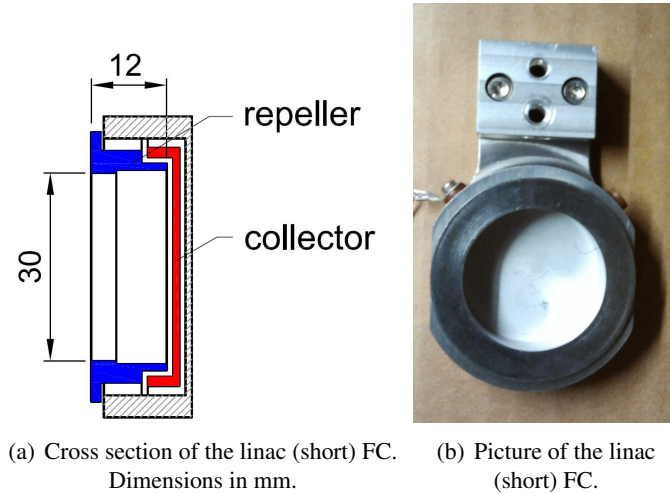
**Fig. 16.2:** Faraday cup for the inter-cryomodules region of HIE-ISOLDE.

## 16.3 Beam transverse profile measurement

The beam transverse profiles are measured with a system composed of a scanning blade with two slits moving upstream of a Faraday cup. The blade moves at 45 degrees to the vertical axis, and has two slits for determining the vertical and horizontal profiles. The slit width is 1 mm and the blade is made of aluminium (Aldural 6082). A schematic showing the implementation of the system is presented in Figure 16.4. A layout of the blade that is used for the beam profiles measurements is shown in Figure 16.5.

Tests of the scanning slit mechanism using a prototype scanning slit (with a slit width of 0.2 mm instead of the final design value) and a FC were performed at REX-ISOLDE on January and February 2013, using the stable pilot beam with $E/A = 2.85$ MeV/$u$ and $A/q = 4$. Some representative results of those measurements are displayed in Figure 16.6.

With a larger slit width, the intensity collected by the detector will be higher, decreasing the influence of the electronic noise in the profiles, but lowering the resolution of the collimated beam (beamlet)
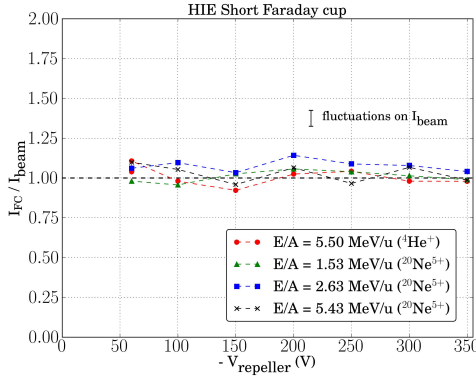
(a) Results from the linac (short) FC       (b) Results from the HEBT (long) FC
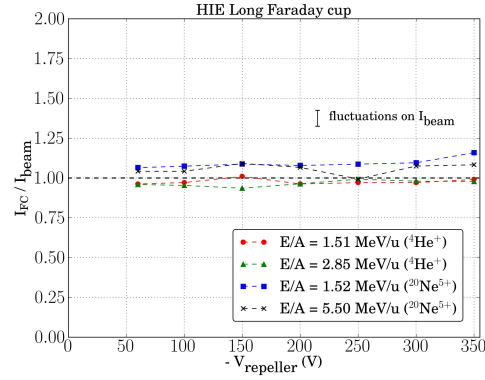
**Fig. 16.3:** Dependence of the Faraday cup current with the applied repeller voltage, for different beam composition and energies. Beam intensity was determined by using a standard FC from REX-ISOLDE. Beam intensity fluctuations were considerably high during the tests, a representation of the typical current oscillations is indicated as an error bar on the figures [2].
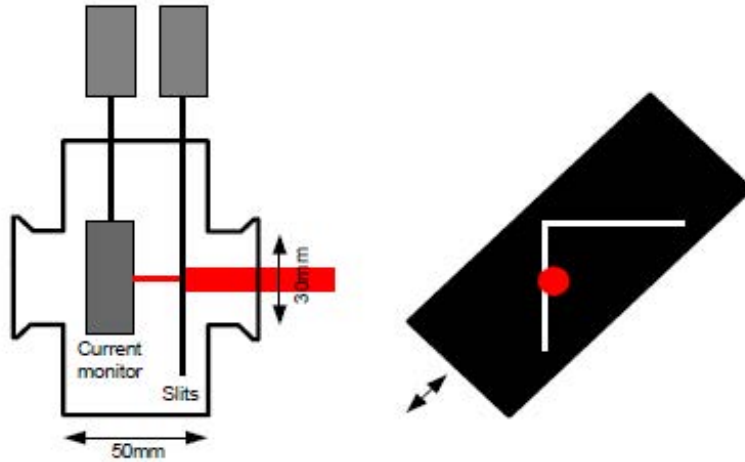


**Fig. 16.4:** Schematic of the slit scanning technique [1].

position. The trade-off between these effects has been studied for different slit widths, beam intensities and shapes, assuming an electronic noise of $I_{rms}^{electronic\ noise} = 0.1$ pA. Based on those studies [3], a slit width of 1 mm is the optimal solution for all the HIE-ISOLDE DBs.

## 16.4 Beam position measurement

The beam position is derived from the beam profiles measurements described in the previous section, by taking the centre of gravity of the acquired distributions.

## 16.5 Beam longitudinal profile measurement

The beam longitudinal profiles, including energy spread and bunch length, are measured using Si detectors [4, 5]. After a first amplifying stage, these devices provide signals on two different channels: a positive pulse with height proportional to the energy deposited by the particles in the active zone of the detector (energy channel) and a fast negative pulse that can be used to trigger a monitor on the time of
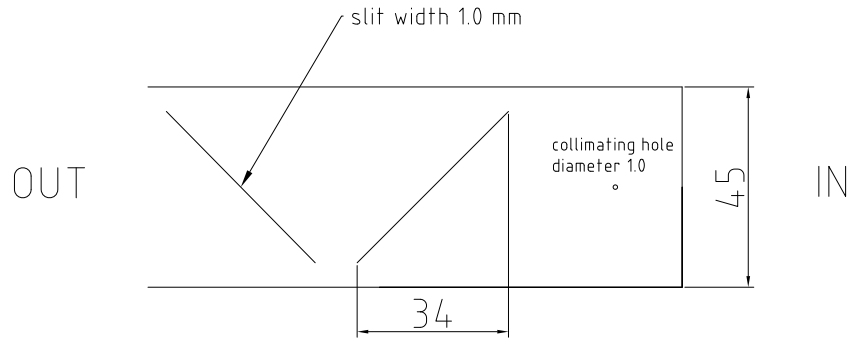
**Fig. 16.5:** Layout of the blade for the scanning slit system (dimensions in mm).



(a) Horizontal profile for a high intensity beam

(b) Horizontal profile for a low intensity beam
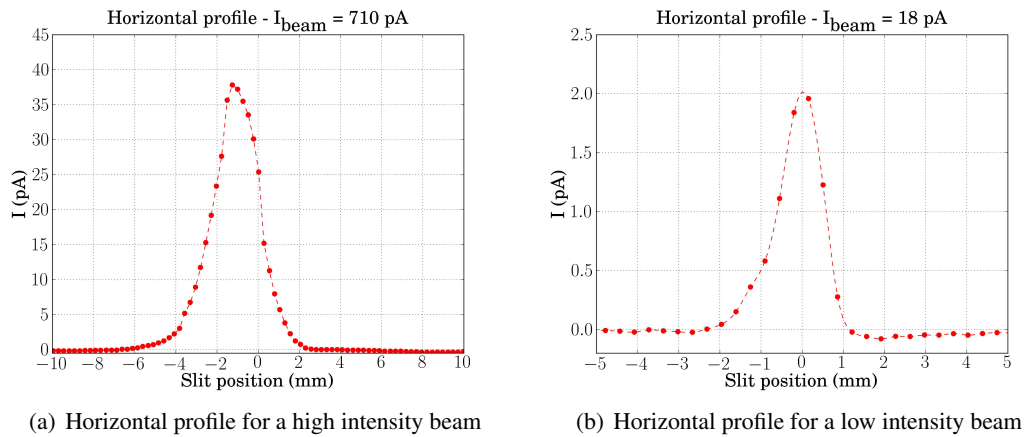
**Fig. 16.6:** Faraday cup measurements performed using the stable pilot beam from REX-ISOLDE.

arrival of the particles to the detector (time channel).

With the use of two detectors the absolute time of flight (TOF) of the particles can be obtained, provided that the particles E/A is known with an accuracy of $< 1\%$, given by an independent measurement done for example with a bender dipole. The beam debunching reduces the accuracy of the TOF technique for very low-energy beams.

By acquiring energy and/or time of flight spectra, relative beam energy shifts can be determined. Those measurements can be used for the phasing of the superconducting cavities [4, 5].

## 16.6 Use of the diagnostic boxes as an emittance meter

As stated in the functional specification for the beam diagnostic boxes of HIE-ISOLDE [1], the main emittance measurement device is the REX emittance meter, which is installed at the end of the XT00 line. Two diagnostic boxes (with scanning slit systems) could also be used as a complimentary method.

## 16.7 Schematic of the diagnostic box

In Figure 16.8 we present a schematic of the short diagnostic box, showing a cross section of the octagonal-shaped tank with the Faraday cup, the scanning slit and a set of circular collimators. There are three other ports that might be used for a connection to the vacuum system, for the Si detector, for other collimators and/or for the stripping foils. A photo of the short diagnostic box installed in the linac region can be seen in Figure 16.7
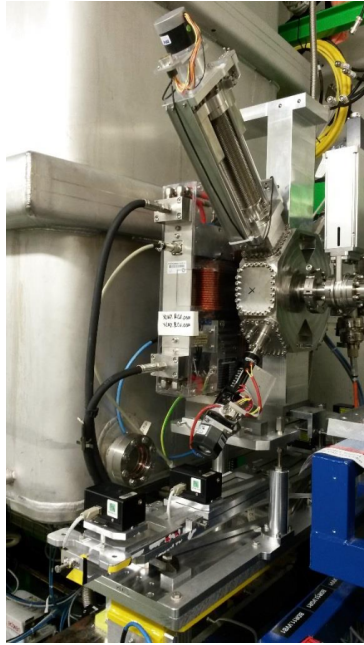


**Fig. 16.7:** Short diagnostic box, installed in the intertank sector.
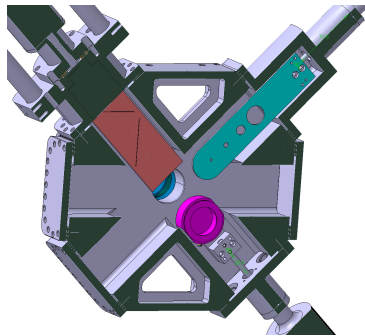


**Fig. 16.8:** Schematic of the interior of the short diagnostic box, to be installed in the inter-cryomodules region of HIE-ISOLDE.

## References

[1] M. Fraser et al., Beam diagnostic boxes for HIE-ISOLDE, Functional specification EDMS 1213401 (CERN, 2014).

[2] E. Bravin, E. D. Cantero and A. Sosa, Tests on Faraday cup prototypes for HIE-ISOLDE, Unpublished, 2014.

[3] E. Bravin, E. D. Cantero and A. Sosa, Optimal slit widths calculation for the HIE-ISOLDE diagnostic boxes, Unpublished, 2014.

[4] F. Zocca et al., *Nucl. Instrum. Methods Phys. Res. A* **672** (2012) 21.

[5] F. Zocca et al., Development of a silicon detector monitor for the HIE-ISOLDE superconducting upgrade of the REX-ISOLDE linac, HIE-ISOLDE-PROJECT-Note-0008 (CERN, 2011).

# Chapter 17

# Normal conducting magnets

J. BAUCHE, S. RUSSENSCHUCK

Dual plane corrector magnets and beam instrumentation devices are hosted between the cryomodules of the superconducting linac. Downstream, after a matching section, the main transfer line adopts a regular lattice with quadrupole doublets up to each experimental line, which switches the beam through a $90°$ double-bend-achromat lattice made of a single quadrupole mirroring the dispersion functions of surrounding dipoles. A final focusing section completes each line to adapt the focal point to the installed experiment. All magnets are powered with individual power converters, in DC current. Figure 17.1 presents the layout of the beam lines and the position of the magnets, while Figure 17.2 shows the magnets installed in the second beam line, XT02.
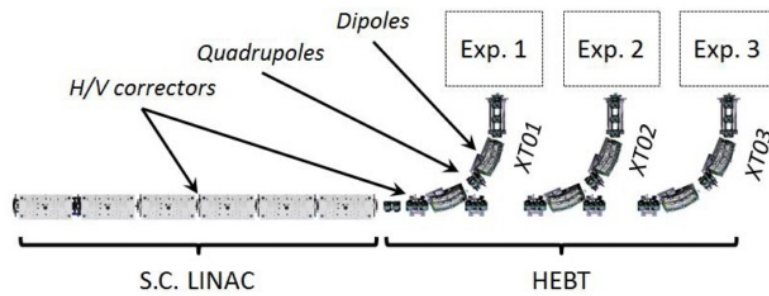


**Fig. 17.1:** Positioning of the magnets in HIE-linac and the HEBT.
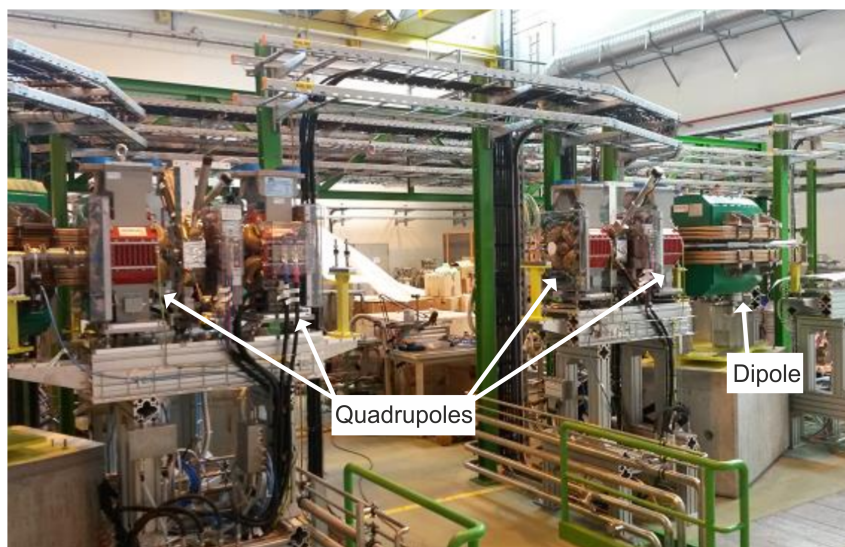


**Fig. 17.2:** Quadrupole and dipole magnets installed in the HEBT.

## 17.1 Dipoles

**Magnetic circuit**

The $1.8$ m bending radius and $45$ ° bending angle set by the layout induce a beam trajectory sagitta of $157$ mm. This has imposed a curved construction to reduce the overall transverse size of the magnet with respect to a straight design by approximately a factor of two. Considering the switching function required for several of the dipoles, the yoke has a C-shape to avoid the straight vacuum chamber of the non-deflected beam to cross the return yoke. This is also convenient for avoiding the mechanical imperfections of a split yoke assembly and allows easy access for the integration of the coils and chamber. The magnet geometry is illustrated in Figure 17.3.



(a)          (b)
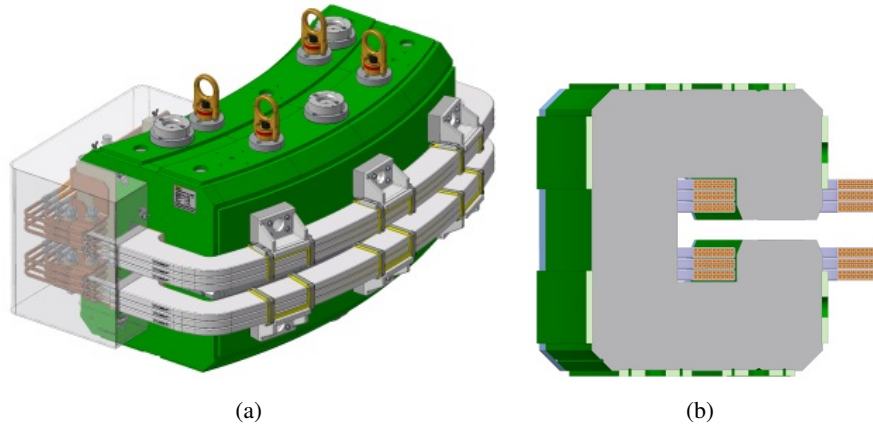
**Fig. 17.3:** Dipole, isometric view (a), simplified cross section (b).

The use of laminated steel, which allows to better control and homogenise the magnetic properties along the yoke, is well adapted to this construction. The lamination packs are glued and reinforced with pure iron [1] 40 mm-thick end plates and welded tension plates on the sides. As no pulsed operation mode is foreseen, a low silicon content electrical steel is used (M1400-100 A [2]), which has excellent magnetic properties. The C geometry is built with a constant width of 210 mm, sufficient to limit the flux density to 1.5 T on average over the return yoke. In the pole region, 23° tapering's reduce this width to 180 mm, leaving 1.4 times the aperture size on both sides of the Good Field Region (GFR). This is sufficient by itself to achieve a $10^{-3}$ field quality range. Nonetheless, small shims of 0.38 mm · 28.5 mm are added in the pole profile extremities to further improve the design field quality. The computed magnetic flux density in the yoke is shown in Figure 17.4.
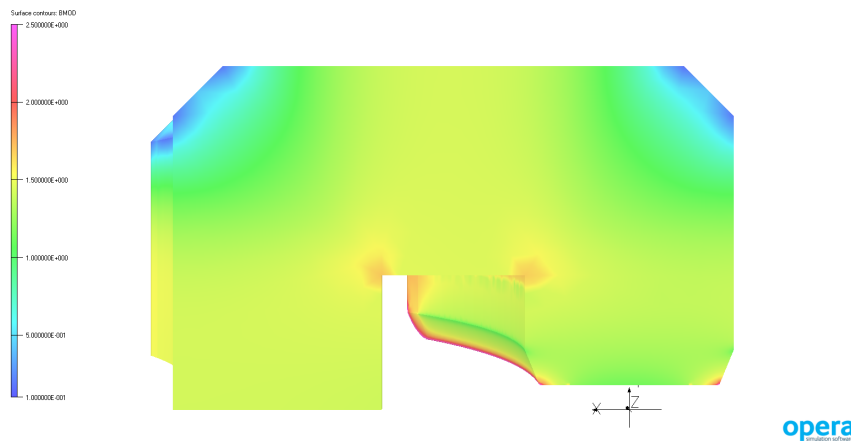


**Fig. 17.4:** Computed magnetic flux density in the yoke at $I_{nom}$.

The pole face rotation of half the bending angle induced by the laminated construction is kept to provide some focusing effect to the beam in the vertical plane, and keep the yoke construction simple. The magnetic length on each side of the beam axis is adjusted in 3D, with the end shims mentioned earlier hosted in slots of the end plates, shaped with the help of magnetic simulation in Opera [3]. These shims are removable on each magnet to allow corrections after magnetic measurements, if required. The design field quality ends up well inside the $\pm 5 \cdot 10^{-4}$ range requested by the beam optics, with a sufficient margin for manufacturing tolerances. The design normalised integrated field harmonics are reported in Figure 17.5.
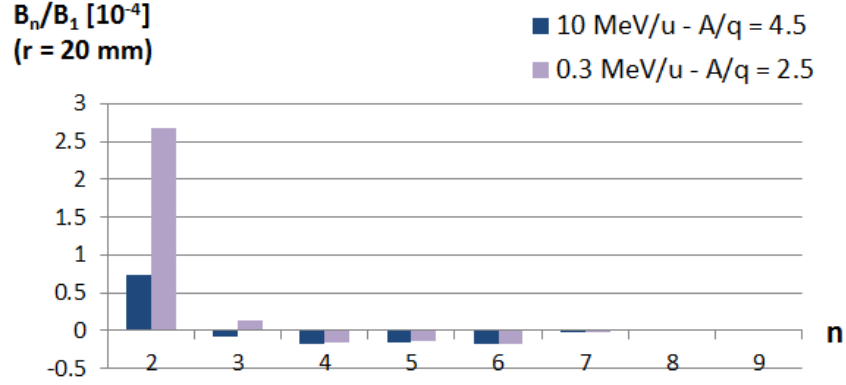


**Fig. 17.5:** Computed integral field normalised harmonics at $r_{ref}$ =20 mm.

**Electrical and hydraulic circuits**

The magnet electrical circuit is optimised for the use of an existing 500 A power converter. The current is carried in a series of 108 turns, distributed along six identical double layer racetrack coils made of hollow copper conductor insulated with vacuum potted epoxy resin reinforced with glass-fibre.

The impedance of the hydraulic circuit is optimised for operating at the nominal differential pressure of the demineralised water distribution network of the facility (10 bar). The conductor cooling duct size and the parallel connection scheme of the coils are designed to match a $\pm 4$ bar operational window, while staying in reasonable values of water velocity, temperature, and Reynolds number [4]. The dipole main parameters are reported in Table 17.1.

**Table 17.1:** Design parameters of dipole magnets.

| Parameter | Value |
|---|---|
| Number of magnets | 6 |
| Peak field in centre [T] | 1.2 |
| Allowed integrated field error | $\pm 5 \cdot 10^{-4}$ |
| Magnetic aperture [mm] | 50 |
| Magnetic length [mm] | 1414 |
| Bending radius [m] | 1.8 |
| Bending angle [deg] | 45 |
| Conductor dimensions [mm] | □10; ⌀6 |
| Nominal current [A] | 423 |
| Magnet resistance (20°C) [mΩ] | 100 |
| Magnet inductance [mH] | 113 |
| Cooling flow ($\Delta p = 10$ bars) [l/min] | 23 |

## 17.2 Quadrupoles

**Magnetic circuit**

A single design covers the requirements of all magnets in the regular lattice and matching sections of the HEBT. The yoke is made of a bolted 4-fold symmetric assembly to allow the integration of the coils. Similarly to the dipoles, the yoke quadrants are made of glued low silicon content grade laminations $(1300 - 100$ A [2]), here reinforced with pure iron [1] 12.5 mm end plates and longitudinal tie rods. The magnet geometry is illustrated in Figure 17.6.



(a)                    (b)
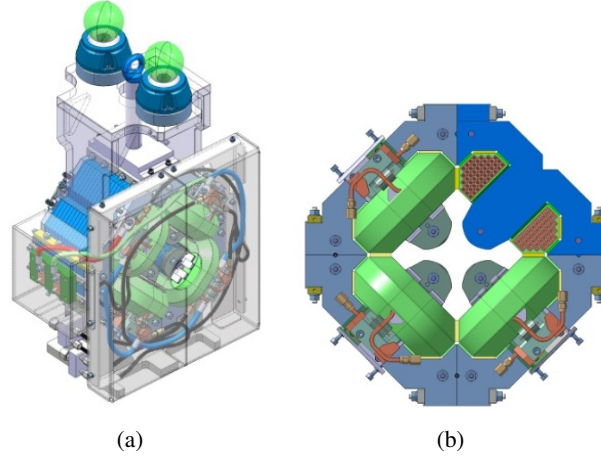
**Fig. 17.6:** Quadrupole, isometric view (a), and simplified front view with quadrant cross section (b).

The return yoke is built with a constant iron cross section, so that the magnetic flux density does not exceed 1.6 T at nominal current to limit the saturation effects. This cross section is however enlarged around the quadrant mating surfaces to improve the stability of the relative orientation of the poles. The poles are straight to host racetrack coils, ending with $18.9°$ tapering's trimmed by short reference surfaces parallel to the mating faces, which are convenient for performing dimensional checks during assembly. In the central aperture, the pole profile is of the classical hyperbolic shape of equation $2xy = r^2$, surrounded by shims to optimise the 2D field quality. This effort is completed by the cancellation of the integrated dodecapole with an end chamfer of 3.5 mm calculated in Opera [4]. This brings the integral field error below the $10^{-3}$ level required by the beam optics, with a comfortable margin. The computed flux density in the yoke is shown in Figure 17.7, and the design normalised integrated field harmonics are reported in Figure 17.8.
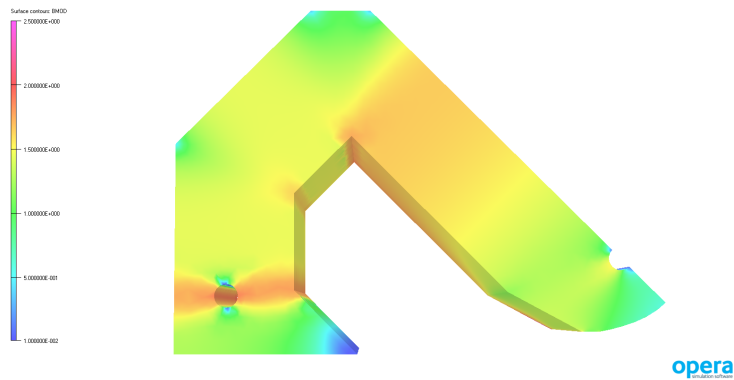


**Fig. 17.7:** Computed magnetic flux density in the yoke at $I_{nom}$.
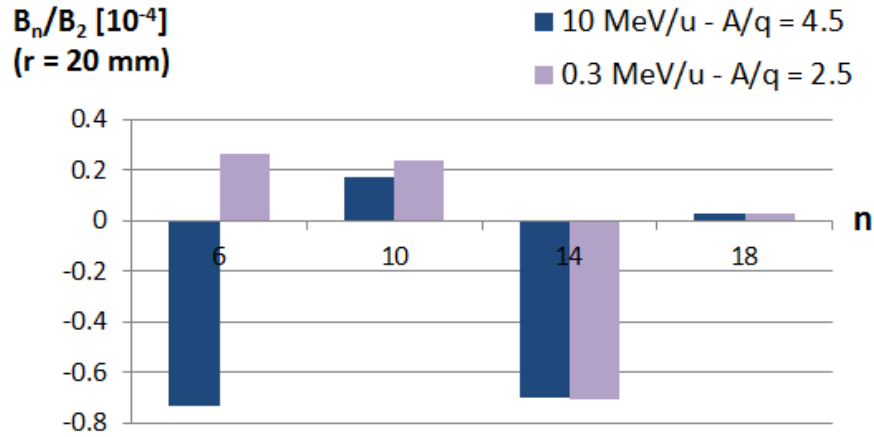
**Fig. 17.8:** Computed integral field normalised harmonics at $r_{ref}$ =20 mm.

**Electrical and hydraulic circuits**

The optimal matching with the power converter characteristics is obtained with four 48-turn coils powered in a series circuit. The technology is the same as for the dipole coils. The hydraulic impedance of the cooling circuit is optimised, in a similar way as explained above, with two parallel branches feeding two coils each. The quadrupole main parameters are reported in Table 17.2.

**Table 17.2:** Design parameters of quadrupole magnets .

| Parameter | Value |
|---|---|
| Number of magnets | 24 |
| Peak field gradient in centre [T/m] | 24 |
| Allowed integrated gradient error | $\pm 1 \cdot 10^{-3}$ |
| Magnetic aperture diameter [mm] | 50 |
| Magnetic length [mm] | 209 |
| Conductor dimensions [mm] | □6; ⌀4 |
| Nominal current [A] | 142 |
| Magnet resistance (20$^\circ$C) [m$\Omega$] | 105 |
| Magnet inductance [mH] | 30 |
| Cooling flow ($\Delta p = 10$ bars) [l/min] | 2.6 |

## 17.3 Dual plane correctors

The beam optics [5] and the integration of components in the confined space between the cryomodules (see Figure 17.9) have imposed challenging requirements on the corrector magnets' total length —92 mm— and field strength —6 mT·m. Those are met with a window-frame design, in which the coil windings are oriented orthogonally with respect to the magnet longitudinal axis, as shown in Figure 17.10. This allows maximising the occupation of the longitudinal space exclusively with the yoke iron and the coil conductors. For cost optimisation reasons, this design has also been standardised in the transfer lines, though more space is available there.

Most of the field strength is provided by the stray field of the magnet, due to its large aperture and short length. In the HEBT transfer lines, some 30% of this stray field is absorbed by the adjacent quadrupoles. The magnet has therefore been designed with a stronger integrated field (9.1 mT·m) to ensure reaching the required integrated field of 6 mT·m in the HEBT lines. This has imposed a water-
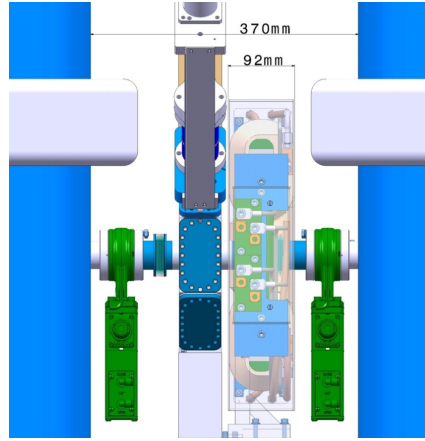
**Fig. 17.9:** Integration of the corrector magnet in the inter-cryomodule region.
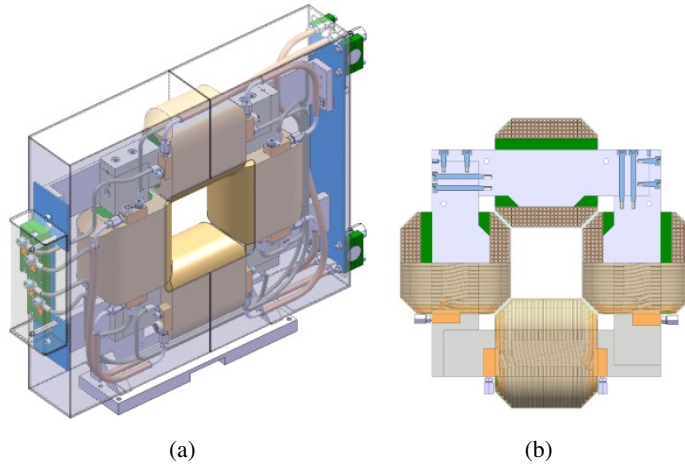


**Fig. 17.10:** Corrector magnet, isometric view (a), simplified front view with cut out of top halve (b).

cooled design to reach the necessary current density. The inner corners of the solid pure iron [1] magnetic circuit are trimmed to create poles, and a trapezoidal cross section is adopted for the coils to limit field errors below the percent level, as shown in Figure 17.11.
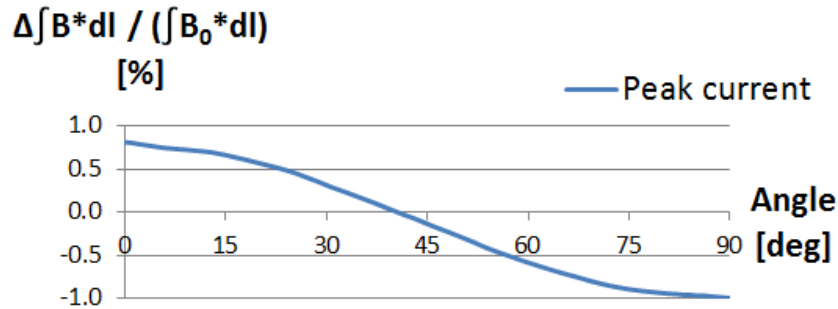


**Fig. 17.11:** Computed integral field relative error at $r_{ref} = 20$ at peak current.

The hydraulic and electrical parameters are optimised for the power converters and cooling water network characteristics, in a similar way as for the dipoles and quadrupoles. The magnet parameters are shown in Table 17.3.

**Table 17.3:** Design parameters of corrector magnets.

| Parameter | Value |
|---|---|
| Number of magnets | 15 |
| Integrated field in centre [mT·m] | 9.1 |
| Allowed integrated field error [%] | $\pm 2$ |
| Free aperture [mm] | $92 \cdot 92$ |
| Magnetic length [mm] | 258 |
| Conductor dimensions [mm] | $\square 4; \oslash 2.5$ |
| Nominal current [A] | 48 |
| Magnet resistance (per plane, $20^\circ$C) [m$\Omega$] | 109 |
| Magnet inductance (per plane) [mH] | 10 |
| Cooling flow ($\Delta p = 10$ bars) [l/min] | 0.4 |

## References

[1] ARMCO Grade 4 from A.K. Steel International, Online, http://www.aksteel.eu/en/1-products/0-ingot-iron.

[2] AFNOR, *Cold rolled non-oriented electrical steel sheet and strip delivered in the fully processed state* (AFNOR, Paris, 2007).

[3] OPERA 3D / TOSCA form Vector Fields, Online, http://www.vectorfields.co.uk.

[4] D. Tommasini, Practical definitions and formulae for normal conducting magnets, EDMS 1162401 (CERN, 2012).

[5] M. A. Fraser and M. Pasini, Misalignment and Error Studies of the High Energy Section of the HIE-ISOLDE Linac, HIE-ISOLDE-PROJECT-Note-0006 (CERN, 2009).

# Chapter 18

# Survey for assembly, installation and alignment

J.C. Gayde, G. Kautzmann

In the HIE-ISOLDE project, the large scale metrology survey work is performed at different steps: design, construction, assembly and alignment of the accelerator elements.

- – Participating to the project at early stage, e.g. collecting the geometrical parameters and alignment needs or discussing the integration of the survey needs in the design of the infrastructure, tools or accelerator elements.
- – Providing the necessary geometrical data for adjustment and control of the assembly infrastructures.
- – Providing the position and orientation information related to the linac cryomodule assembly and tests, i.e. the geometrical information:
    - – for the cryomodule assembly tooling alignment,
    - – for the geometrical follow-up and adjustment of the cryomodule elements during assembly and
    - – for the positioning of the cryomodule for tests.
- – Establishing, measuring, computing and maintaining geodetic networks or coordinate systems and defining the parameters linking different ones when needed.
- – Providing position and orientation information to locate the new beam lines in the CERN Coordinate System (CCS).
- – Providing, when necessary, metrology measurements for the fiducialisation of the accelerator and beam line elements as well as of module assemblies.
- – Providing the control of the position and the alignment of standalone elements and module assemblies on the accelerator beam lines.
- – Providing the accelerator elements and modules alignment and smoothing in the ISOLDE hall in their theoretical position along the beam line.

This covers both theoretical and practical aspects of the large scale metrology work for the HIE-ISOLDE project. The theoretical position of the beam line elements was provided by the accelerator optics team. In-field measurements were performed using suitable survey instrumentation and methods, such as total stations, optical levelling, photogrammetry, 3D laser scanners or laser trackers.

## 18.1 Specification

The specifications in Table 18.1 are derived from references [1] and [2]. They are expressed in a local reference frame, where Z is along the beam and X lays in a horizontal plane. The dipole specifications in roll angle and longitudinal position are expressed as tolerances. For the other elements, the specification is expressed at one sigma level.The positioning specification for the diagnostic boxes is not given specifically but follows the one for the steerer. The two elements are installed on the same support and are co-dependent. The element that is effectively aligned is the diagnostic box; the steerer alignment relies on the mechanical assembly.

(a)
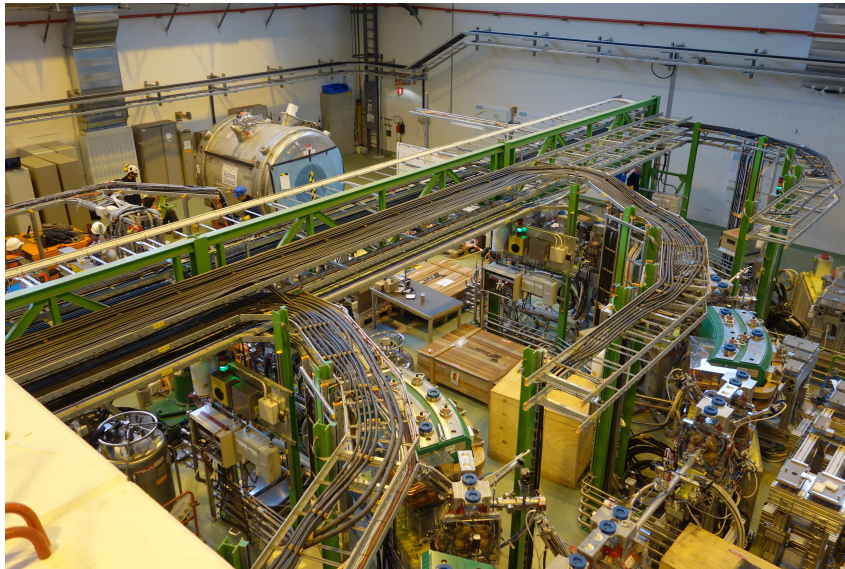


(b)

**Fig. 18.1:** Photo of the superconducting linac with three cryomodules installed (a) and of the HEBT (b).

**Table 18.1:** Tolerances and precisions for HIE-ISOLDE elements.

| Element | Values | Distribution |
|---|---|---|
| Dipole | Roll angle [rad] $2.0 \cdot 10^{-4}$ | Uniform |
| | Longitudinal position [m] $1.0 \cdot 10^{-3}$ | Uniform |
| Quadrupole | dX, dY [m] $2.5 \cdot 10^{-4}$ | Gauss ($1\sigma$) |
| Steerer | dX, dY [m] $2.5 \cdot 10^{-4}$ | Gauss ($1\sigma$) |
| Cavity | dX, dY [m)] $3.0 \cdot 10^{-4}$ | Gauss ($1\sigma$) |
| Solenoid | dX, dY [m] $1.5 \cdot 10^{-4}$ | Gauss ($1\sigma$) |

## 18.2 Support and alignment reference system

A pre-existing geodetic network is established along the linac and transfer lines into the ISOLDE hall. Additional geodetic points are installed in the new HIE-ISOLDE area. Those points are materialised by either wall brackets, permanent pillars or ground inserts equipped with the CERN standard survey reference sockets. Holes, filled with lead plates during normal operation, in the linac shielding tunnel provide lines of sight to strengthen the geodetic network inside the shielding area. The complete network is determined in the CSS and measured by total stations, laser trackers and direct levelling. The geodetic network of the area is updated periodically.

All the elements to be aligned are equipped with survey reference points and —for some— a tilt reference surface. Three different configurations exist for the new elements of HIE-ISOLDE. Each quadrupole and diagnostic box is equipped with two fiducials and a flat surface to measure the tilt. Dipole magnets and cryomodules are equipped with three and four fiducials respectively, but no reference tilt surface.

The supports of the elements dissociate the movements in the horizontal and vertical planes. Each quadrupole or diagnostic box is supported on sliding tables that can be levelled. Each dipole or cryomodule is sitting on three Linac 4 type jacks. The survey group helped with the definition and placement of these fiducials/supports and is included in the approval of the final designs.

## 18.3 Geometrical quality control measurement

The survey provides some of the geometrical and dimensional control measurements for the prototype and production elements.

## 18.4 Fiducialisation measurements

The determination of the survey reference target positions with respect to the reference system of the element or module on which they are placed is called fiducialisation. If the fiducialisation of an element cannot be guaranteed by construction or achieved by the Metrology Lab due to object size or specificity, it will be carried out by the survey group.

The survey group performs the fiducialisation of the cryomodule, i.e. determining the geometrical relations between the external survey reference sockets and the cryomodule cavity/solenoid entry and exit points. This operation embeds several ones and is achieved by laser tracker measurements during the cryomodule construction and by a mix of laser tracker and MATHILDE (see Chapter 8 or [3]) measurements once the cryomodule is fully assembled.

The parameters for fiducialisation are stored into the SURVEY database (GEODE) and, depending on the object, can be extracted from metrology reports, geometrical quality control measurement or from a specific fiducialisation operation.

## 18.5 Theoretical data

The spatial position and orientation data for the beam line elements of the linac and transfer lines is extracted from MADX beam line definition files. Additional parameters necessary for the large scale metrology can be derived from the layout drawings for the machines. The MADX file and the layout plans are to be provided to the survey group prior to any survey or alignment work.

The MADX file and additional parameters are inserted into the SURVEY database, which is the principal repository for all data and measurements related to the large scale metrology activities for accelerators at CERN. If possible, all measurements and results from metrology, survey and alignment activities are stored in the SURVEY database, and the theoretical data and results are available for consultation.
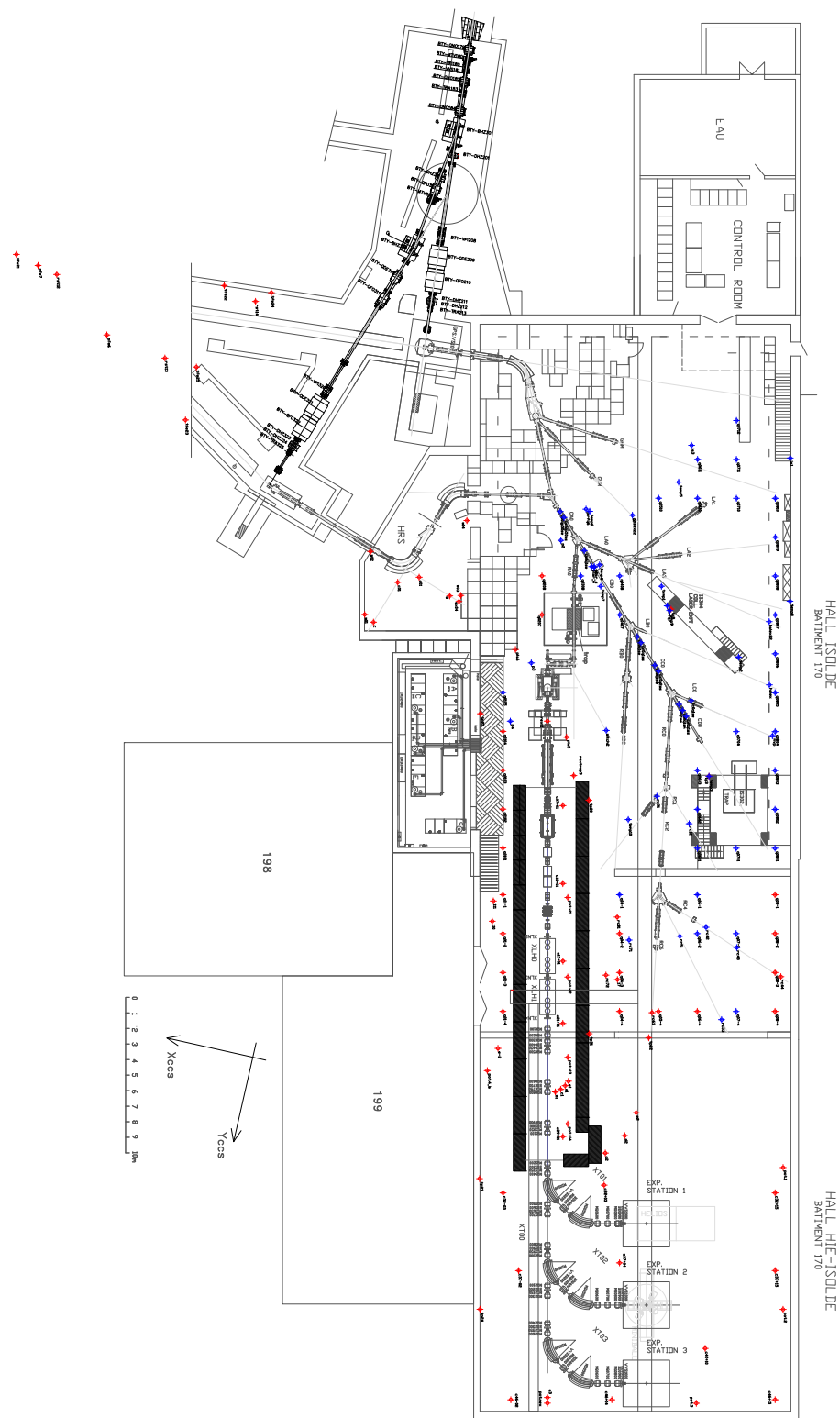
**Fig. 18.2:** Geodetic points (in red) located in the ISOLDE hall.

## 18.6   Marking out

With respect to the geodetic network, reference marks, representing the beam line and the elements to be aligned, are painted on the floor and walls. These marks provide help for the installation of services and beam line elements. Everybody working in their vicinity shall ensure that these marks remain visible. The required marks and annotations are defined in collaboration with the coordination of the concerned area.

## 18.7   Positioning and smoothing

Prior to the installation of the beam line elements, their supports are installed by others and pre-adjusted to their nominal position by the survey group. Those survey interventions can also happen before the support installation, if shims are required to overcome local floor deformations.

Once the beam line elements are installed, their initial positioning is carried out with respect to the geodetic network of the area. Precise survey methods and instrumentation are used, such as laser trackers, total stations and direct levelling. In the case of the cryomodule, the module is not necessarily installed in order to put its internal active element on the theoretical beam line. The cryomodule tank is placed considering the surrounding elements and their integration. Each cryomodule tank position is to be defined with the Installation Coordination. The cavities and solenoids can be adjusted to their best positions onto the beam line using remote motors, see Chapter 8.

After the elements are interconnected, and prior to commissioning, a final smoothing is made in order to achieve the desired relative alignment of the modules and other elements along the HIE-linac and transfer lines. This activity does not refer to the geodetic network, as the elements are considered to be at their correct absolute positions. Only the relative position between elements is considered, and the measurements are taken only from element to element.

This smoothing is carried out using any appropriate survey method and instrumentation, such as laser tracker measurements, nylon wire offset measurements for the radial position, direct levelling for the vertical position and inclinometer observations for the tilts.

## 18.8   Clean room installation, maintenance and specifics

The clean room requires a specific geodetic network made of standard ground survey sockets. The rails and the gantry are marked on the floor ahead of installation. The rails, gantry and different tooling used in the clean room assembly process are controlled, installed and adjusted in collaboration with the cryomodule assembly coordination. Geometrical controls for the tooling and an update of the geodetic network is part of a periodical clean room maintenance. When a survey intervention is needed in the cryomodule assembly process, the laser tracker is stationed outside the clean room in front of the protective plastic curtains. Access is needed in the $10,000$ and $100$ areas for one trained person to install, orient and move the clean room dedicated survey targets.

## 18.9   Cryomodule, vacuum and cryogenic test specifics

The test area requires a specific geodetic network made of standard ground survey sockets and wall-brackets. The position of the cryomodule supports and associated services results from a marking out by surveyors. After their installation in the area, the cryomodule supporting jacks are to be adjusted to their nominal position. The cryomodule positioning in the test area is carried out using appropriate survey instruments such as laser trackers, total stations and direct levelling.

To understand and follow the cryomodule behaviour during vacuum and cryogenic tests, a two-metrological-table MATHILDE set-up is installed and adjusted in the test area. MATHILDE is able to monitor the position of the cavities and solenoids during the different states (under vacuum, at cryogenic condition, etc.) of the cryomodule.

## 18.10    As-built measurements

In order to save time during the infrastructure installation and provide 3D documentation of the installed machine, a number of as-built measurements of the civil engineering structures are made, followed by as-built measurements of the installed infrastructure and finally of the machine. Two 3D scans in the ISOLDE hall around the HIE-ISOLDE area are anticipated before the start of the civil engineering work in the hall and after installation work. These measurements are pre-processed by the survey group to give the point clouds and their 3D coordinates in the CCS to the integration team.

## References

[1]  M. A. Fraser, R. M. Jones and M. Pasini, *Phys. Rev. ST Accel. Beams* **14** (2011) 020102.

[2]  A. Parfenova et al., HIE-ISOLDE HEBT beam optics studies with MADX, ACC-NOTE-2014-0021 (CERN, 2014).

[3]  G. Kautzmann et al., HIE-ISOLDE – general presentation of MATHILDE, ACC-2015-0084 (CERN, 2014).

# Chapter 19

# Controls and interlocks

J.A. RODRIGUEZ, F. LOCCI, R. MOMPO

## 19.1 Control infrastructure

The control system architecture for HIE-ISOLDE relies on the standard solutions proposed by the CERN Beam Controls group and largely deployed in the whole accelerator complex. As shown in Figure 19.1, the control system splits over three different responsibility tiers which communicate among them by the use of TCP-IP protocol over Gigabit Ethernet connection.
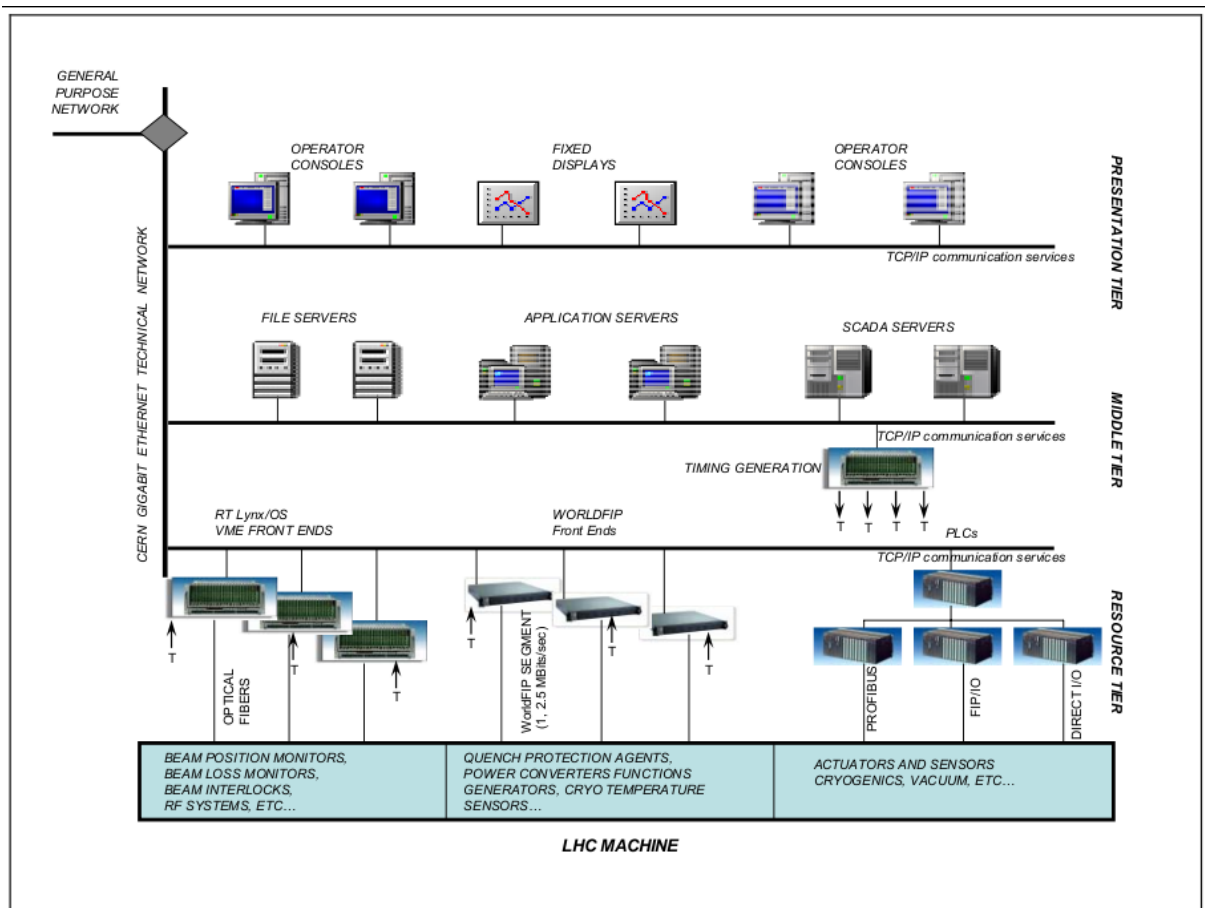


**Fig. 19.1:** Three-tier control system.

The presentation tier, the highest level of abstraction, hosts all the software actually used to operate the accelerator, relying on Front-End Computers (FECs) sitting in the resource-tier (custom CERN or SCADA sub-systems). HIE-ISOLDE will be operated from the existing ISOLDE control room (ICR), relying on custom and graphical Java application (Linux or Windows PCs).

Going down, one step toward the physical layer, in the middle tier, are all the services, the protocol, the programming interface and the software framework responsible for allowing seamless communication among all the application layer software and the control devices responsible for data acquisition
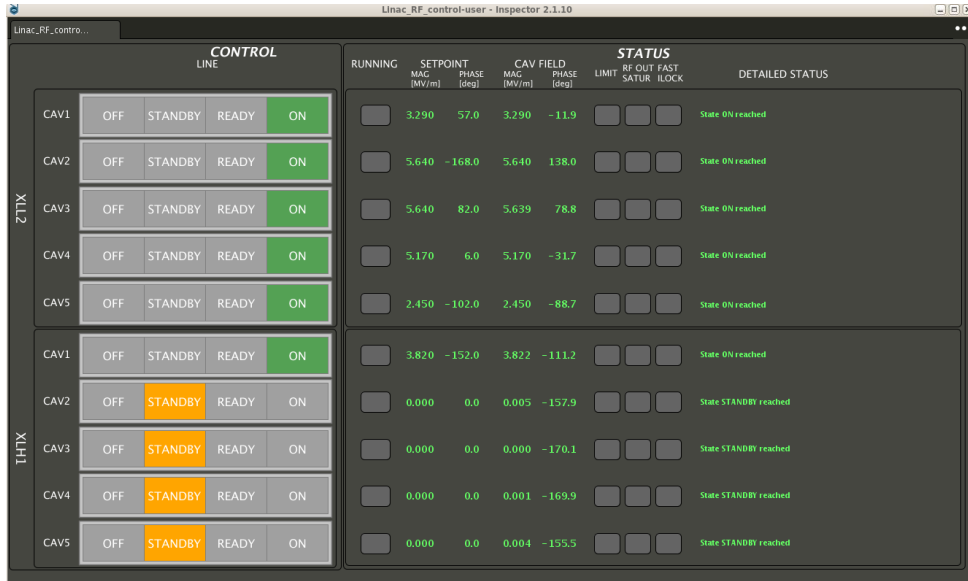
**Fig. 19.2:** HIE-ISOLDE Users Interface for the RF Controls.

and actuations. This middle-tier software is typically programmed in Java and provides services such as access to databases, data logging for off-line analysis and arbitration for competing requests to access hardware. One example of a three-tier application is the Open Analog Signals Information System (OASIS), which lets users view analog signals from front ends in virtual oscilloscope screens on an operator console.

Both equipment controllers, Programmable Logic Controllers (PLCs) and FECs, belong to the resource tier. The latter act as bridges between the presentation tier (operation tools and control room software) and the physical layer. The FEC is implementing the accelerator device model and its publish/subscribe paradigm and handles timing and synchronisation. Two types of FEC are mainly adopted: VME platform with extension modules (Timing, AC/DC, DIO, function generator, field buses, etc.) and Industrial PC rackmounted crate (mostly used for general services and network gateway). Both platforms run 64 bits real-time Scientific Linux. The Front End Software Architecture (FESA) abstracts all these components providing a comprehensive framework for designing, coding and maintaining Linux equipment software [1, 2].

The broad experimental programme means that the same beam species and energy are rarely studied twice, so the superconducting linac must be re-phased for each experiment. In order to ensure a fast set-up, three applications have been developed. A diagnostics application monitors beam current and beam profile with the help of a Faraday cup and a scanning slit respectively. A converter application allows operators to convert machine settings into an optics file to visualise the beam envelope and vice versa. Finally, a phase-up application allows operators to quickly phase-up each cavity, by finding the maximum energy gain as a function of the cavity phase. More information on the software tools used in HIE-ISOLDE can be found in [3].

Table 19.1 summarises the general infrastructure required for the HIE-ISOLDE controls (resource tier).

## 19.2   RF controls

The RF control system for the superconducting linac will be based on Schneider PLC and standard RF fast interlock system. There will be one main PLC for each cryomodule to control the RF parameters and exchange information with other systems like low-level RF, cryo and vacuum. The fast interlock

Table 19.1: General control infrastructure.

| System | Platform | Number | Purpose |
| --- | --- | --- | --- |
| RF interlock & slow controls | PC Linux computer | 1 | FESA & SILECS gateway |
| RF low-level | VME Linux computer | 7 | LLRF |
| Magnet power converters | PC Linux computer | 2 | FGC gateway |
| Solenoid power converters | PC Linux computer | 1 | FGC gateway |
| Beam instrumentation Diagnostic boxes | VME Linux computer | 2 | Beam diagnostics |
| Beam instrumentation Survey linac supra | PC Linux computer | 1 | Beam alignment |
| Supra Solenoid | PC Linux computer | 1 | CRYO WorldFIP gateway |
| Central Timing | VME Linux computer | 1 | Timing generation |

controller will produce the RF veto in order to switch off the RF drive to individual cavities. This is the interlock system based on the RF standard system used in all new projects since LHC. It is a modular fault detection system that has interfaces to the slow control PLC and to external services. More information on the RF slow control and interlocks can be found in [4].

The RF switch will be in the low-level RF system.

There will be hardware links between the RF slow control and the following external services:

– Access — to switch off the RF drive in case of access.
– Cryogenics — to enable/maintain RF drive if the cryogenic system is operational.
– Radiation — to switch off the RF drive in case radiation level is too high during personnel access; this is still to be validated.
– Vacuum — to switch off the RF drive in case of bad vacuum in the module.

## 19.3   Powering interlock controller for normal conducting magnets

The interlock system is required to avoid overheating of magnets in case of lack of cooling water or overcurrent, therefore several temperature probes are installed on the magnets. If the temperature exceeds a predefined value, a relay opens and the signal is sent to the interlock controller. The controller has the task of removing the permit for the power converter, thus stopping the converter. The required response time for switching off the power converter to avoid overheating is of the order of seconds. In general, normal conducting magnets have a large resistance and a low inductance. The time for the current decay is of the order of some seconds.

The powering interlock system for normal conducting magnets that is implemented is a generic solution, already in operation in many installations at CERN, such as the LHC, SPS, PSB, Linac 3 and LEIR.

The powering interlock system comprises two controllers. The first controller interfaces to power converters for 54 electrical circuits and 65 magnets of the Linac and the XT00 transfer line, whereas the second controller interfaces to power converters for 25 electrical circuits and 25 magnets of the XT01, XT02 and XT03 experimental lines. The controllers are implemented with industrial PLCs. The exchange of signals with other systems is done via input/output modules. A SCADA supervision allows

remote monitoring of all input and output statuses of both controllers, as well as the logging of faults that may occur with accurate timestamping.

The powering interlock system is designed to embrace the three phases for the project. All modifications of the machine layout between the three phases are managed by software means and recombination of interlock cables without any hardware modification on the interlock system.

## References

[1] M. Arruat et al., Front-end software architecture, Proceedings of ICALEPCS 2007, Knoxville, 2007, pp 310–312.

[2] J. L. Nougaret, Fesa essential, 2004, CERN, http://project-fesa.web.cern.ch/projectfesa/ binaries/documents/FesaEssentialsBundle.pdf.

[3] D. Lanaia, HIE-ISOLDE software report, EDMS 1389927 (CERN, 2014).

[4] D. Glenat, HIE-linac RF slow control and interlocks, EDMS 1458699 (CERN, 2014).

# Chapter 20

# Civil engineering and infrastructure

E. SIESLING

Civil engineering work and installation of the main services such as power, ventilation and cooling took place while the ISOLDE facility was running for the experiments. To guarantee a minimum of perturbation to the operation of the facility, the main services were connected and the existing services modified only during the CERN Long Shutdown 2013/14. Civil engineering work inside the experimental hall, such as the construction of the new tunnel housing the linac, as well as the move of the existing Miniball experiment to its new position were also carried out during this period of shutdown.

## 20.1 Location and vicinity

Since HIE-ISOLDE is an upgrade of the current ISOLDE facility, the location remains the same, see Figure 20.1. The installation is located in the PS complex.
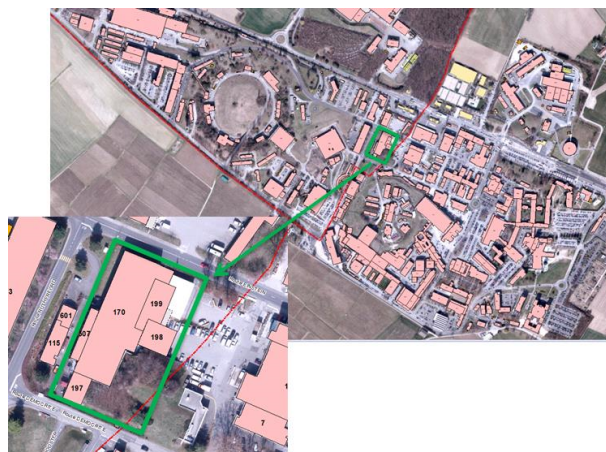


**Fig. 20.1:** Geographic location of the facility.

Only the ISOLDE experimental area is concerned in this upgrade. A design study is ongoing for the upgrade of the primary area for the high intensity part of the project but this document does not take it into account.

The safety file of the primary area of the ISOLDE facility [1] provides all the information concerning primary beam characteristics, ISOLDE location and vicinity.

## 20.2 Technical description

The HIE-ISOLDE facility consists of four principal parts:

- HIE-linac (building 170).
- High Energy Beam Transfer Lines (HEBT) (building 170).
- Compressor building (building 198).
- Cold box building (building 199).
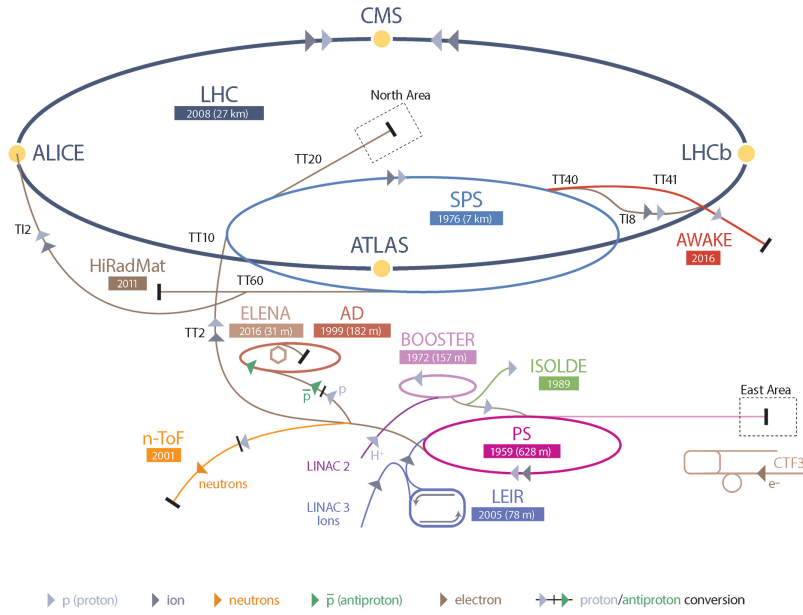
**Fig. 20.2:** ISOLDE location on the CERN accelerators layout.

HIE-linac requires a major increase of the services. For that purpose, two new buildings (198 and 199) (see Figure 20.4) were constructed to house the helium compressor station and the helium refrigerator cold box. A new gate chamber building was built to protect the material entrance from weather conditions and acts as a buffer storage area. The Demineralised Water station is located in building 197. A small parking was built next to the two new buildings.

All information regarding the evacuation plans and fire fighting equipment for each of the buildings is in [2].

**Compressor building**

The compressor building is located next to the experimental hall and cold box building, as seen in Figure 20.4. Its dimensions are approximately 17 m×15 m, i.e. a surface of around 218 m$^2$. It is a non-designated area from a radiological standpoint and is accessible through a big door (material entrance, 400 cm) and one pedestrian door (100 cm), seen in Figure 20.5; it also has an emergency exit (90 cm) to building 199. There is a main passageway to allow the transport of materials with trucks and the passage of pedestrians.

The lighting maintenance is performed using the crane. The compressors produce more than 85 dB(A); this and all other hazards present in the building are described in the HIE-ISOLDE demonstrative part [3].

The compressor building houses the following equipment (seen in Figure 20.5):

– A helium compressor station (1).
– Primary water cooling station (2).
– Cryo equipment (3).
– Ventilation units (4).
– One crane (5).

184
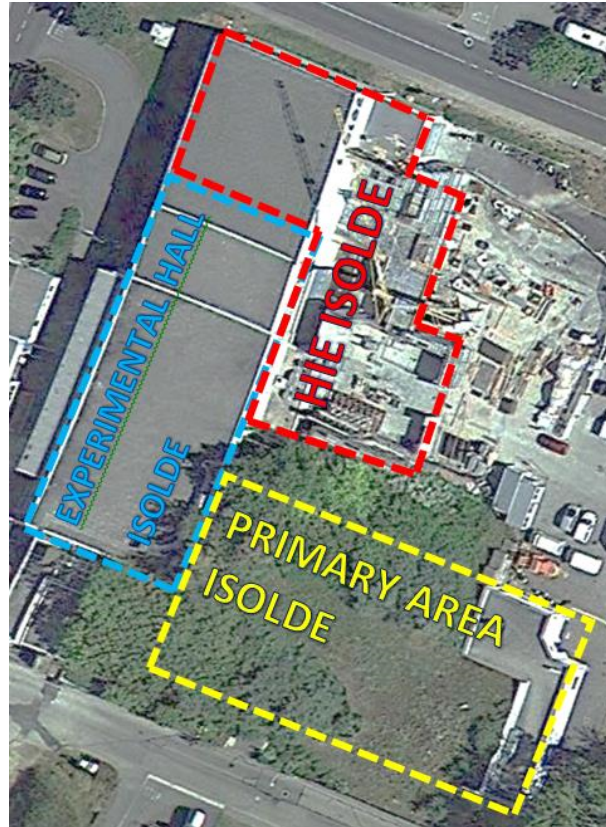
**Fig. 20.3:** Aerial view of the complex.
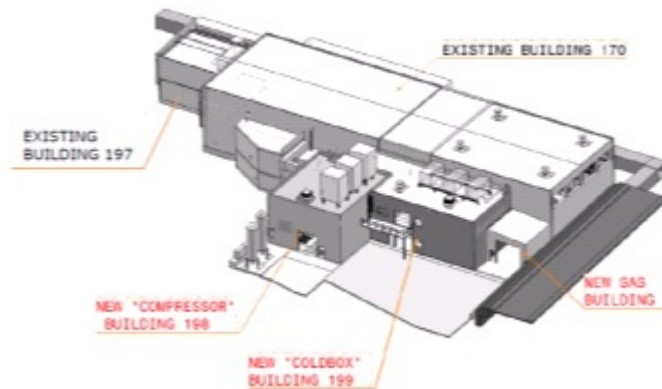


**Fig. 20.4:** Buildings for the HIE-ISOLDE project.

The ventilation units are installed on a platform; all other equipment is situated at the ground level. The roof has two cooling towers and is accessible through stairs located outside (see Figure 20.6).

**Cold Box building**

The Cold box building is located between the gate chamber building and the compressor building, as seen in Figure 20.4. The building is around 22 m long and 12 m wide, plus a small square of 6 m by 9 m, which makes a total surface of 630 m$^2$, distributed over two floors. It is a non-designated area from a radiological standpoint. There are two doors for materials (350 cm and 400 cm at the first floor), one
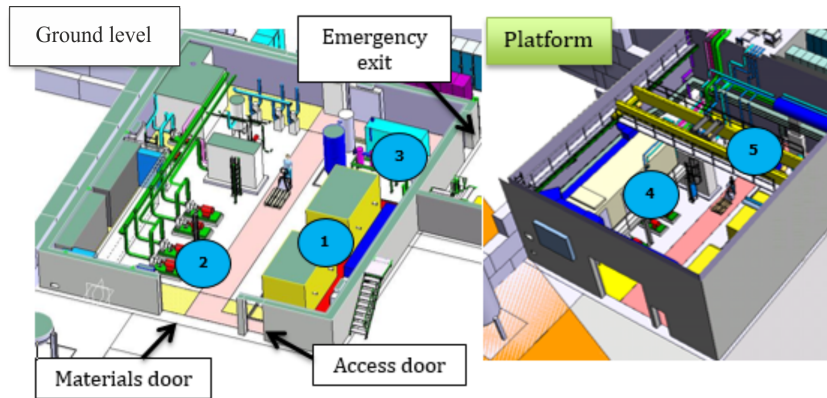
**Fig. 20.5:** Compressor Building.



**Fig. 20.6:** Layout of buildings 198 and 199.

access door for pedestrians (100 cm) and two emergency exits (90 cm), seen in Figure 20.7. Building 170 is only accessible through a revolving door located in the ground floor.

The lighting maintenance is performed using a mobile platform; to avoid possible problems, the lighting system has not been installed above the cold box. All hazards present in the building — cryogenics related, among others— are described in the HIE-ISOLDE demonstrative part [3].

Building 199 houses the following equipment, seen in Figure 20.7:

– A helium cold box and a helium dewar (2000 litres capacity) (1).
– Cryogenic control room (2).
– Electrical and control racks (3).
– Access door to building 170 (4).
– UPS (5).
– Distribution UPS (6).
– 3.3 kV Station (7).
– 400 V Station (8).
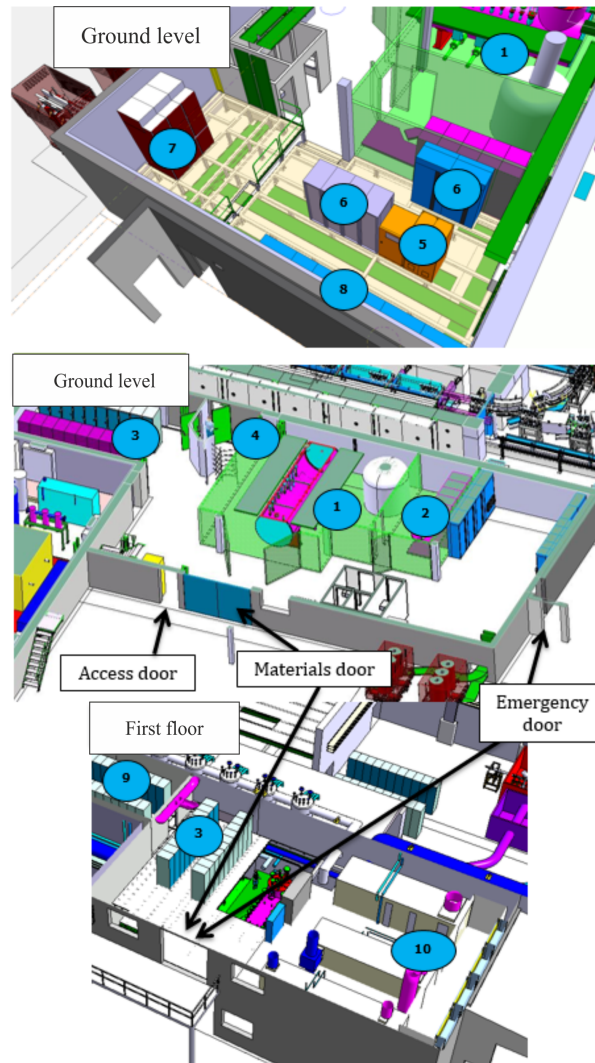
**Fig. 20.7:** Cold Box building disposition.

– Faraday Cage (9).
– Ventilation units and fresh air plenum (10).

The roof of building 199, which is accessible through stairs situated outside, has two chillers, as can be seen in Figure 20.6.

**Experimental hall**

The experimental hall, seen in Figure 20.8, is located in building 170. The building is a Supervised Area, class C work sector [4], however, it is foreseen that the area will be classified as Simple Controlled before operation resumes after LS1. The experimental hall is separated in the low-energy area, which remains the same, and the high-energy area, which houses the linac and HEBT.

During operation, dose rates inside the linac exceed 100 mSv/h due to X-rays generated by radiofrequency. For this reason, access to the linac is be forbidden during operation. The main access door is locked with the same key used for the RF control to ensure the absence of personnel inside the shielding enclosure during RF operation. Access to the roof is also restricted with a locked physical barrier due to high dose rate.
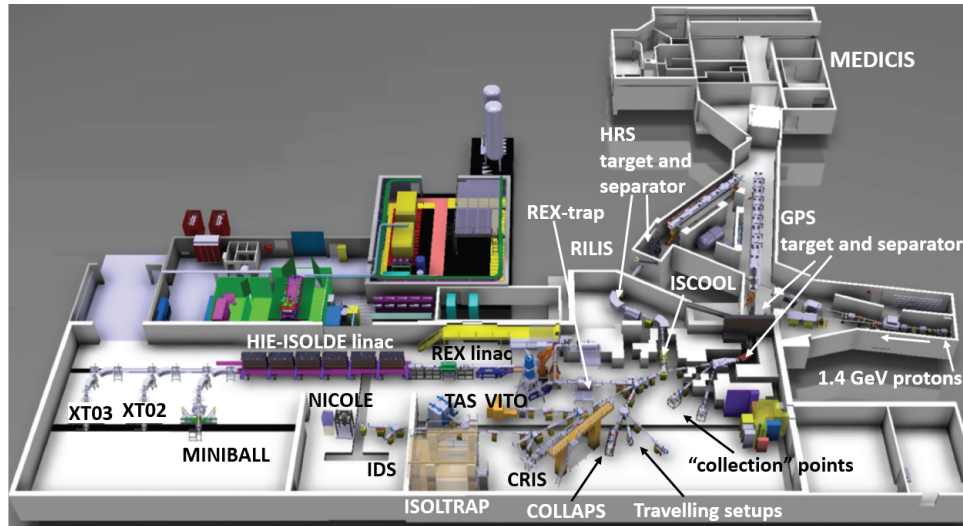
**Fig. 20.8:** 3D view of the ISOLDE experimental hall.

During shutdown, the access system is same as the ISOLDE one. The technical specifications of the existing system can be found in [5].

**References**

[1] E. A. Macario, Descriptive part : Zone cible, zones séparateurs, salle de controle, EDMS 1168185 (CERN, 2013).

[2] A. Sprang and L. Mora, Descriptive part HIE-ISOLDE buildings: Escape routes and fire fighting equipment, EDMS 1189202 (CERN).

[3] C. Lemesre, L. Kobzeva and L. Mora, HIE-ISOLDE safety file – demonstrative part, EDMS 1308956 (CERN).

[4] HSE, Radiological risk areas inventory (RAISIN), https://service-raisin.web.cern.ch.

[5] D. Voulot, Safety file – REX-ISOLDE linac shielding tunnel, EDMS 1016852 (CERN, 2013).

# Chapter 21

# Cranes and handling tools

C. BERTONE

## 21.1 Crane in building 170

A big staircase and access platform to the crane was installed inside the building along the north wall. For that reason, the hook coverage in this area was not good. With the design of HIE-ISOLDE and the definition of the access area just toward this wall, this situation was not compliant for the unloading of trucks, nor with the installation of the new accelerator lines. In fact, hook coverage did not even include the mid-point of the material door.

As a consequence, the size of the platform has been significantly reduced and access to the crane is now possible from below the catwalk by a dedicated staircase that is concealed inside the crane structure when not used. A couple of laser cells are blocking crane movements when the staircase is below (access position). This allowed increasing the hook coverage more than 1 m and ensured good coverage of the door area and HIE-ISOLDE developments.To limit shocks during handling, a continuous variable speed control has been installed on the three movements of the building crane.

## 21.2 Shielded door in building 170

The HIE-ISOLDE linac installed inside the bunker needed a rapid access way. A motorised shielded door [1] made of concrete was developed and installed to allow rapid access and proper protection when equipment is pressurised and the accelerator is on. It measures 2250 mm in length, 2800 mm in height, 800 mm in width and has a mass of 18 t. It is interlocked with the beam permit.

## 21.3 Crane in building 198

Building 199 has been equipped with a double girder 5 t crane for everyday maintenance of the equipment inside.

## 21.4 Tooling: intertank installation tooling

Between cryomodules, a small element called "intertank" [2] is installed. It is composed by several ancillary systems assembled on a unique short support. Its weight of about 120 kg prevents manual installation.

The difficulty of the installation is that this element is installed between two vertical walls, i.e. the two cryomodule sides. The intertank had to be moved above its installation point and then transferred in suspension and unloaded at its final destination.

There was no possibility to suspend the load from the wall, since the space above the cryomodules is crowded. The possibility to create a bridge between cryomodules on which the transfer rail would be suspended was excluded, since this could potentially misalign them. Moreover, the intertank surroundings vary from one place to another. The possibility to install a rail from a tunnel wall to another was discarded because this one had to be removed after installation and the chance of it falling over the intertank was too big. The solution consisted of installing an extruding rail on one forklift [3]. The intertank was suspended to a tool that was attached to the forks of a forklift. Once in place, this tool extended
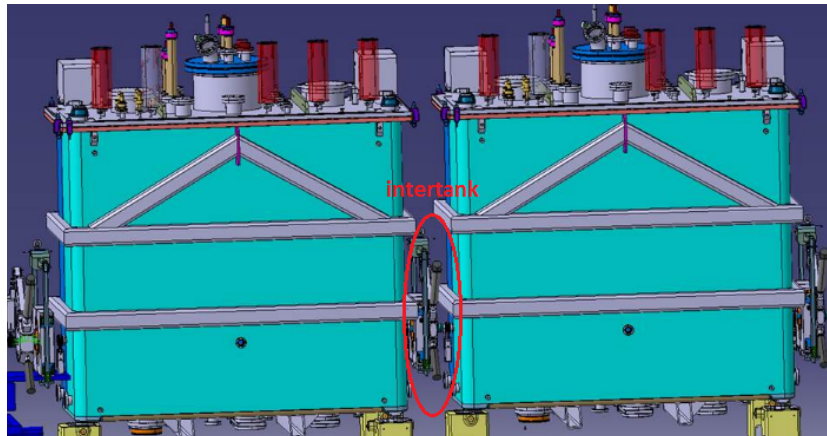
**Fig. 21.1:** Schematic of the intertank section.

laterally and entered the zone between the two tanks. It was then possible to move the intertank in its final position via this rail and correct the placement via the forklift (height, longitudinal position, etc.).

## 21.5   Tooling: spreader for power converters

To handle the S500 Comet power converters installed in HIE-ISOLDE, a tailor-made spreader with 3 t lifting capacity was designed and procured [4]. It had to be adapted to the particular shape of the upper lifting points and the limited room for maneuvering with the crane above the already installed power converters. The outcome is a particularly compact tool, as Figure 21.2 shows.



**Fig. 21.2:** Three-tier control system.

## References

[1]  F. Delsaux, Bat 170-blindage mobile + rails, EDMS ISLHHJ__0001 (CERN, 2013).

[2] E. Urrutia, HIE-ISOLDE linac – XLN2 intertank general assembly, EDMS ISLLMCBA0033 (CERN).

[3] F. Delsaux, Outillage manutention intertanks, EDMS ISLHHJ__0113 (CERN, 2015).

[4] J. Bonnamy, COMET S500's lifting beam, EDMS ISLHKLDV0001 (CERN, 2015).

# Chapter 22

# Cooling and ventilation

P. PEPINSTER

## 22.1 Cooling

The cooling system is composed of the primary cooling system, equipped with cooling towers, which are located on the roof of building 198 (primary water), and of a redesigned secondary cooling station located in building 197 (demineralised water). Besides that, a part of the HIE-ISOLDE equipment is cooled down by means of mixed water, which is provided by chillers located on the roof of building 199. The reasons for designing and installing of a new primary cooling system at ISOLDE were the following:

– Replace the existing tap water cooling open circuit, which disposed water to the sewage after use (environmental issue), by a closed circuit with cooling towers.
– Provide primary water cooling to the new cryo compressing station.
– Provide appropriate cooling power to cover the new cooling needs.

**Operating conditions**

Primary (or raw) water cooling (RW), provided by cooling towers, is needed for the cooling of the cold box and of the cryogenic compressors, as well as for the primary cooling of the demineralised water cooling station.

The adoption of a primary closed circuit with cooling towers leads to an evolution of the operating temperature conditions in the secondary side cooling (demi water) for the ISOLDE equipment as shown Table 22.1. Demineralised water (DW) cooling at maximum 27°C is acceptable for the magnet lines,

**Table 22.1:** Evolution of the Demineralised Water cooling parameters.

| Demi water | Supply temperature [°C] | Maximum return temperature [°C] | Temperature range [K] |
|---|---|---|---|
| Former operating conditions (ISOLDE) | 20 | 35 | 15 |
| New operating conditions (HIE-ISOLDE) | 27 | 37 | 10 |

power converters, radiofrequency racks for the SC-Linac and other vacuum equipment.

The accelerating cavities and RF amplifiers of HIE-Linac, which used to be supplied with demineralised water at 20°C, cannot accept the new DW temperature at 27°C. A separated mixed water cooling circuit at maximum 20°C is required for them. The operating conditions given at Table 22.2 result from the parameters requested by the users, i.e. required flowrate and heat dissipation.

**Separation of the BTY magnets cooling**

For safety reasons, the separation of the cooling of the BTY magnets from the overall demineralised water cooling system has been implemented in order to avoid the circulation of contaminated water throughout the ISOLDE hall.

**Table 22.2:** Mixed water cooling parameters.

| Mixed water | Supply temperature [$^\circ$C] | Maximum return temperature [$^\circ$C] | Temperature range [K] |
|---|---|---|---|
| Operating conditions (HIE-ISOLDE) | 20 | 22.5 | 2.5 |

These magnets now have a dedicated cooling circuit that goes directly from the building 197 cooling station to the ISOLDE tunnel.

**Technical description**

The primary cooling system (see drawing [1]) consists in two cooling towers of 2 MW (N+1 redundancy) providing raw water cooling at a temperature range of $35 - 25^\circ$ C (return temperature —supply temperature) under extreme summer conditions, and of two distribution circuits each equipped with two motor-pump sets (N+1 redundancy).

The first circuit [PTB-511/521] is dedicated to the cooling of the cryogenic equipment (compressors and cold box) and the second circuit [PTB-531/541] is dedicated to the primary cooling of the demineralised water cooling station in building 197.

The primary cooling system is equipped with a sand filter, a water make-up system and a water treatment plant.

Table 22.1 shows how the system has been sized according to the initial user requirements and what is the cooling capacity that remains available today.

**Table 22.3:** Primary water thermal balance.

| Primary water distribution circuit for: | Users | Baseline Installing heat loads [a] [kW] | Final heat cooling capacity [b] [kW] | Available loads as built [kW] | cooling capacity [c] [kW] |
|---|---|---|---|---|---|
| Cryo (B198-199) | Compressors [d] | 752 | 882 | 500 | 347 |
| | Cold box | 35 | | 35 | |
| Demi water primary cooling | Cooling station B197 | 718 | 1045 | 615 | 430 |
| **Total** | | **1496** | **1927** | **1150** | **777** |
| Cooling towers | | | 2000 | | |

[a] Following user requirements.
[b] Given by the nominal flowrate of the primary water distribution pumps.
[c] Available cooling capacity is here purely theoretical, being deducted from the design data. The real values could only be known after on-site measurements in nominal operating conditions.
[d] The baseline of the project included two compressors of 376 kW each.

A new demi water cooling station has been installed in building 197 (see drawing [2]), in replacement of the former ISOLDE cooling station. The latest has been dismantled except the "target tunnel" cooling circuit which remains as it was. Besides the target circuit, the cooling station consists of two cooling circuits, each equipped with one heat exchanger and two motor-pump sets (N+1 redundancy). The first circuit [PPC-0701/0702] distributes demineralised water at $27^\circ$ C to building 170 whose hydraulic layout is slightly modified compared to before the HIE-ISOLDE project. The modifications are:

– Disconnection of the RF room from the demi water circuit and reconnection to the mixed water circuit, except the 9GP amplifier.

– Connection of the 9GP amplifier to the demi water circuit.

– Addition of booster pumps [PPC-0703/0704] to increase the available differential pressure from 7 bars (hall 170 circuit) to 10 bars as required for the HIE magnets.

The second circuit [PPC-0711/0712] is dedicated to the cooling of the BTY magnets.

A mixed water plant provides the necessary cooling at $14^\circ$C for the HVAC systems, and at $20^\circ$C the radiofrequency amplifiers and cavities (see drawing [3]). Two screw compressors (redundancy N+1), air-cooled chillers units, are installed on the roof of building 199. Each compressor has a cooling capacity to cover the maximum cooling demand.

The two evaporator pumps are installed at ground level of building 198 and separated from the distribution circuits by means of a buffer tank.

## 22.2   Heating, Ventilation, Air Conditioning (HVAC)

The goal of the HVAC system is to maintain appropriate indoor conditions at each building with regard to the operating requirements of the hosted equipment and to conform to criteria for the personnel working inside while respecting applicable standards and rules.

The indoor conditions required for the project are summarised in Table 22.4.

**Table 22.4:** Required indoor conditions.

| Zones | Temperature [$^\circ$C] | | Humidity |
|-------|-------|--------|----------|
| | **Winter** | **Summer** | |
| 198 | $18 \pm 2$ | $26 \pm 2$ | Not controlled |
| 199 | $18 \pm 2$ | $26 \pm 2$ | Not controlled |
| 199 - Faraday Racks room | $22 \pm 2$ | $22 \pm 2$ | Not controlled |
| 170 | $18 \pm 2$ | $26 \pm 2$ | Not controlled |

It must be highlighted that the Linac tunnel room conditions are not controlled and that the ventilation of this space is only assured by natural convection phenomena across the openings located at the lower and upper levels of the concrete shielding blocks.

**Technical description**

All the air handling units are designed to work in free-cooling (i.e. cooling capacity of the outside air) whenever possible, and to assure a minimum of hygienic air renewal in the buildings. Each of the processes described below is equipped with its own control cubicle.

The air handling unit UAPX-00288 is located on a steel structure platform inside building 198. It supplies the air-conditioning for the compressor building through a duct network and air displacement grilles.

Excess air, corresponding to the fresh air flowrate introduced in the building, escapes outside the building through two static exhausts (UAT1-00014 and UAT1-00015) located on the roof.

The air handling unit UAPX-00285 is located at first floor of building 199. It supplies air-conditioning for the cold box building through a duct network which splits itself in two antennas, respectively distributing the ground floor and the first floor. These ducts are equipped with air supply grilles.

Excess air, corresponding to the fresh air flowrate introduced in the building, escapes outside the building through two static exhausts (UAT1-00016 and UAT1-00017) located on the roof. A common

fresh air plenum equipped with noise attenuators and pre-filters has been built to feed all the air handling units building 199.

The Faraday racks are located in a dedicated room at first floor of the building. They are conditioned by means of two redundant air handling units UAPX-00286 and UAPX-00287 (one duty, one spare), the spare starting automatically in case of failure of the duty. UAPX-00286/287 are located at the first floor of building 199, and blow the air directly inside the Faraday racks at constant temperature of $22^{\circ}$C by means of two ducts each located below the racks row. Excess air, corresponding to the fresh air flowrate introduced in the room, escapes outside the room through an overpressure damper located on above the access door.

The air handling unit UAPX-00284 is located at first floor of building 199 and is separated from building 170 by two fire dampers (air supply duct and air recycling duct). The AHU supplies the air for the ISOLDE extension hall through a duct network and air displacement diffusers. Excess air, corresponding to the fresh air flowrate introduced in the building, escapes outside the building by means of two dampers installed at the upper level of the Gex-side facade. Two roof smoke extractors (UAT2-00013 and UAT2-00014) are foreseen to extract smoke from building 170 in case of fire. The dedicated switchboard (coffret pompiers) is located in the vicinity of the building's main entrance.

A mixed water plant provides the necessary water cooling for the HVAC systems, and to the radiofrequency amplifiers and cavities. Two screw compressors, air-cooled chillers units, are installed on the roof of building 199 to produce water at $13^{\circ}$C. Each compressor has a cooling capacity of $100\%$ of the maximum cooling demand. The two evaporator pumps are installed at ground level of building 198, and separated from the distribution circuits by means of a buffer tank. On the distribution side, two separate circuits are dedicated to the feeding of the air handling units cooling coils at $14^{\circ}$C, respectively to the radiofrequency amplifiers and cavities with mixed water at $20^{\circ}$C.

# References

[1]  F. Borralho, Primary water production and distribution, EDMS ISLF01980009 (CERN, 2015).

[2]  F. Borralho, Demineralized water cooling station, EDMS ISLF01970006 (CERN, 2015).

[3]  F. Borralho, Demineralized water distribution bldg.170, EDMS ISLF01700008 (CERN, 2015).

# Chapter 23

# Electrical system

R. NECCA

## 23.1 General supply and autotransfer

The CERN general electrical power source and auto transfer is the same as at ISOLDE; more information can be found in [1]. However, some modifications have been made to distribute electrical power to the existing facilities and new buildings (198 and 199).

The ISOLDE facility is supplied by the electrical sub-station M80, which is part of a loop that includes other sub-stations, as shown in Figure 23.1.
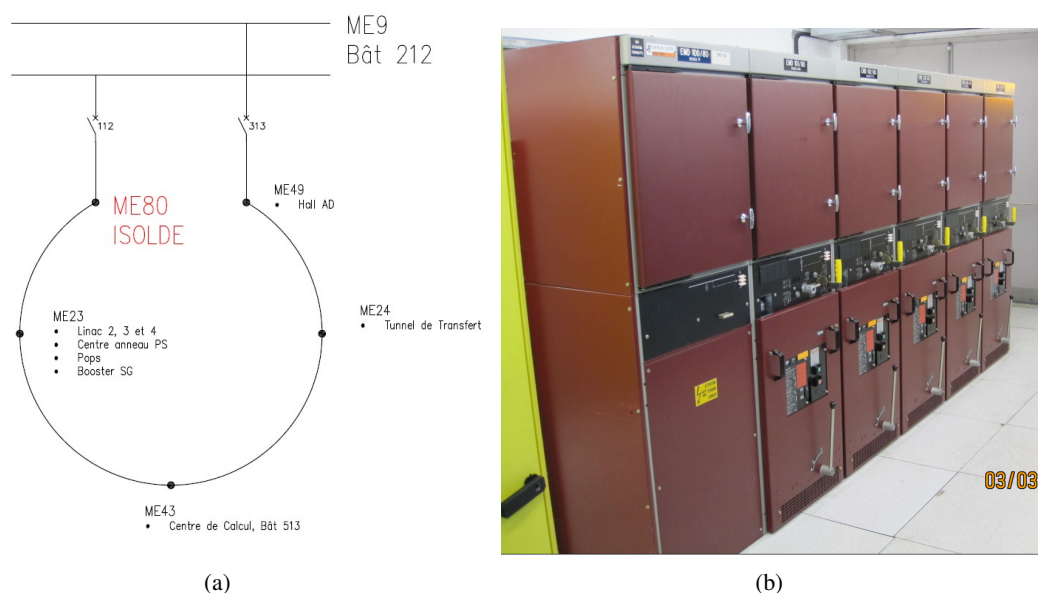


**Fig. 23.1:** Electrical supply diagram (a) and photo of the 18kV rack (b) of the ME80 station.

The power source that feeds the ME9 station can be switched thanks to an automatism called auto-transfer. An 18 kV automatic source transfer exists between the two 400 kV and 130 kV incomers. In case of a main failure on the bus-bar in service, the load is transferred to the other source. The source transfer causes a supply interruption of about 30 seconds.

Two transformers are installed, one (3.3 kV) to supply the cryogenic compressors and the other (400 V) to supply all other installations (power converters, experiments, cooling system, vacuum system and beam lines). The old one supplies the general services. These transformers are located next to the cold box building.

All information regarding the new electrical installation can be found in [2].

## 23.2 Power supply without interruption (UPS)

In case of failure of the normal network, the UPS automatically takes over and provides power to some equipment for a given time according to its load. Although there is a UPS system in the old ISOLDE

part, the total power needed for HIE-ISOLDE is too high (56.5 kW), therefore a new UPS system with a total capacity for 100 kW will be installed in HIE-ISOLDE. The UPS supplies the interlock system, the cryogenic system (buildings 198 and 199) and Faraday cages. The UPS used is B9000FXS 100 kVA; all technical specifications can be found in ANNEX 2 of [3]. There is one UPS, located at the ground floor of building 199.
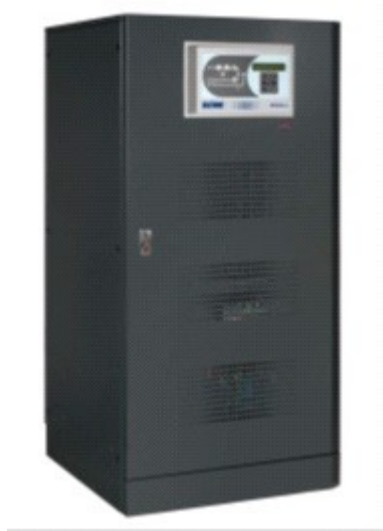


**Fig. 23.2:** UPS B9000 FXS.

The UPS system has four different operating modes [4]:

– Normal operation: during normal operation all the circuit breakers/isolators are closed, except for maintenance bypass.
– Bypass operation: the load can be switched to bypass either automatically or manually.
– Battery operation: in case of power failure or rectifier fault, the battery feeds the inverter without interruption.
– Manual bypass: the manual bypass operation is necessary whenever the UPS functionality is tested and during maintenance or repair work.

The UPS is equipped with two independent temperature sensors which are designed for protection in case of failure of ventilation (internal fans UPS off) or air conditioning (excessive ambient temperature). Upon activation of one of these two sensors, the UPS decouples and transfers the output to the bypass.

A maintenance performed by the manufacturer is scheduled every year. The different operating modes and the battery's life (ten minutes at full load) are tested. Since the UPS does not supply equipment devoted to the safety of persons, it is not intended to be fed via the emergency network, (the UPS system does supply such equipment in case of loss of power until the emergency network takes over).

## 23.3   Emergency network

The emergency network (dedicated to the safety of persons) is powered by the normal network in normal operation. In case of loss of power, the network is backed-up by the diesel generators in the JURA sub-station (ME9).

The sub-station is equipped with three diesel generators with a total power of 7.2 MVA. The recovery time of the emergency system through the diesel generators is approximately 30 seconds. Cou-

pled with the autonomy of the UPS network, it ensures that no off time is perceived by the equipment described above.

The emergency network underwent some modifications in order to install an emergency line connected directly to HIE-ISOLDE. It covers the smoke extraction system, fire detection and ODH system.

## References

[1] E. A. Macario, Descriptive part : Zone cible, zones séparateurs, salle de controle, EDMS 1168185 (CERN, 2013).

[2] R. Necca, Electrical planning HIE-ISOLDE project, EDMS 1143514 (CERN, 2011).

[3] L. Mora, HIE-ISOLDE safety file descriptive part, EDMS 1258062 (CERN, 2014).

[4] BORRI, Industrial Power Solutions, *Operating Manual UPS, B9000FXS 60-80-100-125-160kVA*.

# Chapter 24

# Power converters

M. MARTINO

The proposed power converters make use of the most advanced technology in the power conversion domain, taking advantage of the most recent advancements in the field of the medium-low voltage semi-conductors, commercial power supplies, switch-mode power supplies, control and measurement electronics. All power converters work in DC operation mode; they can all reach their nominal current within 5 s, however the ones powering the SC solenoids are software-limited to a much slower time to avoid quenches. All converters share the same main features: high efficiency, forced air cooling, redundant current sensing (by means of 2 DCCTs) and CERN EPC control and measurement electronics. There are four different types of power converters, one for each different type of magnet, as reported in Table 24.1. Each magnet is individually powered by a dedicated power converter, except for the HEBT correctors, which have two independent circuits (horizontal and vertical correction) and therefore two independent power converters. All power converters, except the ones powering the HEBT dipoles, are modular: they are composed of a power module (voltage source), which is housed in a 19" standard rack, and by dedicated measurement and control electronics, which can be housed either inside the power module itself or in the dedicated rack.

**Table 24.1:** Different types of power converter classified per magnet type.

| Magnet | Converter name | Assembly |
|---|---|---|
| HEBT Dipole | COMET_2p | Monolithic |
| HEBT/REX Quadrupole | COBALT | Modular |
| HEBT Corrector | CANCUN | Modular |
| Linac SC Solenoid | LHC120A10V HEj | Modular |

## 24.1  COMET_2p (COnfigurable MEdium power converTer)

COMET is a low-medium power solution (60 kW peak power) based on a main module rated 120 V/ $\sin 250$ Apk. For the COMET module, a 50 Hz transformer (galvanic isolation—voltage adaptation—phase shift), a diode rectifier, and a DC-Link filter are used for the AC/DC conversion. An IGBT bridge (four-quadrant operation) with an output filter are used for DC/DC conversion. The energy of the magnet is (i) recovered in a capacitors bank on the DC-Link during the cycling mode of operation, (ii) dissipated in a brake chopper in case of too small energy storage on the DC-Link, (iii) dissipated in a bipolar crowbar in case of fault. Two COMET modules are assembled in parallel to increase the current capability (COMET_2p) and achieve the requested ratings for the HEBT dipoles.

## 24.2  B-field regulation

For the HEBT dipoles, a direct B-field feedback regulation is implemented. B-field is measured in a calibrated position inside the magnet by means of the AS-NTM-2 Hall-probe. Its value is sampled by means of an FGC3 used as a local digitiser (each FGC3 acquires the B-field of the two dipoles of each of the XT01, XT02 and XT03 lines). The measured B-field is then "published" on the local Ethernet network. The upcoming software libraries will allow FGC3 to handle this feature internally: the "power" FGC3

**Table 24.2:** COMET_2p main parameters.

| Parameter | Value |
|---|---|
| Ratings | $\pm500$ A / $\pm120$ V |
| Precision | $\pm100$ ppm [of 500 A] |
| Allowable Load | [10 m$\Omega$; 240m$\Omega$] / [1 mH; 100 mH] |
| Dissipated Power | 6 kW |
| Input AC | 3-phase (no neutral) 400 V - 63 A$_{rms}$ |
| Cooling | Forced Air (Fan) |
| Weight | 1150 kg |



(a)



(b)
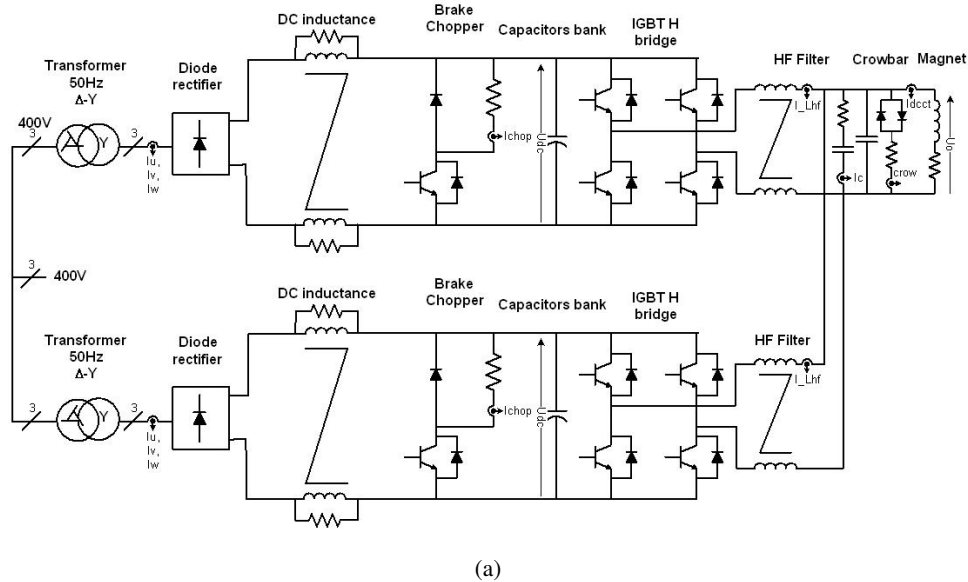
**Fig. 24.1:** COMET_2p: (a) simplified schematic, (b) picture of the full converter (control electronics excluded).

unit that controls the COMET_2p converter for a given dipole will close the control loop, settling the voltage reference of the converter according to the measured value of the B-field. Before that, the B-field regulation loop will be implemented by a software module running in the FEC (Front End Computer) as shown in Figure 24.2. This module implements an integral control with adaptive gain correction that sets the current reference of the regulating FGC3 (which in turn implements a sophisticated RST current regulation, as described in subsection 24.7).

## 24.3  COBALT (COnverter Brick Adapted to control Loop Tuning)

COBALT is a versatile 10 kW, 200 A, 50 V one-quadrant power converter. The converter is the assembly of a power module, a voltage source, built in accordance with a CERN technical specification, [1], and located in a CERN-designed power rack. The topology of the converter is based on two cascade power stages: the first stage is in charge of providing an isolated constant voltage level to the input of the second stage. It is based on a LLC inverter, which provides very good efficiency, highly limiting commutation losses. The second power stage is based on two buck converters operating in parallel, delivering the final output voltage to the load. The two power stages are using SiC components, which provide an overall very low level of losses on semiconductors. The power rack is equipped with up to three power modules, which give up to almost 5 kW to be extracted without perturbing the high precision elements. An original design, based on purely passive individual chimneys (one per power module) was chosen to guarantee a temperature increase of less than three degrees for the high precision components from 0 W to 30 kW (10 kW per converter). The power rack also guarantees fast exchange of any faulty component and integrates output current limitation circuitry, which also features remote monitoring.

**Table 24.3:** COBALT main parameters.

| Parameter | Value |
|---|---|
| Ratings | 200 A / 10 V |
| Precision | $\pm 100$ ppm [of 200 A] |
| Allowable Load | [0.01 m$\Omega$; 1 $\Omega$] / [0 mH; 200 mH] |
| Dissipated Power | $\leq$ 1.4 kW (depending on use) |
| Input AC | 3-phase (with neutral) 230 V - 20 A$_{rms}$ |
| Cooling | Forced Air (Fan) |
| Weight | 55 kg |

## 24.4  Polarity Reversal Unit

The Polarity Reversal Unit is designed relying on the use of Bi-stable DC-Contactors type providing the capability of inverting the load output polarity, with maximum safety; a complete loss of AC power will indeed not provoke the opening of the bi-stable switches. The purpose of this unit is to allow the use of an one-quadrant converter providing negative or positive current to the load. The inversion is done at 0 A, ideally, controlling the unit polarity by means of FGC3. Its power module is an air cooled plug-in module that has been entirely designed at CERN and is mechanically compatible with 19" standard dimensions. The Polarity Reversal Unit can also be integrated in a demanding environment, where up to two external systems can interlock the unit: additional interfaces provide an interlock input signal blocking the polarity switch, positive or negative, and a fault status. The unit is also inherently protected against a polarity inversion above a predefined current threshold. Freewheeling diodes are included in the polarity switch, ensuring a safe path for a high inductance – high time constant – magnet. Polarity Reversal Units equip the following circuits: XT00.RQ.100, XT00.RQ.300, XT00.RQ.300 and XT00.RQ.500.

## Architecture Overview
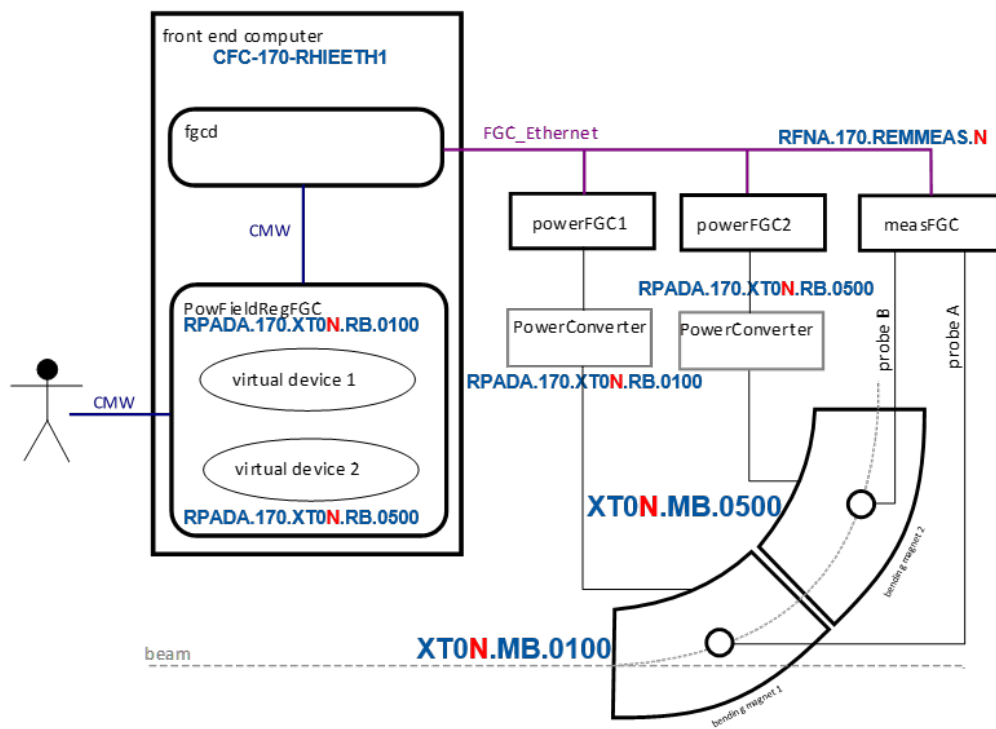


(a)

## Logical View
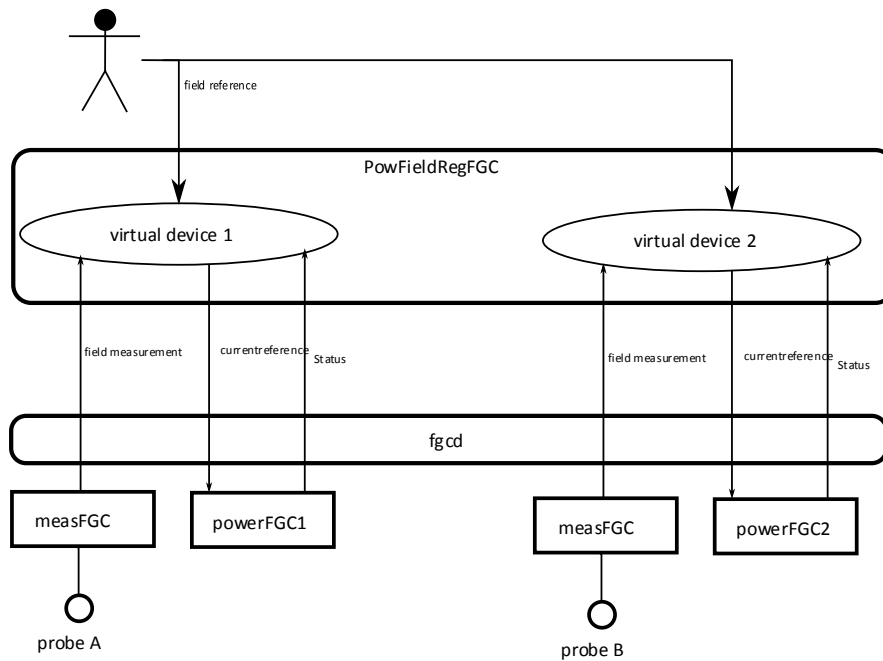


(b)

**Fig. 24.2:** Software layout of the B-field regulation - FEC Implementation.

(a)



(b)

**Fig. 24.3:** COBALT: (a) simplified schematic, (b) picture of the power module.

**Table 24.4:** Polarity Reversal Unit main parameters.

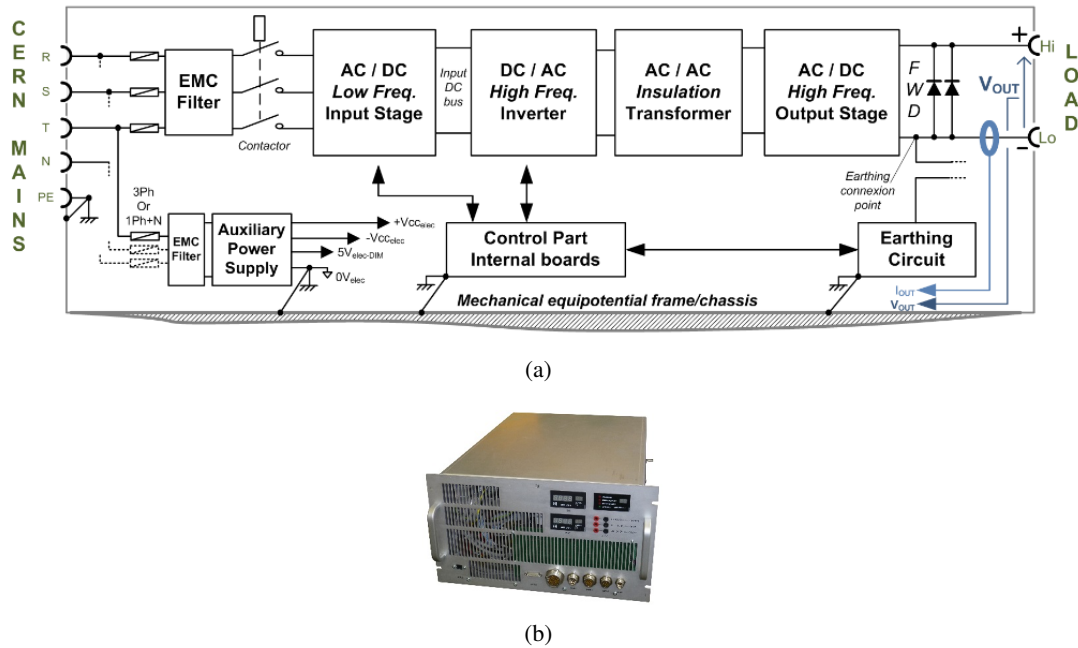| Parameter | Value |
|---|---|
| Ratings | 300 A / 80 V |
| Dissipated Power | $< 0.135$ kW (depending on use) |
| Input AC | 1-phase + neutral $230V_{ac}$ ; $< 1A_{rms}$ |
| Cooling | Forced Air (Fan) |
| Weight | 25 kg |

## 24.5 CANCUN (Cern Acdc Narrow CoNverter)

CERN makes extensive use of true bipolar power converters, with a regulated high precision output current requirement and high bandwidth for corrector magnets. Special design and topology allow high performance throughout the converter operating area, including quadrant transitions. The CANCUN design is adapted for a wide range of magnet loads, from 10 $\mu$H to 100 mH, with stringent EMC requirements. The converter module is equipped with a quick-connect system to allow easy installation and maintenance operations. The converter uses very well-known phase-shifted DC/DC power converter topology. The intermediate high frequency DC/DC converter results in a small size/ low weight power module. A three-level modulation provides excellent quadrant transitions.

## 24.6 SC solenoids – LHC 120 A 10 V High Ej

This converter is a slightly modified version of the LHC 120 A 10 V converter used in the LHC, comprising an upgraded crowbar (its resistor, mainly) capable of handling 19 kJ of energy. The voltage source is based on a full bridge phase shifted topology followed by a four quadrant linear stage to allow the converter to provide energy to the magnet or to retrieve energy from it, depending on the current reference to be followed. This topology gives a very low output EMC noise level, at a cost of complexity with regards to the four quadrant linear stage, combining several regulation loops: the main control loop, an additional circulating current loop and another one controlling the IGBT based high switching frequency DC/DC stage 24.6. [2]

(a)



(b)
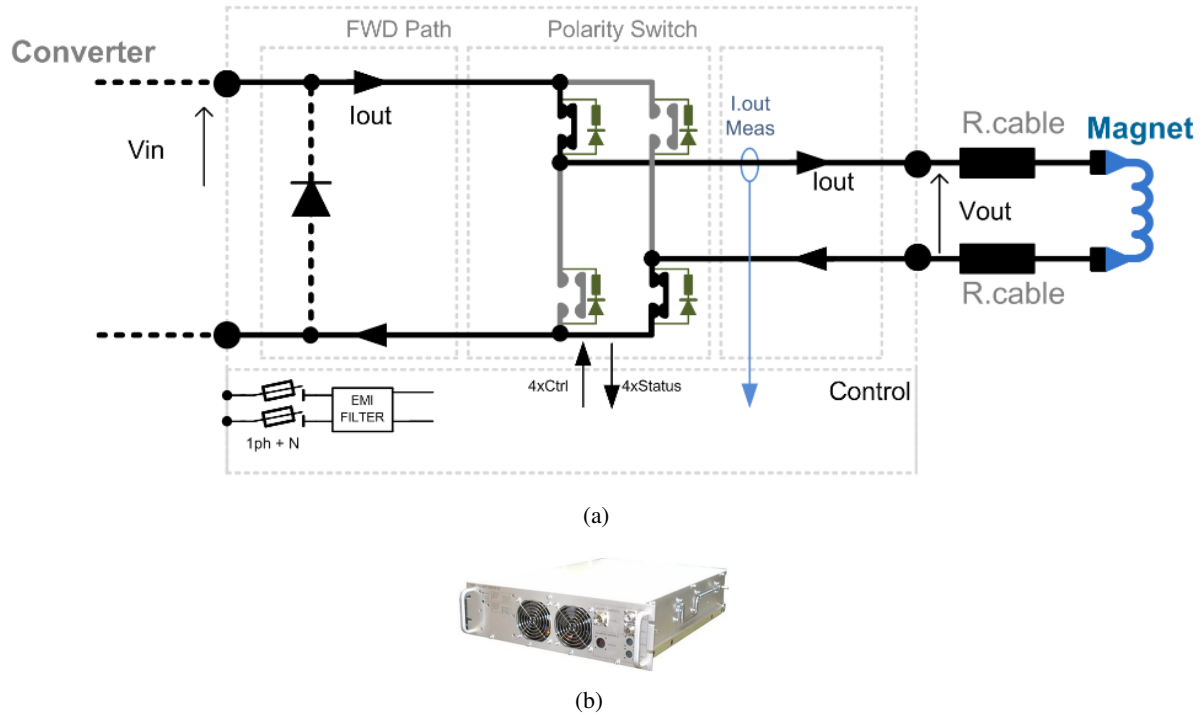
**Fig. 24.4:** COBALT Polarity Reversal Unit: (a) simplified schematic, (b) picture of the module.

**Table 24.5:** CANCUN Main Parameters.

| Parameter | Value |
|---|---|
| Ratings | $\pm 50$ A / $\pm 30\text{V}_{PEAK}$ |
| Precision | $\pm 100$ ppm [of 50 A] |
| Allowable Load | [10m$\Omega$; 600 m$\Omega$] / [10 $\mu$H; 100 mH] |
| Dissipated Power | 0.35 kW |
| Input AC | 3-phase (with neutral) 230 V - 3A$_{rms}$ per phase |
| Cooling | Forced Air (Fan) |
| Weight | 29 kg |

**Table 24.6:** LHC120A10V High Ej Main Parameters.

| Parameter | Value |
|---|---|
| Ratings | $\pm 120$ A / $\pm 10$ V |
| Precision | $\pm 100$ ppm [of 120 A] |
| Allowable Load | [1 m$\Omega$; 1 $\Omega$] / [10 mH; 2.37 H] |
| Dissipated Power | 0.6 kW |
| Input AC | 3-phase (with neutral) 230 V 3 A$_{rms}$ per phase |
| Cooling | Forced Air (Fan) |
| Weight | 47 kg |

(a)



(b)
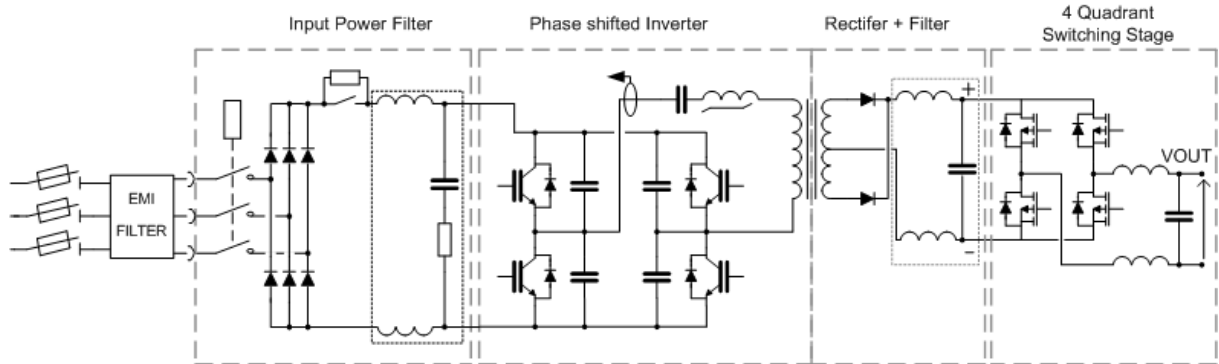
**Fig. 24.5:** CANCUN: (a) simplified schematic, (b) picture of the full converter (control electronics included).
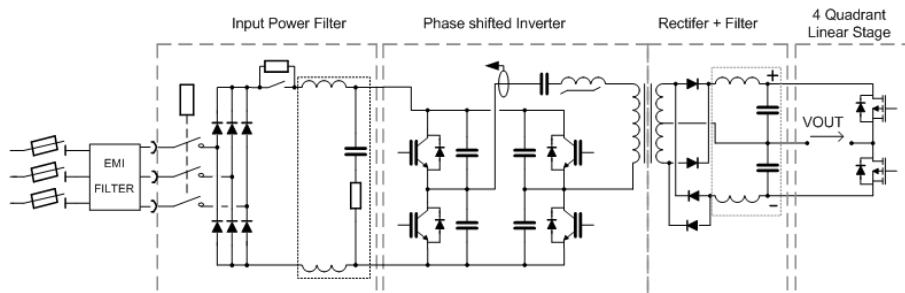


(a)



(b)
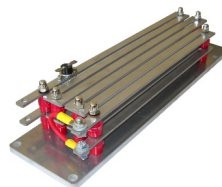


(c)

**Fig. 24.6:** LHC120A10V: (a) simplified schematic, (b) picture of the power module and (c) the specific crowbar resistor.

The crowbar is based on a 70 mΩ Power Resistance series 2× back-to-back thyristors (TT142N12KOF, [142 A; 1200 V]) being fired at a given output voltage (±13 V) and then providing a safe path for magnet current. The energy that the crowbar can handle is based on a 2.37 H magnet at 116 A, which amounts to a maximum of less than 19 kJ. It should be noted that a power module dying with its output stage (Power Mosfet based) in short-circuit would prevent the crowbar from dissipating magnet energy. However, this potentially dangerous failure case does not present any risk for the SC solenoid, which can handle its own energy, so no DC contactor in series is provided. [3].

## 24.7 Control

Control is based on custom EPC FGC (Function Generator Controller) architecture [4]. Two different versions are used: FGC2, which controls the LHC 120 A 10 V High Ej for the SC solenoids, and FGC3, which controls all other circuits. The FGC2 adopts WorldFIP fieldbus, whereas the FGC3 adopts the Ethernet FGC_Ether fieldbus. The functionalities of the two versions are very similar, so only FGC3 will be detailed. The FGC3 module acts at the same time as the digital feedback controller of the converter's current (or magnet's B-field) by means of an RST algorithm and as an interface to the CERN control hardware/software infrastructure as shown in Figures 24.7 and 24.8 [5]. The control electronics for FGC3 (COMET_2p and CANCUN) is called RegFGC3 and consists of a standard 19" crate, in which EPC dedicated electronics boards are connected to implement all the functions needed to control and operate the converter, such as high precision measurements, interlocking, DCCT interface, etc., as shown in Figure 24.9.
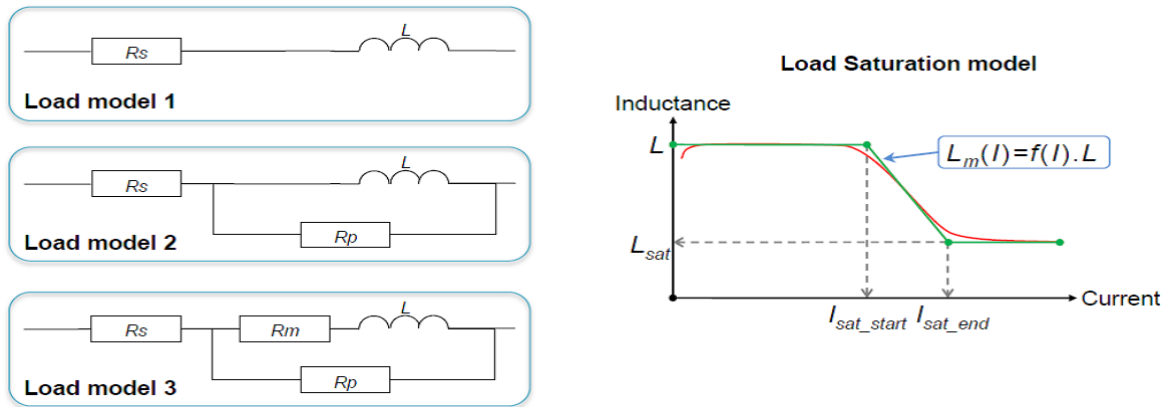


**Fig. 24.7:** Magnet models used for current regulation by FGC3 including a simplified model of magnet saturation.

## References

[1] Y. Thurel, IT-3933 Cobalt: Technical specification (updated version), EDMS 1377049 v.A.01 (CERN, 2014).

[2] Y. Thurel, PAC2007 Four quadrant 120A-10V power converters for LHC, EDMS 851714 v.1 (CERN, 2016).

[3] B. Favre, LHC120A crowbar inox-resistor – datasheet, EDMS 1296140 v.1 (CERN, 2015).

[4] A. H. Dinius, Q. King, J. G. Pett and J. C. L. Brazier, The all-digital approach to LHC Power Converter Current Control, SL-2002-002-PO (CERN, 2002).

[5] Q. King et al., CCLIBS: The CERN Power Converter Control Libraries, Proceedings of ICALEPCS 2015, Melbourne, 2015, pp 950–953.
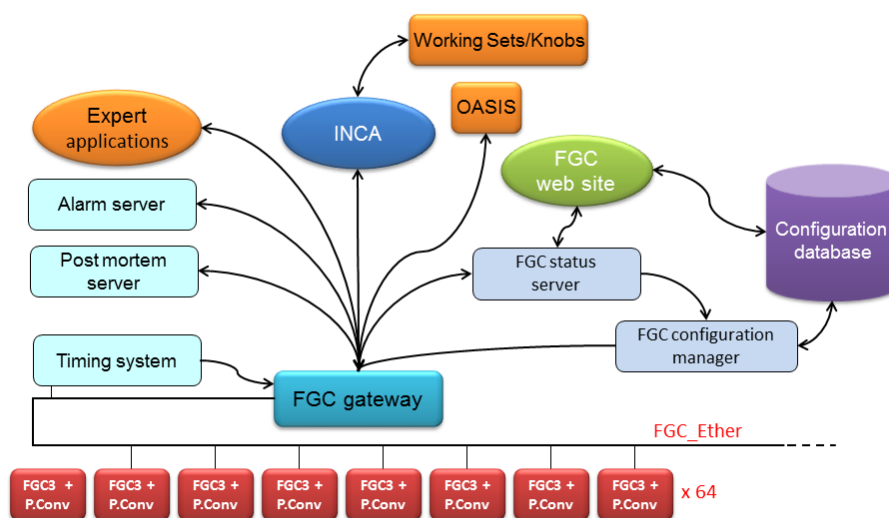
(a)
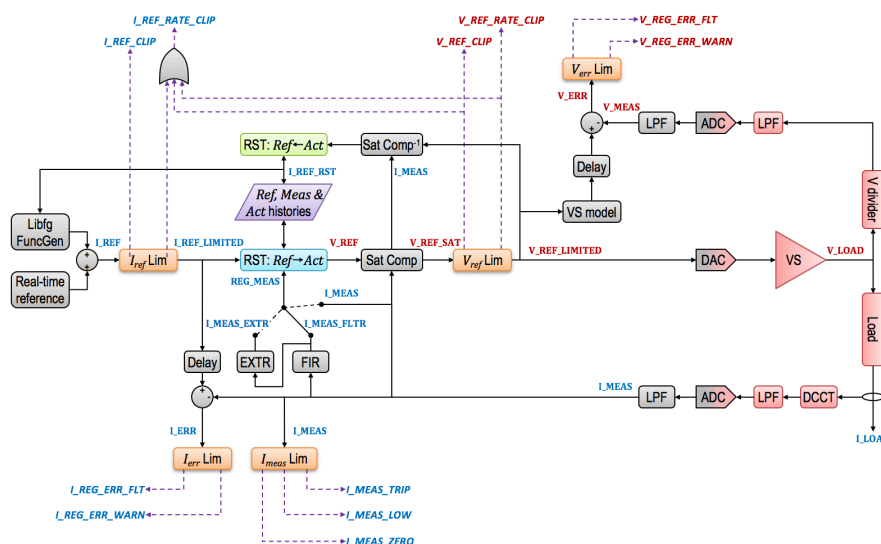


(b)

**Fig. 24.8:** FGC Control: (a) hierarchy, (b) RST regulation of the output current.
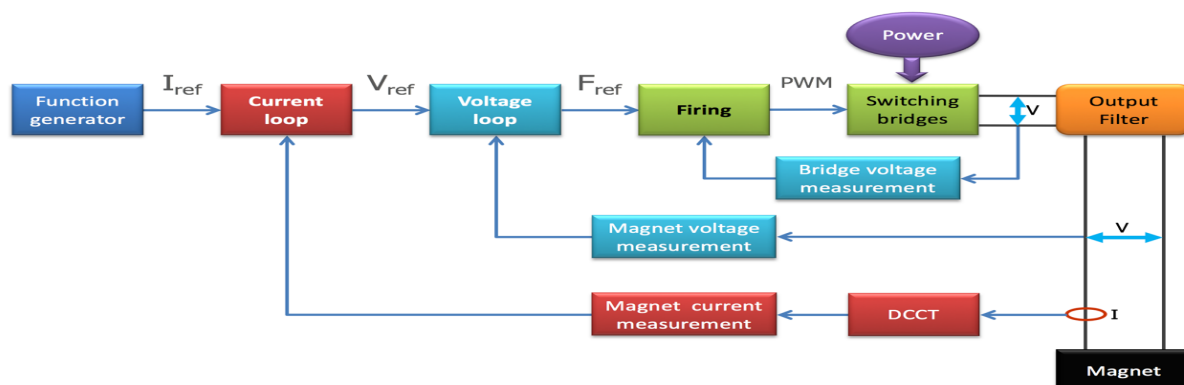


**Fig. 24.9:** Full control of the power converter implemented by means of FGC3 + RegFGC3 electronics.

**Part V**

# Safety and Radioprotection

# Chapter 25

# General safety

A.P. BERNARDES

Safety concepts were integrated into the HIE-ISOLDE facility at the design stage. There are four main potential risks concerning the HIE-linac environment.

- – Ionising radiation.
- – Magnetic risk.
- – Cryogenic risks.
- – Electrical risks.

## 25.1 Ionising radiation risks

The risk of ionising radiation and the strategy for the protection against it is extensively discussed in Chapter 26.

## 25.2 Cryogenic risk

A cryogenic plant cools down and maintains the beam line and accelerator equipment at 4.5 K. At HIE-linac only helium will be used as cryogenic fluid. Liquid helium will be distributed to Dewar and cryomodules via a cryogenic transfer line and interconnecting valve boxes. Two main hazards are linked to the usage of liquid or gaseous Helium fluid: cold burning hazard and oxygen deficiency hazard (asphyxiation). These hazards are located in the buildings that house the components of the cryogenic plant: the compressor building (B.198), the cold box building (B.199) and in the HIE-linac tunnel, at the experimental hall. To reduce the cryogenic risk the ODH detection system will be installed in the Compressor Building (B.198), Cold Box building (B.199), and in the linac tunnel. The implementation of the ODH detector system has been performed in such way that the operators working in areas subject of ODH would be quickly alerted in order to evacuate in the most effective way [1]. Moreover all safety devices of the cryomodules located in the HIE-linac tunnel will be routed outside the tunnel, thus substantially reducing cryogenic risks inside.

## 25.3 Magnetic field

Owing to the generation of the magnetic field by new post-accelerator and HEBT magnets, the magnetic hazard is located in proximity to HIE-linac tunnel and HEBT. Figure 25.1 depicts its location in HIE-linac.

The expected value of the magnetic flux density does not exceed the exposure limit for the public. The stray field map will be performed during commissioning and will be posted at the entrance of the magnetic field area, clearly indicating which regions are above 0.5 mT and 10 mT respectively. Moreover, the presence of a magnetic field will be announced by flashing warning panels.

## 25.4 Electrical risk

Electrical risks are mainly related to the electrical installation (high/low voltage and high current AC and DC power) and will be addressed by the usual safety procedures. The equipment will be closed in a rack

**Fig. 25.1:** Location of the magnetic hazard within HIE-linac.

or protected by a cover and labelled. Access to the HIE-linac tunnel and Faraday cage will be restricted.

## 25.5   Other safety issues

**Noise hazard**

The sources of noise outside the compressor building (B.198) and the cold box building (B.199) can affect the environment. The noise impact on the nearest neighbouring offices and CERN boundary will be reduced by the installation of an acoustic door at the compressor building (B.199), acoustic buffers on the air inlets and the use of low noise equipment for the cooling towers and chillers.

**Fire hazard**

Fire hazard at the HIE-ISOLDE buildings is associated with the presence of combustive materials, such as cables, oil of compressors and electrical racks. The compressor building (B.198), the cold box building (B.199) and the experimental hall (B.170) will be equipped with a fire detection system. In the case of activation of the fire detector, the ventilation system will be shut down, stopping the fire spreading in the facility. Furthermore, smoke extraction will be integrated into the compressor building (B.199) and experimental hall (B.170) [2].

**Radiofrequency hazard**

The main radiofrequency hazard comes from the RF for the superconducting cavities. The RF hazard is located in the linac (experimental hall, B.170) and RF amplifiers (Faraday Cage, first floor B.199). Since the linac is already shielded against X-rays, the radiofrequency radiation it emits will not cause any hazard. To significantly reduce the personel exposure to radiofrequency radiation, the RF amplifiers are enclosed in racks with RF leak detectors installed near them.

## References

[1] D. Phan,  ODH assesment of the buildings 198 and 199 and HIE-ISOLDE tunnel,  EDMS 1279878 (CERN, 2013).

[2] L. Mora Vallejo,  HIE-ISOLDE safety file – descriptive part,  EDMS 1258062 (CERN, 2014).

# Chapter 26

# Radioprotection and general safety

A.P. BERNARDES

## 26.1 Radiological hazards

The radiological hazards at HIE-linac are identified as X-ray production in the superconducting cavities during radiofrequency (RF) operation, the possibility of neutron emission when the ion beam at energies above the Coulomb barrier interacts with the intercepting devices, and the risk related to the delivery of the radioactive ion beam (RIB) to the experimental hall. In terms of radiation exposure, the HIE-ISOLDE hall is classified as simple controlled area, according to the CERN radiation safety code [1], due to ambient dose rate and contamination. The linac tunnel is a controlled prohibited radiation area, where the ambient dose rate may exceed 100 mSv/h. The compressor building (B.198) and the cold box building (B.199) are not designated areas, since the ambient dose rate will be below 0.5 $\mu$Sv/h.

Table 26.1: Designation of radiation areas.

| Building | Type of area | Ambient dose equivalent rate (at permanent workplaces) $\mu$Sv/h | Ambient dose equivalent rate (in low-occupancy areas) $\mu$Sv/h | Requirements |
|---|---|---|---|---|
| Compressor B-198 | Non-designed | 0.5 | 2.5 | No restriction to access, dosimeters (passive or active) are not required |
| Cold box B-199 | Non-designed | 0.5 | 2.5 | No restriction to access, dosimeters (passive or active) are not required |
| Experimental Hall B-170 | Simple Controlled | < 10 | < 50 | Active monitoring, personal dosimeter |
| Linac tunnel B-170 | Controlled | - | - | Active monitoring, personal dosimeter |

**Normal operation**

The normal operation of HIE-linac is associated with the following radiological hazards:

***X-rays production in the HIE-linac cavities***

X-rays are identified as the main radiological hazard of the HIE-ISOLDE facility, produced in the cavities of the superconducting HIE-linac. Sources of X-rays are shown in Figure 26.1.

At the last upgrade stage, the HIE-ISOLDE post accelerator will consist of 32 superconducting niobium-sputtered copper (Nb/Cu) RF cavities. The presence of defects and dust at the cavity surface
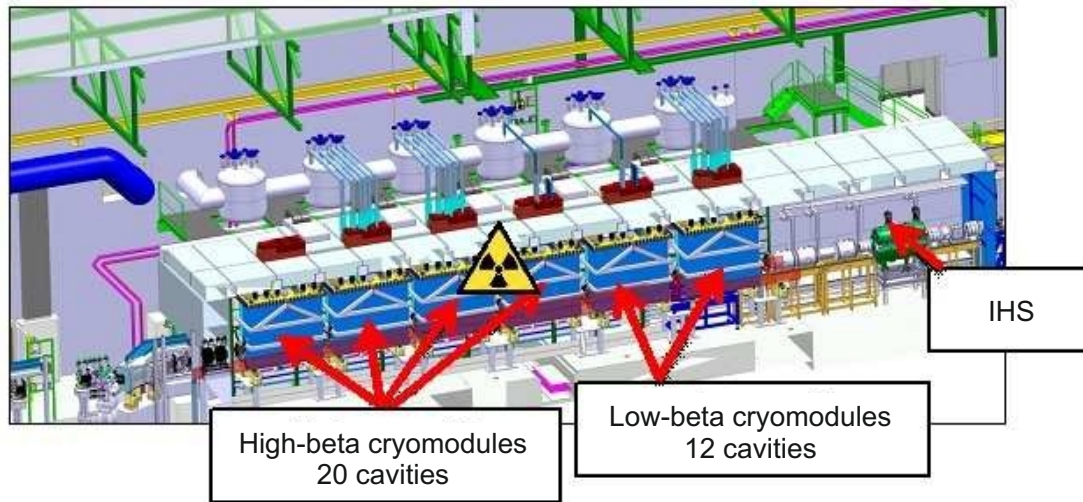
**Fig. 26.1:** Linac layout and X-ray source at HIE-linac.

will lead to permanent emission of electrons during RF operation. These electrons, accelerated by the accelerating field, will produce Bremsstrahlung X-rays by hitting the cavity walls. During the lifecycle of RF cavity, different operational conditions can be distinguished:

– Normal operation.
– Helium processing, special case of cavity conditioning (possible occurrence is less than five times per year in one or several cavities).

During normal and conditioning operation of the cavity, the maximum dose rate around the cavity of 20 mSv/h was observed. The maximum dose rate of approximately 350 mSv/h was detected during the helium conditioning in close proximity to the cryostat. The results of the dose rate measurement are presented in more detail in Figure 26.2.
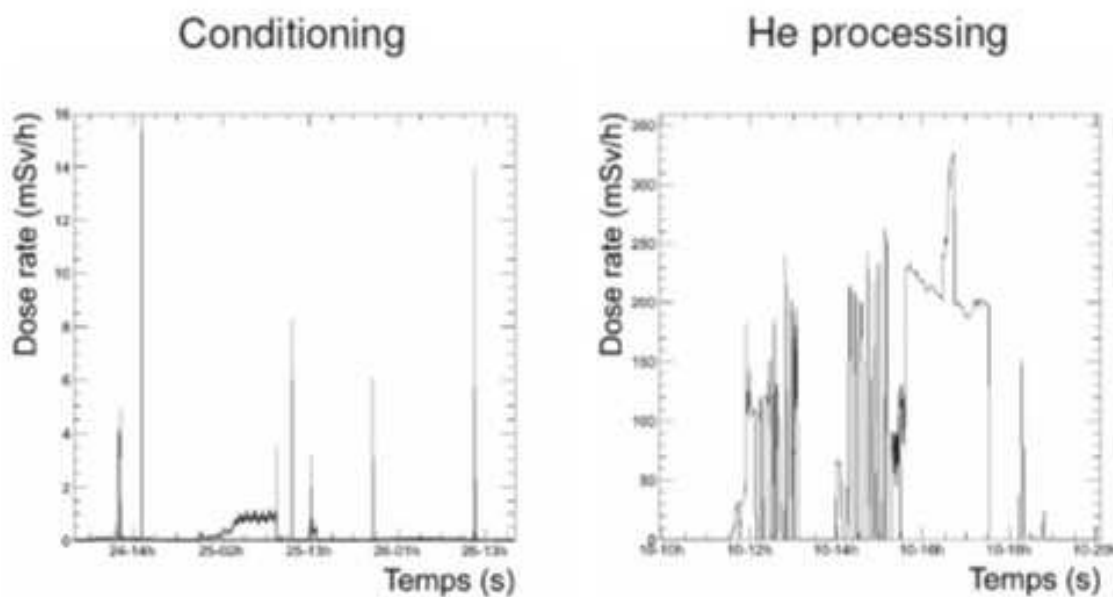


**Fig. 26.2:** Results of the dose rate measurement [2].

Helium conditioning of the 32 cavities at the same time is the most conservative scenario, from the radiological point of view, that has been taken into consideration for the definition of the shielding geometry for HIE-linac by the FLUKA simulation.



**Fig. 26.3:** Normalised simulation of dose rate for He processing of 32 cavities at the same time. Vertical cut, beam axis [3].

### Neutron production

The energy of post-accelerated ions above the Coulomb barrier induces the possibility of neutron generation in the event of ion beam impinging on intercepting devices such as experimental dumps, Faraday cups or magnets due to beam losses. This leads to radiological hazards along the linac and HEBT lines.
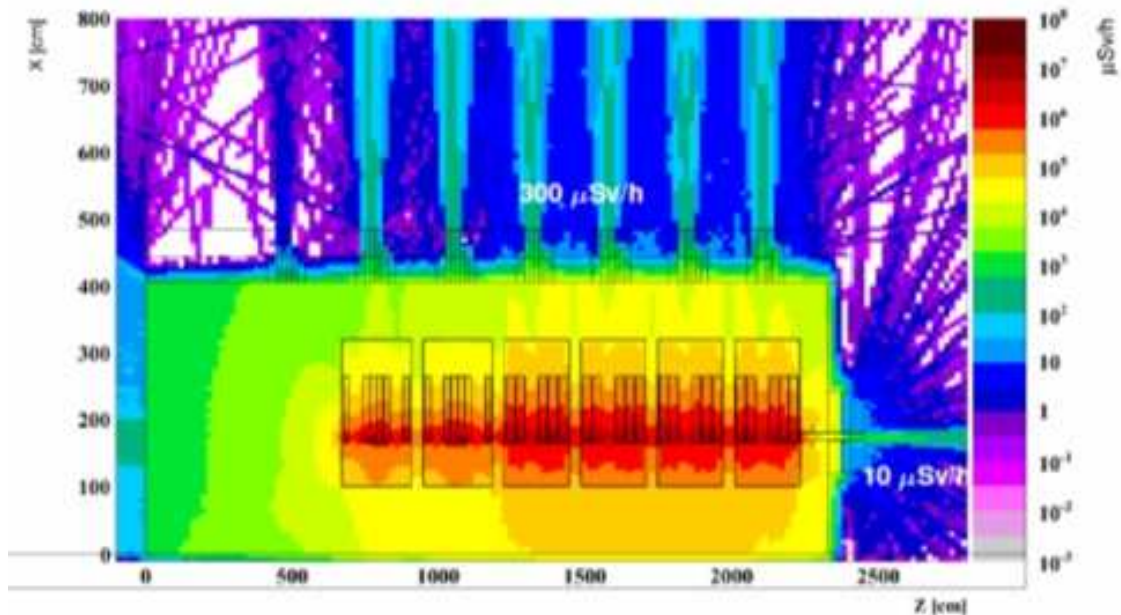
The different operational modes of the post-accelerator are characterised by the different intensity of the beam: radioactive ion beams during physics experiments (1 ppA), stable beams for machine settings (up to 10 ppA) and high intensity stable beams for beam emittance measurements (200 ppA) [4].

Beam settings and emittance measurements due to high intensity are the worst case scenarios taken into consideration for evaluation of maximum expected neutron dose rate. The shielding around the post-accelerator, primarily designed to protect against X-rays, is also efficient against neutron radiation, therefore the hazard related to the neutron production is located only in proximity to the HEBT.

The experimental hall (B.170) remains accessible during the settings of the machine and beam line, without a permanent workplace around the experiments and HEBT lines. During stable beams for machine settings, the intensities of the beam are restricted to the value listed in [5] which corresponds to a dose rate of 3 $\mu$Sv/h at 1 m at maximum energy. An annual beam permit is in place, specifying the limit of beam intensities. In the some specific cases, such as emittance measurements (200 ppA) with high intensity stable beam, setting temporary restricted areas around hot spots (mainly Faraday cups and beam dumps) allows the mitigation of neutron hazard.

### Activation

The study of the expected activation of the surrounding material at HIE-linac has been performed with FLUKA code, for the most conservative scenario —accidental beam loss (100% of the beam loss) in the

beam dump, Faraday cup and magnets for thirty years of operation. Figure 26.1 illustrates the result of the prompt dose rate and residual dose rate after 1 s of cooling the dose distribution in the copper [3] .
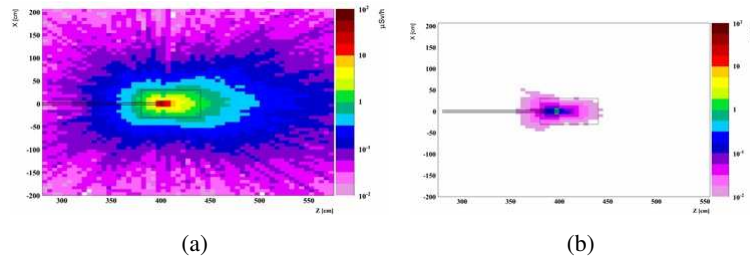


**Fig. 26.4:** Dose rate distribution in the copper for the case of full beam loss a) Prompt dose rate b) residual dose after 1 s of cooling.

Activation levels expected in the different beam intercepting devices after 30 years of operation are low enough with respect to Safety Code F [6] to be considered as free release candidates from the activation point of view.

*Contamination*

One of the principal hazards in a radioactive beam facility is the contamination of the vacuum system. The problem of contamination had already existed for REX-ISOLDE and will not increase after the upgrade of the facility. The vacuum level for the HIE-linac is $10^{-7} - 10^{-8}$ mbar and will be reached by the primary and turbo pumps network. Pumped gases could be trapped in the oil of the pumps. Sampling of this oil allows performing a quantitative inventory of the isotopes trapped in it. These measurements have been made using gamma spectrometry that found just some traces of 125-I with the maximum activity of 35 Bq/kg. This activity is very low in a comparison with the CERN exemption limit of 700 Bq/kg for 125-I.

**Accidental operation**

The accidental operation implies full beam loss due to failure. The radiological issues will be the same as for the settings of the machine.

**HIE-linac shielding**

X-ray emission is the main radiological hazard driving the shielding requirements. The design objective of the shielding for X-ray radiations is 1 $\mu$Sv/h, in order to assure the ambient dose rate coming from all sources of radiation in the experimental hall (B.179) below 3 $\mu$Sv/h. The geometry of the shielding enclosure for the HIE-linac tunnel is shown in Figure 26.5. The lateral walls and sliding door at the end of the shielding enclosure are made of 80 cm thick concrete blocks. The roof is made of 40 cm thick concrete blocks.

Integration and radioprotection issues require the safety devices to be routed on the top of the tunnel, though the chicane. At both extremities and around the beam pipe, shielding is made of lead plates. At the end of the tunnel, close to experimental areas, the lead plate is 13 cm thick. An 1 cm lead plate will be placed at the entrance of the tunnel. Additional shielding plates will be installed inside the tunnel as shown on Figure 26.6. The upper lead plate is 5 cm thick, and the two down parts are 2 cm thick. For phase three, a 5 cm lead plate could be used [7]. For more information on the HIE-linac shielding tunnel, see Chapter 27.
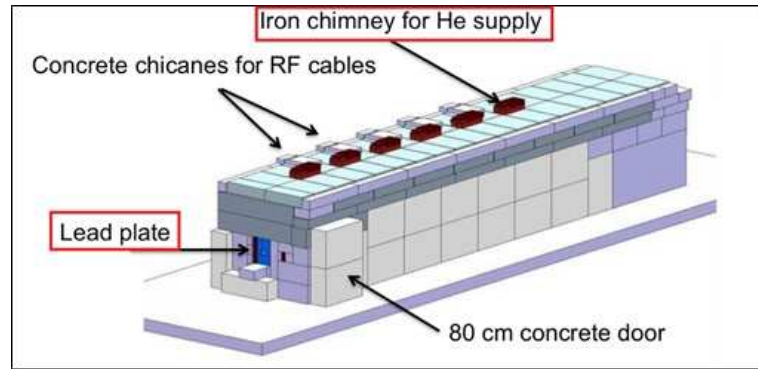
**Fig. 26.5:** Shielding design for the HIE-ISOLDE post-accelerator.
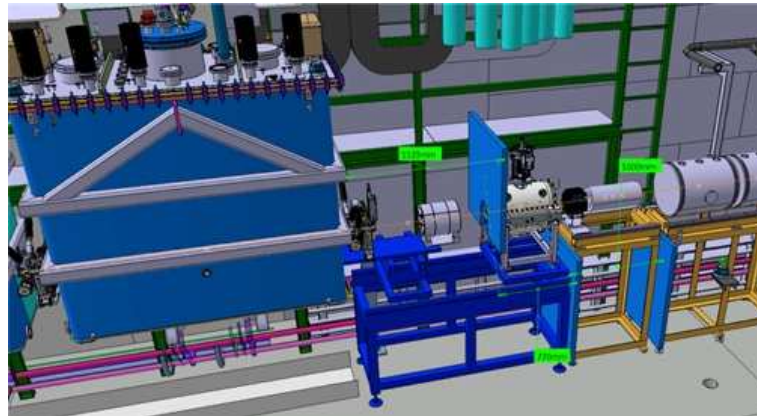


**Fig. 26.6:** Position of the shielding plates inside the shielding enclosure.

## 26.2 Access control and monitoring

**Access**

The experimental hall and linac are classified as controlled areas, by cause of effective dose and contamination. These controlled areas will be delimitated and necessary precautions will be taken as required. The general requirements for access to controlled radiation areas are the following:

– The experimental hall will remain accessible all the time. Radioprotection monitoring will ensure that any anomalies are detected. For exceptionally stable beams of high intensities, the physical barrier will be installed in proximity to the HEBT.
– The HIE-linac tunnel will be accessible during operation (for short-term access), technical stops and shutdown.
– The cryo-line platform will remain accessible at all times.
– Access to the HIE-linac is forbidden during RF operation. A special grid will be installed on the roof of the tunnel preventing human intrusion. There is no beam operation possible if the protection grid is not installed.

**Radiation monitoring**

The radiation monitoring system at the HIE-ISOLDE facility consists of RAMSES (Radiation Monitoring System for the Environment and Safety) and GRAMS (Gamma radiation monitoring system) that will be installed according to the requirements defined by Radiation Protection group and connected to the CERN Control room. In case of alarm, the operator will receive the signal and cut the beam.

## References

[1] D. Forkel-Wirth and T. Otto, Règles générales d' explotation – consignes générales de radioprotection: Zonage radiologique au CERN, EDMS 810149 (CERN, 2014).

[2] S. Giron, Dose and dose rates measurements close to a HIE-ISOLDE cavity in Orsay, EDMS 1284523 (CERN, 2013).

[3] S. Giron, Estimation of neutron emissions from beam losses and material activation for radioactive waste study related to the new HIE-ISOLDE post-accelerator, EDMS 1393705 (CERN, 2014).

[4] D. Voulot, Specification of the sources of radiation and maximum beam intensities and energies of the HIE-ISOLDE linac, EDMS 1224228 (CERN, 2014).

[5] A. Bernardes and D. Voulot, Beam operation and neutron production at HIE-ISOLDE, EDMS 1339059 (CERN, 2014).

[6] CERN, *Protection against Ionizing Radiation: Radiation Safety Manual*, 1996.

[7] S. Giron, Design report on the shielding of the future post-accelerator for the HIE-ISOLDE project, EDMS 1362196 (CERN, 2014).

# Chapter 27

# Shielding tunnel

S. GIRON

## 27.1 Shielding requirements

### Access and operation of the machine

Shielding of the post-accelerator was designed to keep the whole experimental hall accessible for users during operation and conditioning of the machine. Moreover, He conditioning should be possible for at least one cryomodule (i.e. 5 high-$\beta$ or 6 low-$\beta$ cavities) at a time.

Considering the possible presence of other radiation sources in the experimental hall, the design objective value for X-rays was fixed to 1 $\mu$Sv/h, in order to keep the limit for external exposure to 6 mSv/year (which corresponds to 3 $\mu$Sv/h for 2000 hours of occupancy) [1].

### Source term

The source term for X-ray radiations was determined from X-ray measurements, for the most constraining conditions of operation (He processing). It was thus fixed to 350 mSv/h for one cavity, which is the maximum dose rate measured during RF tests.

### Simulations of the test bench to define I (e/s)

To reproduce the X-ray emission observed during RF tests of a single cavity at SM18, the cryostat test bench was simulated with FLUKA. The geometry used for these calculations is presented in [2]. The ground is made of concrete, the cavity of copper and the cryostat of iron.
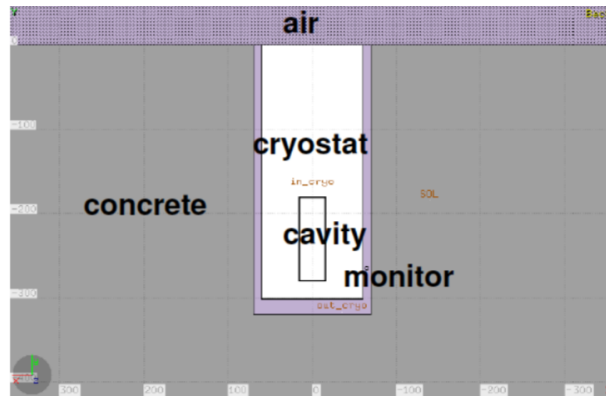


**Fig. 27.1:** FLUKA geometry of the SM18 test bench.

The source was defined as two orthogonal mono-energetic electron beams at 900 keV impinging on the cavity surface (in two ways). The dose rate distributions obtained in the cavity plan and in the beam pipe plan at beam height are presented in Figure 27.1. Dose rates were normalised to 350 mSv/h at the position of the ionisation chamber. The rate of electrons removed from the surface determined in this way is $1.5 \cdot 10^{14}$ electron/s. This intensity per cavity was later used to normalise calculations performed for the entire tunnel (32 cavities).
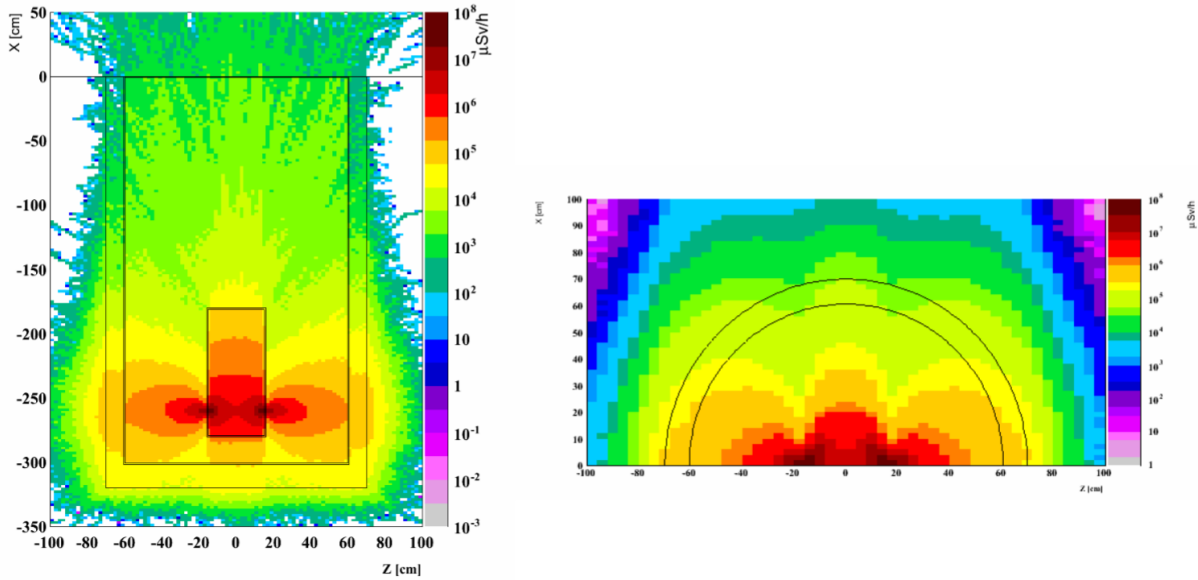
**Fig. 27.2:** Dose rate distribution ($\mu$ Sv/h) around one cavity during He processing.

**Shielding thicknesses for different material**

The maximum energy that electrons can reach while accelerated by a superconducting high-$\beta$ cavity is 900 keV. Dose rates expected with these cavities were extrapolated from Legnaro measurements (300 keV electrons) using [3] to define a bulk shielding ahead of X-ray measurements at HIE-ISOLDE prototype cavities.

Shielding thicknesses calculated for different materials for these extrapolated dose rates are presented in Table 27.1. More details on the calculation can be found on [4].

**Table 27.1:** Equivalent thickness of shielding in different material.

| Material | Length [cm] |
|----------|-------------|
| Concrete | 80.5 |
| Iron | 26.8 |
| Lead | 13.4 |

## 27.2 Shielding design and validation

**Constraints for services integration**

The shielding design has been defined in close collaboration with the team responsible for the integration of all the services (RF, HV, He supply and exhaust, cables) to the post-accelerator. The final geometry chosen is shown in Figure 27.3. The shielding enclosure is later in the text referred to as tunnel.

The lateral walls are made of 80 cm thick concrete blocks, as well as the sliding door at the end of the shielding enclosure. The roof is made of 40 cm thick concrete blocks, where chicanes have been implemented for RF cables.

The chimneys for He supply are made of iron with a straight penetration. No chicane could be installed because of the rigidity of the He pipe. In addition, two trenches for cables have been excavated on the ground below the future post-accelerator . The first one is perpendicular to the beam line and the other is parallel to it.

At both extremities and around the beam pipe shielding is made of lead plates. At the end of
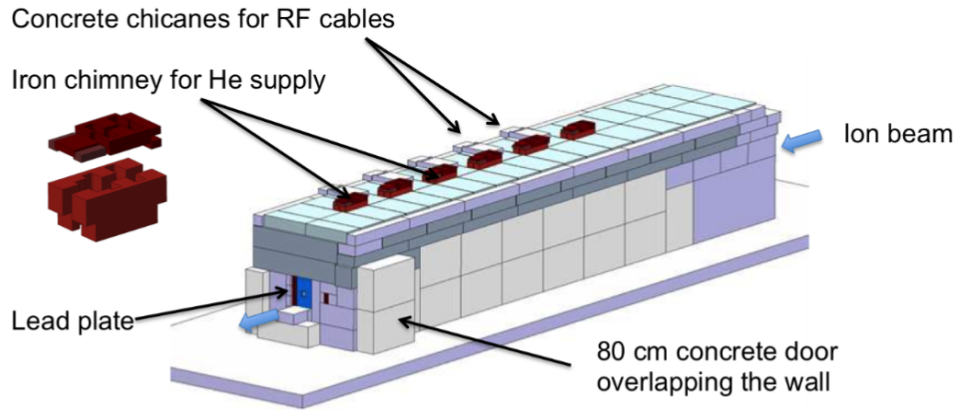
**Fig. 27.3:** Shielding design for the HIE-ISOLDE post-accelerator.

the tunnel close to experimental areas, the lead plate is 13 cm thick. At the entrance of the tunnel, the 1 cm-thick lead plate of the existing REX-ISOLDE will remain the same at least for phase 1 of the HIE-ISOLDE post-accelerator (see Figure 27.4). Additional shielding plates will be placed locally inside the tunnel to reduce the radiation level outside of the tunnel. The upper lead plate inside the tunnel is 5 cm thick, while the two down parts are 2 cm thick each (see Figure 27.5). For phase 3, a unique 5-cm lead plate could be used.
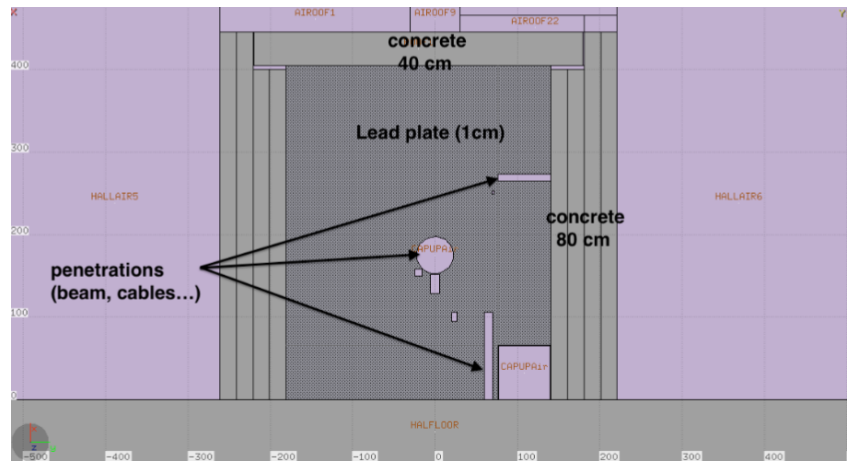


**Fig. 27.4:** Geometry of the current 1-cm lead plate upstream REX-ISOLDE.

**Results of calculations for the post-accelerator shielding (X-rays)**

FLUKA calculations were performed to assess the shielding requirements determined analytically (see section 3.4 of [5]). The adopted geometry presented in 4.1 of the same document was implemented in FLUKA to identify possible weaknesses of the shielding. All penetrations for beam pipe, RF cables, He pipes and HV were left empty in the FLUKA geometry.

A mono-energetic electron beam at 900 keV (for the 22 high-$\beta$ cavities), and 600 keV (for the 10 low-$\beta$ cavities) was distributed randomly between the cavities, creating Bremsstrahlung X-rays when impinging on the copper surface.

As phase 3 is the most constraining phase in terms of radiation, it was used to validate the bulk shielding (concrete walls and downstream lead plate). Dose rate distributions were normalised using the

**Fig. 27.5:** Position of shielding plates inside of the tunnel.

intensity determined with FLUKA simulations of the SM18 test bench for one cavity times the cavity number. Simulations results are given in the next subsections for He processing of all the cavities at the same time in the tunnel, which is the most constraining scenario in terms of shielding. During normal operation, dose rates are expected to be at least ten times lower than during He processing.
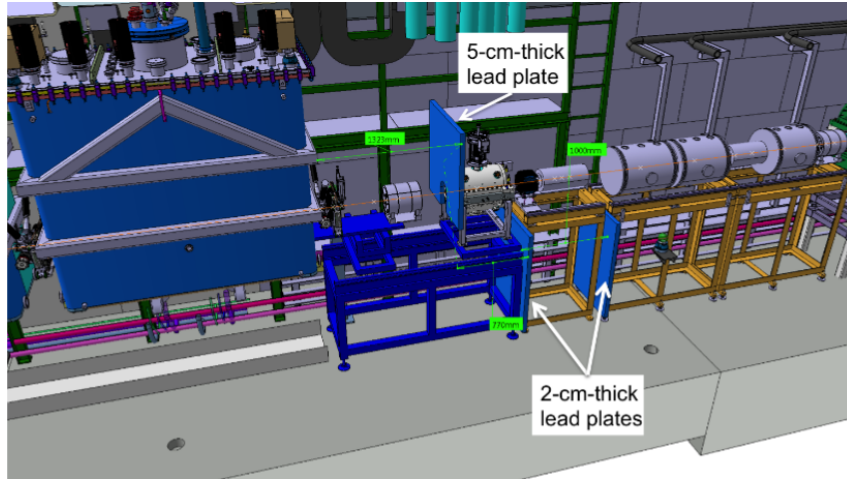
### *Phase 1*

During phase 1, two cryomodules (i.e. 10 high-$\beta$ cavities) were added to REX-ISOLDE. The bulk shielding (80 cm concrete) is sufficient to reach $1\mu$Sv/h in the experimental hall. On the tunnel roof, due to chimney straight penetrations, dose rates can reach up to a few hundreds of $\mu$Sv/h. Access to the roof will be forbidden during RF operation, unless measurements indicate a sufficiently low radiation level to allow access.
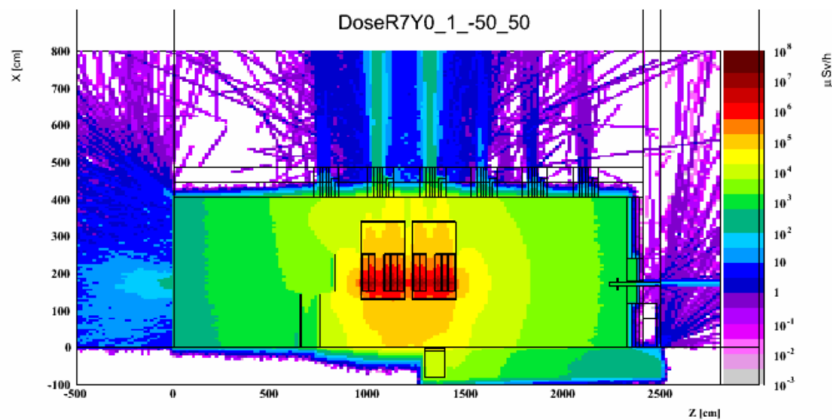


**Fig. 27.6:** Dose rate distribution ($\mu$Sv/h) around the post-accelerator: vertical cut at beam position.

Upstream the post-accelerator, it was suggested to add three lead plates inside the shielding enclosure (see 4.1) during phase 1, to avoid the replacement of the current 1-cm-thick lead plate by a thicker shielding plate. Dose rates observed upstream the post-accelerator at 40 cm from the 1 cm-thick lead plate can locally reach up to 10 $\mu$Sv/h. Additional lead shielding will be added around cable penetrations to reduce this value.

He processing should be limited to one cryomodule at a time at least during the first commissioning

224
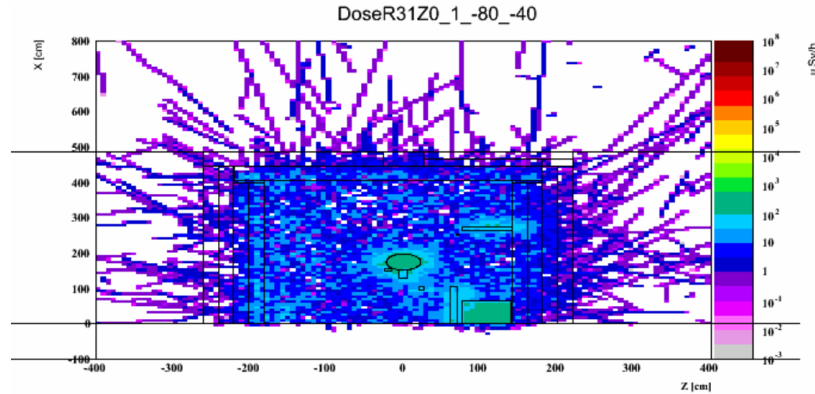
**Fig. 27.7:** Dose rate distribution ($\mu$Sv/h) upstream the post-accelerator: vertical cut at 40 cm on the outside of the 1 cm-thick lead plate.

campaign to limit X-ray emission. This restriction could be relaxed after cavity characterisation if the radiation levels turned out to be lower than expected.

*Phase 2*

No specific calculations were performed for phase 2. For the bulk shielding and the roof, the situation remains the same as for phase 1. For the upstream lead plate, the shielding configuration proposed for phase 1 could be conserved for phase 2, by considering He processing of only one cryomodule at a time. During normal operation, dose rates remain in any case below a few $\mu$Sv/h.

*Phase 3*

The bulk of shielding was assessed for phase 3, so that the operation and the commissioning of the machine can be performed without access restriction to the experimental hall.

Inside the tunnel, dose rates can reach up to 300 mSv/h between cryomodules and 30 mSv/h on top of a cryomodule during He processing.

For these calculations, a unique 5 cm-thick lead plate was implemented upstream the post-accelerator in the FLUKA geometry. However, the 1 cm lead plate could remain a viable solution if lead plate positions inside the tunnel are adapted to the low-$\beta$ cryomodule position for phase 3 and He conditioning remains limited to one cryomodule at a time. The strategy to adopt will be decided depending on measurements performed during phase 1 and 2.

Above the post-accelerator, dose rates can reach few hundreds of $\mu$Sv/h, because of the chimneys and chicanes at the top of the tunnel. Access to the roof will be forbidden during RF operation, unless measurements indicate a sufficiently enough radiation level to allow access.

Dose rates expected at both extremities from the post-accelerator reach locally up to 10 $\mu$Sv/h for He processing of all the cryomodules at the same time, and with a 5 cm lead shielding plate. The limitation of conditioning one single cryomodule at a time will probably be required if the current lead plate is not replaced by a 5 cm-thick lead plate for phase 3. Depending on the dose rates measured during He processing in the tunnel, this limitation could be relaxed.

At the other extremity of the post-accelerator, behind the 13 cm lead plate, dose rates could locally reach a few $\mu$Sv /h. Filling the beam aperture with lead may reduce radiation leakages near the experimental areas.

**Results of calculations for the post-accelerator shielding (ions)**

To assess the compatibility of the shielding against neutrons, neutron equivalent dose rates expected in the event of a total ion beam loss in the last cavity of the post-accelerator have been calculated with FLUKA for the operational ion beam intensity at HIE-ISOLDE. Neutron dose rates do not exceed 1 $\mu$Sv/h outside the shielding enclosure in that configuration.

## References

[1] D. Forkel-Wirth and T. Otto, Règles générales d' explotation – consignes générales de radioprotection: Zonage radiologique au CERN, EDMS 810149 (CERN, 2014).

[2] S. Giron, CATHI Technical Report: Mesure des rayonnements X autour de la cavité HIE-ISOLDE Q2_6 au SM18 du 30 avril au 8 mai 2012 (M44), EDMS 1235259 (CERN, 2014).

[3] National Council on Radiation Protection and Measurements, Radiation protection design guidelines for 0.1-100 MeV particle accelerator facilities, NCPR Report 51 (NCPR, 1977).

[4] S. Giron, CATHI Technical Report: CATHI Technical Report: Preliminary estimation of the shielding requirements of the SC linac of the HIE-ISOLDE project (D45), EDMS 1235410 (CERN, 2014).

[5] S. Giron, Design report on the shielding of the future post-accelerator for the HIE-ISOLDE project, EDMS 1362196 (CERN, 2014).

# Part VI

# Commissioning

# Chapter 28

# Commissioning

W. Venturini, J. A. Rodriguez

In 2015, one high-$\beta$ cryomodule was installed at the ISOLDE facility as part of the HIE-ISOLDE energy upgrade, followed by a second identical cryomodule one year later. Together, they extended the energy reach of the facility to 5.5 MeV/$u$ for $A/q = 4.5$. The following sections describe the hardware and beam commissioning activities of 2015, 2016, and 2017.

## 28.1 Commissioning 2015

### REX commissioning

Several components of the REX post-accelerator were upgraded or underwent maintenance in preparation for the energy increase of HIE-linac. New water cooling circuits for the magnets, cavities and RF amplifiers were installed, along with thermal sensors for the quadrupoles. Interlock levels were set following cooling water flow and temperature rise measurements. In addition, two fast Penning gauges and a fast acting valve were added to prevent damage to the cavities in case of accidental venting of the beam lines. Repairs to the cooling fans, power converters and LLRF of the amplifiers were carried out [1].

### Hardware commissioning

Following the installation of the first cryomodule in 2015, hardware commissioning was carried out to establish operation parameters, ensure that the risk of damage after the first powering was minimal, test controls and hardware components.

**Table 28.1:** Commissioning steps of the HIE-ISOLDE cryomodules.

| Step | Activity |
|------|----------|
| 1 | Slow pump-down |
| 2 | Interlock checks |
| 3 | Instrumentation checks |
| 4 | LLRF setup |
| 5 | Cool-down |
| 6 | Alignment and monitoring |
| 7 | RF conditioning above Tc |
| 8 | RF tests at cold |
| 9 | Solenoid tests |
| 10 | Heat load measurements |

The vessel was transported to the linac under static vacuum conditions. During pump-down, gas velocity was limited to below 0.3 m/s, until the molecular regime was reached, to prevent contamination of the cryomodule from dust particles. The cryomodule was cooled down to 4.5 K and achieved excellent vacuum performance with pressures in the range of $10^{-11}$ mbar.

The first cryomodule was cooled down in approximately three weeks' time. The procedure presented challenges because the commissioning of the cryogenics facilities took place at the same period. The permitted temperature gradients in the subsystems of the cryomodule also imposed limitations to

the cool-down process, as well as the need to avoid excessive cryo-pumping of residual gas on the cavity surfaces. A boil-off technique was used to measure the static heat load; which was found to be in the order of 10 W at 4.5 K, in accordance with the design values.

A new system using optical targets that can be viewed from the exterior of the cryomodule was devised to observe the positions of active elements on the beam line, in particular during cool down. The accelerating cavities and the solenoid magnet were intentionally placed approximately 4 mm lower than the nominal beam line when the cryomodule was manufactured, as the supporting system was expected to move upwards by the same amount during cooling due to thermal shrinkage. All elements were aligned within 0.1 mm from the ideal beam line, well within the design requirement of 0.3 mm and 0.15 mm rms in the case of the cavities and the solenoid respectively.

The accelerating cavities are controlled by a new digital Low Level RF (LLRF) system. Besides controlling the couplers and tuning system, it offers the possibility of running the cavities with a self-excited loop for measurement and conditioning. The cavities can also be locked on amplitude and phase set-points for beam operation. In the beginning of commissioning, cavities were set at 101.28 MHz. Conditioning of the multipacting bands up to 60 kV/m was carried out during cool-down, thanks to the variable couplers and self-excited loop function of the LLRF system. A multipacting band is also present in the superconducting cavities around 1.5 MV/m. Following conditioning of the cavities, their Q vs E was measured accurately in critical coupling. All cavities attained the nominal field free from field emission, except one in which a field emission onset above 5 MV/m was observed.

Remarkably, it was noted that the RF performance in terms of Q values of the cavities in the cryomodule was significantly enhanced in comparison to the performance of the separate cavities in vertical tests. Following a thorough investigation, this phenomenon was attributed to the cryomodule's optimal cooling conditions whereby the temperature gradients across the cavities are minimised during the superconducting transition. To verify that the solenoid stray field did not cause any perturbation on the cavities, both the solenoid and the cavities were powered at nominal fields simultaneously. When measurements of the cavities ended, the couplers were moved to reach the selected bandwidth for beam operation (10 Hz) and the LLRF feedback loops were set up. The design requirements for 0.1% rms stability in amplitude, and 0.2 degrees in phase were amply satisfied, as shown in Figure 28.1.
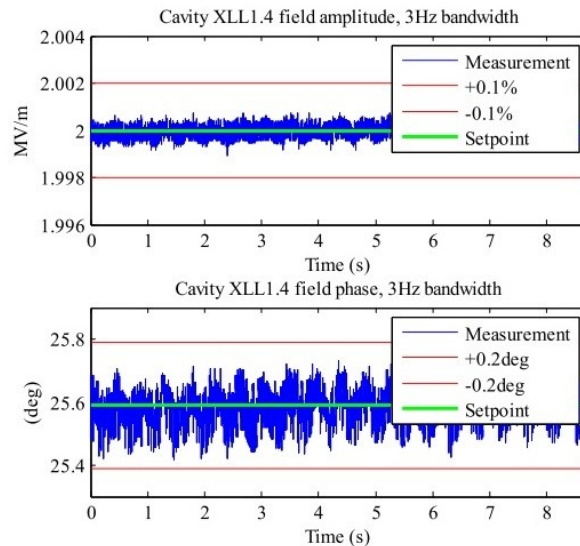


**Fig. 28.1:** Performance of the LLRF loops at 3 Hz bandwidth. The design requirements for 0.1% rms stability in bandwidth and 0.2 degrees in phase are satisfied by a wide margin.

The superconducting solenoid magnets in the cryomodules were operated at nominal current, as

they had already been trained in the factory, without any quenches. To inspect the behaviour of the cryogenic system, one quench was deliberately caused, and the expected small increase in pressure was observed. A minor issue arose when systematic trips of the power converter in current regulation mode operation were observed—caused by the change of differential impedance when polarity was reversed. This was addressed by using voltage mode to switch polarity.

The RF measurements were verified with the acceleration of a stable beam. Beam energies were measured both with a silicon detector and with a dipole magnet at the HEBT used as spectrometer. Scans of cavity phases were also performed to study the output energy variation. The accelerating voltages obtained via these three methods match within $3\%$.

A major issue arose when a design flaw was discovered in the RF feed system, that would result in thermal breakdown after some hours of operation. Following the increase in bandwidth and subsequent rise in RF power as the cavities were moved to higher fields, it was noticed that the way the RF signals drifted pointed to the slow expansion of the coupler antenna, an observation verified by additional tests. To address this problem for the 2016 physics run, both cryomodules were equipped with new coupler lines that used an improved design. In order to maintain at least part of the 2015 physics programme, it was determined that the best course of action was to reduce forward power by optimising the operation of the LLRF system and limiting the bandwidth at $3-4$ Hz. Cavities operated at 4 MV/m with 35 W forward power and powering was limited to six hours per day, allowing the RF couplers and lines to cool down in between runs.

More details on the first commissioning experience with HIE-ISOLDE can be found in [2].

**Beam commissioning**

Beam commissioning was performed in several stages. First, the REX diagnostics box, located between the RFQ and the buncher, was recommissioned by a $0.3$ MeV/$u$ beam and all diagnostic elements were found to be in good working order. The commissioning of the first HIE-ISOLDE diagnostic box followed, using a beam with the same energy. Its equipment fulfilled the design requirements. Transverse beam profiles with intensities of a few epA were measured using the Faraday cups, scanning slits and collimators. Silicon detectors measured the energy and energy spread of beams with low intensity and recognised beam contaminants. Carbon foils will be used to alter the mass-to-charge ratio of the ions in order to clean beam contaminants in some experiments. The determination of operational settings for the RF amplifiers was necessary, as several of their components were replaced and their calibration had changed. The transmission through the RFQ for different RF powers was measured and an operation point with $95\%$ transmission plateau was chosen. Amplitudes and phases of the rest of the RF structures were found using a silicon detector. A $2.85$ MeV/$u$ beam was used to commission the rest of the diagnostic boxes and the magnets along HIE-linac and the first HEBT line. Owing to time limitations, beam optics measurements were confined to the absolutely necessary. Beam transmission from separator magnet to the end of experimental lines was found to be $\sim 75\%$ and alignment of the optical elements was satisfactory. In the last stage, cavities were phased with a silicon detector located at the end of the linac tunnel and the second HEBT line was commissioned. The 2015 beam commissioning in HIE-ISOLDE is described in [1].

**Physics run**

In October 2015, a five-week run took place at HIE-linac, which was then equipped with one high-$\beta$ cryomodule. The first experiment performed Coulomb excitation of the neutron-rich zinc isotopes. A radioactive beam was accelerated to $4$ MeV/$u$ in the new superconducting linac and in the following weeks, different charge states of zinc isotopes were sent to the experimental station. An overview of the physics run can be seen in Table 28.2, while the energy and gamma ray spectrum of the Zn beam is presented in Figures 28.2 and 28.3.
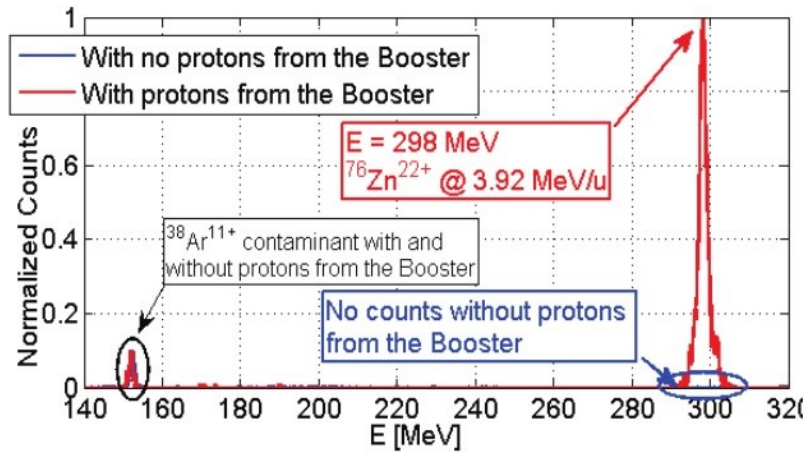
**Fig. 28.2:** Energy spectrum of the beam delivered to the Miniball experimental station. The beam of interest, $^{76}Zn^{22+}$, and a contaminant, $^{38}Ar^{11+}$, are presented in red.
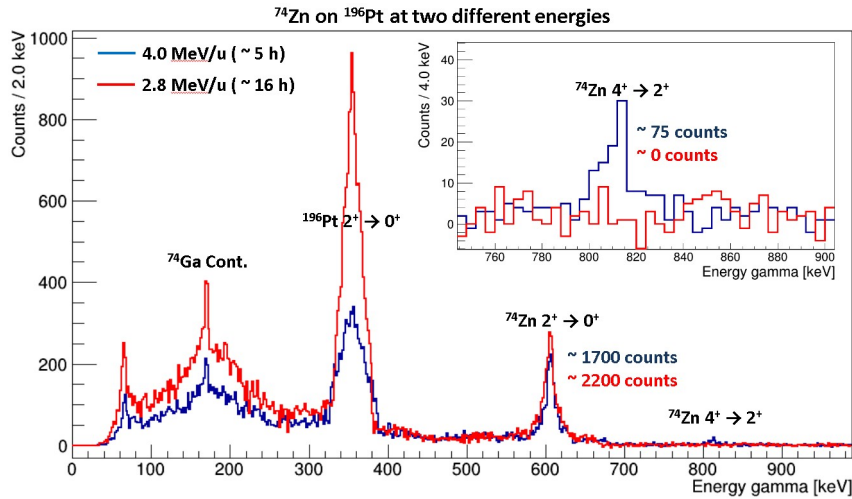


**Fig. 28.3:** Doppler-corrected gamma ray spectrum obtained in the Coulomb excitation of the first radioactive beam delivered at 4.0 MeV/$u$: $^{74}$Zn beam impinges on a $^{196}$Pt target (blue) and the equivalent gamma spectrum for 2.8 MeV/$u$ (red). The higher energies of HIE-ISOLDE show an increase of cross section and markedly improve the population of higher-lying states. (Courtesy of Illana Sison Andres)

**Table 28.2:** Overview of the 2015 operations at the two beam lines.

| | Beam | Energy [MeV/$u$] | Origin | HEBT | Experimental Station | Time [hours] |
|---|---|---|---|---|---|---|
| RIBs | $^{74}Zn^{25+}$, $^{74}Zn^{21+}$ | 2.85/4.0 | GPS target | XT01 | Miniball Spectrometer | 50 |
| | $^{76}Zn^{22+}$ | 2.85/4.0 | GPS target | XT01 | Miniball Spectrometer | 83 |
| Stable | $^{22}Ne^{7+}$ | 2.85 | REXEBIS | XT01 | Miniball Spectrometer | 31 |
| | $^{14}4N^{4+}$ | 2.85/4.0 | REXEBIS | XT02 | Scattering Chamber | 2 |
| | $^{12}C^{4+}$ | 4.0 | REXEBIS | XT02 | Scattering Chamber | 2 |
| | $^{133}Cs^{39+}$ | 2.85/4.0 | Ion Source | XT01 | SPEDE | 105 |

## 28.2   Commissioning 2016

**Hardware commissioning**

In preparation for the 2016 physics run, the first cryomodule was removed, vented and equipped with new couplers in an ISO5 clean room. It was installed again in the beam line with the second cryomodule in May 2016. The cool-down of the two cryomodules took longer than expected, and highlighted limitations in the management of transients from the cryogenics plant. Active cooling of the two cryomodules was performed in several stages with floating periods in-between and, as a result, passive cooling of cavities and solenoids through radiation on the thermal shields lasted a few weeks. As customary, multipacting levels at a low field were conditioned before reaching the superconducting transition. A spontaneous increase in vacuum pressure was observed in the second cryomodule some days after its temperature reached $4.5$ K. Pressure became steady at $10^{-9}$ mbar.
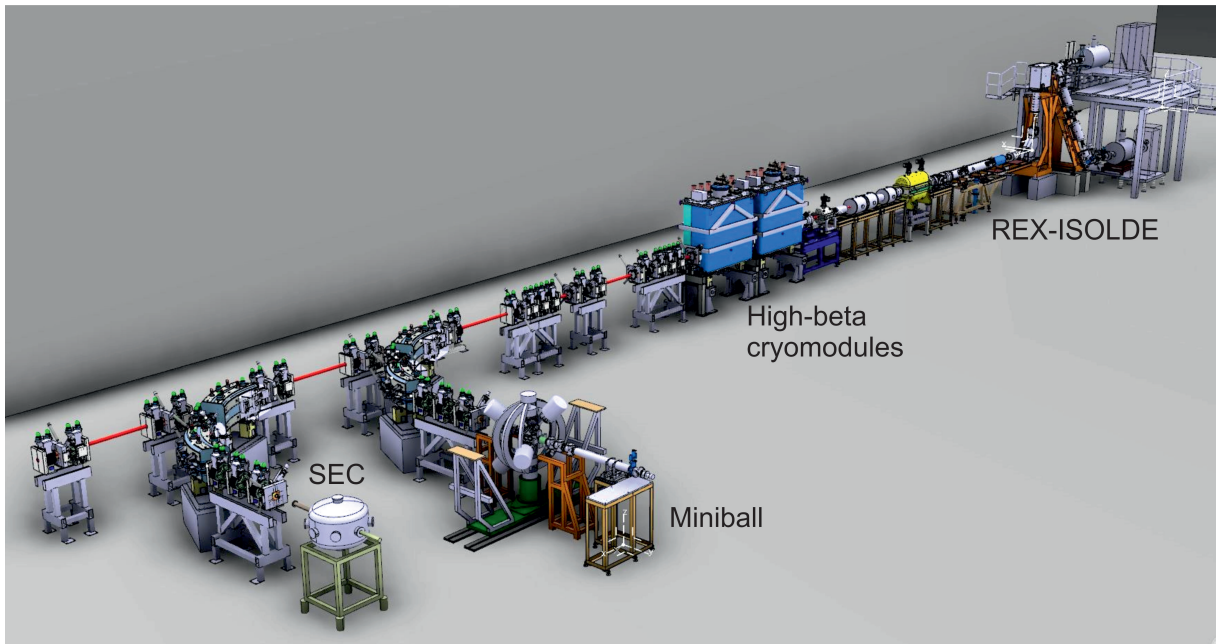


**Fig. 28.4:** 3D view of the HIE-linac layout during the 2016 commissioning.

The RF measurements at cold highlighted a degraded performance on the first and the last cavity of the second cryomodule, which had been transported back to the clean room and vented to exchange the RF couplers. All other cavities reached the nominal field of 6 MV/m, close to the required power dissipation of 10 W, in particular those of the second cryomodule, which was a confirmation of the soundness of the assembly procedure and slow pump-down. As in the first commissioning experience of 2015, it was found that the RF performance of the cavities in the cryomodule exceeded that shown in the vertical tests.

Owing to the contamination of the two cavities, their maximum fields were limited to below the onset of field emission, i.e. to 3.5 MV/m. A suitable optics solution was accordingly found and the requested beams were delivered to the experiments for the 2016 physics campaign. The Q-E curves of all ten cavities can be seen in Figure 28.6. Operational bandwidths varied between 5 and 10 Hz. The LLRF loops were set up individually to achieve the most stable operation possible. Severe perturbations were found to detune all the cavities in a coherent fashion, which made the LLRF job particularly challenging. After a thorough search, the cause of the perturbation was localised in the cryogenics distribution system. The situation was somewhat mitigated by changing the operation point of the cryogenics process. A systematic investigation of the cryogenics performance, as well as all attempts to condition the two cavities with He processing, were postponed until after the physics run.
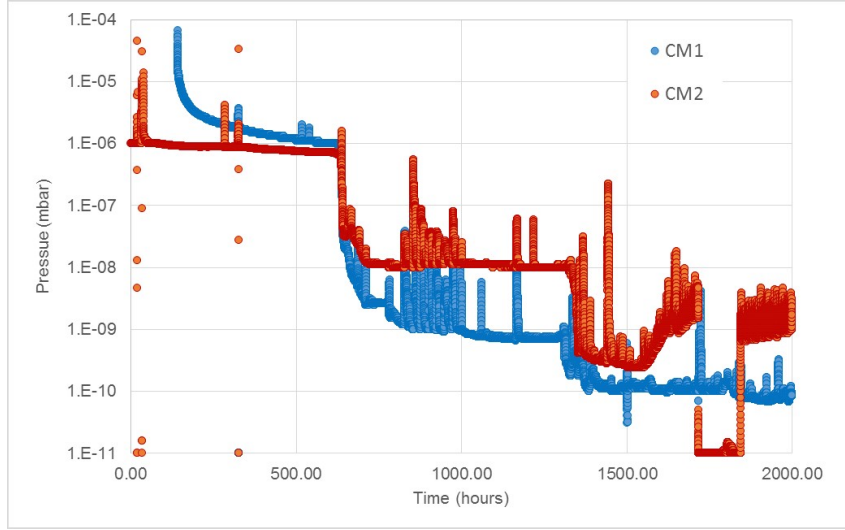
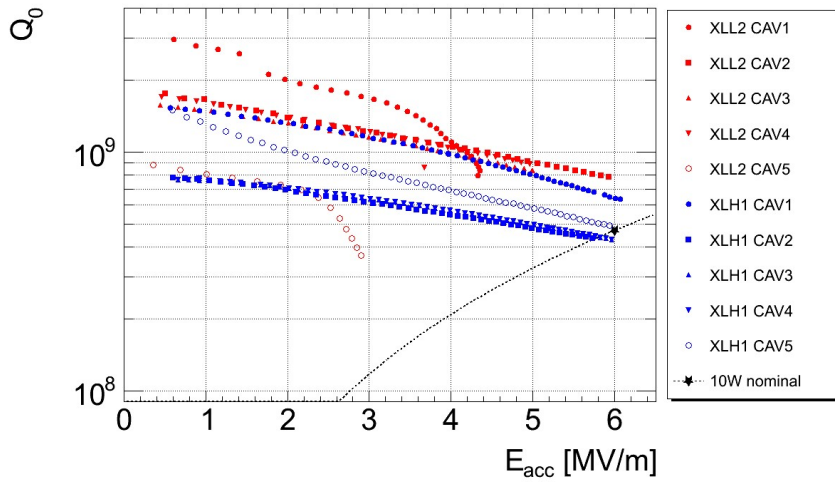**Fig. 28.5:** Beam vacuum in the two cryomodules during the 2016 run.



**Fig. 28.6:** Q vs $E^{acc}$ curves of diode sputtered cavities, July 2016.

During the commissioning of the solenoids, a short circuit to ground was identified in one of the bus-bars. The circuit could still be powered after securing the connection to ground, which was displaced very close to the earth fault. The operational current was limited to the minimum necessary for good beam transmission, in order to reduce the magnetic stored energy. The second solenoid underwent a training quench at 60 A and reached the nominal current of 110 A.

Alignment of active components was monitored and ensured by the MATHILDE system. Thermal contraction caused as expected 4 mm vertical shift, while lateral movement was negligible. Figure 28.7 depicts the horizontal and vertical positions of the cavities and solenoids during alignment.

After the physics run, He processing was successfully applied in situ to the two cavities in the first cryomodule which were affected by field emission from 2.5 and 3 MV/m respectively, resulting in recovering of the RF performance up to 5 MV/m for both cavities.

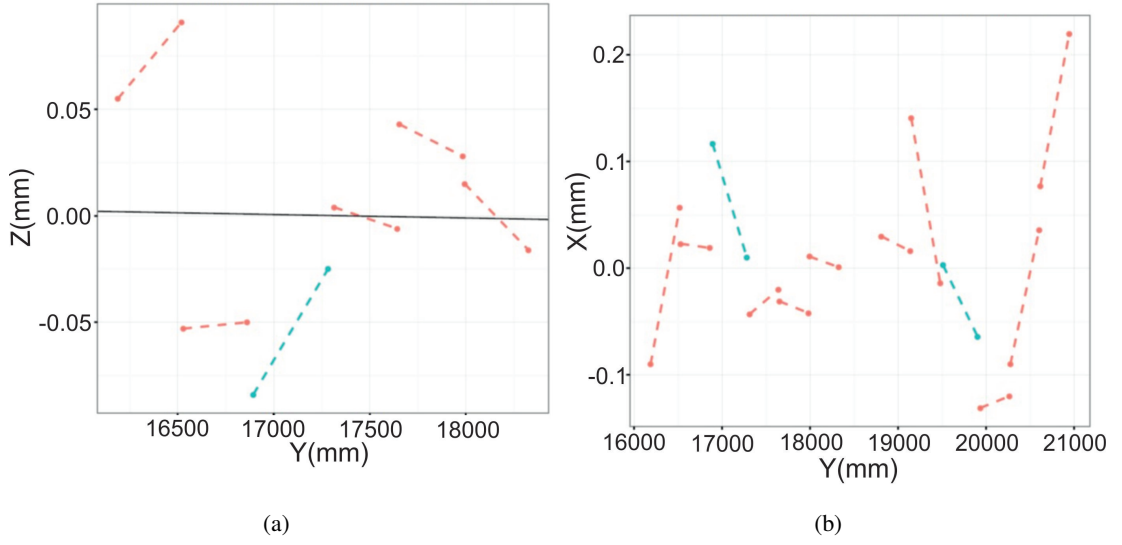The 2016 hardware commissioning campaign is presented in [3].

(a)                 (b)

**Fig. 28.7:** Longitudinal (Z) and transversal (X) positions of the cavities (in red) and solenoid (in blue) during cryomodule alignment.

**Beam commissioning**

Beam commissioning activities at the REX normal conducting injector were performed simultaneously with hardware commissioning at HIE-linac. A mixture of helium, carbon, oxygen, neon and argon beams with $A/q = 4$ was used for the setup beam. The beam was drifted through the cryomodules into the HEBT lines with REX energy and was used to commission the diagnostic boxes. Then, the superconducting cavities were phased, a process which also verified that the calibration of the gradients was accurate. The beam energy was measured using the first dipole of the first HEBT line, silicon detectors and a time-of-flight system.

Characterising the energy and energy spread of the beam is important for the users of the facility. The post-accelerator is equipped with several diagnostic devices that can be used to do the measurements that were commissioned during the 2016 campaign:

– Silicon detectors. Four detectors located in different positions along the linac and HEBT lines were used to measure changes in the beam energy and the energy spread of the beam, as seen in Figure 28.8.
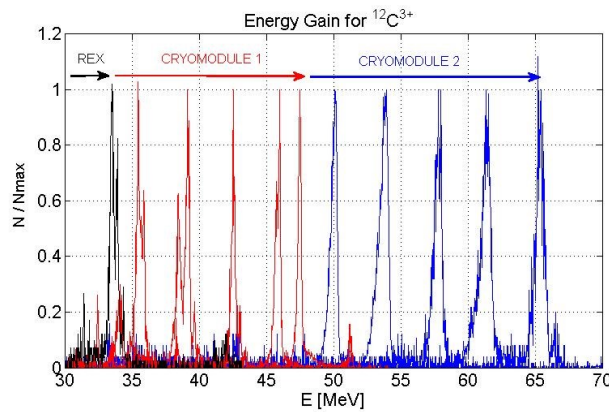


**Fig. 28.8:** Beam energy spectrum for all cavities.

– Dipole as an energy spectrometer. Slits before and after the first dipole of the first HEBT line were used to collimate the beam and select ions on the beam axis after the focusing and steering optical elements were turned off. The beam current past the dipole was measured for different magnetic fields, as shown in Figure 28.9. Both the energy spread and the absolute energy could be determined by this method using the previously-measured effective magnetic length of the dipole.
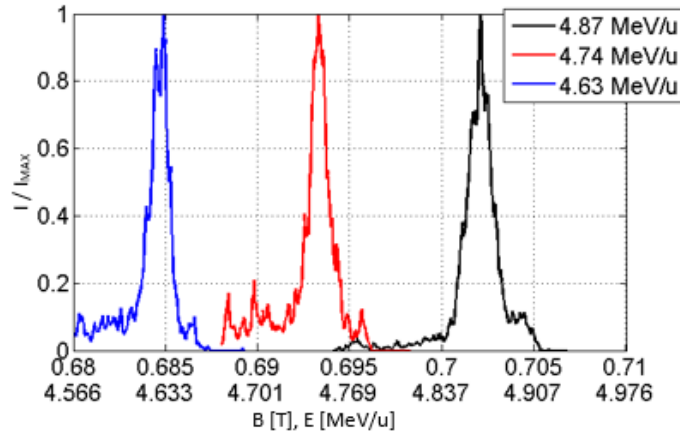


**Fig. 28.9:** Beam current measurement for different magnetic fields.

– Time of flight. The time-of-flight information provided by two of the silicon detectors located after the second cryomodule and separated by 7.76 $m$ was also used to measure the energy of the beam. The results of the measurements conducted during the beam commissioning showed that the uncertainty in the beam energy using this method was lower than $\pm 0.5\%$.

– Calibration of the RF systems. The energy of the beam can be calculated using the accelerating gradients, the Transit Time Factor (TTF) of the cavities and the synchronous phases of the beam. The typical uncertainty determining the energy of the beam using this method for a single cavity is $\pm 1\%$. The transverse profiles of the beam were measured using the scanning slits in several diagnostic boxes. The measurements conducted during the beam commissioning showed that beam profiles could be clearly determined for intensities as low as 10 epA. For example, Figure 28.10 shows three beam profiles measured for a beam with a total intensity of 42 epA. The three profiles correspond to different focusing strengths of a quadrupole located before the diagnostics box.

More details about the 2016 beam commissioning can be found in [4].

**Physics run**

Following the 2016 commissioning campaign, six experiments with radioactive ion beams (Table 28.3) took place in September 2016, taking advantage of the higher energies provided at the upgraded facility. The experimental teams mainly utilised transfer reactions and Coulomb excitation to investigate radioactive isotopes with masses ranging from $^{142}$Xe to $^{9}$Li. The success of the physics campaign both confirmed the technical choices of the HIE-ISOLDE team and showcased the remarkable extension of experimental opportunities that are now opening up thanks to the upgrade. Figure 28.11 provides an excellent example of HIE-ISOLDE's increased capabilities in comparison to REX. In early 2018, the energy upgrade will have been completed, allowing energies of up to 10 MeV/$u$ for $A/q = 4.5$.
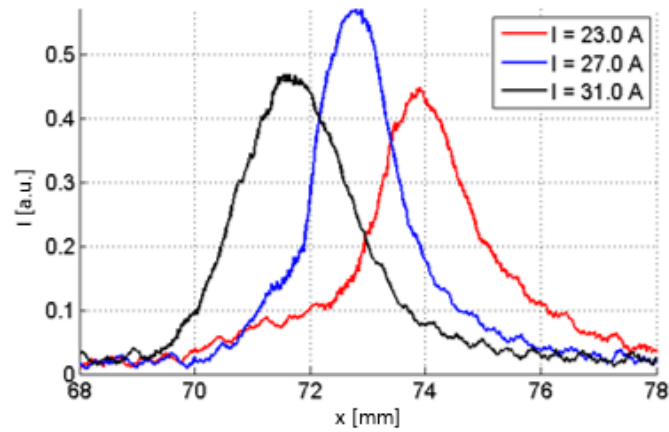
**Fig. 28.10:** Transverse beam profiles, measured for a beam with a total intensity of 42 epA; they correspond to the different focusing strengths of the quadrupole magnet before the diagnostic box.

**Table 28.3:** Overview of the six experiments that took place during the 2016 physics run.

|  | Beam | Energy [MeV/$u$] | Origin | HEBT | Experimental Station | Time [hours] |
|---|---|---|---|---|---|---|
| RIBs | $^{110}$Sn$^{26+}$ | 4.5 | GPS target | XT01 | Miniball Spectrometer | 115 |
|  | $^{142}$Xe$^{33+}$ | 4.5 | HRS target | XT01 | Miniball Spectrometer | 100 |
|  | $^{78}$Zn$^{20+}$ | 4.3 | GPS target | XT01 | Miniball Spectrometer | 130 |
|  | $^{132}$Sn$^{31+}$ | 5.5 | HRS target | XT01 | Miniball Spectrometer | 130 |
|  | $^{9}$Li$^{3+}$ | 6.7 | GPS target | XT02 | Scattering Chamber | 70 |
|  | $^{66}$Ni$^{16+}$ | 4.5 | GPS target | XT01 | Miniball Spectrometer | 140 |
| Stable | $^{22}$Ne$^{5+}$, $^{22}$Ne$^{6+}$ | 2.8 | REXEBIS | XT01 | Miniball Spectrometer | 60 |
|  | $^{12}$C$^{4+}$ | 6.7 | REXEBIS | XT02 | Scattering Chamber | 7 |
|  | $^{132}$Xe$^{32+}$ | 4.5 | GPS target | XT01 | SPEDE | 85 |
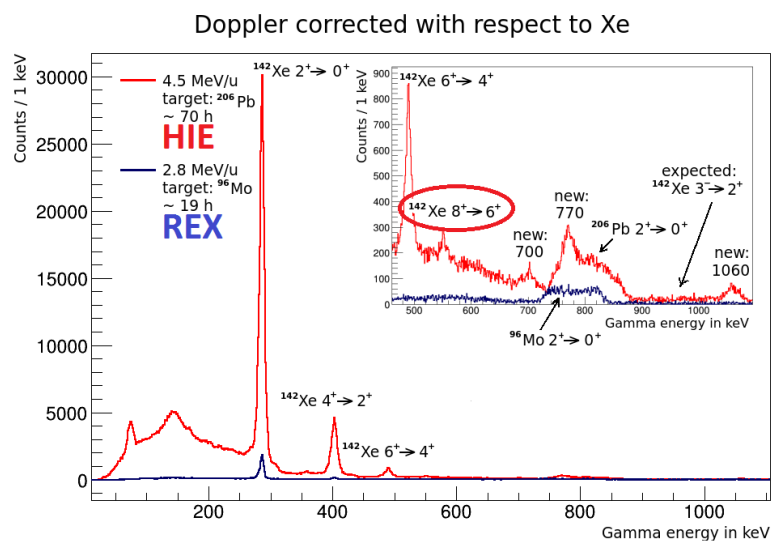


**Fig. 28.11:** Doppler corrected gamma ray spectrum of 4.5 MeV/$u$ $^{142}$Xe beam Coulomb excited on $^{206}$Pb target (in red) and the equivalent gamma spectrum for 2.8 MeV/$u$ $^{142}$Xe beam on a $^{96}$Mo target (in blue).

## 28.3   Commissioning 2017

### 28.3.1   Hardware commissioning

During the 2016 operations, several issues were identified in the cryogenic system, mainly related to CP flow limitations, bad LHe quality supply and strong oscillations in the 4.5 k return line. However, once the operational conditions were found, the cryogenic availability exceeded 99% and no unplanned stops occurred. Preventive and corrective maintenance was carried out during the Extended Year-End Technical Stop, including updates to the cryo plant logic to allow full performance and ease restarts, and the development a more robust refrigerator control system and processes, with automatisms allowing reconnection of cryomodules during cool-down. Endoscopic investigations revealed that the excessive heat load in the distribution system was caused by contact of the 4.5 K process pipes with the shield, as well as a hole in the shield that allowed the 300 K surface to radiate inside the JB. To remove major non conformities, a crash programme was launched, involving the insertion of spacer material around the process pipes to remove direct contacts. Thanks to the successful intervention, the performance of the cryo plant is now nominal. Capacity tests confirmed that it will be able to cope with the fourth cryomodule, scheduled for installation in 2018.

The 2017 hardware commissioning began on March 20 with warm tests. Cool-down started one week later and all cavities reached 4.5 K on April 18. Multipacting conditioning and radiofrequency measurements were done on all 15 cavities, as seen in Figure 28.12. While the overall RF performance is very good, two cavities were found to suffer from field emission: the fifth cavity of CM1 (XLL2.5), which was known to be vulnerable from the previous year, and the second of CM3 (XLH2.2). Their field emission onsets were at 4 MV/m and 3 MV/m respectively. Once again, a frequency perturbation was detected in the superconducting cavities, correlated to the liquid helium temperature and pressure oscillations, although it was less severe than the one observed in 2016. As the cavity frequency shift was slow (repeating every $10 - 20$ minutes) and limited to only about 10 Hz, it could be easily corrected by the cavity tuning system. In the following weeks, the LLRF system was set up and the solenoids powered.
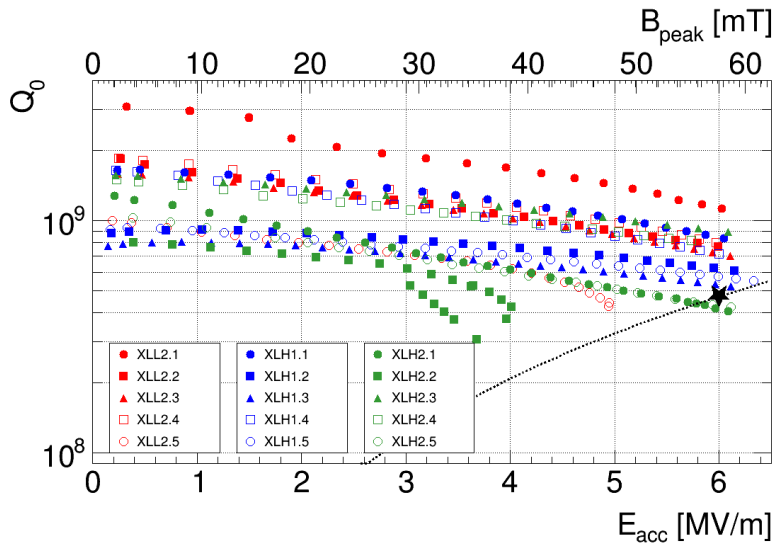


**Fig. 28.12:** Q vs $E_{acc}$ curves of the HIE-ISOLDE linac cavities.

### 28.3.2   Beam commissioning

Beam commissioning started in late May 2017, when hardware tests were completed. The count rate of the silicon detector after the first dipole of the XT01 line was used in combination with a collimator

slit to measure the energy and energy spread of the beam, presented in Figure 28.13. This method is especially effective, as it can be used for low intensity beams and can be completed in less than one hour.
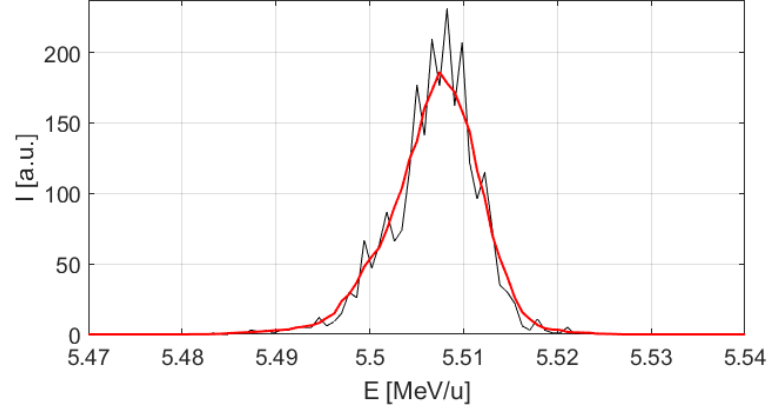


**Fig. 28.13:** Measurements of energy and energy spread of a $^{28}Mg^{9+}$ beam.

A phase scan was carried out using the count rate measured at the silicon detector. Certain unexpected behaviours were observed; needed beam attenuation varied by several orders of magnitude from cavity to cavity and the distance between zero-crossing phases was not always $180^{o}$. It was also possible to use a Faraday Cup for phase scans (Figure 28.14. Even though the measurements of the zero-crossing phases are less precise, they are faster and less likely to damage the silicon detector, therefore this method was chosen to phase the cavities.

Multiple beam set-ups were prepared and beam transmissions and transverse beam profiles were measured at each diagnostics box. It was concluded that low energy beams can be transported without additional losses and beam losses in HIE-ISOLDE are negligible.

In late June, cavities in the second and third cryomodules were phased with a $^{14}N^{4+}$ beam that reached a final energy of 6.6 MeV/$u$. The second and the third high-energy beam lines were commissioned a few weeks later. The first stable stable beam $^{22}$Ne at 4MeV/$u$) was delivered to the Miniball Spectrometer for testing and calibration. Both REX and HIE-linac demonstrated quite stable operation over 60 hours. Operation with radioactive beams ($^{72}$Se) began in early July.
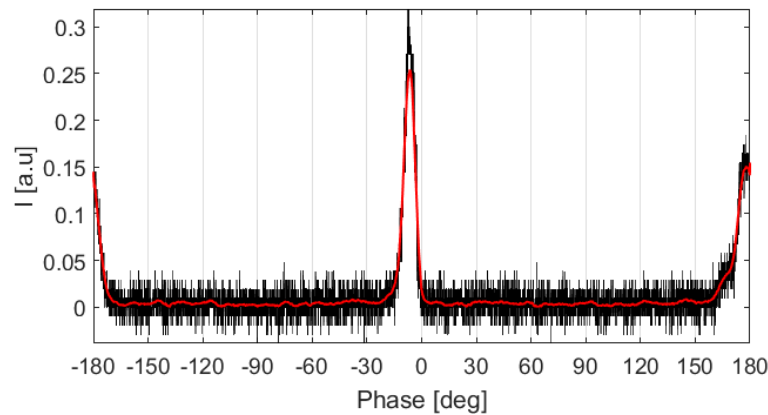


**Fig. 28.14:** Phase scan done during the phasing procedure of the second SRF cavity of the first cryomodule.

239

### 28.3.3   Physics run

A busy physics run was in line for 2017 with 12 scheduled experiments in 136 days. Most of them used the Miniball spectrometer, mainly to conduct Coulomb excitation studies, while others take advantage of the scattering chamber and visiting setups. A wide range of isotopes was be studied, from $^{9}$Li to $^{206}$Hg.

Phase 2 of the HIE-ISOLDE energy upgrade will be completed in 2018, with the installation of the fourth high-beta cryomodule, which is currently being assembled. Cavity production for CM4 has almost been concluded. It will be ready for bunker tests in September. Its addition to the linac will allow beam energies up to $10 - 15$ MeV/$u$, depending on the $A/q$, opening up new physics opportunities and making ISOLDE the only facility in the world capable of accelerating medium to heavy radioactive isotopes in this energy range.

### References

[1] J. Rodriguez et al., Beam commissioning of the HIE-ISOLDE post-accelerator, CERN-ACC-2016-230 (CERN, 2016).

[2] W. Venturini Delsolaro et al., HIE-ISOLDE: First commissioning experience, CERN-ACC-2016-227 (CERN, 2016).

[3] W. Venturini Delsolaro, HIE ISOLDE HW commissioning in 2016, ISOLDE workshop, 2016.

[4] J. Rodriguez, Beam commissioning and operations of the REX/HIE-ISOLDE post-accelerator, ISOLDE Workshop and Users Meeting, 2016.